Shock and Vibration

Vibration and Failure of Transmission Line Systems under Extreme Loading Conditions

Lead Guest Editor: Li Tian
Guest Editors: Bing Qu and Zhitao Yan

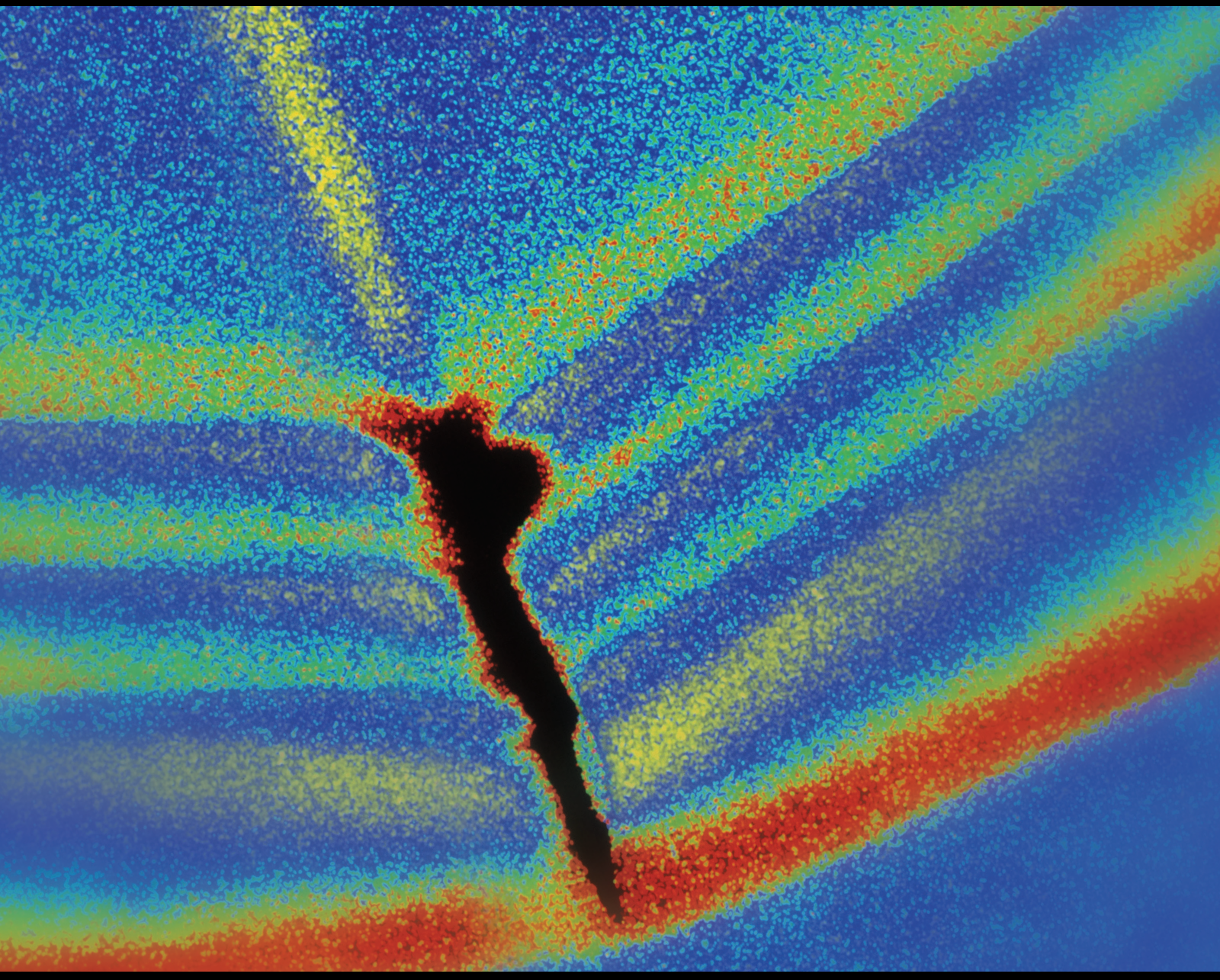

Vibration and Failure of Transmission Line Systems under Extreme Loading Conditions

Shock and Vibration

Vibration and Failure of Transmission Line Systems under Extreme Loading Conditions

Lead Guest Editor: Li Tian
Guest Editors: Bing Qu and Zhitao Yan

Contents

Hindawi
Shock and Vibration
Volume 2022, Article ID 4924091, 12 pages
https://doi.org/10.1155/2022/4924091

Research Article

Analysis of Wind-Sand-Load-Induced Dynamic Response of Transmission Tower-Line Systems

Zhuoqun Zhang,[1,2] **Jiashu Liu**,[3,4] **Kangjie Shao**,[5] **and Peng Zhang**[3]

[1]*State Grid Economic and Technological Research Institute Co Ltd, Beijing 102209, China*
[2]*State Nuclear Electric Power Planning Design & Research Institute CO. LTD, Beijing 100095, China*
[3]*Institute of Road and Bridge Engineering, Dalian Maritime University, Dalian 116023, China*
[4]*China Nuclear Power Engineering Co., Ltd, Beijing 100089, China*
[5]*China Academy of Building Research, CABR Technology CO LTD, Beijing 100013, China*

Correspondence should be addressed to Peng Zhang; peng.zhang47@dlmu.edu.cn

Received 12 October 2021; Revised 9 July 2022; Accepted 12 July 2022; Published 25 August 2022

Academic Editor: Ahmed Ibrahim

Sandstorms are a common natural phenomenon that has the potential to cause severe disruptions to civil infrastructure. However, the effect of sandstorms on transmission tower structures has not received much attention. This paper proposes the simulation of the wind-sand loads for the analysis of transmission tower structures under sandstorm excitation by superposing the wind loads and sand particle loads. The wind load is generated based on Kaimal fluctuating wind power spectrum and the harmonic superposition method, and the sand load is constructed based on the law of conservation of momentum and sandstorm classification. A transmission tower was modeled and simulated in SAP2000 to explore the dynamic response of the tower towards wind-sand loads. A comparison of wind-induced and wind-sand-induced responses shows that the structural dynamic responses of transmission towers due to the wind-sand effect are pronounced. Particularly, the maximum longitudinal displacements and axial forces increased greatly. The results showed that the sandstorm loads for transmission towers cannot be neglected, and more attention should be paid to the structural design of transmission towers to resist such loads.

1. Introduction

Power transmission tower-line systems, which are the physical structures supporting the massive national power grid of China, have seen large-scale constructions during the past decades to meet the ever-increasing energy demands associated with the rapid growing economy. Several lines composed of ultra-high voltage transmission towers have been built to convey clean energies from northwestern China to eastern China. These structures are all exposed to the harsh environmental hazards of this arid area, of which the seismic activities, strong winds, erosions, and corrosions have been carefully dealt with during the design and/or maintenance process. However, the action of sandstorms is not yet fully considered, even though they may cause severe destruction to the transmission towers, as shown in Figure 1.

The sandstorm is harmful weather that commonly occurs in the Gobi or desert regions. He et al. [1] simulate a local dust storm through a cold pool with certain vorticity. When the wind speed reaches a certain level, it can lift the top layer of sand from the ground and smash it against any obstacle that confronts it. As the wind speed increases, the destructive power grows exponentially since more particles will be driven by stronger winds.

Sandstorms have attacked many countries and regions around the world, including China, Africa, western United States among others, causing pollution of air, loss of property, and even death of humans and animals. Chinese scholars Yang et al. [2] have discovered the catalytic effect of sandstorms on PM2.5 in high-altitude areas in southern China, which is harmful to humans. American scholars Prospero et al. [3] use a spectrometer to determine the

(a) (b)

Figure 1: Facilities of the power grid subjected to a sandstorm: (a) power substation; (b) tower-line system.

source of sand particles in the atmosphere and the environmental characteristics of sandstorms.

Another hazard of the sandstorm is the moving dunes, which may cause permanent foundation displacement. Qian et al. [4] conducted experiments on building foundations under wind and sand loads, and the foundation moved under horizontal loads. Besides, the impact of subsoil flexibility should be considered in the computations. In order to analyze the hazard of the sandstorm, the sand transmission has been extensively studied during the past decades. Yang et al. [5] proposed a method to determine the velocity fields based on fluorescent tracer particles. Sherman and Li [6] compared eight sand-transport models based on field data. Experiments were conducted to reveal the relationship between the transport rate of dry sand and shear velocity [7]. The recently developed models can also be found in the following review papers [8, 9].

The hazards of sandstorms also attracted some attention from the electrical and structural engineers when they design transmission towers. One major hazard that has been intensively investigated and evaluated is the corona effect induced by the floating sand particles. Gao and Shi [10] researched the discharge mechanism of transmission lines under wind-sand load. Yunpeng et al. [11] analyzed the wires of ultra-high voltage AC lines in high-altitude areas and found that they would produce corona loss under sand and dust conditions.

There are two main types of wind involved in the engineering structure, one is large-scale winds (temperate and tropical cyclones, etc.); the other is small-scale local strong winds (typhoons, tornadoes, thunderstorms, etc.). Ishac and White [12] first proposed the basic design load of the tornado on the transmission tower-line system through investigation and research based on the relevant records of tornadoes in Ontario, Canada. Milford and Goliger [13] proposed a model formula for the probability of a tornado on the basis of previous studies, but the model did not consider the azimuth relationship between the transmission tower line, the tornado path, and the transmission tower. Savory et al. [14] established models of transient tornadoes and micro-storms, and at the same time calculated the wind speeds of the two high-strength winds over time and the loads acting on the lattice tower. And under the action of the two high-strength winds, the structure was dynamically analyzed, and the shear failure of the structure under the tornado was successfully predicted. Oliver et al. [15] assumed that the damage shape of the downburst wind accompanying a thunderstorm was a rectangle, and the transmission line was studied as a line, and established a practical model to evaluate the damage caused by the downburst wind acting on a specific length of wire. Li [16] proposed a probabilistic model for the design of transmission towers to actually and accurately simulate the wind load generated by the burst wind. This model is calibrated with previous meteorological data. Its biggest advantage is that it takes into account the influence of the size of the lower burst stream. Shehata et al. [17] established a mathematical model describing the burst wind based on the calculation data of the effective computational fluid dynamics model developed and verified by the predecessors. The geometric nonlinearity of the wire was considered, and the power transmission caused by the burst wind was analyzed and calculated.

In a related field, it is proved that the wind-driven rainfalls can severely aggravate the wind-induced vibration of high-rise or long-span structures, including suspension bridges, transmission towers. Orr and Cassar [18] use extreme wind-driven rainfall to calculate the exposure index of buildings to rainwater. Hao [19] studied the surface characteristics of large-diameter composite pillar insulators for

Table 1: Parameters of the typical intensity of sandstorms.

Parameters	Floating dust	Blowing sand	Sandstorm			
			Weak	Medium	Strong	Extra strong
Horizontal visibility	10 km	1–10 km	1 km	750 m	500 m	50 m
Wind speed (m/s)	3	6	10	15	20	25
Particle diameter (μm)	0.5	2	5	20	40	100
ρ_{TSP} (mg/m^3)[1]	0.3	1	6 (3–10)	15	25 (10–30)	100
Volume ratio	1.2	4.0	24	60	100	400

[1]ρ_{TSP} denotes the mass density of a sandstorm. TSP is the abbreviation of traveling sand particles.

transmission towers when rainfall is considered through experiments. An et al. [20] studied Windage Yaw Flashovers of transmission lines under wind and rain loads. Zhou et al. [21] studied the performance of large swing amplitude of overhead transmission lines under rain load. Compared with a raindrop, a floating sand particle contains more mass and thus has more kinetic energy at the same velocity. There are amounts of water from intensive rainfalls that flow relatively slowly from the lightweight steel structures, causing the temporary but possibly high structural mass increase, and snowstorms do not trigger such reactions.

It can be seen from the researches of the above scholars that most of the previous studies on the transmission tower-line system only analyzed the effect of other external loads such as wind load or rain load on the tower-line system and ignored the impact of sandstorms that may be caused by sand particles in the wind. Factor: in this paper, by formulating the calculation formula model of the sand storm, using the SAP2000 finite element software component linear tower-line system model, the deduced wind-sand load is applied to the tower-line system, and the straight-line tower is compared between the pure wind load and the sand load. The dynamic response of the line system: the results derived in this paper prove that sandstorms can amplify the dynamic response of power transmission towers. When the wind speed intensity of the sandstorm reaches 25 m/s, the sand load has the most obvious effect on its dynamic response amplification.

2. Wind-Sand Load Model

2.1. Sand Load Model. In order to enable the dynamic analysis of a transmission tower-line system subjected to wind-sand loads, the behavior and key parameters of sandstorms need to be characterized. The portion of a sandstorm depends on the wind speed and the general configuration of the land surface it passes. According to the existing literature and comprehensive analysis of sandstorm observation data [22], there is an obvious and direct correspondence between the sandstorm intensity and sand concentration, as shown in Table 1. It can be observed that as the wind speed increases, more sand particles can be lifted from the ground, resulting in an increasement in mass density ρ_{TSP} and volume ratio.

The momentum theorem has been widely accepted for analysis of the erosion of the sandstorm on the surface coatings of steel members [23]. According to the momentum theorem, when a sandstorm occurs, an individual sand particle can generate an impact load on the structure [24] as follows:

$$F_s(\tau) = \frac{1}{\tau}\int_0^{\tau} f(t)\mathrm{d}t = \frac{mv_1 - mv_2}{\tau}, \tag{1}$$

where m is the mass of the single sand particle; v_1 is the velocity of the sand particle before acting on the structure; v_2 is the velocity of the sand particle after acting on the structure; and $F_s(\tau)$ is the impact force generated by the individual sand particle.

Assuming that the collision between the individual sand particle and structural components is elastic, the sand particle velocity is kept constant in the opposite direction. Besides, it requires perpendicularity of element area to the wind direction.

$$v_1 = -v_2 = v_s. \tag{2}$$

Here, v_s is the average velocity of a single sand particle during the sandstorm; $F_s(\tau)$ is the impact force vector of the single sand particle acting on the transmission tower.

The impact force of a single particle of sand can be converted into a uniformly distributed load. During the collision, the shape of a single sand particle is regarded as a spherical shape. The mass of the sand grain is $m = \rho\pi d^3/6$; τ is the time when the load acts on the transmission tower; m_i ($i = 1,2, \ldots, N$) is the weight of the ith sand grain. The impact force τ of a single sand particle on the transmission tower in a unit time interval can be calculated by the following formula:

$$\begin{aligned} F_s(\tau) &= \frac{2v_s}{\tau}\sum_{i=1}^{N} m_i \\ &= \frac{1}{\tau}2v_s\frac{1}{6}\pi\sum_{i=1}^{N}\rho_i d_i^3 \\ &= \frac{1}{3\tau}\pi v_s\sum_{i=1}^{N}\rho_i d_i^3. \end{aligned} \tag{3}$$

Suppose the surface of the transmission tower is impacted by sand particles all with a specified diameter, their combined impact force can be calculated as follows:

$$F_i = F_s(\tau)n_i, \tag{4}$$

where F_i is the summation of impact forces during the time τ; n_i is the number of sand particles that impacted on the tower during the time τ.

During τ, the volume of air and sand that flows across the steel member of the transmission tower can be calculated as follows:

$$V = 2Al, \tag{5}$$

where A is the windward area exposed to the sand load; l is the distance that the wind-sand flow travels within the duration τ. So the sand load can be calculated as follows:

$$\begin{aligned} F_s &= F_i V = F_i 2Al \\ &= \frac{2}{3}\pi v_s^2 A \sum_{i=1}^{N} \rho_i n_i d_i^3. \end{aligned} \tag{6}$$

Based on the sand storm intensity (Table 1 [22]), the accumulated sand particles at a selected height can be estimated by a simplified equation as follows:

$$Q = \sum \rho_{\mathrm{TSP}} A_s V_h T. \tag{7}$$

Here, Q is the total sand accumulation amount observed at a certain height; ρ_{TSP} denotes the sand flow density of a specific wind speed (as listed in Table 1); A_s is the inlet area of sand collection equipment of the sediment observation system; V_h is the velocity of the sand particle; and T is the sampling interval of the actuation duration.

Equation (6) and (7) can be manipulated as follows:

$$\sum \rho_{TSP} A_s v_s T = \frac{1}{6}\pi \sum_{i=1}^{N} \rho_i n_i d_i^3 T A v_s. \tag{8}$$

Suppose the unit area of the transmission tower section is A, the windward area of the round steel pipe is the vertical projection of the round steel pipe under the action of wind speed, and the diameter projected on the Z-axis is the area corresponding to the round steel pipe. The total weight of steel used in the transmission tower is W, the section thickness is T, and the weight density of angle steel or steel pipe is γ, then the area A is

$$A = \frac{W}{T\gamma}. \tag{9}$$

Therefore, the final calculation formula of sand load related to sand storm concentration, sand speed, and sand load's action area is:

$$F_s(t) = 4\rho_{\mathrm{TSP}} v_s(t)^2 A. \tag{10}$$

Here, $F_s(t)$. is the sand load, v_S is the average velocity of a single sand particle; ρ_{TSP} is sand particle concentration in a unit volume, and A is the area acted on by the sand load.

2.2. Wind Load Model. The calculation of the dynamic wind load of the transmission tower-line adopts the bridge quasi-steady aerodynamic formula. When the MATLAB software is used to calculate the time history curve of the dynamic wind load of the transmission tower, the calculation formula of the wind speed changing with time at the nodes of the transmission tower structure is:

$$V(z,t) = \overline{V}(z) + V_f(z,t). \tag{11}$$

In this equation, $\overline{V}(z)$ is the average wind speed at height z; $V_f(z,t)$ denotes the fluctuating wind speed at height h. In this paper, the power transmission tower system uses a logarithmic-based wind profile.

$$\overline{V}(z) = \frac{1}{k} u_* \ln\left(\frac{z}{z_0}\right). \tag{12}$$

Here k is the Karman constant, which is an empirical coefficient introduced by von Karman's assumption of the relationship between the mixing length and the velocity profile. The measured value of the laboratory and the surface layer of the atmosphere is between 0.35 and 0.43. In recent years, 0.40 is considered to be more reasonable. In (12), z_0 = 0.2m is the ground roughness length, and u_* is the friction speed.

In addition, Kaimal considers the variation of the turbulence power spectrum with height in the atmospheric turbulence movement, and its longitudinal turbulence power spectrum expression is:

$$S_u(f) = \frac{200K\overline{V_{10}}^2}{f} \times \frac{x}{(1+50x)^{5/3}}, \tag{13}$$

where $x = hf/\overline{V_{10}}$ is the dimensionless Monin coordinate. h is the height of the simulation point, and f is the frequency of fluctuations in the wind.

The harmony superposition method is a discrete numerical method to simulate the steady random process. An arbitrary signal can be decomposed into a series of sinusoidal waves with different frequencies and amplitudes through the discrete Fourier transform. The time series describing the fluctuating wind velocity can be regarded as a stochastic process and can be characterized by its power spectrum. When $N \longrightarrow \infty$, with the theory presented by Shinozuka [25], the fluctuating wind velocity time series $\mu_i(t)$ can be modeled by

$$\begin{aligned} u_i(t) &= \sum_{l=1}^{i}\sum_{k=1}^{N} \left|H_{il}(\omega_k)\right| \sqrt{2\Delta\omega_k} \cos\left[\omega_k t - \theta_{il}(\omega_k) + \varphi_{lk}\right], \\ i &= 1, 2, \ldots, m, \end{aligned} \tag{14}$$

where i is the number of calculation points, H_{il} is obtained from the Cholesky decomposition of the wind cross-spectral density matrix, $\theta_{il}(\omega)$ is the argument of $H_{il}(\omega)$, and φ_{lk} denotes the uniformly distributed random numbers in [0, 2π]. Integrate the density in the power spectrum:

$$\int_0^{\omega_u} S(\omega)d\omega = (1-\varepsilon)\int_0^{\infty} S(\omega)d\omega, \tag{15}$$

where ω_u is the upper limit of the angular frequency in the wind fluctuation, $S(\omega)$ is the auto-power spectrum density function, and $S(\omega)$ <1. The increase in frequency is:

$$\Delta\omega = \frac{(\omega_u - \omega_s)}{N}, \tag{16}$$

in which, $\Delta\omega$ is frequency increment; N represents the divisor of fluctuating wind frequency. To increase the period of the simulated sample, Shinozuka [26] suggested that

$$\omega_k = k\Delta\omega_k - \frac{N-l}{N}\Delta\omega_k = (k-1)\Delta\omega_k + \frac{l}{N}\Delta\omega_k. \quad (17)$$

Here, N should be a sufficiently large positive integer to avoid distortion. The time increment of the simulated time series can be determined in the following ways:

$$\Delta t = \frac{T_0}{M} = \frac{2\pi}{M\Delta\omega} = \frac{2N}{M} \times \frac{\pi}{\omega_u}. \quad (18)$$

The number of samples in the simulation time series is M, where M is an integer, and M should be greater than 2N; and the time increment should be small enough, Ensure that $\Delta t \leq \pi/\omega_u$.

2.3. Wind-Sand Loads Applied to the Transmission Tower. The dynamic response of the transmission tower subjected to a sandstorm can be analyzed as the response of the tower to wind loads and sand loads, similarly to the wind-rain effect [27, 28]. Thus, the load per unit volume F experienced by the transmission tower structure can be calculated as follows:

$$F = F_w + F_s, \quad (19)$$

where F_w represents the wind load per unit volume and F_s the sand load per unit volume.

The along-wind loads are calculated by:

$$F_w(t) = \frac{\mu_s A v_s(t)^2}{1.6}, \quad (20)$$

where A is the area acted on by wind, μ_s is the shape coefficient, and $v_s(t)$ is the wind speed.

Substitution of (10) and (20) into (22) yields:

$$F(t) = F_w(t) + F_s(t) = \frac{\mu_s A v_s(t)^2}{1.6 + 4\rho_{TSP} v_s(t)^2 A}. \quad (21)$$

3. FE Model of the Transmission Tower-Line System and the Wind-Sand Loads

3.1. Structural Model of Transmission Tower. The prototype tower of this study is the SZ27104 J straight-line tower (Figure 2), with a height of 123.6 m, a width of 24.48 m, and a typical horizontal span length of 400 m. The structure is constructed mainly from Q235 and Q345 steel pipes and angle irons with an elastic modulus of 206 GPa. According to the linear tower model in SAP2000, the overall control parameters of the model in MATLAB are determined. This article takes the SJ27103JD linear tower as the engineering background. The linear tower finite element model contains 306 nodes, 888 members, 41 cross section types, 4 boundary conditions, and 1836 degrees of freedom members are made of Q345 steel, while the auxiliary members are made of Q235 steel. The dimensions of the main cross-sections of the linear tower are marked in Figure 2. In Figure 2, R-means round steel pipe, and L-means angle steel. The tower-line system (Figure 3) consists of 4 self-supporting towers and 5 spans. Each span is composed of three levels of eight-bundle conductors and optical ground wires (OPGW), of which the model number and specifications are listed in

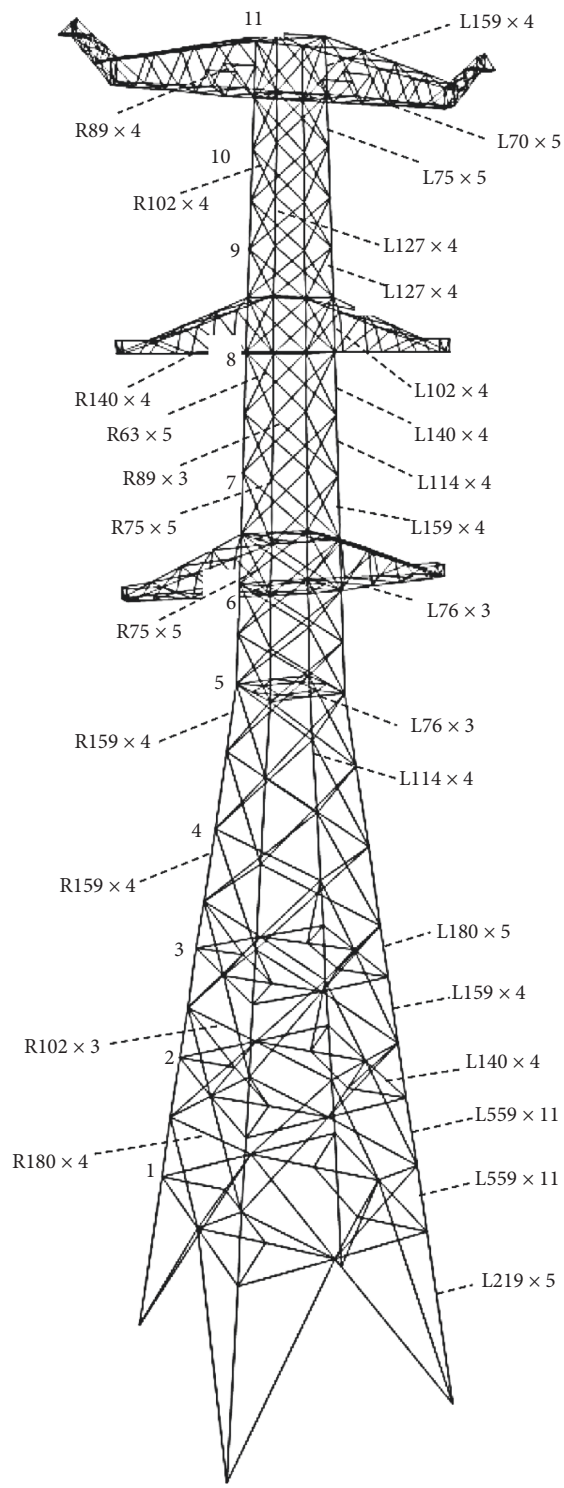

Figure 2: The finite element model of the SZ27104J linear tower and the dimensioning of its section.

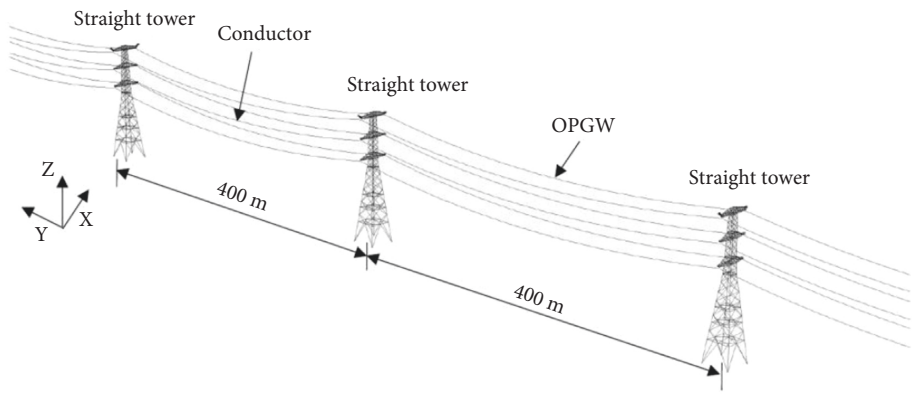

Figure 3: Model of the transmission tower-line system established in SAP2000.

Table 2: Specification of conductors and OPGW.

Type	Conductor	OPGW
Line model number	JL1/LHA1-465/210	OPGW-185
Cross section area	673.73 mm^2	184.38 mm^2
Diameter	33.75 mm	18.2 mm
Mass per unit length	1.8642 kg/m	1.256 kg/m
Tensile capacity	130169 N	211700 N
Elastic modulus	55000 N/mm^2	162000 N/mm^2
Thermal expansion coefficient	23×10^{-6}°C	13×10^{-6}°C
Bundle number	8	1

Table 2. Simulations were conducted using the finite element software SAP2000.

3.2. Wind-Sand Load Simulation. In this paper, Kaimal fluctuating wind energy spectrum and harmonic superposition method are used to simulate wind load in MATLAB. According to Table 1, the average wind speed $V10$ at a height of 10 m is set to 3 m/s, 6 m/s, 10 m/s, 15 m/s, 20 m/s, and 25 m/s. When the average wind speed V_{10} of the transmission tower at a height of 10 m is set to 3 m/s, 6 m/s, and 10 m/s, the response value of the linear tower-line system under the action of wind-sand load and pure wind load does not exceed the difference 1.54%, so in the analysis in Section 4, only wind speeds of 15 m/s, 20 m/s, and 25 m/s are selected to act on the linear tower-line system.

The foundation flexibility in desert conditions may highly affect dynamic structural response compared to standard subsoil foundations. There are a large number of nodes in the transmission tower, so it is impossible to perform a time history analysis of the wind speed at each node in the transmission tower. Since it is necessary to analyze the dynamic response of the entire transmission tower-line system under wind load conditions, it is also necessary to determine the point of action of the wind load on the conductor in the tower-line system. According to Figure 4, the transmission tower is simplified to 11-layer mass points. Figure 4 shows the simplified number and number of nodes in the straight-line tower. The other

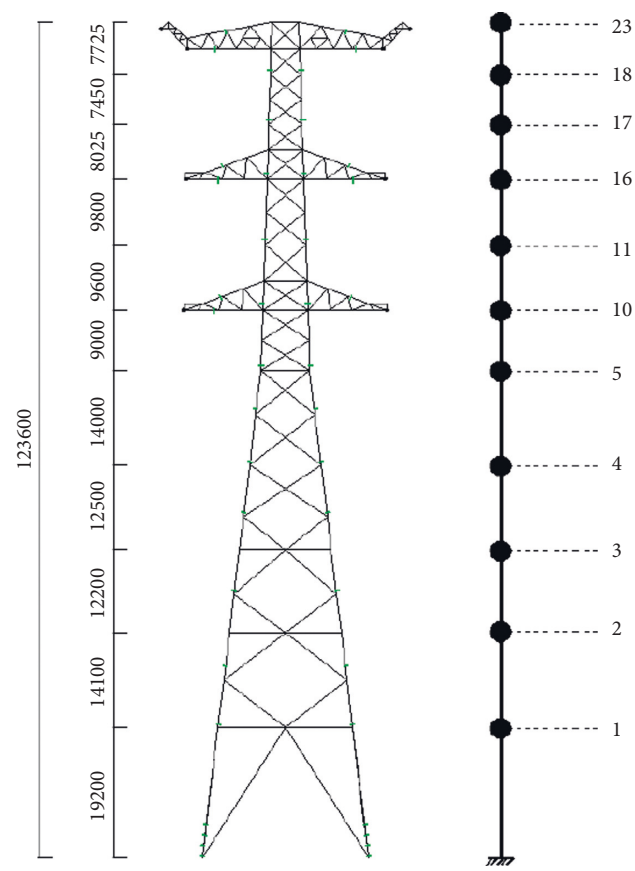

Figure 4: Wind simulation points.

numbers not shown in Figure 4 are simplified mass points selected on the wire; therefore, the straight-line tower-line system is divided into 23 mass point regions in total. The position of the load and the windward areas are listed in Table 3.

In order to simulate wind loads in MATLAB, the parameters of the wind speed time history model need to be determined.

The simulation coverage interval is 8.3 min, the frequency of wind speed fluctuation is f_s, and the value range is 0.1~100 Hz. Due to:

Table 3: The positions of wind load and windward areas.

Point	Height (m)	Area (m^2)	Point	Height (m)	Area (m^2)	Point	Height (m)	Area (m^2)
1	19.20	35.63	9	76.32	0.03	17	103.09	0.18
2	33.30	22.13	10	81.00	19.49	18	105.07	0.13
3	45.50	17.14	11	83.89	0.18	19	108.43	4.96
4	58.00	16.19	12	85.87	0.13	20	109.02	0.08
5	64.49	0.18	13	89.82	0.08	21	114.92	0.03
6	66.47	0.13	14	90.60	7.49	22	115.88	4.41
7	70.42	0.08	15	95.72	0.03	23	123.60	13.42
8	72.00	13.79	16	100.40	15.84			

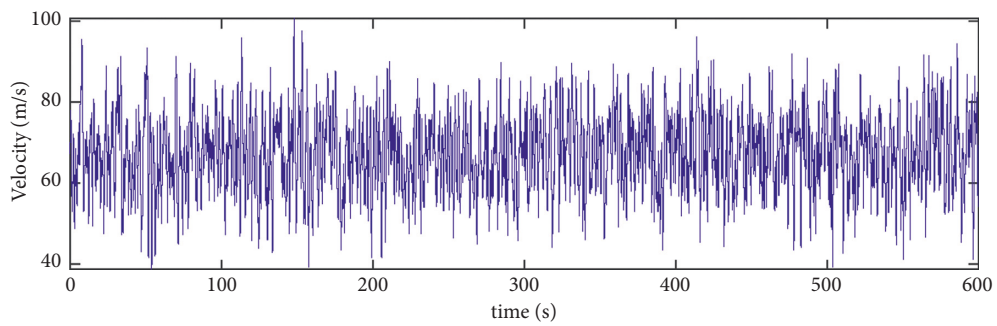

Figure 5: The time history of wind speed at the top of the tower, $V_{10} = 25$ m/s.

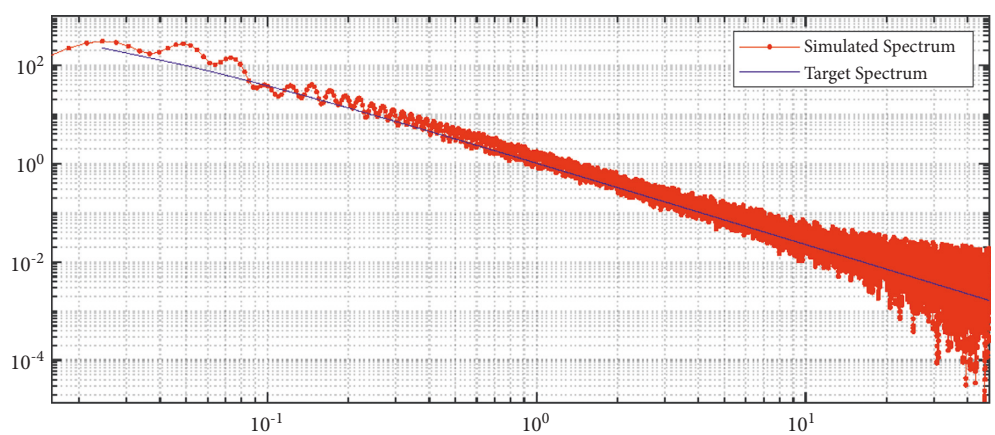

Figure 6: Power spectral comparison at the top of the tower, $V_{10} = 25$ m/s.

$$dt = \frac{1}{f_s}. \tag{22}$$

To capture higher frequency fluctuations in the wind, the f_s value is 100 Hz, so the time interval dt is 0.01 s. Figure 5 shows the simulated wind speed at the top of the tower, when the wind speed at 10 m, $V_{10} = 25$ m/s. The turbulence intensity in this situation is 0.366. Figure 6 shows the power spectrum density of the simulated fluctuating wind compared to the target spectrum.

4. Dynamic Response Analysis of the Tower-Line System under Wind-Sand Load

The dynamic response of the power transmission tower-line system can be obtained by the following motion equation:

$$[\mathbf{M}]\{\ddot{x}(\mathbf{t})\} + [\mathbf{C}]\{\dot{x}(\mathbf{t})\} + [\mathbf{K}]\{\mathbf{x}(\mathbf{t})\} = \{\mathbf{P}(\mathbf{t})\}, \tag{23}$$

where $[\mathbf{M}]$, $[\mathbf{C}]$, and $[\mathbf{K}]$ represent structural mass, damping and stiffness matrices, respectively; $\{\ddot{x}(\mathbf{t})\}$, $\{\dot{x}(\mathbf{t})\}$, and $\{\mathbf{x}(\mathbf{t})\}$ are the acceleration, velocity, and displacement vectors, respectively; $\{\mathbf{P}(\mathbf{t})\}$ is the vector of the loads generated by (20) (pure wind load) or (10) (wind-sand load). In this study, six levels of wind-sand loads are generated based on the parameters of the sandstorms, as listed in Table 1. Pure wind loads are also generated to compare the increasement of dynamic response. In equation (24), the damping matrix $[\mathbf{C}]$ can be expressed in the form of Rayleigh damping, assuming that the modal damping ratio is 2%, according to the design manual.

It should be noted that the stiffness of the wire is a time-varying parameter, since it depends on the time-varying shape of the wire (also known as geometric nonlinearity). Therefore, the nonlinear time-domain analysis shall be performed to

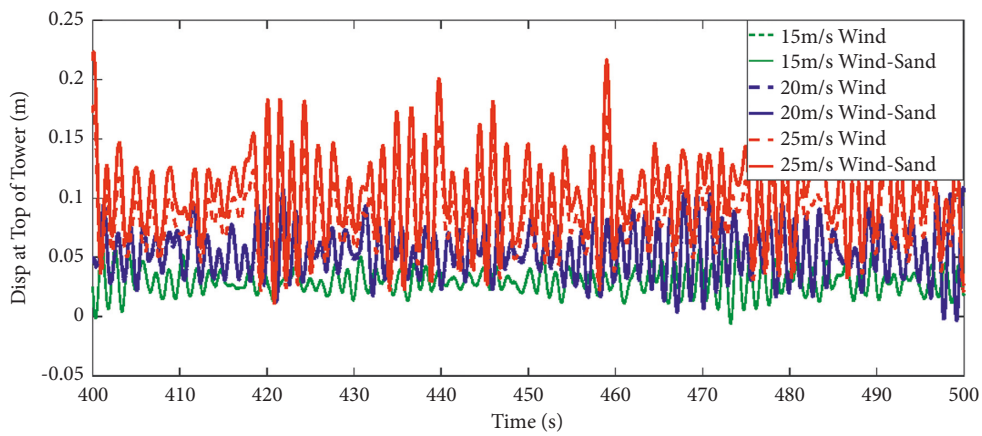

Figure 7: Displacement at the top of tower 2#.

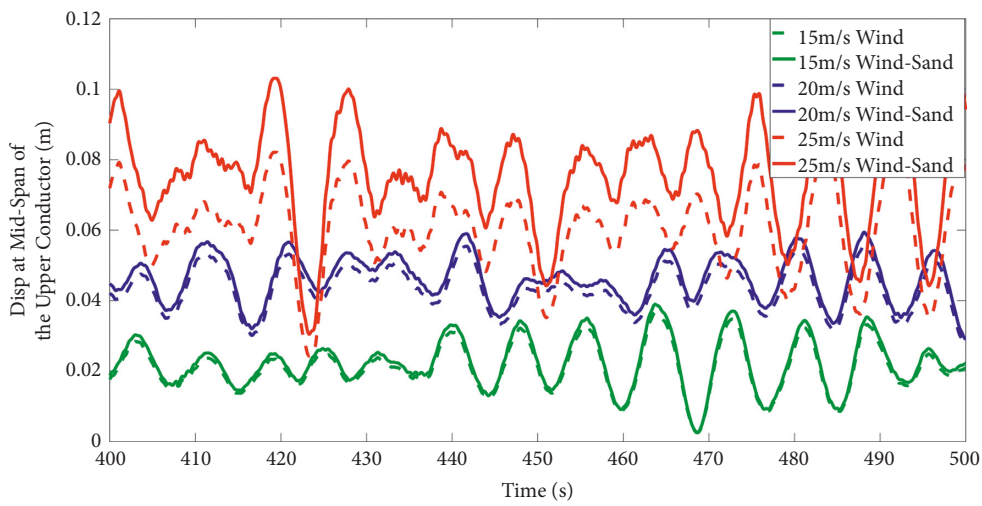

Figure 8: Displacement at the mid-span of the upper conductor.

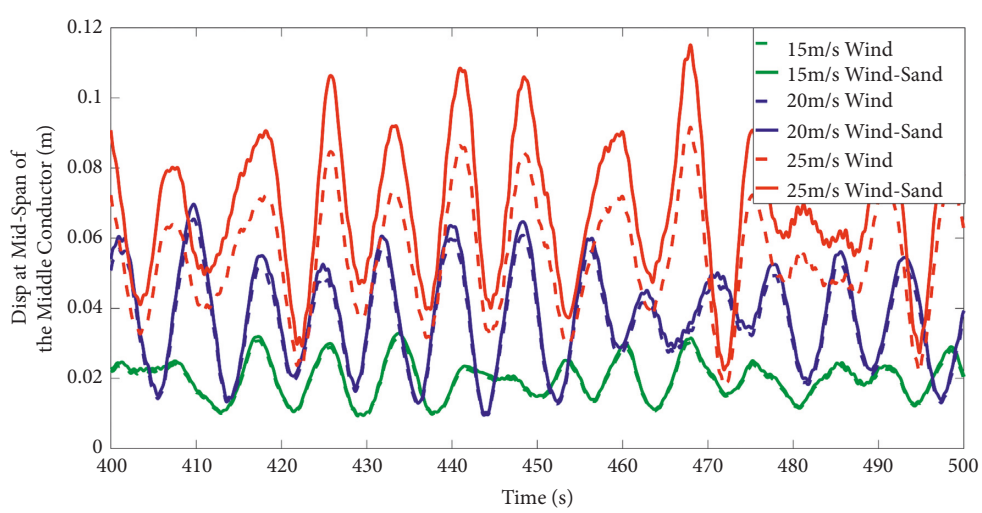

Figure 9: Displacement at the mid-span of the middle conductor.

acquire accurate results for the power transmission tower-line system. The direct integration method embedded in SAP2000 was utilized to solve (21) with the P-Delta effect and large displacement is considered. Hilber–Hughes–Taylor (HHT) method is selected as the time integration method and other parameters are set to the default value of SAP2000.

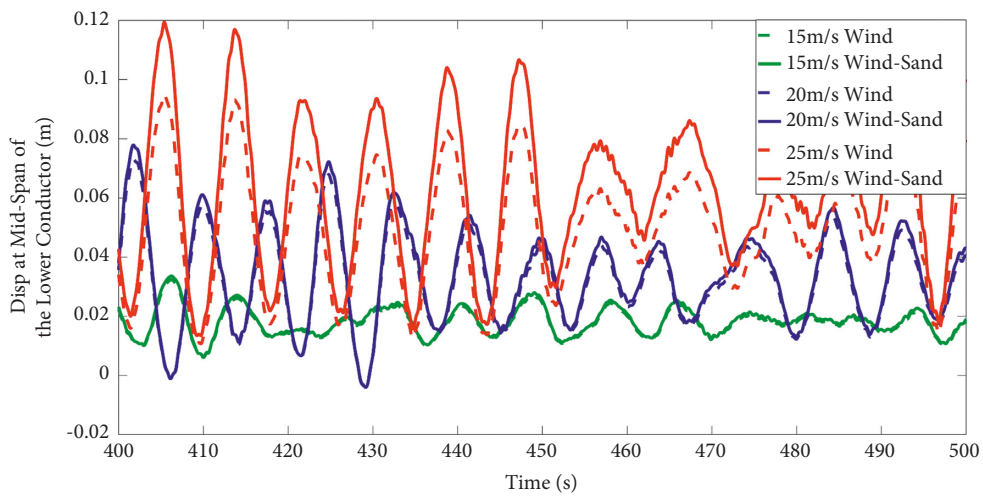

Figure 10: Displacement at the mid-span of the lower conductor.

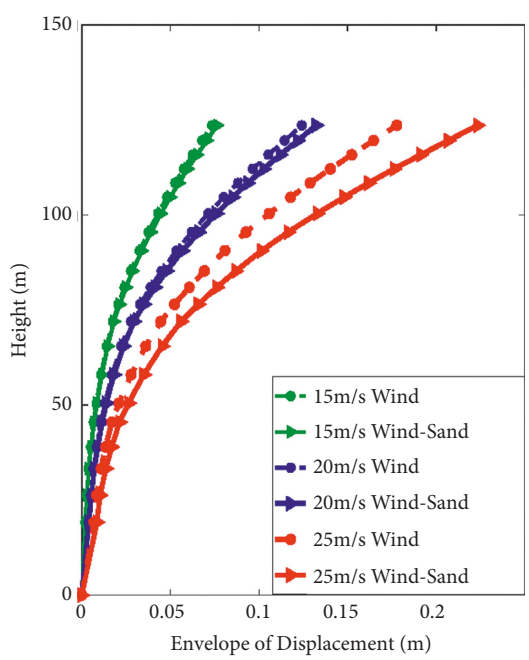

Figure 11: Displacement envelope.

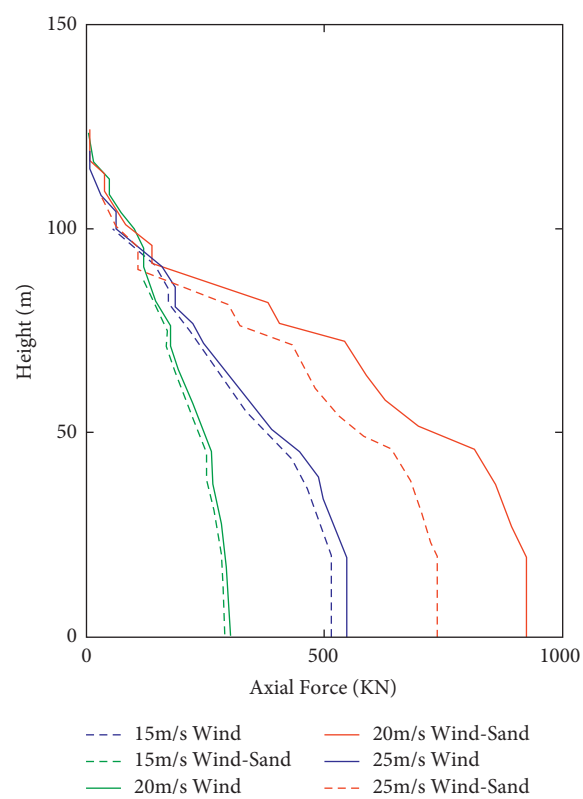

Figure 12: Axial force envelope.

The time step selected for the dynamic time history is dt = 0.01, and the interception time of the time history graph is 6.7 min–8.3 min.

For the time history diagram of tower top displacement in Figure 7, the amplitude range is 0–0.25 m. At this time, the frequency of the fluctuation of the tower top displacement is larger, and a denser fluctuation curve is obtained.

Observing Figure 8, the displacement value of the uppermost conductor in the tower-line system at 15–25 m/s wind speed ranges from 0 to 0.12 m, and the maximum displacement fluctuation range is at 25 m/s wind speed.

Observing Figure 9, the displacement of the middle layer of the tower-line system is still 0~0.12 m when the wind speed is 15–25 m/s. And the displacement fluctuation range at each wind speed is more obvious than that of the upper conductor, and the displacement amplitude is the largest at a wind speed of 25 m/s.

Observing Figure 10, the displacement value of the bottom conductor in the tower-line system at the wind speed of 15–25 m/s is still 0–0.12 m. At this time, the amplitude of the displacement at the wind speed of 25 m/s and the wind speed of 15 m/s are both larger than the amplitude at 15 m/s.

Comparing Figures 8–10 with Figure 7, it can be seen that the displacement fluctuation frequency of the mid-span node of the wire is smaller than that of the tower top node

Table 4: Dynamic response value and growth rate.

Dynamic response	Load cases	Floating dust	Blowing sand	Sandstorm			
				Weak	Medium	Strong	Extra strong
Displacement at tower top (mm)	Wind	2.92	11.72	32.61	73.498	124.18	177.72
	Wind-sand	2.93	11.75	33.11	76.32	155.97	223.22
	Increment	0.08%	0.26%	1.54%	3.84%	6.40%	25.60%
Acceleration at the tower top (m/s^2)	Wind	0.1	0.41	1.12	2.51	4.45	6.95
	Wind-sand	0.1	0.41	1.13	2.61	4.73	8.7292
	Increment	0.08%	0.26%	1.54%	3.84%	6.40%	25.60%
Max. axial force (kN)	Wind	1.16	4.65	12.96	29.24	51.61	73.92
	Wind-sand	1.16	4.66	13.16	30.36	64.82	92.84
	Increment	0.08%	0.26%	1.54%	3.84%	6.40%	25.60%
Max. disp. of upper conductor (mm)	Wind	1.29	5.67	16.96	40.49	76.72	113.54
	Wind-sand	1.29	5.68	17.22	50.86	81.63	142.61
	Increment	0.08%	0.26%	1.54%	3.84%	6.40%	25.60%
Max. disp. of middle conductor (mm)	Wind	1.32	5.94	18.06	43.64	71.81	119.44
	Wind-sand	1.32	5.96	18.34	45.32	76.4	150.02
	Increment	0.08%	0.26%	1.54%	3.84%	6.40%	25.60%
Max. Disp. of lower conductor (mm)	Wind	1.3	5.43	15.58	35.94	73.19	111.51
	Wind-sand	1.3	5.44	15.82	37.32	77.87	140.06
	Increment	0.08%	0.26%	1.54%	3.84%	6.40%	25.60%

under the same period of time and the same wind speed, and other conditions are the same.

The numerical results are presented in Figures 7–12. It can be observed that as the wind speed increases, the wind-sand coupling effect is more obvious. In Figure 7, for instance, when the wind speed is 15 m/s (corresponding to the medium sandstorm according to Table 1), the displacement response at the top of Tower 2 under pure wind excitation is identical to that under the wind-sand load. When the wind speed reaches 25 m/s (extra strong sandstorm), the displacement of the displacement is amplified. A similar trend can also be observed in Figures 8–10, which display the displacement at the mid-span of the three levels of conductors.

Figures 11 and 12 present the envelope of displacement and axial forces of the main members along the height of the tower. These curves indicate that the internal forces are amplified by the wind-driven sands.

In Table 4, the responses under all the six levels of sandstorms and pure winds are compared. It is obvious that the displacements, accelerations, and internal forces of key structural members are all increased, especially under the extra strong sandstorms, when the responses are increased by 25.6%. Therefore, it is suggested that the wind-sand load be considered in future design codes of transmission tower-line systems.

The maximum displacement of the mid-span node of the middle-level conductor is greater than the maximum mid-span displacement of the upper conductor, and the mid-span node of the bottom conductor fluctuates most obviously at a wind speed of 25 m/s. The maximum displacement of the mid-span node on the traverse is similar for each layer, the maximum displacement of the tower top is 223.22 m, and the growth rate under the state of sand particles and pure wind at various wind speeds maintains a stable law.

5. Conclusions

This paper presents an analysis method of transmission tower-line system under wind-sand load. According to the law of conservation of momentum, the impact force generated by a single sand particle hitting the steel structure is derived. Then the wind-sand load is simulated with the help of graded sand-dust storm intensity. An actual transmission tower-line system was established in SAP2000 to realize time-domain analysis. Some conclusions revealed by the data results are summarized as follows:

(1) Besides the erosion actions and corona effects, the floating sand particles in wind will also amplify the dynamic response of the power transmission tower-line system. Neglecting this amplification effect, which is commonly applied in the current design procedure may underestimate the potential danger of the sandstorm.

(2) The wind-sand loads are determined by the wind speed and the ratio of the sand particles floating in the air. As the sandstorm level increases, the wind-sand load grows rapidly.

(3) Compared to the dynamic response from wind-induced loads, the nonlinearity of the tower dynamic response increased clearly under increasing levels of the sandstorm intensity. The higher the sandstorm level, the greater the displacement of the top tower and axial force experienced by the principal material. Under extreme conditions, i.e., the extra strong sandstorm, the response can be increased by 25%. Therefore, an amplification factor of 1.25 is suggested to consider the influence of the wind-driven sand for future design codes.

In addition, field observation or long-term health monitoring shall be conducted to further reveal the intensity of wind storms and their influence on the response of the tower-line system in future work.

Data Availability

The data used to support the findings of this study are available from the corresponding author upon request.

Conflicts of Interest

The authors declare that there are no conflicts of interest regarding the publication of this paper.

Acknowledgments

This research was funded by the National Natural Science Foundation of China (NSFC), grant number 51808092, the United Navigation Foundation of Liaoning Province, grant number 2020-HYLH-48, the National Key Research and Development Program of China (2021YFB2601102), and the Open Fund of the State Key Laboratory of Coastal and Offshore Engineering (DUT-LP2122).

References

[1] Y. He, Z. Gu, Q. Shui et al., "RANS simulation of local strong sandstorms induced by a cold pool with vorticity," *Atmosphere*, vol. 11, no. 4, p. 321, 2020.

[2] M. Yang, Y. Wang, Q. Liu, A. Ding, and Y. Li, "The influence of sandstorms and long-range transport on polycyclic aromatic hydrocarbons (PAHs) in PM2.5 in the high-altitude atmosphere of southern China," *Atmosphere*, vol. 6, no. 11, pp. 1633–1651, 2015.

[3] JM. Prospero, P. Ginoux, O. Torres, S. E. Nicholson, and T. E. Gill, "Environmental characterization of global sources of atmospheric soil dust identified with the NIMBUS 7 Total Ozone Mapping Spectrometer (TOMS) absorbing aerosol product," *Review of Geophysics*, vol. 40, no. 1, pp. 2-1–2-31, 2002.

[4] Z. Qian, X. Lu, and S. Ding, "Full-scale tests on pad and chimney foundation subject to uplift combined with horizontal loads in aeolian sand," *Yantu Lixue/Rock and Soil Mechanics*, vol. 30, pp. 257–260, 2009.

[5] B. Yang, Y. Wang, and J. Liu, "PIV measurements of two phase velocity fields in aeolian sediment transport using fluorescent tracer particles," *Measurement*, vol. 44, no. 4, pp. 708–716, 2011.

[6] DJ. Sherman and B. Li, "Predicting aeolian sand transport rates: a reevaluation of models," *Aeolian Research*, vol. 3, no. 4, pp. 371–378, 2012.

[7] G. Strypsteen, L. C. Van Rijn, and P. Rauwoens, "Comparison of equilibrium sand transport rate model predictions with an extended dataset of field experiments at dry beaches with long fetch distance," *Aeolian Research*, vol. 52, Article ID 100725, 2021.

[8] P. Zhang, D. J. Sherman, and B. Li, "Aeolian creep transport: a review," *Aeolian Research*, vol. 51, Article ID 100711, 2021.

[9] Z. Zheng, S. Du, H. Taubenbock, and X. Zhang, "Remote sensing techniques in the investigation of aeolian sand dunes: a review of recent advances," *Remote Sensing of Environment*, vol. 271, Article ID 112913, 2022.

[10] Q. Gao and YH. Shi, "Research on the mechanism of discharge of transmission line in wind-sand-electric field," *Applied Mechanics and Materials*, vol. 43, pp. 169–172, 2010.

[11] L. Yunpeng, H. Feng, L. Chen et al., "Corona loss of the bundle conductors on EHV/UHV AC power lines under sandy and dusty conditions in high-altitude areas," *J Electrostat*, vol. 107, Article ID 103476, 2020.

[12] M. F. Ishac and H. B. White, "Effect of tornado loads on transmission lines," *IEEE Transactions on Power Delivery*, vol. 10, no. 1, pp. 445–451, 1995.

[13] R. V. Milford and A. M. Goliger, "Tornado risk model for transmission line design," *Journal of Wind Engineering and Industrial Aerodynamics*, vol. 72, pp. 469–478, 1997.

[14] E. Savory, G. A. R. Parke, M. Zeinoddini, N. Toy, and P. Disney, "Modelling of tornado and microburst-induced wind loading and failure of a lattice transmission tower," *Engineering Structures*, vol. 4, pp. 365–375, 2001.

[15] S. E. Oliver, W. W. Moriarty, and J. D. Holmes, "A risk model for design of transmission line systems against thunderstorm downburst winds," *Engineering Structures*, vol. 9, pp. 1173–1179, 2000.

[16] C. Q. Li, "A stochastic model of severe thunderstorms for transmission line design," *Probabilistic Engineering Mechanics*, vol. 4, pp. 359–364, 2000.

[17] A. Shehata, A. El Damatty, and E. Savory, "Finite element modeling of transmission line under downburst wind loading," *Finite Elements in Analysis and Design*, vol. 1, pp. 71–89, 2005.

[18] SA. Orr and M. Cassar, "Exposure indices of extreme wind-driven rain events for built heritage," *Atmosphere*, vol. 11, no. 2, p. 163, 2020.

[19] Y. Hao, Y. Liao, Z. Kuang et al., "Experimental investigation on influence of shed parameters on surface rainwater characteristics of large-diameter composite post insulators under rain conditions," *Energies*, vol. 13, no. 19, p. 5011, 2020.

[20] A. An, G. Guan, Z. Zhu, and Y. Zhang, "Research on windage Yaw Flashovers of transmission lines under wind and rain conditions," *Energies*, vol. 12, no. 19, p. 3728, 2019.

[21] C. Zhou, J. Yin, and Y. Liu, "Large swing behavior of overhead transmission lines under rain-load conditions," *Energies*, vol. 11, no. 5, p. 1092, 2018.

[22] T. Li, *Approaches and Dynamic Performances of High-Speed Train Fluid-Structure. PhD*, Southwest JiaoTong University, Chengdu, China, 2012.

[23] J. Cheng, F. Jiang, C. Xue, and Q. Pang, "Computational method for maximum sediment discharge and sand-carrying wind load in the prevention and treatment of wind drift sand for railway in strong wind area," *Zhongguo Tiedao Kexue/China Railway Science*, vol. 33, pp. 1–5, 2012.

[24] F. Jiang, Y. Li, K. Li, J. Cheng, C. Xue, and S. Ge, "Study on structural characteristics of Gobi wind sand flow in 100 km wind area along Lan-Xin Railway," *Tiedao Xuebao/Journal of the China Railway Society*, vol. 32, pp. 105–110, 2010.

[25] M. Shinozuka and CM. Jan, "Digital simulation of random processes and its applications," *Journal of Sound and Vibration*, vol. 25, no. 1, pp. 111–128, 1972.

[26] M. Shinozuka and G. Deodatis, "Simulation of stochastic processes by spectral representation," *Applied Mechanics Reviews*, vol. 44, no. 4, pp. 191–204, 1991.
[27] X. Fu, HN. Li, and J. Wang, "Failure analysis of a transmission tower subjected to combined wind and rainfall excitations," *The Structural Design of Tall and Special Buildings*, vol. 28, no. 10, 2019.
[28] X. Fu and G. Li, "Fragility analysis of a transmission tower under combined wind and rain loads," *Journal of Wind Engineering and Industrial Aerodynamics*, vol. 199, Article ID 104098, 2020.

Hindawi
Shock and Vibration
Volume 2022, Article ID 2983700, 18 pages
https://doi.org/10.1155/2022/2983700

Research Article

Study on Vibration Control and Parameters Influence of Cable Inerter Viscous Damping System

Ruoyu Zhang[1] and Meigen Cao[2]

[1]*School of Mechanics and Engineering Science, Shanghai University, Shanghai 200444, China*
[2]*School of Civil Engineering, North China University of Technology, Beijing 100144, China*

Correspondence should be addressed to Meigen Cao; caomeigen@ncut.edu.cn

Received 4 November 2021; Revised 18 February 2022; Accepted 21 February 2022; Published 20 April 2022

Academic Editor: Zhitao Yan

In this study, a single-degree-of-freedom (SDOF) model with cable inerter viscous damper (CIVD) is established, and the vibration control equations and frequency response functions are established. Then, the influence of parameters, including inertia mass ratio, additional damping ratio, and stiffness ratio, is studied. Finally, the dynamic time history analysis of SDOF with CIVD under earthquake and fluctuating wind load is carried out to verify the damping performance of CIVD. The research shows that the additional mass and damping of CIVD can be amplified hundreds of times through the rotation, so as to realize the lightweight and high efficiency of the damper and make up for the engineering defects of the traditional TMD system. Meanwhile, when designing CIVD, the inertia mass ratio and additional damping ratio should be reduced as much as possible under the condition of meeting the target damping ratio. The CIVD can significantly suppress the resonance response of the structure and the continuous vibration response in the stable state. The peak displacement can be reduced by 30%–50%. Installing the cable and inerter element can control only the structural vibration, but it cannot reduce the amplitude in the steady state. The CID can control the inertial force output of the original structure, but the rotating speed of the inerter element is high, and the shaking speed of the original structure is fast. Therefore, in order to control the acceleration, velocity, and displacement of the original structure at the same time, we must add the appropriate inerter, additional damping, and additional stiffness.

1. Introduction

Building and lifeline structures have high vulnerability under earthquake and fluctuating wind load [1], such as super-high structures, industrial plants, and transmission tower line systems [2]. The main reason is that the natural vibration frequency of the structure is close to the predominant frequency of external excitation [3], resulting in the amplification of vibration response [4], so the vibration mitigation and control of the structure are particularly important. Therefore, many researchers have studied reinforcement measures and energy dissipation devices for reducing wind-induced or seismic response and the design methods of these devices for vibration control of different structures [5, 6]. At present, TMD is the most widely used [7], and it is applied to varying degrees in the fields of electronics, machinery, building, and so on [8]. Although electronic and mechanical equipment have higher requirements for the accuracy and robustness of vibration control than building structures, because the weight, size, and height of building structures and other special structures are much larger than other equipment and they are exposed to the external environment for a long time [9], the load conditions are more complex [10]. To achieve a certain vibration control effect, TMD needs a larger size and mass [11]. Many high-rise structures and super high-rise structures adopt the TMD design scheme. Although the wind-induced vibration control is good, the volume of TMD is large due to the large mass of the original structure itself. However, from the perspective of economy and applicability, this is unrealistic for many structures, such as high-rise space truss structures like transmission towers. The

structure itself is flexible, and the towers in the tower line system are coupled with conductor and ground cable strongly during vibration. For structures with a large mass participation coefficient during vibration, it is difficult to realize large-scale vibration mitigation measures based on TMD in areas with frequent earthquakes or typhoon transit. Therefore, it is necessary to design a lightweight and efficient damping system, which is easy to install and has little impact on the original structure.

In recent ten years, the electromechanical similarity theory [12] has provided a theoretical basis for the proposal of inerter element, and the vibration mitigation and isolation technology has been developed based on the inerter element. Compared with the traditional TMD, the damper with the inerter element can directly and effectively control the inertial force at the two terminals. Moreover, the inerter element can effectively enlarge the small actual mass through methods such as ball screw to convert the translational motion into rotary motion. In 2001, Smith [13] puts forward the concept of inerter element based on electromechanical similarity theory, gives the basic forms of ball screw inerter element and rack and pinion inerter element, and designs hydraulic inerter element in 2013 [14], which has a simpler structure and stronger robustness. Subsequently, shock absorbers were developed based on different inerter element connection forms, such as tuned viscous mass damper (TVMD) with mass element in parallel with damping element and tuned inerter damper (TID) with stiffness element in parallel with damping element. At the same time, the design method of inerter system is also studied. Ikago et al. [15] derived a simple formula for TVMD optimization design based on fixed-point theory. *Pan* et al. [16] studied the parameters of single-degree-of-freedom structures with different inerter systems, considering the natural damping of the original structure and the output cost control of the damper and making up for the deficiency of the design method based on the fixed-point theory, and proposed the design method of SPIS-II inerter damping system [17]. Hwang et al. [18] proposed a ball screw inerter system connected with a toggle brace. Through theoretical analysis and numerical calculation, it is shown that the system can be effectively used in the structure even when the drift is very small. Zhang et al. [19–21] applied the inerter damper system to high-rise structures such as chimneys and wind power towers, made a systematic theoretical analysis and parameter influence analysis, and proved the effectiveness of the inerter damping system in high-rise structures. Gao et al. [22] put forward an optimum design procedure of VID based on the output feedback control theory for controlling specific cable mode vibrations.

At present, although some Japanese scholars have used the inerter damping support in practical engineering [23], most of the research on the inerter damping system are still in the stage of theoretical analysis and numerical simulation, only the simplified mechanical model is used for the damping analysis of various structures, and only a few scholars have proposed the connection mode and design method of the inerter system applied in building structures [24]. Xie et al. [25, 26] put forward a cable-bracing inerter system (CBIS), which is composed of cable and inerter energy dissipation system fixed at the bottom of interlayer of structure. And the study shows that it is easy to install and can effectively control structural displacement. Wang et al. [27] put forward a new tuned inerter-negative-stiffness damper (TINSD) for seismic protection of structures, which is more effective than the TID, TVMD, and INSD in reducing the dynamic response of structures.

In this study, a cable inerter viscous damper (CIVD) system is proposed. The end of the lightweight inerter viscous damper is directly connected with the elastic cable, which can be quickly installed in various plane and space structures. The system can not only realize structural reinforcement and improve the integrity of the structure but also realize the lightweight of the shock absorber. Firstly, Section 2 introduces the basic principle of IVD. By installing cables, the translation of the original structure is transformed into the rotation of IVD and the equivalent mass and equivalent damping of the shock absorber are improved. Then, in Section 3, the motion control equations and frequency response functions of the structure with CIVD are established. In Section 4, the parameter analysis is carried out to obtain the minimum inertia mass ratio and additional damping ratio of CIVD under different vibration mitigation standards. Finally, it carries out that the dynamic time history analysis of the structure installed with CIVD under the action of earthquake and fluctuating wind load in Section 5, verifies the vibration control effect of CIVD, and explains the vibration mitigation mechanism and the action of each element of CIVD in detail from the aspects of vibration mitigation rate and energy dissipation. The research in this study can provide a reference for the design of efficient and lightweight vibration mitigation scheme of plane and space structures based on the inerter damping system.

2. Theoretical Analysis of CIVD

2.1. Mechanical Model of Inerter Unit and CIVD. Compared with the mass unit, the inertia unit can increase the inertia by rotating. The two ends of the unit have different accelerations, and its output is also directly proportional to the relative acceleration at both ends, which can be expressed as follows:

$$f_I = m_d(a_2 - a_1), \tag{1}$$

where f_I is the output force of the inerter unit and a_1 and a_2 are the accelerations at both ends, and Figure 1 shows the mechanical model of the inerter element.

The inerter unit is the same as the mass unit and cannot dissipate energy by itself. It is generally used in combination with the damper. Figure 2(a) shows the inerter viscous damper (IVD), and the translation (Δ)can be converted into rotation (ϕ) in the damper through the ball screw. The mass in the damper generates kinetic energy through rotation, and the input energy can be dissipated by the viscous fluid in the damper. The

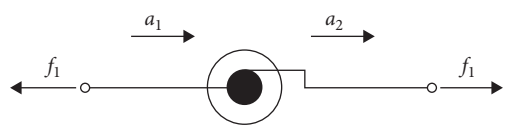

Figure 1: Mechanical model of an inerter element.

mechanical model of IVD is shown in Figure 2(b).Here, m_d and c_d are equivalent mass and equivalent damping coefficient, corresponding to the translation Δ at both ends of IVD; J and c_{vd} are the moment of inertia and viscous damping constants, corresponding to the rotation ϕ inside the IVD. The expressions of m_d and c_d can be obtained, where L is the lead of the ball screw:

$$m_d = \frac{4\pi^2}{L^2} J,$$
$$c_d = \frac{4\pi^2}{L^2} c_{vd}, \tag{2}$$
$$\phi = \frac{2\pi}{L} \Delta.$$

Cable inerter viscous damper (CIVD) is an elastic cable device added at the end of viscous inerter damper. Its mechanical model is basically consistent with tuned viscous mass damper (TVMD), and it is composed of series stiffness elements based on IVD. The mechanical model of CIVD is shown in Figure 3, and k_d is the equivalent stiffness of the cable device.

2.2. Mechanical Model of Single-Degree-of-Freedom (SDOF) System with CIVD. For a single-degree-of-freedom (SDOF) system, if only the installation of IVD is considered, the optimal value of the installation of IVD can be directly selected without considering the installation of angle (translation Δ of IVD is the same as the translation u of the single-degree-of-freedom system). The layout and mechanical model of the single-degree-of-freedom system installed with IVD are shown in Figure 4, where m, k and c are the mass, stiffness, and damping coefficients of the single-degree-of-freedom system respectively.

When considering layout of CIVD, the layout angle θ shall be considered. The layout efficiency β can be introduced, $\beta = \cos^2\theta$. After CIVD is installed, the equivalent stiffness k_d, equivalent damping coefficient c_d, and equivalent mass m_d shall be multiplied by the installation of efficiency β, becoming βk_d, βc_d, and βm_d. The single-degree-of-freedom system with layout of CIVD and mechanical model is shown in Figure 5.

2.3. Motion Control Equation and Frequency Response Function of SDOF with CIVD. If only the installation of IVD is considered, there is no relative displacement between SDOF and IVD because the IVD has no stiffness element ($\Delta = u$ and $\beta = 1$). According to the internal deformation coordination conditions of IVD provided by equation (2), it can be seen that the motion equation and dimensionless form of single-degree-of-freedom system with IVD under the action of vibration load $F_v(t)$ are as follows:

$$\begin{aligned} &m\ddot{u}'(t) + c\dot{u}'(t) + ku'(t) + m_d\ddot{u}'(t) + c_d\dot{u}'(t) \\ &= F_v(t), \ (1+\mu_d)\ddot{u}'(t) + 2(\zeta+\zeta_d)\omega_0\dot{u}'(t) + \omega_0^2 u'(t) \\ &= f_v(t), \end{aligned} \tag{3}$$

where $u\prime(t)$ is the displacement response of SDOF with IVD installed, μ_d and ζ_d are inertia mass ratio and additional viscous damping ratio respectively, κ_d is the additional stiffness ratio, ζ and ω_0 are the damping ratio and circular frequency of the original structure respectively, and $f_v(t)$ is the equivalent vibration load. If it is seismic action, $-f_v(t)$ is the acceleration of ground motion, and the expression of each parameter is as follows:

$$\begin{aligned} \zeta &= \frac{c}{2m\omega}, \\ \omega_0 &= \sqrt{\frac{k}{m}}, \\ f_v(t) &= \frac{F_v(t)}{m}, \\ \mu_d &= \frac{m_d}{m}, \\ \zeta_d &= \frac{c_d}{2m\omega_0}, \\ \kappa_d &= \frac{k_d}{k}. \end{aligned} \tag{4}$$

On considering the stiffness of cable , the relative displacement will occur between SDOF and IVD ($\Delta \neq u$ and $0 < \beta < 1$). So CIVD generates additional degrees of freedom. $u(t)$ and $u_d(t)$ are the displacement responses of SDOF and CIVD respectively, and the following equation represents the motion control equation of SDOF with CIVD installed:

$$\begin{cases} m\ddot{u}(t) + c\dot{u}(t) + ku(t) + k_d(u(t)\cos\theta - u_d(t))\cos\theta = F_v(t), \\ \beta m_d\ddot{u}_d(t) + \beta c_d\dot{u}_d(t) = k_d(u(t)\cos\theta - u_d(t))\cos\theta. \end{cases} \tag{5}$$

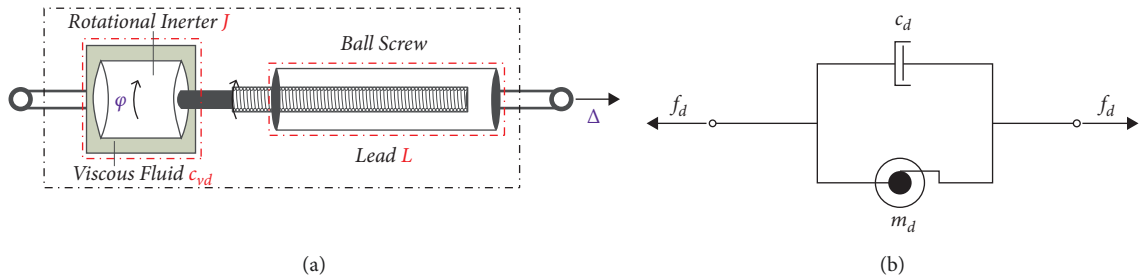

Figure 2: Structure and mechanical model of an inerter viscous damper (IVD): (a) IVD; (b) mechanical model.

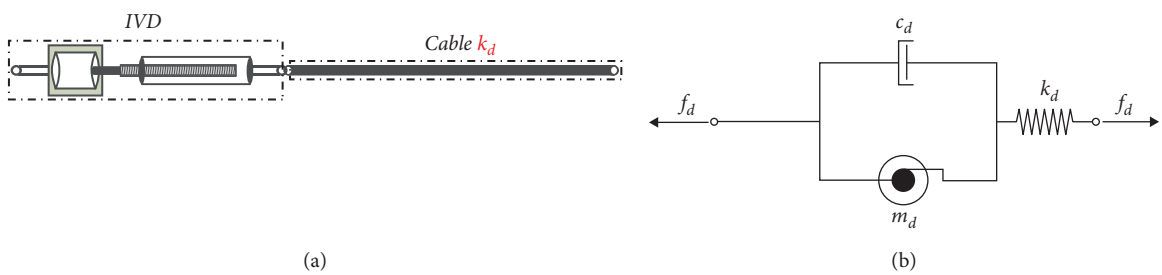

Figure 3: Mechanical model of a cable inerter viscous damper (CIVD): (a) CIVD; (b) mechanical model.

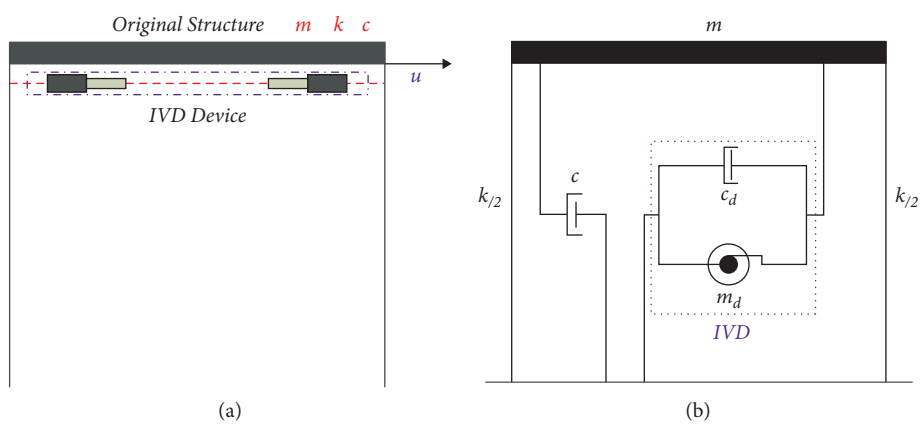

Figure 4: Layout and mechanical model of a SDOF with inerter viscous damper: (a) layout; (b) mechanical model.

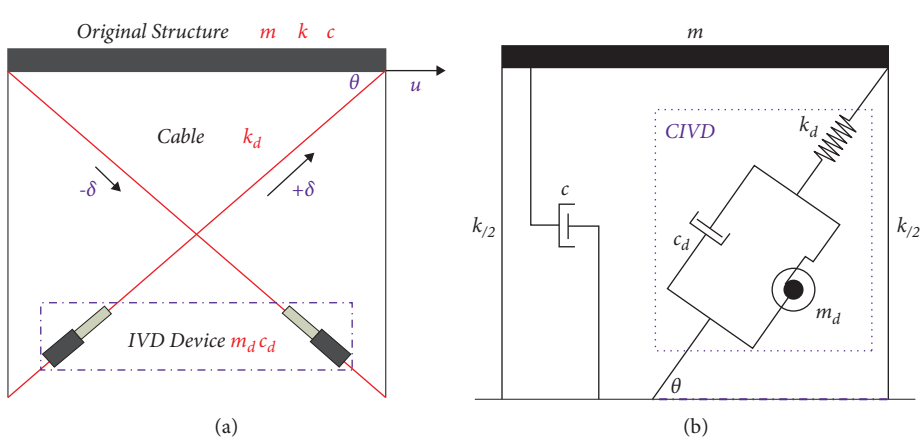

Figure 5: Layout and mechanical model of a SDOF with cable inerter viscous damper: (a) layout; (b) mechanical model.

Rewriting equation (5) into dimensionless form, the following equation can be obtained:

$$\begin{aligned}&\left\{\ddot{u}(t)+2\zeta\omega_0\dot{u}(t)+(1+\beta\kappa_d)\omega u(t)-\kappa_d\cos\theta\omega_0^2u_d(t)=f_v(t),\beta\mu_d\ddot{u}_d(t)+2\beta\zeta_d\omega_0\dot{u}_d(t)\right.\\&\quad=(1+\beta\kappa_d)\omega_0^2u(t)-\kappa_d\cos\theta\omega_0^2u_d(t).\end{aligned}\tag{6}$$

Laplace transform of equation (5) can be obtained:

$$\begin{cases}s^2U(s)+2\zeta\omega_0sU(s)+(1+\beta\kappa_d)\omega_0^2U(s)-\kappa_d\cos\theta\omega_0^2U_d(s)=F(s),\\ \beta\mu_ds^2U_d(s)+2\beta\zeta_d\omega_0sU_d(s)=(1+\beta\kappa_d)\omega_0^2U(s)-\kappa_d\cos\theta\omega_0^2U_d(s),\end{cases}\tag{7}$$

where $S=i\Omega$, Ω is the excitation frequency of vibrational load, and $U(s)$, $U_d(s)$, and $F(s)$ are the Laplace transform of $u(t)$, $u_d(t)$, and $f_v(t)$ respectively. From equation (7), $U(s)$ and $U_d(s)$ can be solved as follows:

$$\begin{cases}U(s)=\dfrac{\left(\beta\mu_ds^2+2\beta\mu_ds\omega_0+\kappa_d\cos\theta\omega_0^2\right)F(s)}{D(s,\beta,\zeta,\mu_d,\zeta_d,\kappa_d,\omega_0)},\\[2ex] U_d(s)=\dfrac{\beta\kappa_d\omega_0^2F(s)}{D(s,\beta,\zeta,\mu_d,\zeta_d,\kappa_d,\omega_0)},\end{cases}\tag{8}$$

where

$$\begin{aligned}D(s,\beta,\zeta,\mu_d,\zeta_d,\kappa_d,\omega_0)&=s^4\beta\mu_d+s^3(2\beta\zeta_d+2\beta\zeta\mu_d)\omega_0+s^2\left(\kappa_d\cos\theta+\beta\mu_d+4\beta\zeta\zeta_d+\beta^2\kappa_d\mu_d\right)\omega_0^2\\&\quad+s\left(2\beta\zeta_d+2\beta^2\kappa_d\zeta_d+2\kappa_d\zeta\cos\theta\right)\omega_0^3+(1+\beta\mu_d)\kappa_d\cos\theta\omega_0^4.\end{aligned}\tag{9}$$

Then, the SDOF displacement response transfer function $H_U(s)$ of the installation of CIVD and the force response transfer function $H_d(s)$ of the CIVD can be obtained from equations (7)–(9):

$$\begin{cases}H_U(s)=\dfrac{U(s)}{F(s)},\\[2ex] H_d(s)=\dfrac{U_d(s)}{F(s)}\left(\beta\mu_ds^2+2\beta\zeta_d\omega_0s\right).\end{cases}\tag{10}$$

3. Parameter Analysis of CIVD System

According to Parseval's theorem, the root mean square response of the system σ excited by white noise is obtained as follows:

$$\begin{aligned}\sigma&=\int_0^T\frac{u^2(t)}{T_0}\mathrm{d}t\\&=\sqrt{\int_{-\infty}^{+\infty}|H(i\Omega)|^2S_0\mathrm{d}\Omega},\end{aligned}\tag{11}$$

where S_0 is the white noise power spectrum. In modern control theory, the root mean square response (RMS) of linear system σcan be referred to as H_2 norm, and the relative frequency α is introduced. Then, the root mean square response can be rewritten as follows:

$$\sqrt{\int_{-\infty}^{+\infty}|H(i\alpha\omega)|^2}=\|H(i\alpha\omega)\|_2,\quad\alpha=\frac{\Omega}{\omega}.\tag{12}$$

Therefore, the effect of the shock absorber can be measured by comparing the reduction rate of the displacement root mean square response of the original system before and after vibration mitigation. For SDOF structure with CIVD installed, its mitigation ratio of displacement response η_U is as follows:

$$\begin{aligned}\eta_U&=\frac{\sigma_U}{\sigma_{U_0}}\\&=\frac{\|H_U(i\alpha\omega)\|_2}{\|H_{U_0}(i\alpha\omega)\|_2}.\end{aligned}\tag{13}$$

where σ_{U0} is the displacement root mean square response of the original structure (SDOF) and H_{U0} is the displacement transfer function of the original structure; σ_U is the displacement root mean square response of SDOF installed with CIVD. The clearer the mitigation ratio of displacement response is, the better the effect of the shock absorber is.

Parameter analysis include inertia mass ratio μ_d, additional viscous damping ratio ζ_d, and additional stiffness ratio κ_d. The natural damping ratio ζ of the original structure (SDOF) is assumed to be 0.02. The mitigation ratio of displacement response η_U of SDOF due to the installation of CIVD is related to all three parameters, which is difficult to see directly changes of η_U with the joint change of the three parameters. Therefore, one should be fixed and the changes of the other two parameters should be observed. The parameter range of inertia mass ratio μ_d during parameter analysis and additional viscous damping ratio ζ_d are [0.01,1] and the parameter range of the stiffness ratio κ_d is [0.01,10]. In addition, due to the layout angle of the cable θ and layout efficiency β, it has a great impact on the performance of CIVD, which should also be considered in the analysis. Therefore, in the following analysis, the layout angle $\theta = 45^\circ$ and layout efficiency $\beta = 0.5$ are considered.

3.1. Stiffness Ratio κ_d. Firstly, the values of κ_d are set as 0.01, 0.02, 0.05, 0.1, 0.2, 0.5, 1, 2, 5, and 10, respectively, and the variation diagram of η_U with $\mu_d - \zeta_d$ two-dimensional space can be seen with variation of κ_d. Figure 6 shows the variation trend of η_U with different stiffness ratios κ_d under $\mu_d - \zeta_d$ two-dimensional space. If the target mitigation ratio of displacement response is determined to be 50%, it can be seen that when $\kappa_d > 0.5$, the area enclosed by the target isopleth of η_U is larger, and when $\kappa_d > 1$, the area enclosed by the isopleth of η_U is basically stable, then the value range of κ_d is determined to be between 0.5 and 1, and η_U with $\mu_d - \zeta_d$ is made at the same time, considering $\kappa_d = 0.5$ and $\kappa_d = 1$.

It can be seen by comparing Figures 6(b) and 6(c), the damping effect is similar under $\kappa_d = 0.5$ and $\kappa_d = 1$, the minimum mitigation ratio of displacement response is about 0.5, the best range of μ_d is 0.2–0.5, and the minimum value of ζ_d is about 0.1. By comparing with the displacement amplification factor of the original structure, it can be seen that the vibration mitigation effect of CIVD is significant and the reduction range of the maximum response is between 70% and 85%, as shown in Figure 7(c). However, compared with Figures 7(a) and 7(b), when $\kappa_d = 0.5$ and additional damping ratio ζ_d increases between 0.4 and 1, the response of the main structure also increases. Although the increase is only about 10%, this is not allowed in practical engineering. Because the additional damping ratio will increase the cost of engineering project. So from the fixed value of the stiffness ratio κ_d, we can determine the optimal value range of $\mu_d - \zeta_d$, but each parameter cannot be obtained in two-dimensional space. To this end, we should continue to analyze $\mu_d - \zeta_d$ and the two-dimensional space variation law of other parameter combinations.

Due to the mass and damping amplification effect of IVD, the effect is higher than the original several times with small mass and small damping coefficient, so as to realize the lightweight of the damper. Therefore, the target mitigation ratio of response of the original structure should be guaranteed while reducing as much as possible μ_d and ζ_d. It is also the basic principle of parameter optimization.

3.2. Inertia-Mass Ratio μ_d. Then the parameters μ_d.will be fixed. The fixed values of μ_d are 0.01, 0.02, 0.05, 0.1, 0.2, 0.5, and 1, respectively, and the variation diagram of η_U under $\kappa_d - \zeta_d$ two-dimensional space can be seen. Figure 8 shows the variation trend of η_U with different inertia mass ratio μ_d under $\kappa_d - \zeta_d$ two-dimensional space. If the target mitigation ratio of displacement response is determined to be 50%, it can be seen that when μ_d is in the range of 0.05–0.2, the area enclosed by the target isopleth of η_U is larger and the area enclosed by the isopleth increases firstly and then decreases, and when μ_d is in the range of 0.01–0.05, the change of η_U is small, so it can be determined that the value of μ_d is between 0.05 and 0.2 and η_U under $\kappa_d - \zeta_d$ two-dimensional space is made under $\mu_d = 0.05$, $\mu_d = 0.1$, and $\mu_d = 0.2$.

It can be seen by comparing Figures 8(b) and 8(c), the maximum mitigation ratio of displacement response is the same under $\mu_d = 0.05$, $\mu_d = 0.1$, and $\mu_d = 0.2$, when $\eta_U = 50\%$ under the same damping ratio; the max requirement of additional damping ratio is $\mu_d = 0.2$ and $\mu_d = 0.05$ and the min requirement of additional damping ratio is $\mu_d = 0.1$. Although when $\mu_d = 0.2$, the area enclosed by the blue damping ratio contour is larger, but the additional damping ratio ζ_d mostly needs more than $\mu_d = 0.05$, which also violates the principle of damping amplification through CIVD system. The value of inertia mass ratio near $\mu_d = 0.2$ should be discarded, and $\mu_d = 0.05 - 0.1$. Figure 8(e) shows the displacement amplification factor of the original structure. Under the same damping ratio, the values of $\mu_d = 0.05$ and $\mu_d = 0.1$ are almost the same, all less than the value under $\mu_d = 0.2$.

3.3. Additional Damping Ratio ζ_d. Finally, the parameters $\zeta_d$will be fixed.The fixed values of ζ_d are 0.01, 0.02, 0.05, 0.1, 0.2, 0.5, and 1, respectively, and the variation diagram of η_U under $\kappa_d - \mu_d$ two-dimensional space can be seen. Figure 9 shows the variation trend of η_U with different additional damping ratio μ_d under $\kappa_d - \mu_d$ two-dimensional space. Similarly, if the target mitigation ratio of displacement response is determined to be 50%, it can be realized when $\zeta_d > 0.05$. η_U is basically stable within the range of 0.2–1 of the additional damping ratio, so we can fix the value range of additional damping ratio to be between 0.05 and 0.2, and η_U under $\kappa_d - \mu_d$ two-dimensional space is made under $\zeta_d = 0.05$, $\zeta_d = 0.1$, and $\zeta_d = 0.2$.

Although the maximum mitigation ratio of displacement response under the value of $\zeta_d = 0.05$ and $\zeta_d = 0.1$ is less than the value of $\zeta_d = 0.2$, the value of ζ_d is in the range of 0.05–0.1. The blue vibration mitigation of η_U is larger than the area enclosed by contour lines, indicating that the value range of κ_d and $\mu_d$is greater. And the

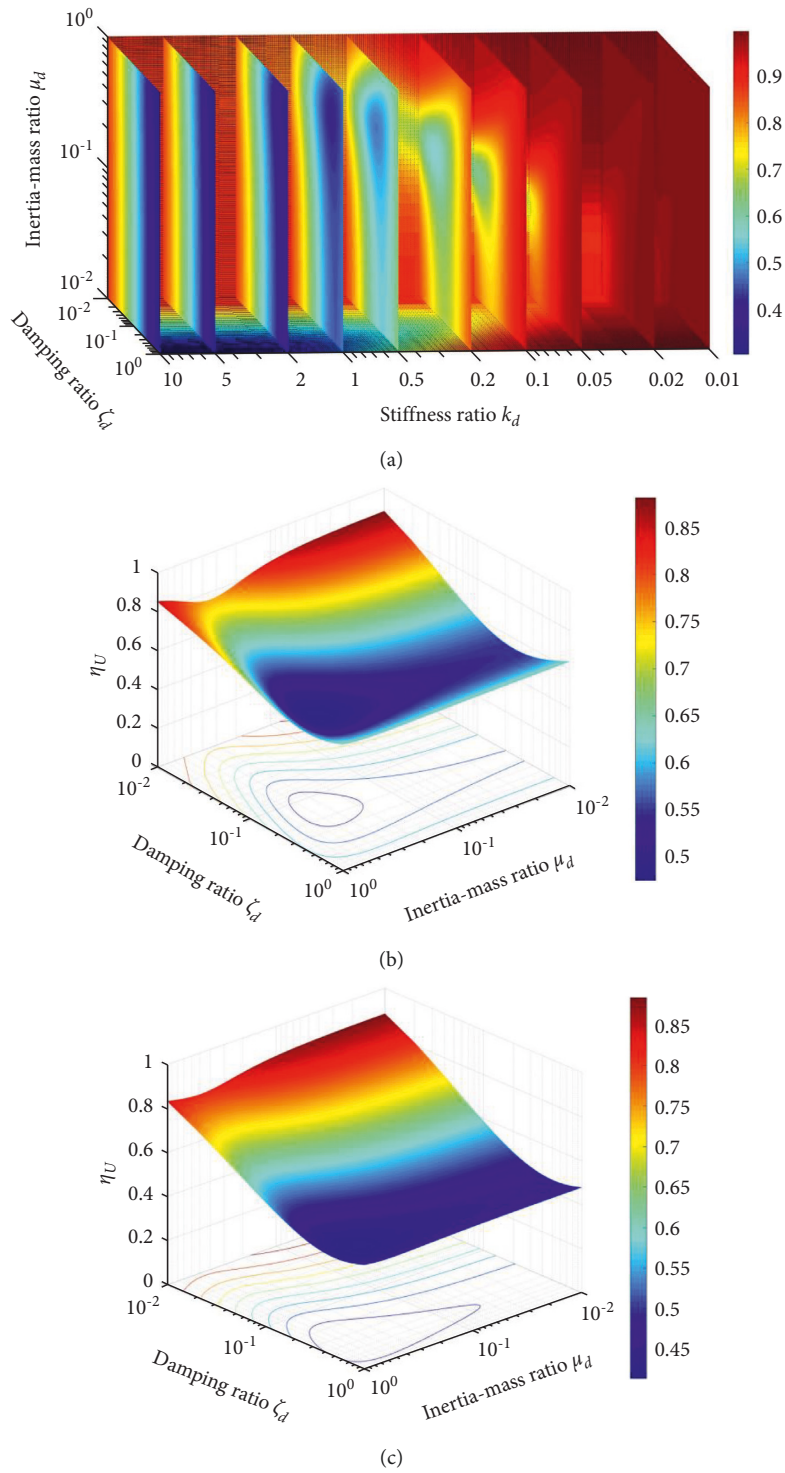

Figure 6: Mitigation ratio of displacement response: (a) changing κ_d; (b) $\kappa_d = 0.5$; (c) $\kappa_d = 1$.

smaller value of $\mu_d$meets lightweight requirements of CIVD's design. If $\eta_U = 0.6$ is the target mitigation ratio of design, then the inertia mass ratio is comprehensively controlled. The value, near $\zeta_d = 0.05$, is the optimal design value. But if $\eta_U = 0.6$ is the target mitigation ratio of design, then the value near $\zeta_d = 0.1$ is the optimal design value. The smaller the mitigation ratio of displacement response is, the better the performance of the IVD shock absorber is, but the more rigorous the selection of parameters is, and the smaller the value range of the optimal parameters is. So the minimum additional damping ratio ζ_d shall be analyzed according to the needs of the project.

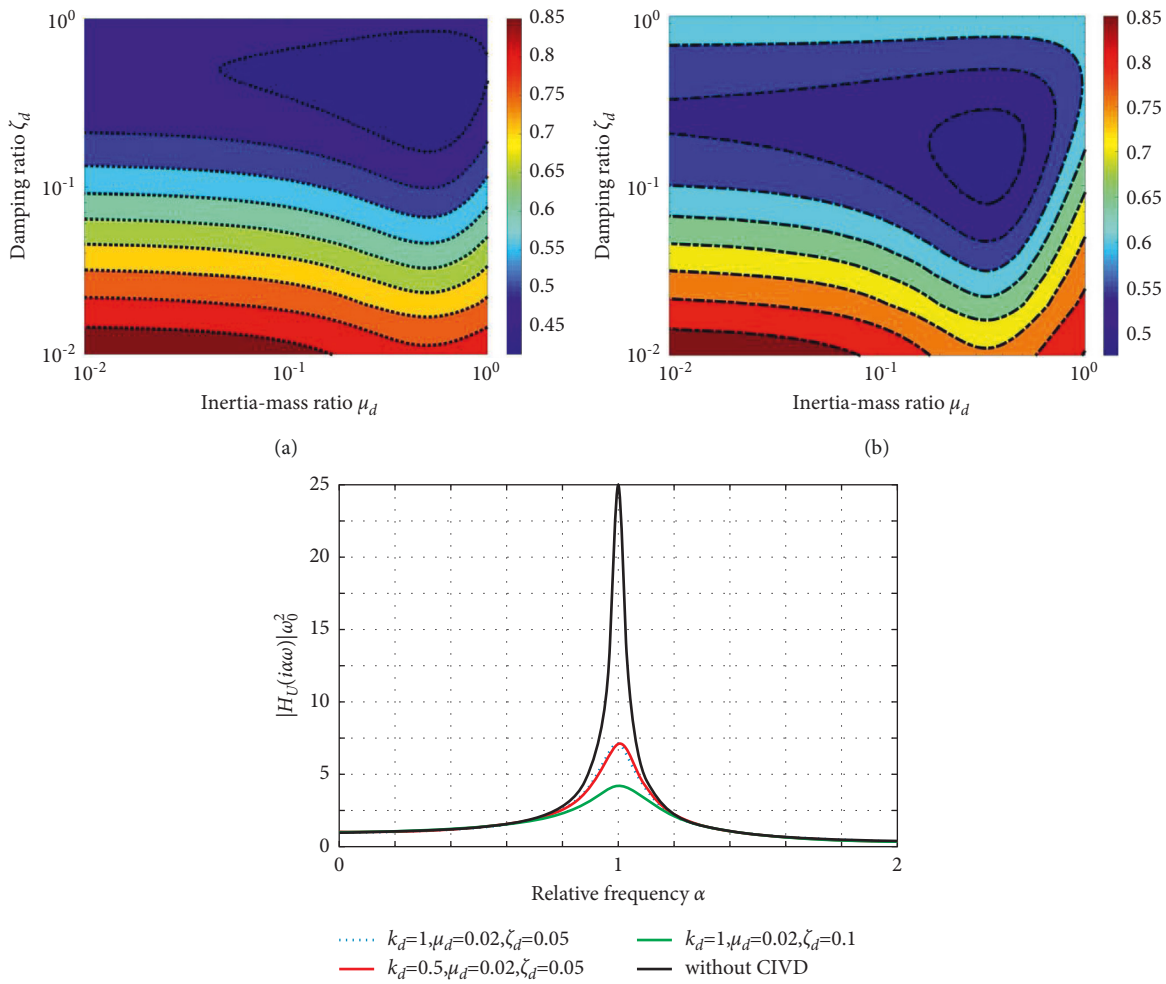

Figure 7: Isopleth of mitigation ratio of displacement response: (a) $\kappa_d = 0.5$; (b) $\kappa_d = 1$; (c) displacement amplification factor.

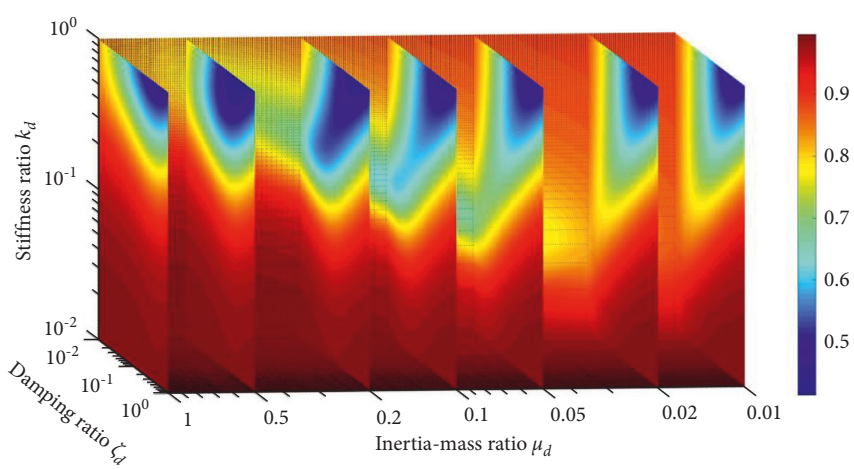

Figure 8: Continued.

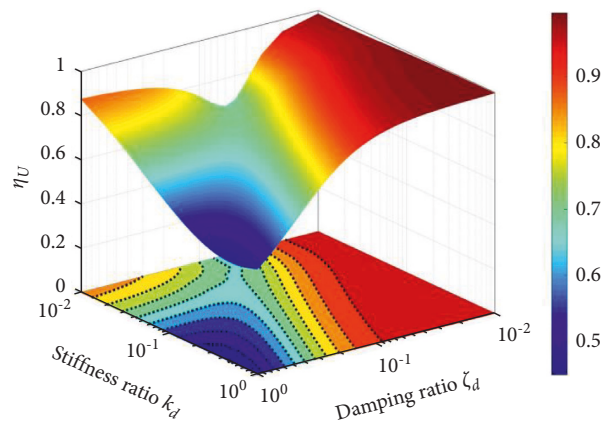

(b)

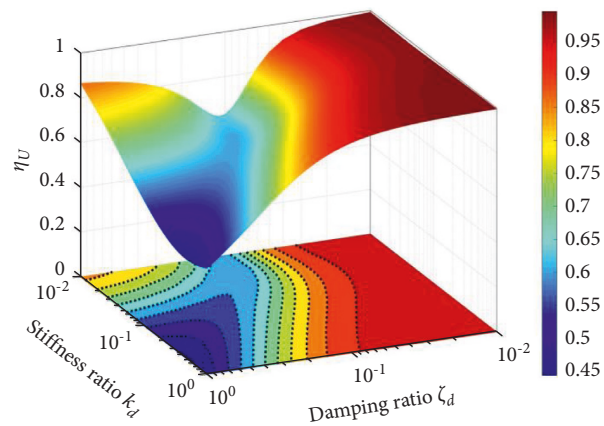

(c)

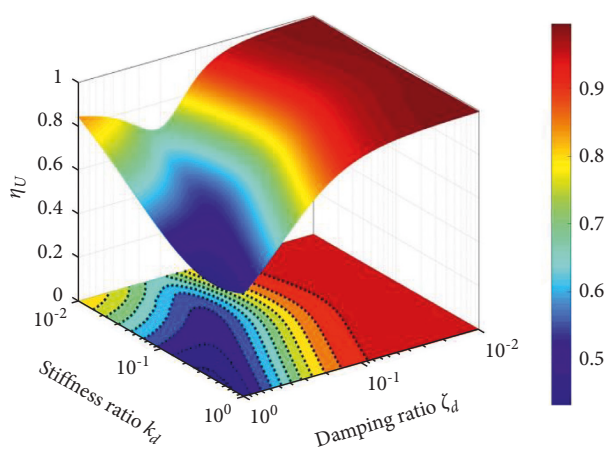

(d)

Figure 8: Continued.

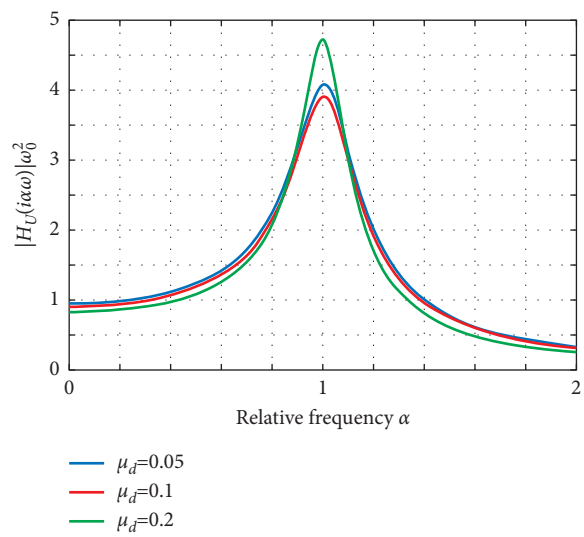

(e)

Figure 8: Mitigation ratio of displacement response: (a) changing μ_d; (b) $\mu_d = 0.05$; (c) $\mu_d = 0.1$; (d) $\mu_d = 0.2$; (e) displacement amplification factor ($\kappa_d = 1$, $\zeta_d = 0.1$).

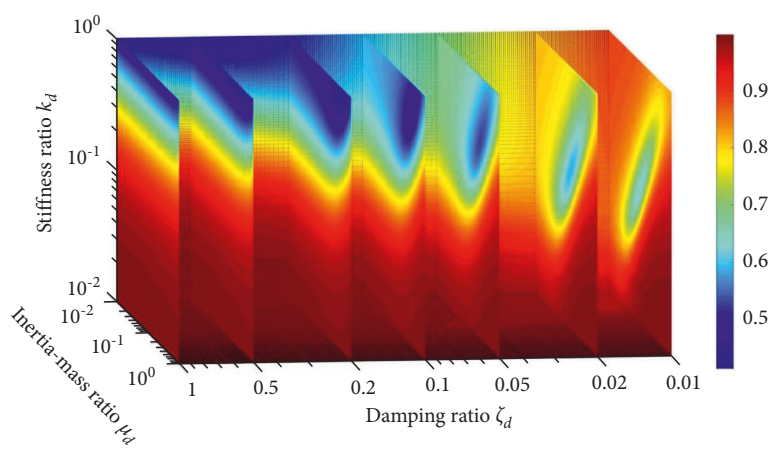

(a)

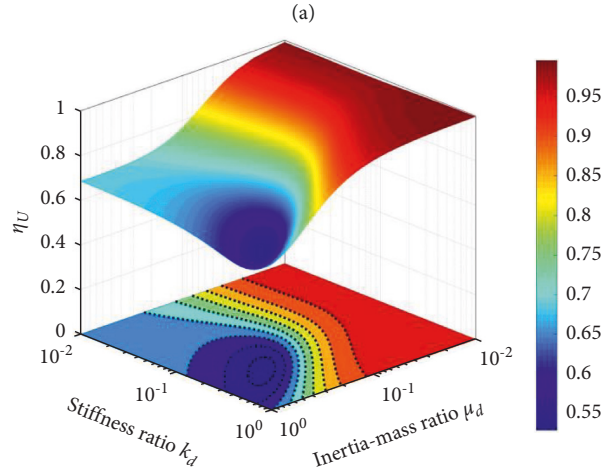

(b)

Figure 9: Continued.

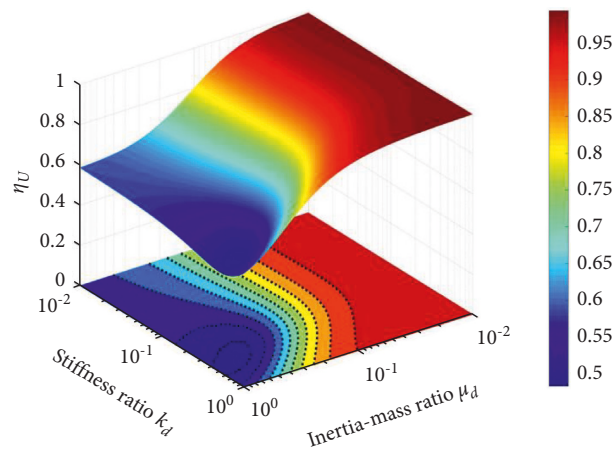

(c)

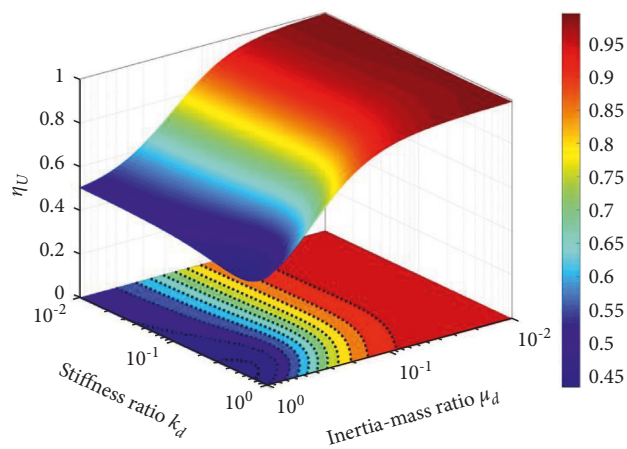

(d)

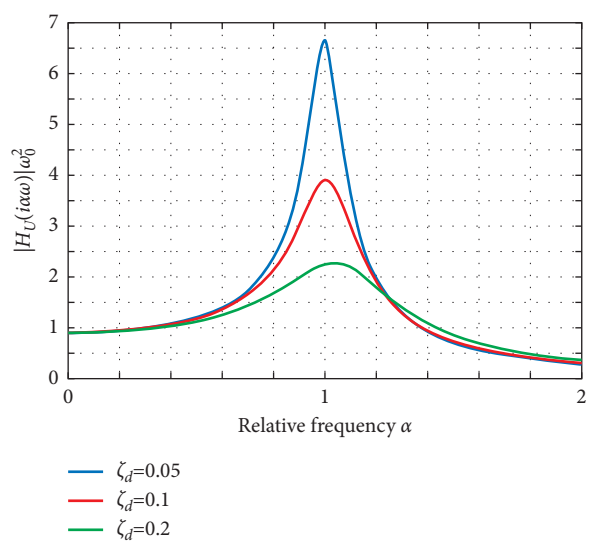

(e)

Figure 9: Mitigation ratio of displacement response: (a) changing ζ_d; (b) $\zeta_d = 0.05$; (c) $\zeta_d = 0.1$; (d) $\zeta_d = 0.2$; (e) displacement amplification factor ($\kappa_d = 1$, $\zeta_d = 0.1$).

Figure 9(e) shows the displacement amplification factor of the original structure, which can be seen that ζ_d can obviously alleviate the resonance response of the original structure and increase the frequency response bandwidth.

3.4. Optimal Design of the CIVD. The selection of design parameters of CIVD or other inerter dampers can be determined by the fixed-point method [28]. Based on the fixed-point theory, Ikago et al. [15]proposed design methods for single-degree-of-freedom structure and multi-degree-of-freedom structure installed with inerter dampers respectively. For the single degree of freedom system with CIVD, after the μ_d is determined, if the layout angle θ of the cable is not considered, the stiffness ratio and damping ratio can be obtained by the following equation:

$$\kappa_d = \frac{\mu_d}{1-\mu_d}, \qquad \zeta_d = \frac{\mu_d}{2}\sqrt{\frac{3\mu_d}{(1-\mu_d)(2-\mu_d)}}. \tag{14}$$

However, the fixed-point theory does not consider the natural damping of the main structure and external excitation characteristics and cannot consider other performance requirements of the main structure. For example, in this study, the key control indexes such as the displacement response of SDOF cannot be reflected. Therefore, when designing parameters of CIVD, we should consider the main performance of the main structure, firstly, such as determining the target mitigation ratio of displacement response η_U according to the structural performance requirements and optimizing the parameters with extremum conditions [16, 29], that is:

$$\eta_U(\zeta_d, \kappa_d, \mu_d) = \eta_{U,t}, \tag{15}$$

$$\frac{\partial \eta_U(\zeta_d, \kappa_d, \mu_d)}{\partial \mu_d} = 0, \qquad \frac{\partial \eta_U(\zeta_d, \kappa_d, \mu_d)}{\partial \zeta_d} = 0, \tag{16}$$

where $\eta_{U,t}$ is the target mitigation ratio of displacement response. The larger the damping ratio and inertia-mass ratio, the more difficult it is to achieve in the installation of CIVD in engineering. So the mathematical problem shows in equation (15) and equation (16): for a given κ_d is equal to the extremum condition that the partial derivative of η_U with respect to μ_d and ζ_d are set as zero. Therefore, the constraint condition of equation (16) is to meet the target mitigation ratio of displacement response $\eta_{U,t}$. At the same time, the damping ratio and inertia-mass ratio are made as small as possible to meet the engineering needs.

4. Dynamic Response Analysis of CIVD System

In order to verify the vibration mitigation effect of CIVD, making $\eta_U = 0.5$ as the target mitigation ratio of displacement response, optimal parameters are taken as $\mu_d = 0.13$, $\zeta_d = 0.11$, and $\kappa_d = 1.0$. The reason for the selection of large stiffness ratio of the cable is to prevent the prestress relaxation of the cable from reducing the nonlinear stiffness of the cable. If the stiffness of cable is nonlinear, the results of analytical stochastic response in this study will be inaccurate and the parameter design method of CIVD will be inapplicable. Therefore, the layout angle of the cable should be small as much as possible to avoid the application of CIVD in long-span structures.

We carry out the dynamic response analysis of the single degree of freedom system with CIVD installed under seismic waves and fluctuating wind load input. Figure 10 shows the corresponding displacement amplification factor of the original structure. The original structural mass $m = 2.1 \times 10^4$kg, stiffness $k = 1.5 \times 10^4$N/m, inherent damping ratio $\zeta = 0.02$, moment of inertia J of inerter viscous damper is $0.007\text{kg} \cdot \text{m}^2$, viscous damping constant is $0.09\text{N} \cdot \text{m} \cdot \text{s}$, and ball screw lead $L = 0.01m$.

El Centro wave, Taft wave, Chi Chi wave and Kobe wave are selected as seismic waves, the peak ground acceleration (PGA) is adjusted to 0.4 g, the davenport spectrum is selected as fluctuating wind spectrum, and the wind speed $v_{10} = 40m/s$, v_{10} is the average wind speed at 10 m. Figure 11 shows the response spectrum of four seismic waves and the power spectrum density of fluctuating wind.

Figure 12 shows the displacement time history response of the original structure. It can be seen that CIVD has good vibration damping performance. At the same time, the peak value and root mean square value of displacement response are selected to evaluate the vibration damping performance of CIVD. The peak value reflects the maximum dynamic response at a certain time, while the root mean square value reflects the overall energy of the whole time history of the structure, that is, the power spectrum corresponding to the dynamic response of the whole time history. Therefore, we define the displacement reduction coefficient to evaluate the vibration damping performance of CIVD, and reduction coefficients are shown in the following equation:

$$\lambda_p = \frac{u_{0p} - u_{cp}}{u_{0p}}, \qquad \lambda_r = \frac{u_{0r} - u_{cr}}{u_{0r}}, \tag{17}$$

where λ_p and λ_r are reduction coefficients of displacement peak value and root mean square value respectively, u_{0p} and u_{cp} are displacement peak values of original structure and CIVD installed structure respectively, u_{0r} and u_{cr} are displacement root mean square values of original structure and CIVD installed structure respectively. Table.1 lists the peak displacement and root mean square reduction coefficient of CIVD system under the action of four seismic waves and fluctuating wind. It can be seen from Figure 12 and Table 1 that the vibration of SDOF system with CIVD is effectively controlled. The peak

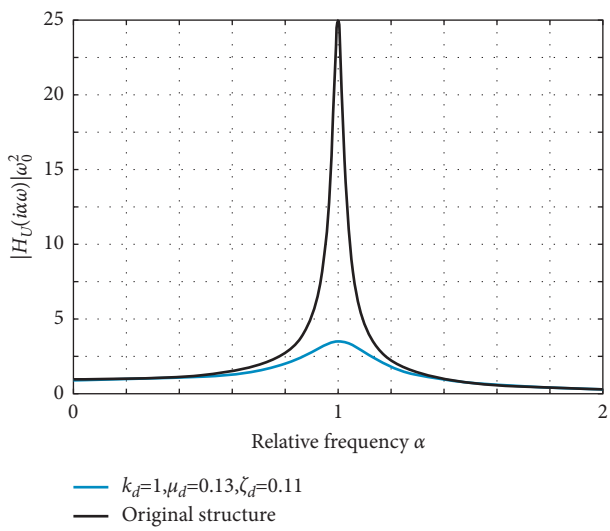

Figure 10: Displacement amplification factor ($\kappa_d = 1$, $\mu_d = 0.1$, $\zeta_d = 0.11$, $\zeta = 0.02$).

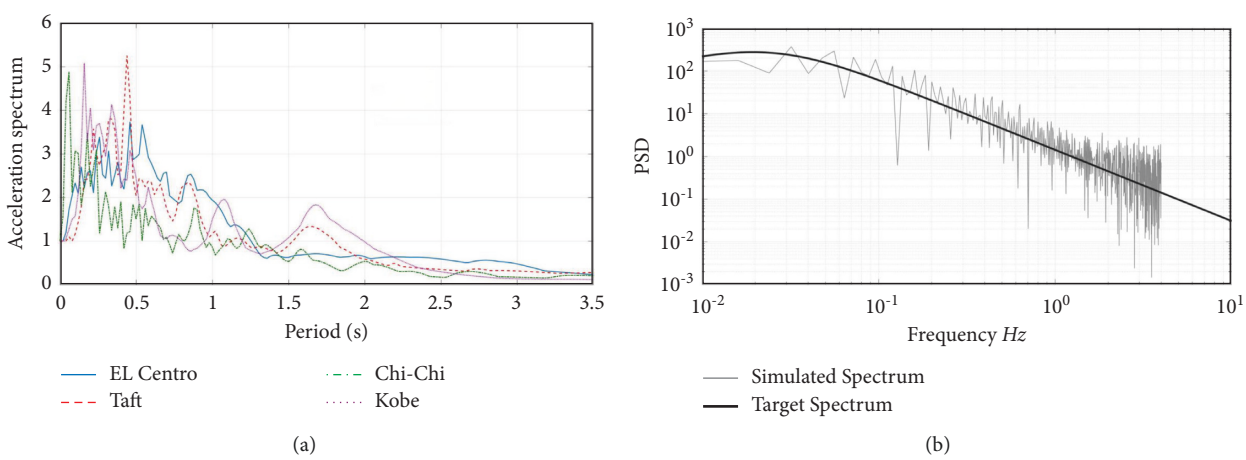

Figure 11: Normalized acceleration spectra of earthquake records and davenport spectrum of fluctuating wind.

displacement control effect is 30%–50%, and the root mean square displacement control effect is 40%–70%. CIVD has a good effect on the continuous vibration control of the original structure, and the controlled structural displacement can quickly enter the stable state of small displacement.

Figure 13 shows the comparison of damping force and displacement of main structure (u) curves between SDOF system with CIVD and the original structure. Under five input conditions, it shows good energy dissipation capacity: large damper output and low displacement response of main structure.

Figure 14 compares the displacement damping effect of cable inerter damping system (CID) and cable inerter viscous damping system (CIVD), the revolutions per second (RPS) of inertia container and the output of inertial force and damping force of structural system. As can be seen from Figure 14(a), even if there is no damping device, the inerter element can obtain a certain vibration mitigating effect on the original structure through mass rotating amplification, so as to make the structure enter a stable state. However, since the inerter element has no energy dissipation effect, the vibration in a stable state cannot be attenuated rapidly. As can be seen from Figure 14(b), the speed per second of CID is much higher than that of CIVD, and the average speed in the whole time range is 2.29 times that of CIVD. It also shows that the horizontal shaking speed of the original structure with CID is higher than that of CIVD, and long-term high-speed rotation will reduce the service life of the inerter element. Therefore, additional damping is needed to restrain the translation of the main structure and the rotation of the inerter element. Figure 14(b) compares the sum of the total inertial force and damping force of the original structure, SDOF system with CID installed and SDOF system with CIVD installed.

It can be seen that the inertial force of the original structure can be greatly reduced, and the additional damping can improve the energy dissipation effect, reduce the displacement, make the additional damping force dominant, and suppress the structural vibration effectively.

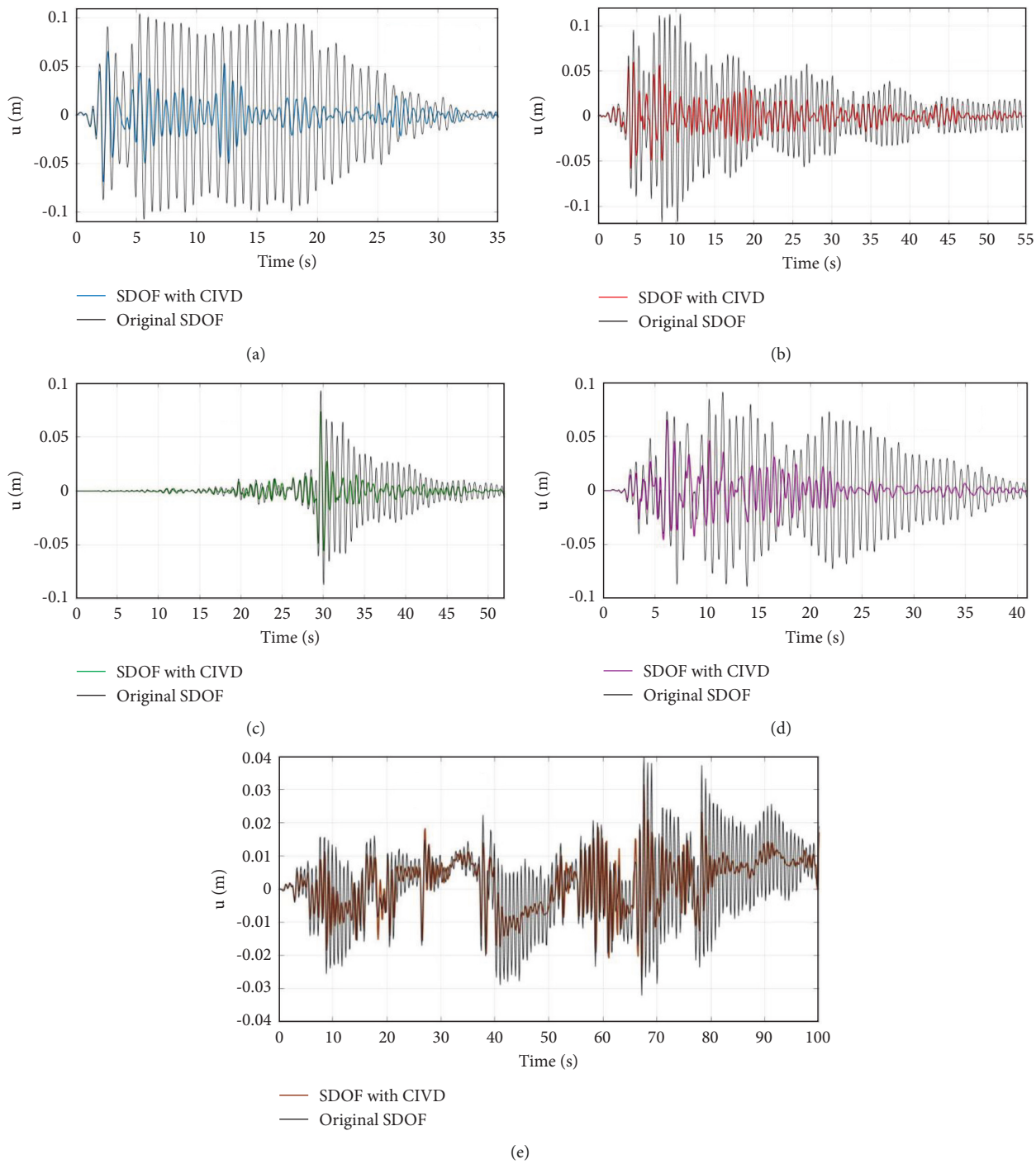

Figure 12: Displacement response (u) time histories of SDOF with and without CIVD under:(a) the El Centro record; (b) the Taft record; (c) the Chi-Chi record; (d) the Kobe record; (e) fluctuating wind.

Figure 15 shows the comparison of the displacement and damping force of the damper when TMD and CIVD are installed in the main structure under the same target mitigation ratio of displacement response ($\eta_U = 0.5$). The optimal design method of TMD is the same as that of CIVD. It can be seen that the deformation of the damping element in CIVD is significantly greater than that in TMD due to the existence of inerter system. Although the damping forces of CIVD and TMD are almost the same, due to the large deformation of the damping element, CIVD can provide a satisfactory effect of energy dissipation.

Compared with TMD, CIVD does not improve the damping effect by increasing the damping coefficient in the damping device directly but increases the equivalent damping through rotating amplification. With a small moment of inertia and damping constant, the additional inertia mass ratio and damping ratio of CIVD under the target damping ratio can be achieved, making shock

Table 1: λ_p and λ_r of original structure under earthquake and fluctuating wind.

Input	El centro	Taft	Chi-chi	Kobe	Fluctuating wind
λ_p (%)	36.10	49.32	30.86	38.18	36.99
λ_r (%)	69.12	62.17	51.90	61.61	40.72

absorber smaller, and it makes up for the defects of traditional TMD due to its large volume and big mass in

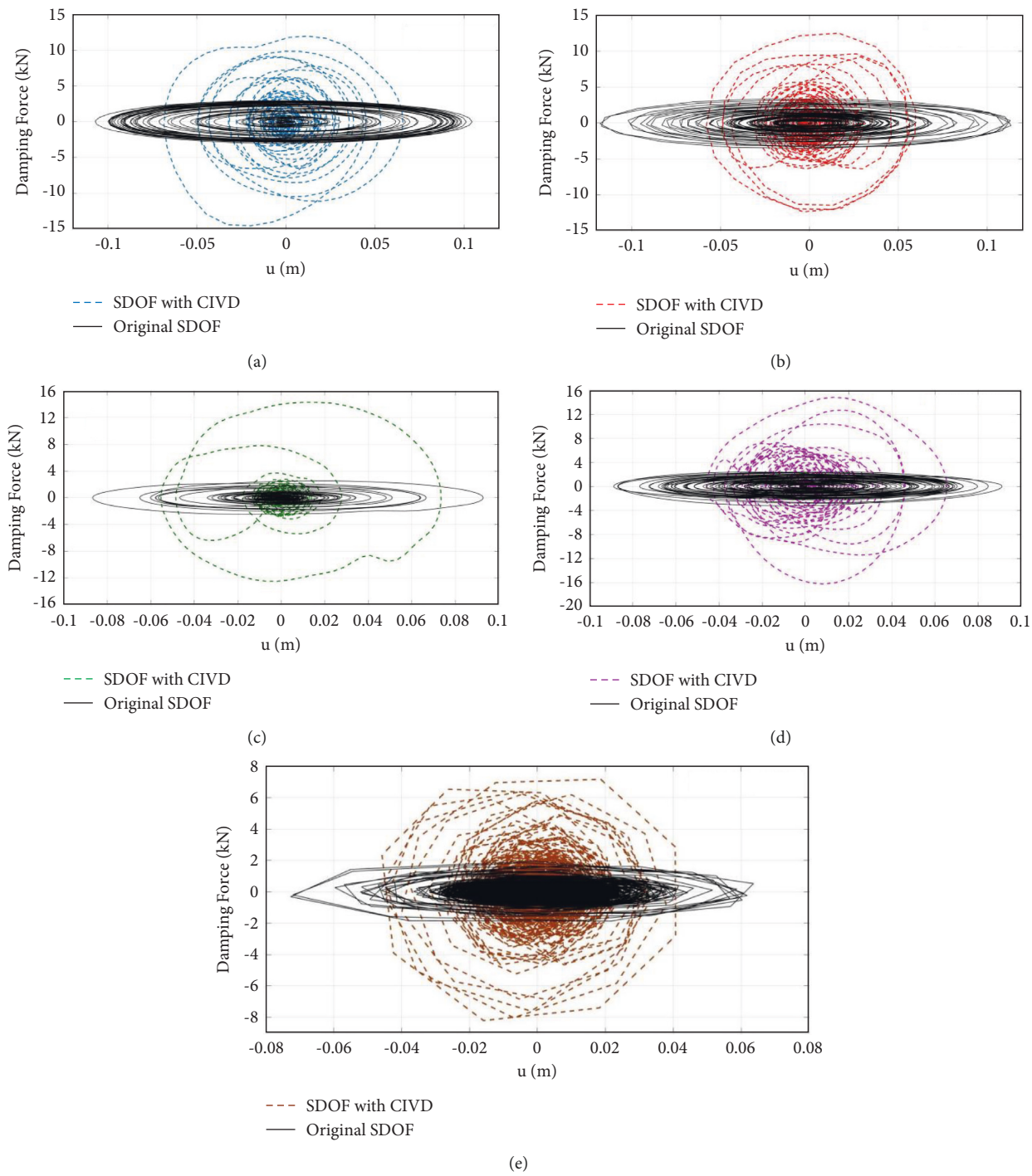

Figure 13: Damping force and displacement of main structure (u) curves of SDOF with and without CIVD under: (a) the El Centro record; (b) the Taft record; (c) the Chi-Chi record; (d) the Kobe record; (e) fluctuating wind.

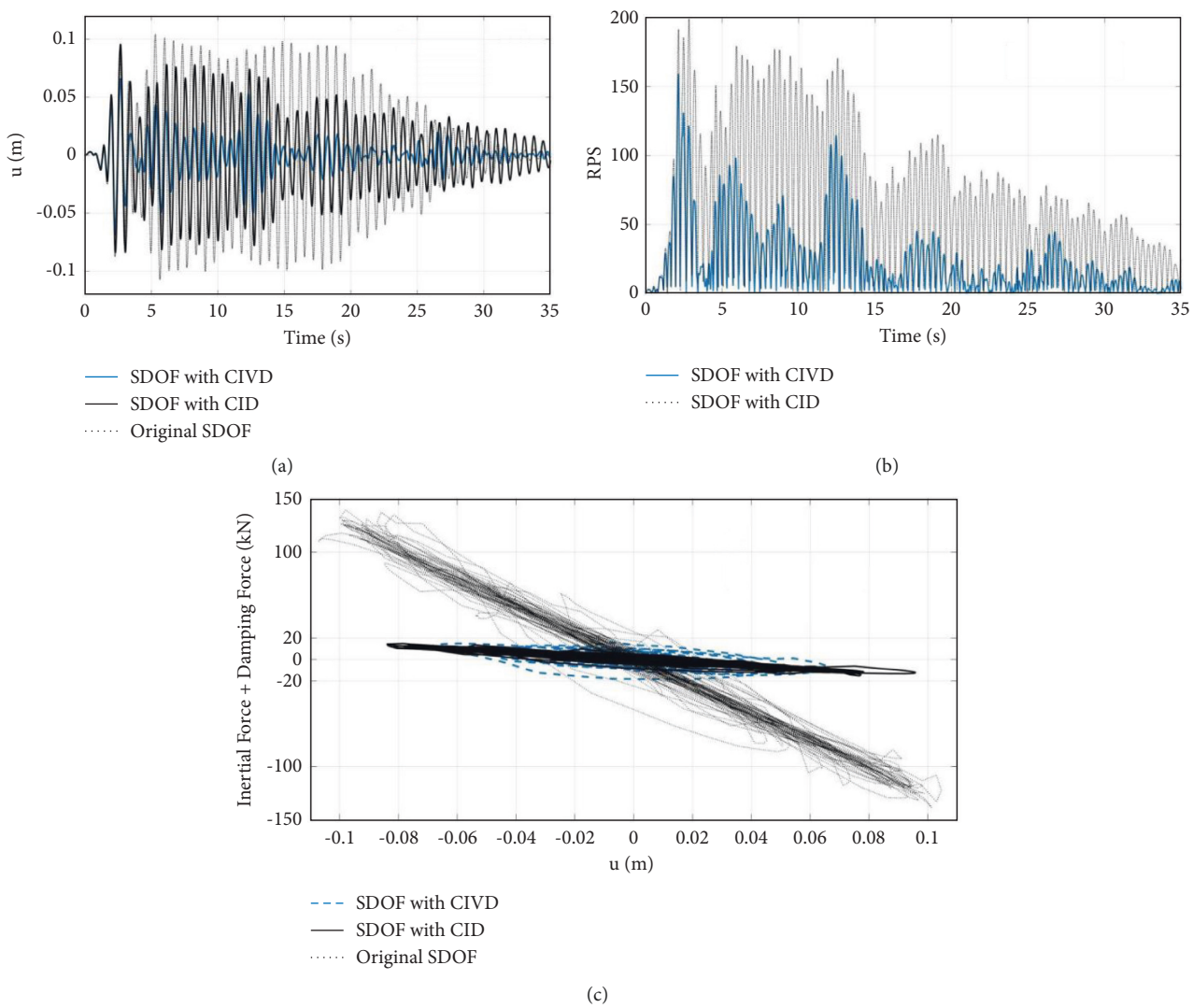

Figure 14: Response of SDOF with CIVD and CID under El Centro wave: (a) time history; (b) RPS of the inerter element; (c) hysteretic curves of the inertial force and damping force.

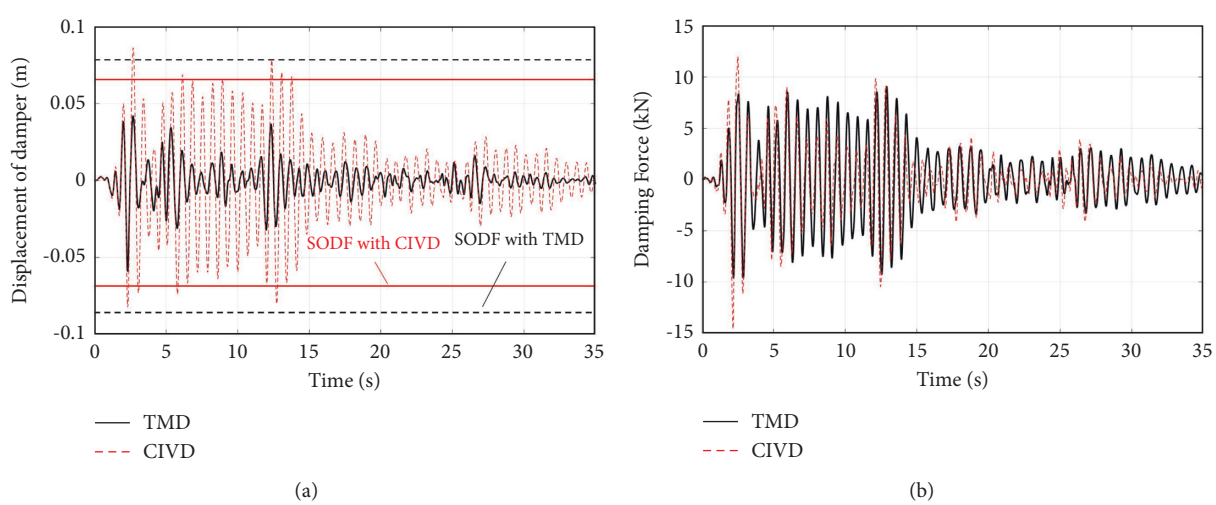

Figure 15: Response of damping element of CIVD and TMD under El Centro wave: (a) displacement; (b) damping force.

practical engineering.

5. Conclusions

Firstly, this study introduces the mechanical model of the cable inerter viscous damping system (CIVD) and establishes the vibration control equation of the single degree of freedom system (SDOF) with CIVD installed. Then, the parameter of inertia mass ratio, additional damping ratio, and stiffness ratio are studied. Finally, the dynamic time history analysis of the SDOF with CIVD installed under seismic action and fluctuating wind load is carried out. The performance of vibration mitigation of CIVD is verified. The main conclusions are as follows:

(1) The cable inerter viscous damping system (CIVD) can enlarge the mass and damping through rotation, realize the lightweight and high efficiency of the damper, and make up for the defects of the traditional TMD system in engineering. When designing CIVD, the inertia mass ratio and additional damping ratio should be reduced as much as possible under the condition of meeting the target damping ratio.

(2) CIVD can significantly suppress the resonance response of the structure and make the continuous vibration response into a stable state. The peak displacement can be reduced by 30%–50%, and the root mean square displacement can be reduced by 40%–70%. At the same time, the energy dissipation capacity of the damping element is also greatly strengthened.

(3) Installing the cable and inerter element (CID) can only control the structural vibration, but it cannot reduce the amplitude in the steady state. The CID can control the inertial force output of the original structure, but the rotational speed of the inerter element is high and the shaking speed of the structure is fast. But we can control the acceleration, velocity, and displacement of the original structure at the same time, if we add the inertia, additional damping, and additional stiffness. Meanwhile, the deformation of the damping element in CIVD is enlarged compared with TMD under the same target mitigation ratio of displacement response.

In conclusion, the CIVD system has a good vibration mitigation effect. This study mainly focuses on the macro-structural design parameters, but there is no detailed analysis on the design parameters of specific cable inerter viscous damper. At present, the cable inerter viscous damping device is in the development stage. The subsequent research will carry out the mechanical performance test according to the specific inerter damping device. Furthermore, the shaking table test will be carried out on the specific structure with CIVD or IVD installed.

Data Availability

The method of this paper is mainly formula derivation, and the data can be obtained from this paper directly. If And the data of section 4 (dynamic analysis) can be obtained with the first author.

Conflicts of Interest

The authors declare that they have no conflicts of interest.

Acknowledgments

This research was supported by State Grid Science & Technology Project (5200–201919121A-0-0-00) and 2020 open fund project of the State Key Laboratory of Disaster Prevention & Reduction for Power Grid Transmission and Distribution Equipment (B316AF190007).

References

[1] M. Cao, F. Zhou, P. Tan, G. Zhang, Y. F. Cheng, and Z. B. Dai, "Seismic response of transformer and bushing isolation system and parameter analysis of isolation layer," *Journal Proceedings of the CSEE*, vol. 32, no. 13, pp. 166–174, 2012.

[2] L. Tian, H. Pan, and R. Ma, "Probabilistic seismic demand model and fragility analysis of transmission tower subjected to near-field ground motions," *Journal of Constructional Steel Research*, vol. 156, pp. 266–275, 2019.

[3] L. Meirovitch, *Dynamics and Control of Structures*, John Wiley & Sons, Hoboken, NJ, USA, 1990.

[4] T. T. Soong and G. F. Dargush, *Passive Energy Dissipation Systems in Structural Engineering*, Wiley, New York, NY, USA, 1997.

[5] G. W. Housner, L. A. Bergman, T. K. Caughey et al., "Structural control: past, present, and future," *Journal of Engineering Mechanics*, vol. 123, pp. 897–971, 1997.

[6] A. Kareem, T. Kijewski, and Y. Tamura, "Mitigation of motions of tall buildings with specific examples of recent applications," *Wind and Structures*, vol. 2, no. 3, pp. 201–251, 1999.

[7] R. J. McNamara, "Tuned mass dampers for buildings," *Journal of the Structural Division ASCE*, vol. 103, 1977.

[8] J.-S. Hwang, J. Kim, S.-H. Lee, and K.-W. Min, "Equivalent damping of a structure with vibration control devices subjected to wind loads," *Wind and Structures*, vol. 6, no. 4, pp. 249–262, 2003.

[9] E. Simiu and R. Scanlan, *Wind Effects on Structures*, Wiley, New York, NY, USA, 1996.

[10] L. Tian, H. Pan, C. Qiu, R.-S. Ma, and Q.-Q. Yu, "Wind-induced collapse analysis of long-span transmission tower-line system considering the member buckling effect," *Advances in Structural Engineering*, vol. 22, no. 1, pp. 30–41, 2019.

[11] S.-H. Lee, K.-W. Min, J.-S. Hwang, and J. Kim, "Evaluation of equivalent damping ratio of a structure with added dampers," *Engineering Structures*, vol. 26, no. 3, pp. 335–346, 2004.

[12] M. C. Smith and F.-C. Wang, "Performance benefits in passive vehicle suspensions employing inerters," *Vehicle System Dynamics*, vol. 42, no. 4, pp. 235–257, 2004.

[13] M. C. Smith, "Synthesis of mechanical networks: the inerter," *IEEE Transactions on Automatic Control*, vol. 47, no. 10, pp. 1648–1662, 2002.

[14] S. J. Swift, M. C. Smith, A. R. Glover, C. Papageorgiou, B. Gartner, and N. E. Houghton, "Design and modelling of a fluid inerter," *International Journal of Control*, vol. 86, no. 11, pp. 2035–2051, 2013.

[15] K. Ikago, K. Saito, and N. Inoue, "Seismic control of single-degree-of-freedom structure using tuned viscous mass damper," *Earthquake Engineering & Structural Dynamics*, vol. 41, no. 3, pp. 453–474, 2012.

[16] C. Pan and R. Zhang, "Design of structure with inerter system based on stochastic response mitigation ratio," *Structural Control and Health Monitoring*, vol. 25, no. 6, 2018.

[17] C. Pan, R. Zhang, H. Luo, C. Li, and H. Shen, "Demand-based optimal design of oscillator with parallel-layout viscous inerter damper," *Structural Control and Health Monitoring*, vol. 25, no. 1, 2018.

[18] J.-S. Hwang, J. Kim, and Y.-M. Kim, "Rotational inertia dampers with toggle bracing for vibration control of a building structure," *Engineering Structures*, vol. 29, no. 6, pp. 1201–1208, 2007.

[19] H. Luo, R. Zhang, and D. Weng, "Mitigation of liquid sloshing in storage tanks by using a hybrid control method," *Soil Dynamics and Earthquake Engineering*, vol. 90, pp. 183–195, 2016.

[20] R. Zhang, Z. Zhao, and K. Dai, "Seismic response mitigation of a wind turbine tower using a tuned parallel inerter mass system," *Engineering Structures*, vol. 180, pp. 29–39, 2019.

[21] Z. P. Zhao, R. F. Zhang, N. E. Wierschem, Y. Y. Jiang, and C. Pan, "Displacement mitigation-oriented design and mechanism for i," *Journal of Vibration and Control*, 2020.

[22] H. Gao, H. Wang, J. Li et al., "Optimum design of viscous inerter damper targeting multi-mode vibration mitigation of stay cables," *Engineering Structures*, vol. 226, Article ID 111375, 2021.

[23] Y. Sugimura, W. Goto, H. Tanizawa, K. Saito, and T. Nimomiya, "Response control effect of steel building structure using tuned viscous mass damper," in *Proceedings of the The 15th World Conference on Earthquake Engineering*, Lisbon, Portugal, September 2012.

[24] M. Kurata, R. T. Leon, and R. Desroches, "Rapid seismic rehabilitation strategy: concept and testing of cable bracing with couples resisting damper," *Journal of Structural Engineering*, vol. 138, no. 3, pp. 354–362, 2012.

[25] L. Xie, X. Ban, S. Xue, K. Ikago, J. Kang, and H. Tang, "Theoretical study on a cable-bracing inerter system for seismic mitigation," *Applied Sciences*, vol. 9, no. 19, p. 4096, 2019.

[26] S. Xue, J. Kang, L. Xie, R. Zhang, and X. Ban, "Cross-Layer installed cable-bracing inerter system for MDOF structure seismic response control," *Applied Sciences*, vol. 10, no. 17, p. 5914, 2020.

[27] H. Wang, H. Gao, J. Li, Z. Wang, Y. Ni, and R. Liang, "Optimum design and performance evaluation of the tuned inerter-negative-stiffness damper for seismic protection of single-degree-of-freedom structures," *International Journal of Mechanical Sciences*, vol. 212, Article ID 106805, 2021.

[28] J. P. Den Hartog, *Mechanical Vibrations*, Dover, Mineola, NY, USA, 4th edition, 1956.

[29] Y. Jiang, Z. Zhao, R. Zhang, D. De Domenico, and C. Pan, "Optimal design based on analytical solution for storage tank with inerter isolation system," *Soil Dynamics and Earthquake Engineering*, vol. 129, Article ID 105924, 2020.

Hindawi
Shock and Vibration
Volume 2022, Article ID 6822689, 12 pages
https://doi.org/10.1155/2022/6822689

Research Article

Dynamic Windage Yaw Angle and Dynamic Wind Load Factor of a Suspension Insulator String

Shuang Zhao,[1,2] **Jiahao Yue**,[1] **Eric Savory**,[3] **Zhitao Yan**,[1,2] **Jiahao Chen**,[1] **Bin Zhang**,[4] **and Liuliu Peng**[5]

[1]*School of Civil Engineering and Architecture, Chongqing University of Science and Technology, Chongqing 401331, China*
[2]*Chongqing Key Laboratory of Energy Engineering Mechanics & Disaster Prevention and Mitigation, Chongqing 401331, China*
[3]*Department of Mechanical and Materials Engineering, University of Western Ontario, London N6A 5B9, Canada*
[4]*CMCU Engineering Co., Ltd.,, No. 17 Yu Zhou Road, Chongqing 400039, China*
[5]*School of Civil Engineering, Chongqing University, Chongqing 400044, China*

Correspondence should be addressed to Zhitao Yan; yzt@cqust.edu.cn

Received 29 July 2021; Revised 27 December 2021; Accepted 17 January 2022; Published 15 February 2022

Academic Editor: Denis Benasciutti

A simplified calculation method is proposed for determining the peak dynamic windage yaw angle ($\widehat{\varphi}$) of electricity transmission line (TL) tower suspension insulator strings (SISs). According to the rigid-body rule, the geometric stiffness matrix in the calculation of the windage yaw angle (φ) of SISs is dominated by the average wind loads, while the fluctuating wind loads are the dominant factor in the elastic stiffness. With the average wind state of conductors as the initial calculation condition, the load-response-correlation (LRC) method can be used to determine the fluctuating windage yaw angle (φ_d) and the corresponding equivalent static wind loads (ESWLs). Then, the improved rigid straight rod model, which uses the actual length of conductors rather than the projected length, was used to determine the average windage yaw angle $\overline{\varphi}$. Through the linear superposition of the horizontal increments of $\overline{\varphi}$ and $\widehat{\varphi}_d$ (the peak value of φ_d), the formulae to calculate the $\widehat{\varphi}$ of SISs were derived. Additionally, the formulae for the dynamic wind load factor, β_c, which is a key factor in designing wind loads for φ, were derived according to the principle of ESWLs, rather than being empirically determined by the Chinese code. Thus, the calculation model regarding the loads and response for the φ of SISs was established, and an actual TL was used to verify the established calculation model. Afterward, the influence of the different engineering design parameters on φ and its β_c were analyzed. The parameter analyses show that the wind speed, span, and ground roughness influence the magnitudes of $\widehat{\varphi}$ and β_c, however, the height difference between the two suspension points of the conductors, the nominal height, and the sag-to-span ratio may be neglected in the approximate calculation. Our method offers a new solution to TL design when there are large deformations and small strains.

1. Introduction

Flashover accidents caused by the windage yaw of insulator strings damage transmission lines (TLs), leading to potential large-scale power failure. These accidents can occur when the wind speed is lower than the design wind speed. Therefore, the windage yaw design scheme for suspension insulator strings (SISs) needs to be improved to increase the reliability of the design.

The wind loads acting on SISs, especially those from the conductors, result in the windage yaw of SISs. Determining the design wind loads of conductors (termed the input problem) and the calculation method of the windage yaw angle, φ (termed the output problem), is important for the calculation of the peak dynamic windage yaw angle, $\widehat{\varphi}$, of SISs. In terms of the input problem, closed-form expressions have been derived for the wind-induced dynamic tension in overhead power TLs [1]. Then, by simplifying the derived root-mean-square (RMS) dynamic tension response spectrum, a calculation formula for the practical design of wind loads was provided [2]. Nonetheless, the background response of conductors was determined by Wang and Li [2] for

using only a few modes, which inevitably introduces errors caused by modal truncation, leading to safety concerns. In China, when calculating $\widehat{\varphi}$, the design wind loads for conductors and insulators in the Chinese technical code for the design of overhead TLs [3] are usually adopted. In the technical code, the design wind loads for conductors are expressed as average wind loads multiplied by the wind pressure nonuniformity factor, α, which allows for the nonuniform distribution of the average wind in the span direction, whilst the dynamic wind load factor, β_c, allows for the action of the fluctuating wind. However, further research [4] found that, in some cases, the value of $\alpha\beta_c$ is less than unity, whereas the design wind loads of conductors in other countries [5, 6] are greater than the average loads. The dynamic magnification effect of the fluctuating wind in the wind yaw calculation cannot be ignored [7]. Furthermore, the microclimate and microterrain factors affect the wind loads for windage yaw calculation [8]. Under rain and wind conditions, negative aerodynamic damping can occur, and the peak swing amplitude of overhead conductors is larger than that under the wind alone, such that rain loads cannot be neglected [9]. Wind loads have been obtained using a two-way fluid-structure interaction simulation by considering the local mountainous terrain and coastal typhoon meteorological conditions, and it was found that the complex wind field has a non-negligible influence on the φ of insulator strings [10]. Regarding the output problem, so far, the rigid straight rod (RSR) model is widely used as a simplified calculation method [11, 12]. The method regards the SIS as a rigid straight rod with one end connected to the fixed hinge support at the tower. Then, φ is determined by applying the equivalent loads from the conductors and SISs to the free end [13]. By comparing with the time-domain results of a finite element model (FEM), it was found that the traditional RSR model is not suitable for determining the dynamic peak response [14]. By considering the shielding effects from bundled conductors and the fluctuating wind effect, a correction formula was provided for the RSR method based on numerical calculations [15]. In a study of the deformation characteristics of the windage yaw of V-type composite insulators, it was found that the included angle of the V-type string is usually small because of the compression of the composite insulator string on the leeward side [16].

These studies helped to develop calculation methods for the φ of insulator strings. However, because of the improper simplifications and the lack of long-term testing, these methods have not been widely used in engineering design. The main issue with the existing windage yaw calculation is the conflict between the nonlinear characteristics of the wind-induced vibration of the lightweight and flexible conductors and the linear wind-induced vibration calculation theory. Yang [17, 18] proposed the theory and algorithm of the rigid-body rule, which has been successfully used to deal with the large deformation and small strain of a truss structure, frame structure, and plate shell structure. However, the concept of the rigid-body rule can also be effectively used to solve the problem of a cable structure, such as the windage yaw of TLs. Here, the windage yaw is dominated by rigid-body displacement and can be solved by decomposing it into a rigid-body displacement and natural deformation. Thus, the fluctuating windage yaw can effectively be solved by frequency-domain calculation methods, such as the gust load factor (GLF) method [19], the load-response-correlation (LRC) method [20], and effective static load distribution methods [21], which apply to linear structures, whereas the average windage yaw, dependent on the average wind, can be easily solved by static calculations. Although research has been conducted to address this issue [1, 22], the decomposition of the response has lacked a reasonable basis. The mode decomposition method with finite modes was inappropriately used to solve the wind-induced vibration of conductors with dense frequencies of each order, and the RSR method was not improved.

In this work, we propose a systematic and simplified calculation method for the $\widehat{\varphi}$ of SISs in the along-wind direction because of the buffeting excited by synoptic wind (that produces Gaussian or weakly non-Gaussian wind loads). Theoretically, this new method offers simplified calculations for the wind-resistant design of TLs considering the influence of windage yaw. The geometric stiffness under the action of the average wind and self-weight is taken as the initial calculation condition, and the equivalent static wind loads (ESWLs) for $\widehat{\varphi}$ are determined based on the LRC method. A more accurate RSR model is proposed to calculate the average windage yaw angle ($\overline{\varphi}$) of the SISs, based on the force balance and triangle principle by taking into account the actual length of the conductors. The peak fluctuating windage yaw angle ($\widehat{\varphi}_d$) of the SISs is determined by the frequency-domain calculation. Then, $\widehat{\varphi}$ is obtained by the linear superposition of the horizontal increments of $\overline{\varphi}$ and $\widehat{\varphi}_d$. Additionally, the dynamic wind load factor, β_c, which is a key factor in the design wind loads for φ, is determined according to the principle of ESWLs. Afterward, the proposed windage yaw calculation model, including loads and response, is verified by the time-domain results. Finally, the influence of important design parameters, such as the wind speed, the height difference between the two suspension points of the conductors (termed "height difference" hereafter), the nominal height, the sag-to-span ratio, the span, and the ground roughness on $\widehat{\varphi}$ and β_c are analyzed using the proposed calculation model. It is anticipated that the results from the present work may be incorporated into the wind-resistant design of TLs.

2. Calculation Methods

2.1. Equivalent Static Wind Loads for Windage Yaw Angle. TLs have a catenary configuration under self-weight and exhibit geometrically nonlinear behavior under wind loads. Research has shown that transmission towers have little influence on the wind-induced vibration response of TLs [23]. To simplify the calculation of the φ of the SIS, the influence of the tower is neglected, and the suspension point of the insulator string on the tower is regarded as fixed hinge support (point A in Figure 1). Additionally, since the study in this paper is within the framework of the Chinese code, when applying the present work in other countries and regions that use different TL design codes, the methodology

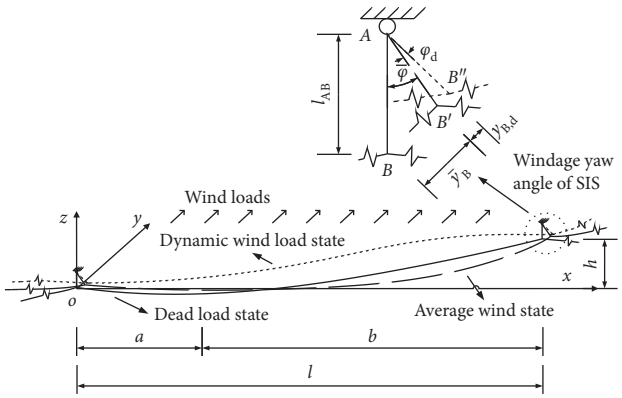

FIGURE 1: Calculation model of the windage yaw angle.

proposed in this paper should be used in relation to those national codes. The calculation model for φ is shown in Figure 1, where a is the horizontal distance from the origin of the coordinates to the lowest point of the conductors, l represents the span, and $l = a+b$, h is the height difference between the two suspension points of the conductors, $\overline{y}_B$ is the along-wind displacement of point B under the average wind loads, and $\overline{y}_B = l_{AB} \sin \overline{\varphi}$, l_{AB} is the length of the insulator string between point A and point B, $y_{B,d}$ is the along-wind displacement of point B under fluctuating wind loads, B is the connection point between the conductor and the SIS, and the superscripts " $'$ " and " $''$ " of this point indicate the average wind state and the dynamic wind state, respectively.

Usually, the wind loads in the along-wind direction can be decomposed into two parts: the average wind loads and the fluctuating wind loads. The matrix expression of the conductor vibration in response to those loads is,

$$\mathbf{M}\ddot{\mathbf{Y}}_d + \mathbf{C}\dot{\mathbf{Y}}_d + \mathbf{K}(\overline{\mathbf{Y}} + \mathbf{Y}_d) = \mathbf{L}(\overline{\mathbf{p}} + \mathbf{p}_d), \tag{1}$$

where M, C, and K are the mass, damping, and stiffness matrices, respectively. L is the transformation matrix composed of the equivalent force at the nodes when unit wind pressure loads are applied to the subordinate areas of the nodes. $\overline{\mathbf{p}}$ and $\mathbf{p}_d$ are the average wind loads and fluctuating wind loads per unit area, respectively. Under the fluctuating wind loads, $\ddot{\mathbf{Y}}_d$, $\dot{\mathbf{Y}}_d$, and $\mathbf{Y}_d$ are the acceleration, speed, and displacement in the along-wind direction, respectively. Under the average wind loads, $\overline{\mathbf{Y}}$ is the displacement in the along-wind direction. Based on the quasi-static assumption, $\overline{\mathbf{p}}$ and $\mathbf{p}_d$ are expressed as follows:

$$\overline{\mathbf{p}} = 0.5\rho_a C_d \overline{\mathbf{v}}^2, \tag{2}$$

$$\mathbf{p}_d = \rho_a C_d \overline{\mathbf{v}}. * \mathbf{v}', \tag{3}$$

where ρ_a is the air density per unit volume, $\overline{\mathbf{v}}$ is the average wind speed, $. *$ indicates that the corresponding elements of the front and rear matrices are multiplied, $\mathbf{v}'$ is the fluctuating wind speed, and C_d is the drag coefficient.

The conductor has a light and flexible structure; under strong wind loads, it can exhibit the following mechanical behavior: (1) the structure has large deformation and geometric nonlinearity, (2) there is a nonlinear relationship between the force and displacement of the structure, and (3) under dynamic wind loads, the structure has time-varying stiffness. Thus, equation (1) is a variable coefficient differential equation so that the linear superposition principle cannot be used to calculate the wind-induced response of the conductors. When conductors undergo large deformation, they are often in the elastic stage. However, if the equilibrium equation is established in the position before the deformation, according to the linear analysis method, the real mechanical behavior of a TL cannot be obtained. It is the key reason why frequency-domain calculation methods, such as the GLF method [19], LRC method [20], and the effective static load distribution method [21] cannot be used for reliable windage yaw calculation of TLs. K includes the geometric stiffness matrix and elastic stiffness matrix [24]. The geometric stiffness matrix reflects the effect of the initial external force because of the change in member shape and position. The rigid-body concept can effectively deal with various large deformation and small strain problems [17, 18]. According to this concept, the windage yaw of TLs is the superposition of two processes: the rigid-body displacement of the TL, which occurs from the dead load state to the average wind state and, consequently, the small amplitude and the back-and-forth motion, which occurs from the average wind state to the dynamic wind load state (as shown in Figure 1). In the first process, the element nodal force has the same rigid body displacement with the element, whose magnitude is unchanged, and this force balance is still maintained in the second process. Thus, the small amplitude motion of the second process is calculated after the end of the first process is set as an initial state. Hence, the first process end accounts for the main part of the windage yaw and determines the geometric stiffness matrix, whereas the second process affects only the elastic stiffness matrix. By the decomposition of the windage yaw, the static calculations and the frequency-domain method can be used to solve the first and second processes, respectively. The above description can be summarized as follows: under the action of fluctuating wind loads, the motion of the conductor is regarded as small displacement, and the load-response relationship is almost linear. The stiffness matrix is consistent with that under the average wind state, $\mathbf{K}_{\overline{Y}}$, i.e., $\mathbf{K} = \mathbf{K}_{\overline{Y}}$.

Therefore, under the action of fluctuating wind loads, the matrix expression for the vibration of the conductors is as follows:

$$\mathbf{M}\ddot{\mathbf{Y}}_d + \mathbf{C}\dot{\mathbf{Y}}_d + \mathbf{K}_{\overline{Y}}\mathbf{Y}_d = \mathbf{L}\mathbf{p}_d. \tag{4}$$

Unlike equation (1), equation (4) is a differential equation with constant coefficients and can be calculated by the linear superposition principle. The average response of the conductors is regarded as a static response, and the average displacement of the conductors can be expressed by the nonlinear static balance equation, which is as follows:

$$\mathbf{K}_{\overline{Y}}\overline{\mathbf{Y}} = \mathbf{L}\overline{\mathbf{p}}. \tag{5}$$

Because of the large aerodynamic damping of the conductors, the resonant response is negligible, and hence, the fluctuating response is dominated by the quasi-static

background response [25, 26]. The resonant response of the conductors is also neglected in the ASCE code [5]. Similarly, regardless of the resonant response, the ESWLs for equation (4) are, herein, calculated by the LRC method. Thus, the background response, $\mathbf{Y}_b$, of the conductors at the node can be expressed as follows:

$$\mathbf{K}\mathbf{Y}_b = \mathbf{L}\mathbf{p}_d. \tag{6}$$

The variance of $\mathbf{Y}_b$ can be expressed as follows:

$$\boldsymbol{\sigma}_b^2 = \mathrm{diag}\left(\mathbf{Y}_P \int_{-\infty}^{+\infty} \mathbf{S}_{pp} \mathbf{d}\omega \ \mathbf{Y}_P^T\right), \tag{7}$$

where diag is the new matrix formed by the diagonal elements of the matrix in parentheses, Y_{P} is the solution of the static balance equation, $\mathbf{K}\mathbf{Y}_P = \mathbf{L}$, and $\mathbf{S}_{pp}$ is the cross-spectrum matrix of the fluctuating wind pressure.

The correlation coefficient between the fluctuating load effect and the fluctuating wind loads is as follows:

$$\boldsymbol{\rho}_{\mathrm{Pr}} = \frac{\overline{\mathbf{L}\mathbf{p}_d \mathbf{r}^T}}{\left(\mathbf{L}\boldsymbol{\sigma}_p \boldsymbol{\sigma}_b^T\right)}, \tag{8}$$

$$\mathbf{r} = \mathbf{I}_r^T \mathbf{L}\mathbf{p}_d, \tag{9}$$

where the overbar indicates a time average, ./ indicates the division of the corresponding elements of the front and rear matrices, and $\boldsymbol{\sigma}_p$ is the standard deviation of $\mathbf{p}_d$. $\mathbf{I}_r$ denotes the influence function for the load effect, r.

The distributions of the ESWLs per unit area of the nodes are as follows:

$$\widehat{\mathbf{p}}(:, i) = \overline{\mathbf{p}} + \widehat{\mathbf{p}}_b(:, i), \tag{10}$$

$$\widehat{\mathbf{p}}_b(:, i) = g\boldsymbol{\rho}_{\mathrm{Pr}}(:, i). * \boldsymbol{\sigma}_p, \tag{11}$$

where $(:, i)$ are all the elements in the i column of the matrix, and g is the background peak factor. Equation (10) is the general formula that can be used to calculate the ESWLs at different locations and the different responses of the conductors. In Figure 1 , point B is selected as the calculation target point. When the along-wind displacement, y_{B}, of the target point reaches its maximum value, the φ of the SIS reaches the maximum $\widehat{\varphi}$. According to equations (7)–(10), $\widehat{\varphi}$ and its ESWLs can be calculated using y_B as the load effect.

2.2. Dynamic Peak Windage Yaw Angle. As shown in Figure 1, under the dead load state, the SIS, which is regarded as a rigid straight rod, is located between the points A and B. Under the average wind state, point B moves to point B′ in the along-wind direction, and the increment of φ is $\overline{\varphi}$. With the addition of the fluctuating wind, point B′ moves to point B″ in the along-wind direction, and the increment of φ is φ_d. The dynamic peak windage yaw angle, $\widehat{\varphi}$, is decomposed into $\overline{\varphi}$ and $\widehat{\varphi}_d$ (the peak value of φ_d). The RSR model is widely used to simplify calculations for the φ of SISs [11, 12]. However, the applicability of this model is limited. Large errors may occur when the layout and horizontal loads of a TL are nonuniform along the span direction, e.g., the TL that has height differences between the two conductor suspension points and experience fluctuating wind loads [14, 15]. The analysis presented in this section improves the traditional RSR model and uses the improved model and the frequency-domain method to calculate $\overline{\varphi}$ and $\widehat{\varphi}_d$, respectively. Based on the force balance and triangle principle, $\overline{\varphi}$ can be derived from the following:

$$\overline{\varphi} = \arctan\left(\frac{0.5\overline{G}_h + \overline{W}_h}{0.5G_v + W_v}\right), \tag{12}$$

where $\overline{G}_h$ and G_v are, respectively, the average wind loads and the weight at the centroid of the SIS, whereas $\overline{W}_h$ and W_v are the horizontal loads and vertical loads at point B′ of the SIS, which are generated by the average wind loads and the weight of the conductors, respectively. The expressions of $\overline{W}_h$ and W_v can be written as follows:

$$\overline{W}_h = \overline{P}_h \Gamma_h, \tag{13}$$

$$W_v = P_v \Gamma_v, \tag{14}$$

where $\overline{P}_h$ and P_v are the horizontal and vertical loads per unit length of the conductors, respectively, Γ_h is the total along-conductor length between the two half-span points ($l/2$) on either side of the tower, and Γ_v is the total along-conductor length between the two lowest conductor points on either side of the tower. The increment of the conductor length caused by the wind loads is very small compared with its total length, and hence, Γ_h and Γ_v can be determined under a dead load state. According to the coordinate system established in Figure 1, the expression of the catenary equation of the conductor is as follows:

$$z = \frac{2\sigma_0}{\gamma} \mathrm{sh} \frac{\gamma x}{2\sigma_0} \mathrm{sh} \frac{\gamma(x - 2a)}{2\sigma_0}, \tag{15}$$

$$a = \frac{l}{2} - \frac{\sigma_0}{\gamma} \mathrm{arcsh} \frac{h}{(2\sigma_0/\gamma)\mathrm{sh}(\gamma l/2\sigma_0)}, \tag{16}$$

$$\gamma = \frac{G_0}{A_s}, \tag{17}$$

where σ_0 is the initial horizontal conductor stress. When the target point is higher than the other suspension point, h is positive. G_0 and A_s are, respectively, the self-weight per unit length and the cross-sectional area of the conductors. Using equation (15), Γ_h and Γ_v can be calculated. Equations (13)–(17) are closed-form formulations that reduce the calculation error of the windage yaw angle compared with the traditional RSR method and are suitable for different cases, especially those with height differences.

Based on the triangle principle, the expression for $\widehat{\varphi}$ is as follows:

$$\widehat{\varphi} = \arcsin \frac{\widehat{y}_B}{l_{AB}}, \tag{18}$$

$$\widehat{y}_B = \overline{y}_B + \widehat{y}_{B,d}, \tag{19}$$

where $\hat{y}_{B,d}$ is the peak along-wind displacement of point B under fluctuating wind loads and can be calculated by the linear superposition principle. Thus, the expression of $\hat{y}_{B,d}$ is as follows:

$$\hat{y}_{B,d} = g\left(\boldsymbol{\rho}_{Py_B} \cdot * \boldsymbol{\sigma}_p\right)^T \mathbf{L}^T \mathbf{I}_{y_B}, \tag{20}$$

where ρ_{Py_B} is the correlation coefficient of the fluctuating wind loads and y_B, and $\mathbf{I}_{y_B}$ is the influence function of y_B. Thus, the calculation model of $\hat{\varphi}$ is established by equations (7)–(20).

2.3. Dynamic Wind Load Factor of the Windage Yaw Angle. The expression for the design wind loads for conductors in the Chinese technical code for the design of overhead TLs [27] is as follows:

$$W_x = \alpha\beta_c\overline{W_x} = \alpha w_0 \mu_z \mu_{sc} \beta_c d L_p B_i \sin^2\theta, \tag{21}$$

where $\overline{W}_x$ is the average wind loads, w_0 is the wind pressure at a reference height of 10 m, μ_z is the wind pressure height variation coefficient, μ_{sc} is the drag coefficient, d is the outer diameter of the conductors, B_i is the amplification factor for the wind loads considering any ice-coverage, and θ is the angle between the along-wind direction and the extension direction of the conductors. Moreover, using Table 10.1.18-1 [27] in this design code to calculate the windage yaw, the value of α is less than unity and related only to the wind speed, and β_c is set to unity. Since α and β_c of this design code are determined empirically, W_x is less than $\overline{W}_x$, which contradicts the concept of ESWLs.

The physical meaning of β_c is consistent with that of β in the Chinese load code [28], both of which consider the dynamic effect caused by the fluctuating wind. According to the concept of ESWLs, $\boldsymbol{\beta}_c = \hat{\mathbf{p}}./\overline{\mathbf{p}}$, $\boldsymbol{\beta}_c$ calculated by the LRC method is not a constant. β_c is averaged according to the distribution characteristics of $\hat{\mathbf{p}}$ to give a value that is then considered to be uniformly distributed, which facilitates the design. $\hat{\mathbf{p}}$ has its maximum value at a selected target point, and it approaches $\overline{\mathbf{p}}$ far away from the target point. Both $\hat{\mathbf{p}}$ and $\overline{\mathbf{p}}$ are nonuniform. Therefore, a calculation range can be set artificially. Within this calculation range, the ESWLs at the target point can be calculated by averaging. For example, when there is no height difference between the target point and the conductor suspension point of the adjacent tower, the left and right half-spans of the target point can be set as the calculation range. Moreover, when there is a height difference between the target point and the conductor suspension point of the adjacent tower, since the ESWLs at the target point are larger in magnitude, the left and right quarter spans of the target point are selected as its calculation range. Under the calculation range, assuming a uniform distribution, β_c, can be calculated using the following:

$$\beta_c = \frac{\hat{q}}{\overline{q}} = 1 + \frac{\hat{q}_b}{\overline{q}}, \tag{22}$$

$$\hat{q}_b = \frac{\sum \hat{\mathbf{p}}_b}{\sum \Gamma}, \tag{23}$$

$$\overline{q} = \frac{\sum \overline{\mathbf{p}}}{\sum \Gamma}, \tag{24}$$

where $\sum$ indicates the sum of elements in the calculation range, and $\sum \Gamma$ is the actual length of the conductors in the calculation range. Equations (22)–(24) have been verified by the present authors (currently unpublished) for several different TLs and the relative errors of $\hat{\varphi}$ from FEM, and the proposed model is less than ±6%. Hence, β_c can be easily obtained with sufficient precision for engineering applications. Thus, the calculation model of the dynamic wind load factor is established using equations (22)–(24), and the value of β_c calculated by this calculation model meets the concept of ESWLs and incorporates the influence of various design parameters. Therefore, this formulation for β_c is more accurate and has a sounder physical basis than that specified in the Chinese technical code for the design of overhead TLs [27]. The design wind loads of the windage yaw angle can be calculated by substituting β_c into equation (21). Some example calculations are presented in the next section.

When determining the windage yaw of SISs, equation (21) is used to calculate the design wind loads, and equation (12) is used to calculate the responses in the existing methods. For complex types of transmission lines, such as those with large spans, large height differences, and significant dynamic effects, the time-domain analysis of finite element models is required to determine the windage yaw. The method proposed in this paper solves the problem of applying the LRC method to calculate the windage yaw and gives closed-form formulations of the dynamic wind loads of SISs. Considering the actual length of the conductors, the RSR model is improved by equations (13)–(17). A two-step method for calculating $\hat{\varphi}$ is proposed. Firstly, the improved RSR model is used to determine $\overline{\varphi}$, and the LRC method is used to determine $\hat{\varphi}_d$. Secondly, β_c is determined based on the LRC method, and its nonuniform distribution is processed to an equivalent average distribution for engineering practice using equations (22)–(24). Compared with the existing methods, the proposed method not only enriches the application scenarios for calculating the windage yaw of SISs in the wind-resistant design codes but also has the advantage of efficient calculation (see the section below for details).

3. Calculations

3.1. Calculation Parameters. A 500-kV TL, whose layout scheme is two tension towers at both ends, with three suspension towers between them, all arranged in a straight line, is selected, and the length between the two tension towers is 2.2 km, as shown Figure 2. In Figure 2, H represents the nominal height and is also equal to the height of the suspension point of the insulator string. Then, the connecting point of the insulator string and the conductor at suspension point 2 is arbitrarily selected as the target point for the calculation case to illustrate the methodology, although the calculation method is also applicable to any other selected point. Moreover, the conductors are type 4 × JLHA1/G1A-575/40-45/7, whose physical parameters

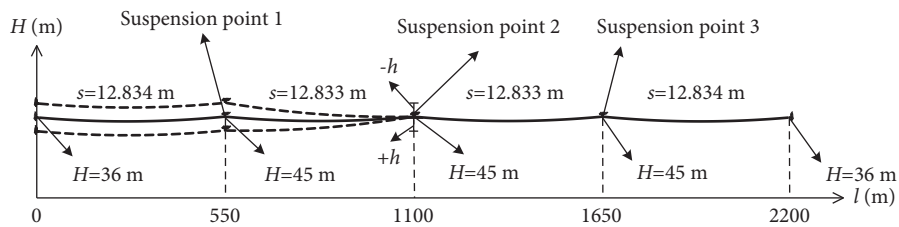

Figure 2: Calculation sketch of the transmission line spans.

are shown in Table 1. According to the Chinese technical code for the design of overhead TLs [27], the drag coefficient of the conductors is $C_d = 1.1$. The physical parameters of the SIS on the tension tower and the suspension tower are shown in Table 2. Meanwhile, the design average wind speed at 10 m height is 30 m/s, the oncoming wind direction is perpendicular to the span direction, and category B ground roughness (the terrain type of open country and towns with sparse houses) is used for the calculations. According to the Chinese load code [28], the peak factor is 2.5.

3.2. Verification of Windage Yaw Angle Calculation. The proposed calculation model for the windage yaw of SISs in section 2 is verified by the FEM in this section. Before the verification, two simplified approaches need to be elaborated. Firstly, in this work, we focus on the overall motion of the conductors under wind loads, rather than the local subspan oscillation, and hence, the bundled conductors are combined into a single conductor according to the force equivalent. Secondly, α considers the nonuniform distribution of the average wind along the span direction, which represents the characteristics of the average wind. Here, we focus on the dynamic effect of the fluctuating wind. Therefore, α is not considered in the following analyses. Using equations (1)–(11), the ESWL per unit area of the conductors and its component distribution are determined, as shown in Figure 3. The components of the ESWLs are dominated by the average component, and the average component distribution is similar to the catenary shape under the dead load state. The background component reaches its peak at the target point and approaches zero at both ends. Because of the symmetry of the structural arrangement and the target point being located on the symmetry axis, the distributions of the ESWLs and their components have symmetry. The wind loads determined in Figure 3 are used to calculate the windage yaw angle and its β_c. Using equations (12)–(14), we obtain $\overline{\varphi} = 51.93^{\circ}$, $\overline{W}_h = 60.35$ kN, and $W_v = 42.08$ kN, and through equations (18) and (19), we derive $\widehat{\varphi} = 58.53^{\circ}$ and $\widehat{y}_B = 5.827$ m. Through equations (22)–(24), we calculate $\beta_c = 1.281$, $\widehat{q}_b = 7.64$ N/m and $\overline{q} = 27.24$ N/m.

The correctness of the proposed calculation model is verified by the time-domain calculation results of the FEM. The harmonic wave superposition method [29] is used to simulate the turbulent wind fields for a Category B ground roughness [28]. Consistent with the Chinese load code [28], the power spectrum function of the height-independent fluctuating wind speed, proposed by Davenport [30], and the spatial correlation function, proposed by Shiotani and Arai [31], are adopted. The greater the number of wind speed samples N, the higher the accuracy of the wind speed simulation, however, this increases the calculation cost. When the fast Fourier transform algorithm is applied to the harmonic wave superposition method, the value of N must be equal to an exponential function of 2 [29]. Herein, we set $N = 4096$ and the cut-off frequency $f_{up} = 4$ Hz for the simulated wind speed. Then, the time interval is $\Delta t = 1/(2f_{up}) = 0.125$ s, and the simulation duration is 1024 s. Only the wind speeds within the height, from 24.228 to 38.168 m, which are the lowest and highest heights of the conductors, respectively, of the conductors, are simulated. The characteristics of the simulated wind field for the average wind profile, the turbulence intensity profile, and the fluctuating wind speed power spectrum at 38.168 m of height are compared with those in the Chinese load code [28], as shown in Figure 4, where $I_z = \sigma_v / \overline{v}$ is the turbulence intensity, σ_v is the standard deviation of v', f is the frequency of the fluctuating wind speed, S_v is the fluctuating wind speed power spectrum function, and the turbulence length scale, L_v, is 1200 m according to Davenport [30]. The difference between the results from the simulated wind field and the Chinese load code can be eliminated when N is infinite. The maximum and minimum relative error of average wind speeds obtained from the Chinese load code compared to those obtained by the simulated wind field are 0.7% and 0.5%, respectively. Similarly, the errors in the turbulence intensity are 4.4% and -4.2%, respectively. The comparison demonstrates that the simulated values are in good agreement with the calculated values from the Chinese load code.

The FEM was conducted using the ANSYS software [32], and the windage yaw of the TL was analyzed under the simulated wind field. The conductor and insulator string are simulated by the Link 180 element [33], whose element length is 10 m and component length, respectively. The element is a uniaxial tension-compression element with three degrees of freedom at each node, and a tension-only (for cable structures) setting is available, which can be used to model trusses, sagging cables, links, springs, and so on. The structural damping ratio is 0.5% according to Loredo-Souza and Davenport [25]. Furthermore, aerodynamic damping and structural self-weight are taken into consideration. The initial operating tension is 55.39 kN according to the actual design parameter. The conductor shape under the dead load state is determined by equations (15)–(17). The analysis type of the ANSYS software is set as transient analysis, and the transient effects and large-deflection effects

Table 1: Physical parameters of the conductors (JLHA1/G1A-575/40-45/7 ACSR type).

Cross-sectional area (A_s) (mm^2)	Elastic modulus (MPa)	Mass per unit length (kg/km)	Outer diameter (mm)
621	63000	1917	32.40

Table 2: Physical parameters of the insulator string.

Position	Length (l_{AB}) (m)	Elastic modulus (MPa)	Mass (kg)	Wind-shielding area (mm^2)
Tension tower	8.33	72000	1614.60	113400
Suspension tower	6.83	72000	1238.08	101800

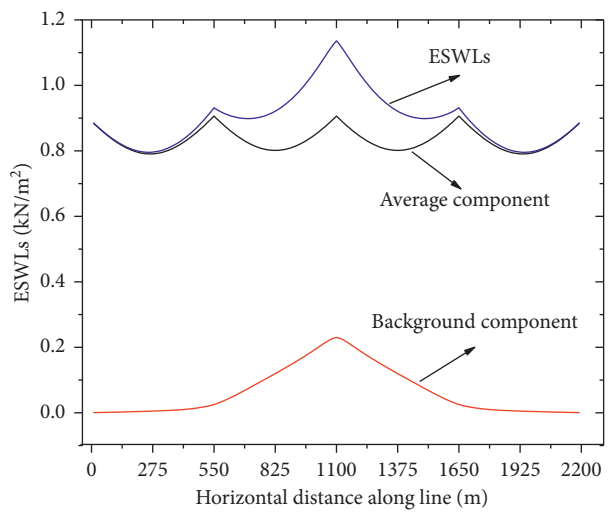

Figure 3: Equivalent static wind loads and the distributions of their components.

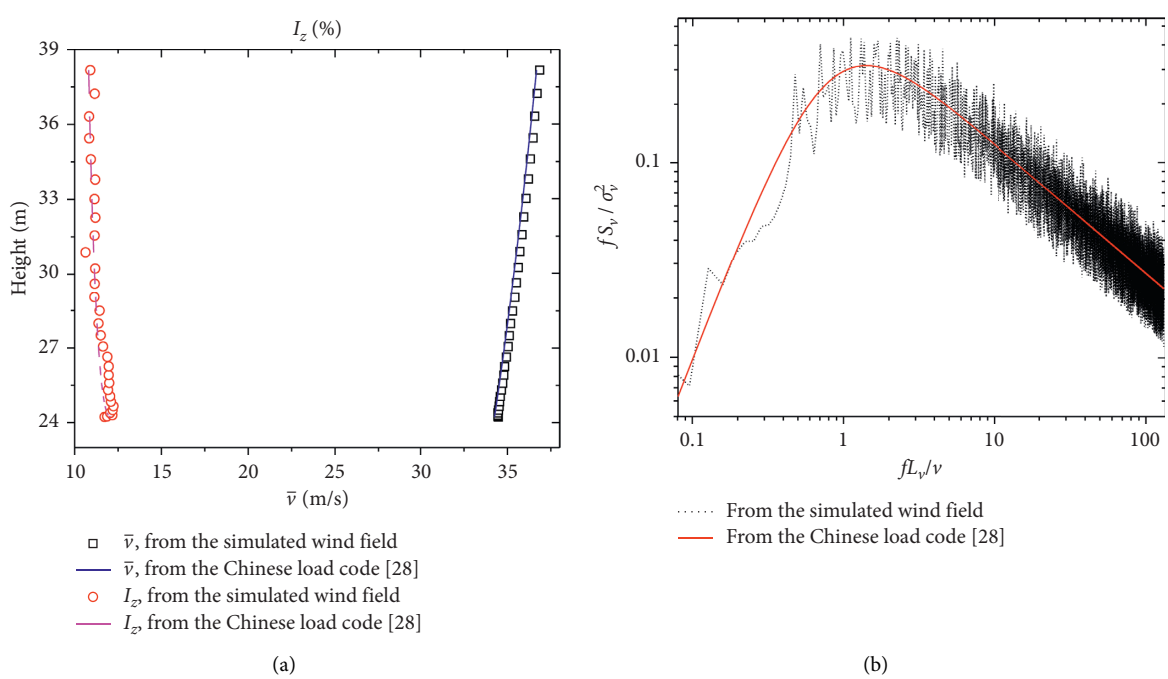

Figure 4: Comparison of the simulated values and the calculated values of the Chinese load code for the wind field characteristics for Category B ground roughness (GB 50009-2012, 2012). (a) Average wind speed ($\bar{v}$) profile and turbulence intensity (I_z) profile. (b) Nondimensional wind speed spectrum at 38.168 m height.

options are turned on. The wind loads of the component elements are applied to its element node equivalently. The restraint mode of the connection between the insulator string and the tower, the physical parameters and the geometric information of the conductors, and the insulator strings are consistent with those in Figure 2 and Tables 1 and 2. Then, the established FEM (as shown in Figure 5) is used for conducting time-domain calculations. In Figure 5, the directions of the x, y, and z axes are parallel to the cross-conductor, along-conductor, and vertical directions, respectively. In addition, the accuracy of the time-domain calculation has been verified [34].

In the time-domain calculation, the $\overline{\varphi}$ and $\widehat{\varphi}$ of the target point are 50.86° and 56.23°, respectively. The relative error of $\overline{\varphi}$ and $\widehat{\varphi}$ obtained from the time-domain calculation compared to those obtained by the proposed calculation model are 2.1% and 4.1%, respectively. Hence, the results of the calculation model are in agreement with those of the time-domain model and can provide sufficient precision in engineering applications. Moreover, the computational times of these results are approximately 3 s and 2 h, respectively, showing that the present calculation model is computationally much more efficient.

4. Analyses of Important Influencing Parameters

The main variables that influence the value of β_c in (22) are the wind speed, the conductor height, the spatial correlation, and the turbulence. These variables can be further subdivided into various influence parameters, such as the height difference, the nominal height, the sag-to-span ratio, the span, and the ground roughness. The codependency of the influence parameters is neglected herein. Taking Figure 2 as an example, the influence parameters are changed independently within the design range, and the proposed calculation model is used to assess their effects research on $\overline{\varphi}$, $\widehat{\varphi}$, and β_c. In practical engineering design, many conductor and SIS types are used, although only one type (as shown in Tables 1 and 2) of each is analyzed in this work. For other types of conductors and SISs, the method proposed in this paper can be used to calculate the windage yaw of the TLs.

4.1. Influence of Wind Speed. The design average wind speed at the reference height of 10 m, $\overline{v}_{10}$, is varied from 10 m/s to 50 m/s, with 10 m/s intervals, and the corresponding change in the windage yaw angle is shown in Figure 6. With increasing wind speed, both $\overline{\varphi}$ and $\widehat{\varphi}$ increase nonlinearly, and the rate of increase decreases, indicating that the tangent stiffness of the conductor windage yaw gradually increases. The influence of the mean wind speed on β_c is shown in Figure 6 and Table 3. With increasing wind speed, β_c increases nonlinearly, and the rate of increase gradually becomes larger because of the influence of the stiffness changes.

4.2. Influence of Height Difference between the Two Suspension Points of Conductors. The influence of the height difference is studied by the overall vertical translation of the conductor of the first span on the left in Figure 2. A downward translation means a positive height difference for suspension point 2, with respect to suspension point 1, whereas an upwards translation means a negative height difference for that point (as shown in Figure 2). The height difference between the target point and the suspension point 1 is between −60 m and 20 m. With the decrease in the magnitude of the height difference, the wind loads and the self-weight of the conductors transmitted to the target point of the insulator string increase and decrease, respectively, which, in turn, results in a change in the stress stiffness of the insulator string. The distribution of the windage yaw angle corresponding to different height differences is shown in Figure 7. With the decreasing height difference, $\overline{\varphi}$ and $\widehat{\varphi}$ gradually increase, and the height difference versus windage yaw angle relationship is approximately linear. The influence of the height difference on β_c is shown in Figure 7 and Table 4. As the height difference increases, β_c first increases, then decreases, and finally, it increases again. β_c is larger when there is a height difference than in the case of no height difference. The absolute maximum deviation of β_c from its average value is 3.2%. Thus, within the range of h = -60 m to 20 m, the height difference only slightly affects β_c.

4.3. Influence of Nominal Height. The nominal height (H) is varied to vertically translate the whole TL from H = 25 m to 105 m at the intervals of 20 m. As shown in figure 4(a), as the nominal height increases, the average wind speed increases, and turbulence intensity decreases. The variation of the windage yaw angle with nominal height is shown in Figure 8, showing that as the nominal height increases, $\overline{\varphi}$ and $\widehat{\varphi}$ increase nonlinearly, while the rate of that increase decreases. The influence of the nominal height on β_c is shown in Figure 8 and Table 5. Under the combined effect of the average wind speed and turbulence intensity, the nominal height has little influence on β_c, and this influence has no obvious regularity.

4.4. Influence of the Sag-to-Span Ratio. Generally, when the sag-to-span ratio, η, increases, the wind loads on the conductor decrease. Because of the decrease in the initial tension, the stress stiffness of the conductor also decreases. Hence, the sag-to-span ratio affects the windage yaw characteristics of conductors from two aspects. The variation of windage yaw angle with sag-to-span ratio, presented in Figure 9, shows that as the sag-to-span ratio increases, $\overline{\varphi}$ and $\widehat{\varphi}$ decrease nonlinearly. The influence of the sag-to-span ratio on β_c is shown in Figure 9 and Table 6. As the sag-to-span ratio is varied, the trend of β_c is not obvious. The absolute maximum deviation of β_c from its average value is 4.7%, and hence, the variability, within the range of η = 1% to 5%, is small.

4.5. Influence of Span. The sag-to-span ratio of the conductor is kept unchanged, and the design span (550 m, as shown in Figure 2) is varied from 150 m to 950 m in the intervals of 200 m. With an increase in span, the spatial correlation of the

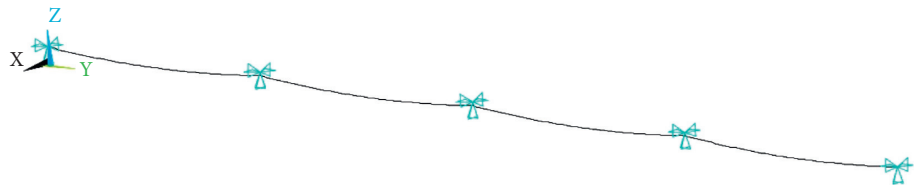

Figure 5: Isometric view of the FEM with four-span conductors in ANSYS software.

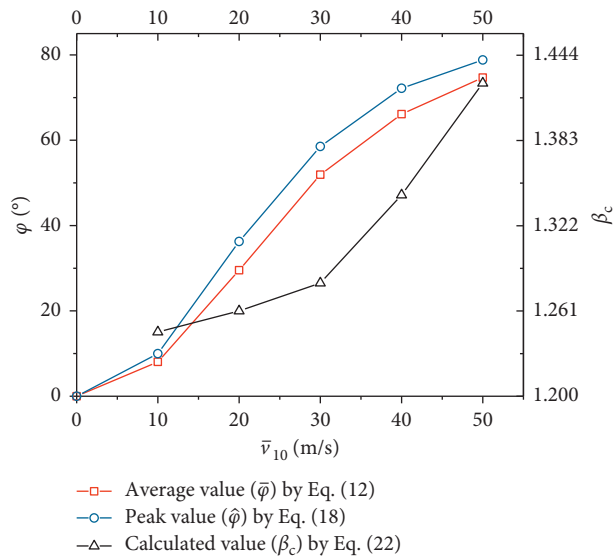

Figure 6: Influence of mean wind speed ($\bar{v}_{10}$) on the windage yaw angle (φ).

Table 3: Influence of wind speed on the dynamic wind load factor of the windage yaw angle.

$\bar{v}_{10}$ (m/s)	10	20	30	40	50
β_c	1.246	1.261	1.281	1.344	1.424

wind loads decreases, however, the wind loads and self-weight of the conductors increase. The windage yaw angle distribution corresponding to different spans is shown in Figure 10. Under the combined action of the wind loads and self-weight, as the span increases, $\bar{\varphi}$ and $\hat{\varphi}$ increase first and then decrease. When the span is 550 m, the windage yaw angle reaches its maximum value. The influence of span on β_c is shown in Figure 10 and Table 7. Because of the joint influence of the wind loads and self-weight, with the increase in span, β_c decreases, and the rate of decrease becomes smaller.

4.6. Influence of Ground Roughness. The ground roughness category of the Chinese load code GB 50009-2012 is divided into four categories. Most TLs belong to category B ground roughness because they are used for fields, villages, jungles, hills, and towns with sparse houses. In addition, long-span TLs are in category A ground roughness, which means that they are used for offshore water surfaces and islands. A few TLs that are located in cities belong to category C or D ground roughness, which are for dense urban areas. The design ground roughness case is changed from A to

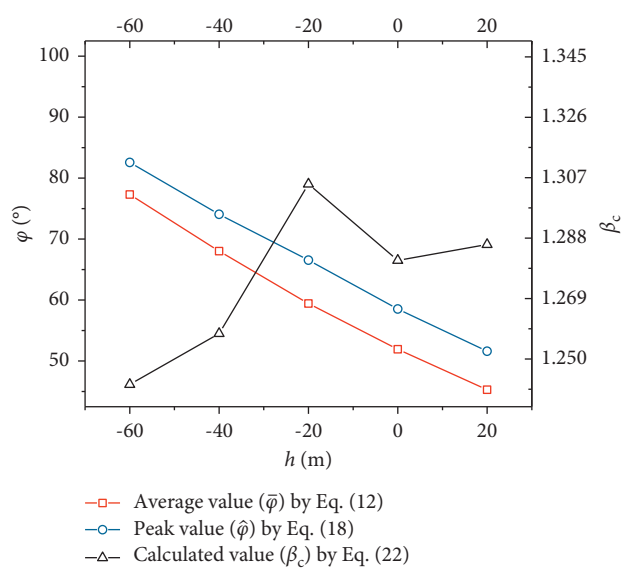

Figure 7: Influence of height difference (h) on the windage yaw angle (φ).

D. Figure 11 shows that when the roughness category is changed from A to D, $\bar{\varphi}$ and $\hat{\varphi}$ decrease. It is because the wind speeds within the conductor height range decrease as roughness increases for a given reference wind speed. The influence of the ground roughness category on β_c is shown in Figure 11 and Table 8. As the ground roughness category

Table 4: Influence of height difference on the dynamic wind load factor of the windage yaw angle.

h (m)	−60	−40	−20	0	20
β_c	1.242	1.258	1.305	1.281	1.286

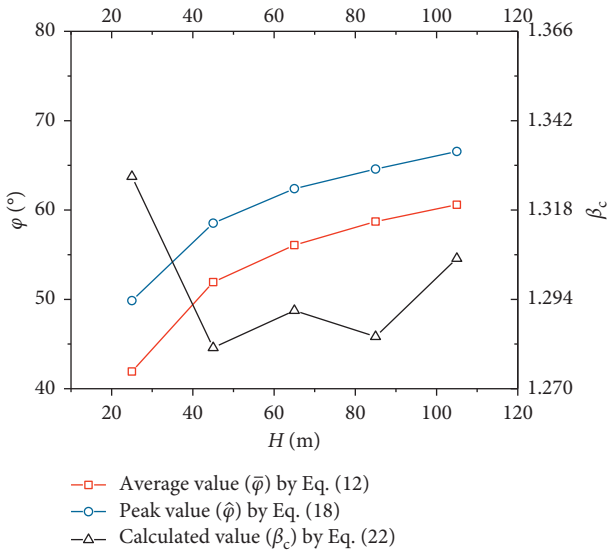

Figure 8: Influence of nominal height (H) on the windage yaw angle (φ).

Table 5: Influence of nominal height on the dynamic wind load factor of the windage yaw angle.

H (m)	25	45	65	85	105
β_c	1.327	1.281	1.291	1.284	1.305

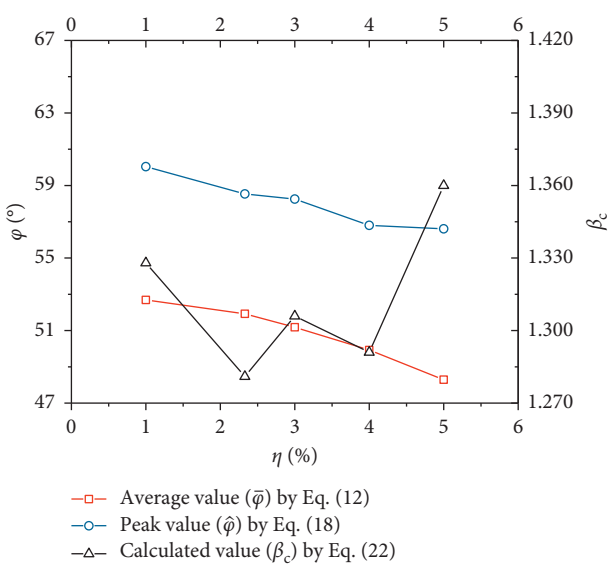

Figure 9: Influence of sag-to-span ratio (η) on the windage yaw angle (φ).

Table 6: Influence of sag-to-span ratio on the dynamic wind load factor of the windage yaw angle.

η (%)	1	2.33	3	4	5
β_c	1.328	1.281	1.306	1.291	1.360

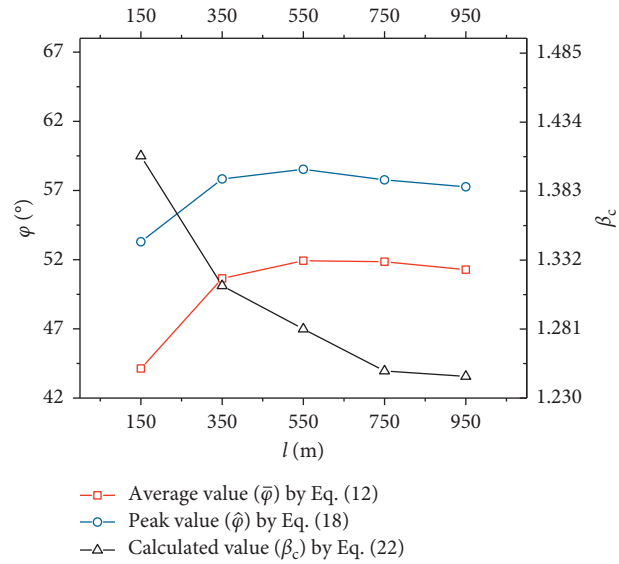

Figure 10: Influence of span (l) on the windage yaw angle (φ).

Table 7: Influence of span on the dynamic wind load factor of the windage yaw angle.

l (m)	150	350	550	750	950
β_c	1.409	1.313	1.281	1.250	1.246

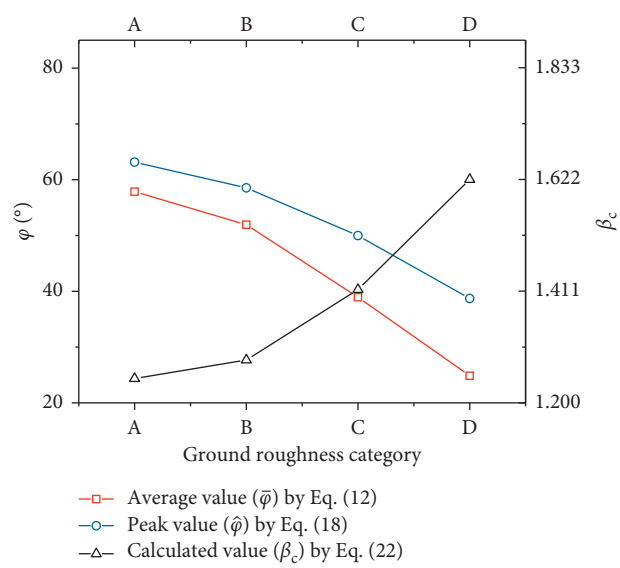

Figure 11: Influence of ground roughness category on the windage yaw angle (φ).

Table 8: Influence of ground roughness category on the dynamic wind load factor of the windage yaw angle.

Category ground roughness	*A*	*B*	*C*	*D*
β_c	1.246	1.281	1.414	1.622

changes from A to D, β_c increases. It is because the static wind effect of the conductors decreases, whereas its dynamic wind effect increases, as roughness increases for a given reference wind speed.

5. Conclusions

By introducing the rigid-body rule and an improvement to the rigid straight rod (RSR) model, a calculation model was proposed to determine the peak dynamic windage yaw angle $\widehat{\varphi}$, together with the dynamic wind load factor β_c, of suspension insulator strings (SISs). The proposed calculation model was then verified by the results from a time-domain calculation. By changing the values of important design parameters within the design range, the influence of these parameters on $\widehat{\varphi}$ and β_c was analyzed. The main findings are summarized as follows:

(i) According to the wind-induced vibration characteristics (large deformation and small amplitude) of the conductors, with the average wind state as the initial calculation condition, the load-response-correlation (LRC) method can be used to calculate the equivalent static wind loads (ESWLs) and $\widehat{\varphi}_0$ of SISs. The established RSR model improves the calculation accuracy, especially for the case where there is a height difference, and it is suitable for calculating the average windage yaw angle ($\overline{\varphi}$). Compared with the calculation of $\widehat{\varphi}$ in the existing method, the proposed method is not only applicable to complex transmission line (TL) scenarios but also computationally more efficient.

(ii) Taking an actual TL as an example, the ESWLs, $\overline{\varphi}$, $\widehat{\varphi}$, and β_c are calculated by the proposed calculation model with regards to the windage yaw of an SIS. The ESWLs reach their maximum value at the selected target point position. $\widehat{\varphi}$ is 1.127 times that of $\overline{\varphi}$, and the corresponding β_c is 1.281, indicating that the dynamic effect and nonlinearity of the windage yaw is obvious and cannot be ignored in the calculation. The accuracy and efficiency of the proposed calculation model are verified by the FEM results.

(iii) For increasing wind speed and nominal height, $\overline{\varphi}$ and $\widehat{\varphi}$ increase. For increasing height difference and sag-to-span ratio and when the ground roughness category is changed from A to D, $\overline{\varphi}$ and $\widehat{\varphi}$ decrease. With increasing span, $\overline{\varphi}$ and $\widehat{\varphi}$ initially increase and then decrease, with a span of 550 m being the most unfavorable. With increasing wind speed and when the ground roughness category is changed from A to D, β_c increases. With increasing span, β_c decreases. The height difference, nominal height, and sag-to-span ratio only have a small influence on β_c and may be neglected in the approximate calculation of β_c.

(iv) In the presented work, reference has been made specifically to the Chinese code, and only one type of conductor and SIS is selected for conducting the influence parameter analyses. For the application of the present work in TL design using other types of conductors in different countries and regions, more types should ideally be considered, and the methodology proposed here can be used to determine the value of β_c for the selected conductor in relation to other national or regional codes.

Data Availability

The source data used in this paper are not generally available; however, the reader may contact the corresponding author for specific information or data.

Conflicts of Interest

The authors declare that they have no conflicts of interest.

Acknowledgments

This study was supported by the Science and Technology Research Program of Chongqing Municipal Education Commission (Grant No. KJQN202001548), Scientific Research Foundation of Chongqing University of Science and Technology (Grant No. ckrc2019036), and National Natural Science Foundation of China (Grant No. 51808078).

References

[1] D. H. Wang, J. Li, and Q. Xie, "Analytical model for dynamic tension in overhead power transmission lines subject to strong wind," *Advances in Structural Engineering*, vol. 14, no. 3, pp. 445–456, 2011.

[2] D. H. Wang and J. Li, "Wind load in design of long-span transmission lines based on RMS dynamic tension response spectrum," *Journal of Vibration and Shock*, vol. 31, no. 9, pp. 82–89, 2012.

[3] National Energy Administration, *Technical Code for the Design of tower and Pole Structures of Overhead Transmission Lines*, National Energy Administration of the People's Republic of China, Beijing, China, 2012, in Chinese.

[4] D. H. Wang, H. Y. Wu, and S. G. Liang, "Theoretical analysis and comparison on typical international wind load codes of transmission conductors," *Proceedings of the Chinese Society for Electrical Engineering*, vol. 34, no. 36, pp. 6613–6621, 2014.

[5] American Society of Civil Engineers, *Guidelines for Electrical Transmission Line Structural Loading*, American Society of Civil Engineers, Reston, USA, 4th edition, 2020.

[6] British Standards Institution, *Lattice Towers and Masts —Part 1: Code of Practice for Loading*, British Standards Institution, London, UK, 1986.

[7] W. J. Lou, Y. Yang, Z. B. Lv, S. F. Zhang, and L. Yang, "Windage yaw dynamic analysis methods for transmission lines considering aerodynamic damping effect," *Journal of Vibration and Shock*, vol. 34, no. 6, pp. 24–29, 2015.

[8] J. Shao, J. Wang, M. Long, J. Wang, Y. Tang, and M. Sun, "Study on windage yaw calculation and real-time warning

method of Shanxi power grid considering microclimate and micro-terrain factors," *IEEJ Transactions on Electrical and Electronic Engineering*, vol. 13, no. 5, pp. 681–688, 2018.

[9] C. Zhou, J. Yin, and Y. Liu, "Large swing behavior of overhead transmission lines under rain-load conditions," *Energies*, vol. 11, no. 5, Article ID 1092, 2018.

[10] J. Li, D. Mao, Q. Zhu, and Q. Gao, "Research on windage yaw characteristics of high-voltage insulators in complex wind field," *IOP Conference Series: Materials Science and Engineering*, vol. 892, no. 1, Article ID 012113, 2020.

[11] B. Bo Yan, X. S. Xuesong Lin, W. Wei Luo, Z. D. Zhongquan Liu, and Z. Q. Liu, "Numerical study on dynamic swing of suspension insulator string in overhead transmission line under wind load," *IEEE Transactions on Power Delivery*, vol. 25, no. 1, pp. 248–259, 2010.

[12] J. C. Wang, S. W. Zhu, B. Peng, S. B. Duan, and P. Li, "Static and dynamic mechanical characteristic comparison research of v-type insulator string under gale condition," *IOP Conference Series: Earth and Environmental Science*, vol. 61, Article ID 012094, 2017.

[13] L. Q. An, Y. Y. Guan, Z. J. Zhu, and R. L. Zhang, "Research on windage yaw flashovers of transmission lines under wind and rain conditions," *Energies*, vol. 12, no. 19, p. 3728, 2019.

[14] Y. Z. Jia, M. X. Xiao, and B. You, "The windage yaw numerical simulation of 500-KV overhead transmission lines," in *Proceedings of the IEEE International Conference on Power System Technology*, Zhejiang, China, October, 2010.

[15] L. Li, L. H. Xiao, X. G. Luo, and X. Min, "Windage yaw calculation method of UHV insulator strings," *High Voltage Engineering*, vol. 39, no. 12, pp. 2924–2932, 2013.

[16] L. Li, C. L. Lin, and X. Wu, "Research on windage yaw of V-type composite insulators in ultra-high voltage," in *Proceedings of the 2nd International Conference on Mechanics, Materials and Structural Engineering*, Beijing, China, April, 2017.

[17] Y. B. Yang and H. T. Chiou, "Rigid body motion test for nonlinear analysis with beam elements," *Journal of Engineering Mechanics*, vol. 113, no. 9, pp. 1404–1419, 1987.

[18] Y. B. Yang and S. R. Kuo, *Theory and Analysis of Nonlinear Framed Structures*, Prentice-Hall, Singapore, 1994.

[19] A. G. Davenport, "Gust load factors," *Journal of the Structural Division – ASCE*, vol. 93, no. ST3, pp. 11–34, 1967.

[20] M. Kasperski and H. J. Niemann, "The L.R.C. (load-response-correlation)–method a general method of estimating unfavourable wind load distributions for linear and non-linear structural behavior," *Journal of Wind Engineering and Industrial Aerodynamics*, vol. 43, no. 1–3, pp. 1753–1763, 1992.

[21] J. D. Holmes, "Effective static load distributions in wind engineering," *Journal of Wind Engineering and Industrial Aerodynamics*, vol. 90, no. 2, pp. 91–109, 2002.

[22] W. J. Lou, G. Luo, and W. K. Hu, "Calculation method for equivalent static wind loads and wind load adjustment coefficients for transmission lines," *Journal of Zhejiang University (Engineering Science)*, vol. 50, no. 11, pp. 2120–2127, 2016.

[23] H. Z. Deng, S. Y. Zhu, and Z. M. Wang, "Dynamic behavior and wind-induced vibration response of long span transmission line system," *Building Structure*, vol. 34, no. 7, pp. 25–28, 2004.

[24] S. Zhao, Z. T. Yan, Z. L. Li, J. Y. Dong, and X. C. Nie, "Design and analysis of an aeroelastic model for the 1000 kV Sutong long span transmission tower-line system," *Journal of Vibration and Shock*, vol. 38, no. 12, pp. 1–8, 2019.

[25] A. M. Loredo-Souza and A. G. Davenport, "A novel approach for wind tunnel modelling of transmission lines," *Journal of Wind Engineering and Industrial Aerodynamics*, vol. 89, no. 11–12, pp. 1017–1029, 2001.

[26] M. M. Darwish, A. A. El Damatty, and H. Hangan, "Dynamic characteristics of transmission line conductors and behaviour under turbulent downburst loading," *Wind and Structures An International Journal*, vol. 13, no. 4, pp. 327–346, 2010.

[27] Ministry of Housing and Urban-Rural Construction, *110kV~750kV Overhead Transmission Line Design Specification*, Ministry of Housing and Urban-Rural Construction of the People's Republic of China, Beijing, China, 2010, in Chinese.

[28] Ministry of Housing and Urban-Rural Construction, *Load Code for the Design of Building Structures*, Ministry of Housing and Urban-Rural Construction of the People's Republic of China, Beijing, China, 2012, in Chinese.

[29] G. Deodatis, "Simulation of ergodic multivariate stochastic processes," *Journal of Engineering Mechanics*, vol. 122, no. 8, pp. 778–787, 1996.

[30] A. G. Davenport, "The relationship of wind structure to wind loading," in *Proceedings of the Conference on Wind Effects on Buildings & Structures*, Teddington, 1965.

[31] M. Shiotani and H. Arai, "Lateral structures of gusts in high winds," in *Proceedings of the International Conference on Wind Effects on Buildings and Structures*, vol. 1, pp. 20–26, Ottawa, Canada, 1967.

[32] ANSYS, *ANSYS Mechanical APDL Structural Analysis Guide*, ANSYS Inc., Pittsburgh, PA, USA, 2020.

[33] X. Fu and H.-N. Li, "Uncertainty analysis of the strength capacity and failure path for a transmission tower under a wind load," *Journal of Wind Engineering and Industrial Aerodynamics*, vol. 173, pp. 147–155, 2018.

[34] S. Zhao, Z. T. Yan, Z. L. Li, J. Y. Dong, and Y. L. Zhong, "Investigation on wind tunnel tests of an aeroelastic model of 1000 kV Sutong long span transmission tower-line system," *Proceedings of the Chinese Society for Electrical Engineering*, vol. 38, no. 17, pp. 5257–5265, 2018.

Hindawi
Shock and Vibration
Volume 2021, Article ID 1959683, 29 pages
https://doi.org/10.1155/2021/1959683

Research Article

Investigation and Development of a Three-Dimensional Transmission Tower-Line System Model Using Nonlinear Truss and Elastic Catenary Elements for Wind Loading Dynamic Simulation

Xiao Zhu and Ge Ou

Department of Civil and Environmental Engineering, University of Utah, Salt Lake City 84112, UT, USA

Correspondence should be addressed to Xiao Zhu; u1271332@utah.edu

Received 12 October 2021; Revised 22 November 2021; Accepted 24 November 2021; Published 20 December 2021

Academic Editor: Li Tian

The accuracy of transmission tower-line system simulation is highly impacted by the transmission line model and its coupling with the tower. Owing to the high geometry nonlinearity of the transmission line and the complexity of the wind loading, such analysis is often conducted in the commercial software. In most commercial software packages, nonlinear truss element is used for cable modeling, whereas the initial strain condition of the nonlinear truss under gravity loading is not directly available. Elastic catenary element establishes an analytical formulation for cable structure under distributed loading; however, the nonlinear iteration to reach convergence can be computational expensive. To derive an optimal transmission tower-line model solution with high fidelity and computational efficiency, an open-source three-dimensional model is developed. Nonlinear truss element and elastic catenary element are considered in the model development. The results of the study imply that both elements are suitable for the transmission line model; nevertheless, the initial strain in nonlinear truss element largely impacts the model accuracy and should be calibrated from the elastic catenary model. To cross-validate the developed models on the coupled transmission tower and line, a one-span eight-line system is modeled with different elements and compared with several state-of-the-art commercial packages. The results indicate that the displacement time-history root-mean-square error (RMSE) of the open-source transmission tower-line model is less than 1% and with a 66% computational time reduction compared with the ANSYS model. The application of the open-source package transmission tower-line model on extreme wind speed considering the aerodynamic damping is further implemented.

1. Introduction

Transmission tower-line systems connect power plants to customers and are widely distributed throughout the country. The failure of the transmission systems can result in tremendous economic and social life loss. In 2018, Hurricane Michael caused a widespread power outage that affected 1.7 million customers in six states in the US [1]. In the report, 116 transmission lines were damaged and led to a blackout with 16 deaths and $25 million in economic loss. Because of the high-rise of the transmission tower and the long span of the transmission line, the transmission system is sensitive to environmental wind loadings [2]. Consequently, the structural response of the transmission tower-line system under wind loading has drawn lots of researchers' attention. The development of a high fidelity and computationally efficient model which can estimate the dynamic response of transmission tower-line system during extreme wind condition is prominent.

The transmission tower-line system contains two major components: the transmission towers and transmission lines. Computational models are used to evaluate the linear and nonlinear time-history of the transmission tower systems. Most of the previous studies have been made to

investigate the stand-alone transmission tower performance. Kemp and Behncke [3] and Alam and Santhakumar [4] conducted full-scale experiments to indicate that large bending moments existed in the tower legs and cross-bracing system. Xie and Sun [5] further investigated the tower failure mechanism under bending and flexure-rotation loading. The results embodied that, at bending load, tower failure was dominated by the leg buckling and at flexure-rotation loading, the diagonal bracing member buckling was the main reason. Tian et al. [6] proposed a beam finite element tower model associated with a user-defined material model in ABAQUS to simulate the behavior of the tower under various loading conditions. The full-scale test obtained tower load-bearing capacity and failure mode verified the accuracy of the proposed finite element model. Battista et al. [7] summarized that the bending stress caused by the tower member connections was important to evaluate the ultimate strength of the tower, and consequently, spatial frame element should be used to build the tower finite element model. From the literature, the failure mechanism of the transmission tower is mainly due to the buckling of the elements.

The transmission line in the transmission tower-line system contains a set of wires connected to the tower, including conductors and ground wires. These wires are considered as cable structures that are highly geometrically nonlinear. Hence, flexibility and large deformation must be taken into consideration in the transmission line model. Owing to the computational complexity in modeling the dynamics of nonlinear transmission line under seismic or wind loading and the coupling between transmission tower and line, researchers started to explore the impact of transmission line dynamic to the transmission tower response. Momomura et al. [8] conducted experiments in mountain areas and concluded that the presence of the conductor significantly affected the vibration of the tower. Deng et al. [9, 10] implemented a series of wind tunnel tests to investigate the influence of the conductor on the transmission tower-line system from different wind angles. They concluded that when the wind direction was perpendicular to the transmission tower-line system, the vibration of the tower increased compared with a single tower, and the conductors enhanced the damping of the tower. Xie et al. [11] performed a wind tunnel test to study the displacement of the tower with and without conductors. They found that 70–90% of the tower displacement was induced by the conductors.

Because of the low flexural stiffness of the transmission line and free of rotational degree of freedom, nonlinear truss element is conventionally used for transmission lines in the transmission system modeling [12–18]. However, the gravity loading cannot be automatically accounted for in the nonlinear truss element; accordingly, calibration of its initial strain is required to be able to well represent the internal stress of the cable as well as the accurate cable shape. McClure et al. [19, 20] proposed that, for the transmission line modeling using the nonlinear truss element, approximated initial strain should be applied at first to avoid singularities in the initial stiffness matrix formulation. The initial strain was calculated from the catenary equation. Zhang et al. [21] stated that the self-weight of the transmission line introduced initial strains in the transmission line, and to find the initial shape and initial strain, a trial-and-error auto-gravimetric analysis in ANSYS should be performed. Although Keyhan et al. [19, 20] and Zhang et al. [21] mentioned how to set the initial strain of the nonlinear truss element, very few research documents have discussed the impact of the importance of calibrated initial strain on static performance of cable and its impacts on the global performance of coupled transmission tower-line systems.

Another candidate for transmission line modeling is the cable element. The elastic catenary cable element takes the self-weight of the transmission line into the internal force vector and stiffness matrix formulation directly without any approximations [22]. Although the elastic catenary equation was first obtained by Leibniz in 1691 [23], the explicit tangent stiffness matrix and the internal force vector have only recently been well studied. Jayaraman and Knudson [24] firstly developed the stiffness matrix and internal force vector of the cable structure in two-dimensional space. Thai and Kim [22] extended the elastic catenary cable elements in three-dimensional space. Salehi et al. [25] further extended the elastic catenary cable element by considering the uniformly distributed load in all directions. Experiments and numerical comparison showed that the elastic catenary element could calculate the displacement of the cable accurately and efficiently [26, 27]. Eventually, the elastic catenary cable element can be treated as a reference to verify the accuracy of the nonlinear truss element formulation under static and dynamic loading. However, the elastic catenary cable element is not supported by most of the popular commercial software packages (ANSYS and ABAQUS). SAP2000 commercial software has built-in elastic catenary cable element, but user-defined dynamic loading is not supported. Besides, the stiffness matrix of the elastic catenary element is calculated by inversing the flexibility matrix, in which the computational complexity increases rapidly with the increasing number of elements.

In summary, the accuracy of transmission line structure will be compromised by using the nonlinear truss element if its initial strain is not carefully calibrated. Elastic catenary element offers analytical formulation of cable structures. However, the computational efficiency of a multiple-line structure can be jeopardized by large matrix inversion operation, specifically during a dynamic simulation. Owing to such stated limitations and drawbacks in the state-of-the-art option, we propose to identify an optimal candidate to represent transmission lines in a high-fidelity and high-computation efficient transmission tower-line model. To achieve such an objective, the performance of an individual transmission line with different elements should be investigated first. Then a transmission tower-line model open-source MATLAB software package with the transmission line utilizing elastic catenary cable element and nonlinear truss element is developed and compared. The initial strain condition of nonlinear truss element is modeled in two forms. The first one is using an uncalibrated strain which is the default of most commercial software, and the initial

strain of the other nonlinear truss element is calibrated to the elastic catenary element under gravity loading. The developed models are compared and cross validated with ANSYS transient, SAP2000, and ANSYS LS-DYNA.

To further investigate the accuracy and the impact of using different models on modeling the large nonlinear transmission line and the coupling between line and tower, the dynamic displacement response of a one-span eight-line transmission tower-line model under different wind speeds and wind angles is compared. In the one-span eight-line transmission system case, four transmission tower-line models are compared: (1) lumped mass transmission tower coupled with elastic catenary cable element line in MATLAB (ECE-MATLAB); (2) lumped mass transmission tower coupled with calibrated nonlinear truss element line in MATLAB (NLTc-MATLAB); (3) transmission tower coupled with calibrated nonlinear truss element line in ANSYS (NLTc-ANSYS); (4) ANSYS auto-gravimetric model (ANSYS Auto-Gravimetric), which is developed by Zhang et al. [21] and discussed in Section 3.2.

The rest of the article is organized as follows: in Section 2, the methodology of developing the transmission tower, transmission line, and transmission tower-coupled finite element models are described. In Section 3, the transmission line initial shape and initial strain finding algorithms are described in detail. In Section 4, the single transmission tower, single transmission line, and a one-span two-line transmission system numerical model comparisons are presented. In Section 5, the numerical model in full transmission tower-line model setting up will be implemented and compared. In Section 6, the effects of the aerodynamic damping on the transmission tower-line system are investigated. Section 7 will conclude and summarize the whole study. The open-source package will be distributed on GitHub at [28] after the article is published.

2. Methodology

The transmission tower-line system contains two separately designed components: the overhanging wires and the supporting structures. The wire system comprises the ground wires and the conductors. Because the functionality of the ground wire and conductor is different, the material and geometric properties are generally different too. The supporting structure consists of transmission towers and foundations. In engineering, the transmission towers are considered fixed at the foundations and provide constraints to the wire system. Consequently, the transmission tower-line structure is fixed at tower bottom position and the transmission lines hanging between adjacent towers.

2.1. Transmission-Line Modeling. Transmission line under gravity forms a natural catenary shape [22]. Thus, the shape of the transmission line can be found by the elastic catenary element under loading without approximating the gravity. The two-node nonlinear truss element not having the rotational degree of freedom is widely utilized for transmission line modeling. Nevertheless, the initial strain of the nonlinear truss element has a significant influence on the structural behavior of the transmission line. Therefore, the calculation of the initial strain of the nonlinear truss element needs to be addressed. The initial strain of the nonlinear truss element can be calculated as

$$\varepsilon_0 = \left(\frac{F}{\mathrm{EA}}\right)_0, \tag{1}$$

where ε_0 is the initial strain of the nonlinear truss element, F is the transmission line end force, E and A are Young's modulus and cross-sectional area, and $(\,)_0$ indicates the initial state. Yet, in most cases, instead of the cable end force, the sag, the initial length of the cable is provided. Hence, the method to find the initial shape and initial strain of the cable under gravity loading needs to be explored. For the static analysis, the mass of each node in the transmission line is not used, whereas in the dynamic analysis, the mass matrix M_L is used to solve the nonlinear equation of motions. For the node in between two elements, the mass of that node sums up half of the two adjacent element mass, whereas for the boundary nodes, the mass takes half of the associated element.

2.1.1. Nonlinear Truss Element. The tension-only two-node three-dimensional truss element is employed both in ANSYS and MATLAB models. The tangent stiffness matrix and internal force vector equations of the nonlinear truss element are derived based on Jürgen and Bathe [29]. With the load applied, the Newton–Raphson iteration is needed to iteratively calculate the current state $(^*)$ tangent stiffness and the internal force vector, which is shown in equations (2) and (3):

$$k^* = \left(\frac{d\sigma^*}{d\lambda^*}A^*\frac{1}{l_0}\right)M^* + \left(\sigma^* A^* \frac{1}{l^*}\right)N^*, \tag{2}$$

$$f_i^* = \sigma^* A^* V^*, \tag{3}$$

where $d\sigma^*$ is the stress change, $d\lambda^*$ is the strain change, A^* is the cross-sectional area, l_0 is the initial truss length, l^* is the deformed truss length, and M^* and N^* are orthogonal coordinate transformation matrices. In this paper, only the geometric nonlinearity is considered; thus, $d\sigma^*/d\lambda^* = E$. For two-dimensional truss element, M^*, N^*, and V^* are given by

$$M^* = \begin{bmatrix} c^2 & cs & -c^2 & -cs \\ cs & s^2 & -cs & -s^2 \\ -c^2 & -cs & c^2 & cs \\ -cs & -s^2 & cs & s^2 \end{bmatrix}^*, \tag{4a}$$

$$N^* = \begin{bmatrix} s^2 & -cs & -s^2 & cs \\ cs & s^2 & -cs & -s^2 \\ -c^2 & -cs & c^2 & cs \\ -cs & -s^2 & cs & s^2 \end{bmatrix}^*, \tag{4b}$$

$$V^* = \left(\{-c, -s, c, s\}^*\right)^T, \tag{4c}$$

where c is $\cos(\theta)$ and s is $\sin(\theta)$.

When the difference between the internal force vector and the applied load vector is smaller than the defined convergence criteria, the iteration will stop. The tangent stiffness matrix, internal force vector, and the displacement can then be obtained. In equations (2) and (3), the nonlinear strain has different definitions in different material laws. In ANSYS, the strain for large elongation is defined as a logarithmic strain. In this paper, the strain adopts logarithmic strain because the developed open-source transmission system finite element model is compared with ANSYS models. The logarithmic strain and cross section are defined as

$$\lambda = \frac{l}{l_0}, \tag{5a}$$

$$\varepsilon = \ln(\lambda), \tag{5b}$$

$$d\sigma^* = E\varepsilon, \tag{5c}$$

$$\sigma^* = \begin{cases} d\sigma^* + \sigma_0 k, & \text{if } d\sigma^* + \sigma_0 \geq 0, \\ 0, & \text{if } d\sigma^* + \sigma_0 < 0, \end{cases} \tag{5d}$$

$$A^* = A_0 \lambda^{-2\nu}, \tag{6}$$

where l is the deformed length, l_0 is the original length, λ is the axial elongation factor, ε is the logarithmic strain, $d\sigma^*$ is the stress change, σ^* is the current state stress, σ_0 is the initial stress, E is the material elastic modulus, and A^* is the cross-section area at current state. In equation (5d), the strain is positive definite because the transmission line is tension-only structure.

For dynamic analysis, the equation of motion under external loading can be written as

$$\mathbf{M}\ddot{U} + \mathbf{C}\dot{U} + \mathbf{K}^*\mathbf{U} = \mathbf{P}(\mathbf{t}), \tag{7}$$

where $\mathbf{M}$, $\mathbf{C}$, and $\mathbf{K}^*$ are the mass, damping, and stiffness matrices; $\ddot{\mathbf{U}}$, $\dot{\mathbf{U}}$, and $\mathbf{U}$ are the vectors of the acceleration, velocity, and displacement; and $\mathbf{P}(\mathbf{t})$ is the external loading vector.

For the transmission line, the aerodynamic damping greatly influences the dynamic displacement response under large wind speed [30]. Consequently, the damping matrix in equation (7) should take the aerodynamic damping into consideration. Wang et al. [31] proposed a closed-form formulation of the aerodynamic damping ratios for the transmission lines. Therefore, to calculate the aerodynamic damping, the method proposed by Wang et al. [31] is adopted. The detailed derivation to calculate the aerodynamic damping can be found in [31]. However, in [31], instead of the explicitly calculating the damping matrix, the aerodynamic damping modal ratio is calculated. To calculate the damping matrix, the following procedures are applied:

(1) From [31], the in-plane and out-of-plane frequencies Ω and the corresponding mode shapes V are calculated and assembled the mass matrix as M

(2) From [31], the in-plane and out-of-plane direction modal aerodynamic damping ratios are calculated as ξ

(3) The aerodynamic damping matrix can be calculated as $C_A = \mathrm{MVM}^{-1}(2\xi M\Omega)\mathrm{MV}'M$

By considering the Rayleigh damping, the damping matrix can be represented as

$$C_R = \alpha_M M + \alpha_K K, \tag{8a}$$

$$C_A = \mathrm{MVM}^{-1}(2\xi M\Omega)\mathrm{MV}'M, \tag{8b}$$

$$C = C_R + C_A, \tag{8c}$$

where α_M and α_K are the mass and stiffness proportional damping coefficients, respectively.

To solve the equation of motion, nonlinear Newmark-Beta method is employed [32]. In Newmark-Beta method, at each time instant i, the displacement is updated at each iteration j until the residual force in the system is less than the convergence criteria. For the material nonlinear model, at each time instant, the stiffness of the system remains constant. However, for the geometric nonlinearity line model, on each time instant i at each iteration j, the stiffness is updated according to the node position and element strain. Consequently, on each time instant i and at each iteration j, the stiffness of the system will be updated. Algorithm 1 shows the steps to solve equation (7) using nonlinear truss element.

2.1.2. Elastic Catenary Cable Element. The basic assumptions of the elastic catenary element are as follows: (1) the strain stress relationship obeys Hooke's law, and the cross-sectional area remains unchanged; (2) the geometric nonlinearity considered is a small strain with large deformations; and (3) the cable is perfectly flexible [25]. Figure 1 shows a single elastic catenary element hanging at two nodes I and J. The coordinates of nodes I and J in Cartesian coordinate are $(0,0,0)$ and (l_1, l_2, l_3). In this figure, the external loads are thermal load ΔT and uniformly distributed loads w_1, w_2, and w_3. In the Lagrangian coordinate, the deformed and undeformed coordinates of the cable are p and s, respectively.

The equations of equilibrium are given by

$$T\left(\frac{\mathrm{d}x_i}{\mathrm{d}p}\right) = -(w_i s + f_i), \quad i = 1, 2, 3, \tag{9}$$

where w_i is the uniformly distributed load in the direction x_i and f_i is the tension force in the direction x_i.

The cable tension at Lagrangian coordinate is

$$T(s) = \sqrt{\sum_{i=1}^{3} (w_i s + f_i)^2}. \tag{10}$$

The cable tension T is related to the strain by Hooke's law as

Input:
Unstrained element length: $\mathbf{L}_0$; Poisson's ratio: ν; Initial element cross section area: $\mathbf{A}_0$;
Initial element strain: σ_0; Elastic modulus: E; Line initial coordinate $\mathbf{coord}_0$;
Mass matrix: $\mathbf{M_L}$; Initial displacement, velocity, and acceleration matrix $\mathbf{u}_0$, $\dot{\mathbf{u}}_0$, and $\ddot{\mathbf{u}}_0$;
Damping matrix $\mathbf{C}$; Convergence criteria: eps
Output:
displacement $\mathbf{u}_{i+1}$; velocity $\dot{\mathbf{u}}_{i+1}$; acceleration $\ddot{\mathbf{u}}_{i+1}$
Begin:
1.0 Initial parameters calculation
1.1 State determinations: the force $(\mathbf{f_s})_0$ and the initial tangent stiffness matrix $(\mathbf{K_{LT}})_0$
1.2 Solve $\mathbf{M}_L\ddot{\mathbf{u}}_0 = \mathbf{P}_0 - \mathbf{C}\dot{\mathbf{u}}_0 - (\mathbf{K_{LT}})_0\mathbf{u}_0 \longrightarrow \ddot{\mathbf{u}}_0$
1.3 Select Newmark-Beta parameters γ and β, and time interval $\mathrm{d}t$
1.4 Calculate $\mathbf{a}_1 = 1/\beta\,\mathrm{d}t^2\mathbf{M}_L + \gamma/\beta\mathrm{d}t\mathbf{C}$; $\mathbf{a}_2 = 1/\beta\mathrm{d}t\mathbf{M}_L + (\gamma/\beta - 1)\mathbf{C}$
2.0 Calculations for each time instant, $i = 0, 1, 2, \ldots$
2.1 Initialize $j = 1$, $\mathbf{u}_{i+1}^{(j)} = \mathbf{u}_i$, $(\mathbf{f_s})_{i+1}^{(j)} = (\mathbf{f_s})_i$ and $(\mathbf{K_{LT}})_{i+1}^{(j)} = (\mathbf{K_{LT}})_i$
2.1 $\widehat{\mathbf{P}}_{i+1} = \mathbf{P}_{i+1} + \mathbf{a}_1\mathbf{u}_i + \mathbf{a}_2\dot{\mathbf{u}}_i + \mathbf{M}_L\ddot{\mathbf{u}}_i$
3.0 For each iteration, $j = 1, 2, 3, \ldots$
3.1 The residual force $\widehat{\mathbf{R}}_{i+1}^{(j)} = \widehat{\mathbf{P}}_{i+1} - (\mathbf{f_s})_{i+1}^{(j)} - \mathbf{a}_1\mathbf{u}_{i+1}^{(j)}$
3.2 Check convergence; if $\widehat{\mathbf{R}}_{i+1}^{(j)} < eps$, skip the following steps and go to step 4.0; otherwise, implement the following steps:
3.3 $(\widehat{\mathbf{K}}_{LT})_{i+1}^{(j)} = (\mathbf{K}_{LT})_{i+1}^{(j)} + \mathbf{a}_1$
3.4 Solve $(\widehat{\mathbf{K}}_{LT})_{i+1}^{(j)}\Delta\mathbf{u}_{i+1}^{(j)} = \widehat{\mathbf{R}}_{i+1}^{(j)} \longrightarrow \Delta\mathbf{u}_{i+1}^{(j)}$
3.5 $\mathbf{u}_{i+1}^{(j+1)} = \mathbf{u}_{i+1}^{(j)} + \Delta\mathbf{u}_{i+1}^{(j)}$
3.6 Update the line coordinate $\mathbf{coord}_{i+1}^{j+1} = \mathbf{coord}_{i+1}^{j} + \Delta\mathbf{u}_{i+1}^{(j)}$
3.7 Update $(\mathbf{f_s})_{i+1}^{(j+1)} = (\mathbf{f_s})_{i+1}^{(j)} + (\mathbf{K}_{LT})_{i+1}^{(j)}\Delta\mathbf{u}_{i+1}^{(j)}$
3.8 Update the line tangent stiffness
3.8.1 From $\mathbf{coord}_{i+1}^{j+1}$, calculate the element length $\mathbf{L}_{j+1}$
3.8.2 Calculate element length incremental: $d\mathbf{L} = \mathbf{L}_{j+1} - \mathbf{L}_0$
3.8.3 Computing axial elongation factor λ using equation (5a)
3.8.4 Computing logarithmic strain ϵ using equation (5b)
3.8.5 Computing the current state stress σ^* using equations (5c) and (5d)
3.8.6 Computing the cross section area $\mathbf{A}^*$ using equation (6)
3.8.7 Calculate the tangent stiffness $\mathbf{K_{LT}}$ at iteration j using equation (2)
3.9 Replace j by $j + 1$ and repeat steps 3.1 to 3.8; after converge, denote final displacement value as $\mathbf{u}_{i+1}$, and the coordinate of the line as $\mathbf{coord}_{i+1}$
4.0 Calculate the velocity and acceleration for time instant $i + 1$
$\dot{u}_{i+1} = \gamma/\beta\mathrm{d}t\,(u_{i+1} - u_i) + (1 - \gamma/\beta)\dot{u}_i + \mathrm{d}t\,(1 - \gamma/\beta)\ddot{u}_i$,
$\ddot{u}_{i+1} = 1/\beta\mathrm{d}t^2\,(u_{i+1} - u_i) - \gamma/\beta\mathrm{d}t\dot{u}_i + (1/2\beta - 1)\ddot{u}_i$
5.0 Replace i by $i + 1$ and implement steps 2.0 to 4.0 for time instant $i + 1$
$*$ $\mathbf{K_{LT}}$: the tangent stiffness of the transmission line using nonlinear truss element; L refers to transmission line; T refers to truss element

Algorithm 1: Nonlinear Newmark-Beta method for nonlinear truss element formulation.

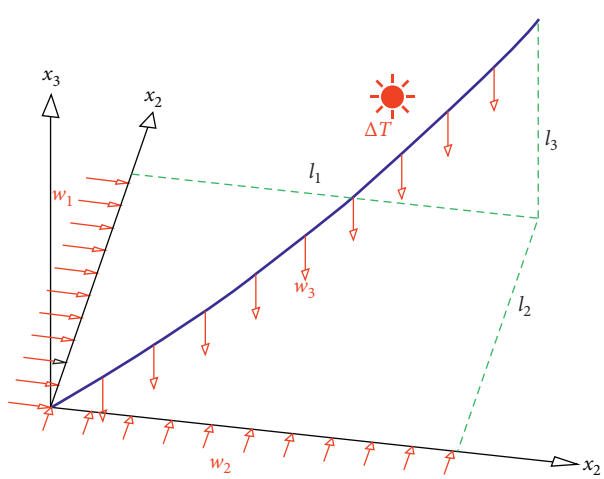

Figure 1: Single cable hanging at two nodes with applied loads.

$$\begin{aligned} T &= \mathrm{EA}(\varepsilon - \varepsilon_t) \\ &= \mathrm{EA}\left(\frac{\mathrm{d}p - \mathrm{d}s}{\mathrm{d}s} - \alpha\Delta T\right) \\ &= \mathrm{EA}\left(\frac{\mathrm{d}p}{\mathrm{d}s} - 1 - \alpha\Delta T\right), \end{aligned} \tag{11}$$

where E is the linear elastic modulus, A is the cross-sectional area, α is the linear thermal expansion coefficient, and ΔT is the temperature change.

The relationship between the Cartesian and Lagrange coordinate is expressed as

$$\begin{aligned} x_i(s) &= \int_0^s \mathrm{d}x_i \\ &= \int_0^s \frac{\mathrm{d}x_i}{\mathrm{d}p}\frac{\mathrm{d}p}{\mathrm{d}s}\mathrm{d}s, \quad i = 1, 2, 3. \end{aligned} \tag{12}$$

Substituting equations (9)–(11) into (12), the cable projected length x_i can be expressed as a function of the undeformed Lagrangian coordinate s:

$$\begin{aligned} x_i(s) = \int_0^s & \frac{-(w_i s + f_i)}{\sqrt{\sum_{i=1}^3 (w_i s + f_i)^2}} \\ & \cdot \left(\frac{\sqrt{\sum_{i=1}^3 (w_i s + f_i)^2}}{\mathrm{EA}} + (1 + \alpha\Delta T)\right)\mathrm{d}s, \quad i = 1, 2, 3. \end{aligned} \tag{13}$$

The boundary conditions of the cable are

$$x_i(l_o) = l_i, \quad i = 1, 2, 3, \tag{14a}$$

$$x_i(0) = 0, \quad i = 1, 2, 3, \tag{14b}$$

where l_0 is the undeformed cable length.

Solving equation (13) and applying the boundary conditions in equations (14a) and (14b), the cable length in Cartesian coordinates can be expressed as a function of the internal force f_i as

$$\begin{aligned} l_i = & -\frac{l_0 f_i}{\mathrm{EA}} - \frac{L_0^2 w_i}{2\mathrm{EA}} + \frac{1 + \alpha\Delta T}{w^3} \\ & \cdot \left(w w_i (T_1 - T_2) + \left(w^2 f_i - a_1 w_i\right)\right. \\ & \left. \cdot \left[\ln\left(\frac{a_1}{w} + T_1\right) - \ln\left(l_o w + \frac{a_1}{w} + T_2\right)\right]\right), \end{aligned} \tag{15}$$

$$\begin{aligned} w &= \sqrt{\sum_{j=1}^3 w_j^2}, \\ c_1 &= \sum_{j=1}^3 f_j w_j, \\ T_1 &= T(0), \\ T_2 &= T(l_0), \\ j &= 1, 2, 3. \end{aligned} \tag{16}$$

Differentiating both sides of equation (15), the relation between projected length and the internal forces is

$$\mathrm{d}l_i = \sum_{j=1}^3 \frac{\partial l_i}{\partial f_i}\mathrm{d}f_i, \quad i = 1, 2, 3. \tag{17}$$

In matrix form, equation (14b) can be expressed as

$$\begin{Bmatrix} dl_1 \\ dl_2 \\ dl_3 \end{Bmatrix} = \begin{bmatrix} f_{11} & f_{12} & f_{13} \\ f_{21} & f_{22} & f_{23} \\ f_{31} & f_{32} & f_{33} \end{bmatrix} \begin{Bmatrix} dF_1 \\ dF_2 \\ dF_3 \end{Bmatrix} = [F] \begin{Bmatrix} dF_1 \\ dF_2 \\ dF_3 \end{Bmatrix}, \tag{18}$$

where $[F]$ is the symmetric flexibility matrix with terms given by

$$\begin{aligned} f_{ij} = b_0(i, j) - \frac{1 + \alpha\Delta T}{w^3} & \left[b_1(i, j) + b_2(i, j)\right. \\ & \left. \cdot \left\{\ln\left(\frac{a_1}{w} + T_1\right) - \ln\left(l_o w + \frac{a_1}{w} + T_2\right)\right\}\right], \end{aligned} \tag{19}$$

$$b_0(i, j) = \begin{cases} -\dfrac{l}{\mathrm{EA}}, & i = j, \\ 0, & i \neq j, \end{cases} \tag{20a}$$

$$\begin{aligned} b_1(i, j) = & -w w_i \left[\frac{f_{j+3}}{T_2} + \frac{F_j}{T_1}\right] + \left(w^2 f_i - a_1 w_i\right) \\ & \cdot \left[\frac{w f_j + w_j (l_0 w + T_2)}{T_2\left(l_0 w^2 + a_1 + w T_2\right)} - \frac{w f_j + w_j T_1}{T_1 (a_1 + w T_1)}\right], \end{aligned} \tag{20b}$$

$$b_2(i, j) = \begin{cases} -\dfrac{l}{\mathrm{EA}}, & i = j, \\ 0, & i \neq j, \end{cases} \tag{20c}$$

The stiffness matrix k is the inverse of the flexibility matrix.

$$k = [F]^{-1}. \tag{21}$$

The global tangent stiffness and the internal force vector are determined by the six degrees of freedom matrix and vector as

$$K_{\mathrm{LC}} = \begin{bmatrix} -k & k \\ k & -k \end{bmatrix}, \tag{22}$$

$$F_{\mathrm{int}} = \{f_1, f_2, f_3, f_4, f_5, f_6\}^T. \tag{23}$$

The nodal force f_4, f_5, and f_6 can be determined through the force equilibrium in x_1, x_2, and x_3 direction as

$$f_4 = -(w_1 l_0 + f_1), \tag{24a}$$

$$f_5 = -(w_2 l_0 + f_2), \tag{24b}$$

$$f_6 = -(w_3 l_0 + f_3). \tag{24c}$$

The stiffness matrix in equation (21) is a function of the internal nodal forces f_1, f_2, and f_3, which is unknown. The internal nodal forces can be initialized based on the equations given by Jayaraman and Knudson [24] and Irvine [26] , which are as follows:

$$f_1 = -\frac{w l_1}{2\lambda_0}, \tag{25a}$$

$$f_2 = -\frac{w l_2}{2\lambda_0}, \tag{25b}$$

$$f_3 = \frac{w}{2}\left(-l_3 \frac{\cosh \lambda_0}{\sinh \lambda_0} + l_0\right), \tag{25c}$$

in which

$$\lambda_0 = \begin{cases} 10^6, & \text{if } \left(l_1^2 + l_2^2\right) = 0, \\ 0.2, & \text{if } l_0^2 \le l_1^2 + l_2^2 + l_3^2, \\ \sqrt{3\left(\dfrac{l_0^2 - l_3^2}{l_1^2 + l_2^2} - 1\right)}, & \text{if } l_0^2 > l_1^2 + l_2^2 + l_3^2. \end{cases} \tag{26}$$

In other cases, when the initial tension T_0 instead of the unstressed length l_0 is given, the stiffness matrix has four unknowns: f_1, f_2, f_3, and l_0. The unstressed length is initialized and the forces are modified by

$$l_0 = \sqrt{l_1^2 + l_2^2 + l_3^2}, \tag{27}$$

$$f_i = -\frac{l_i}{l_0} T_0, \quad i = 1, 2, 3. \tag{28}$$

Equations (19), (27), and (28) can be solved using Newton–Raphson iteration. The Jacobian of the nonlinear systems of equations is computed from the following equations:

$$H = \begin{bmatrix} [F] & \left\{\dfrac{\partial l}{\partial l_0}\right\}^T \\ \left\{\dfrac{\partial T}{\partial f_i}\right\}^T & 0 \end{bmatrix}, \tag{29}$$

$$\left\{\frac{\partial T}{\partial f_i}\right\}^T = \left\{\frac{f_1}{T}, \frac{f_2}{T}, \frac{f_3}{T}\right\}^T, \tag{30}$$

$$\left\{\frac{\partial l}{\partial l_0}\right\}^T = \left\{\frac{\partial l_1}{\partial l_0}, \frac{\partial l_2}{\partial l_0}, \frac{\partial l_3}{\partial l_0}\right\}^T, \tag{31}$$

$$\frac{\partial l_i}{\partial l_0} = -\left(\frac{1 + \alpha \Delta T}{T_2} + \frac{l_0}{\mathrm{EA}}\right) f_{i+3}, \quad i = 1, 2, 3. \tag{32}$$

The same procedures are employed to solve the nonlinear equation of motion under external loading using the elastic catenary finite element model. Algorithm 2 illustrates the steps to solve equation (7) using elastic catenary cable element.

To obtain the tangent stiffness of the transmission line in Algorithm 2, during each Newmark-Beta iteration, the elastic catenary finite element method needs to iteratively calculate the flexibility matrix first and then take the inverse to obtain the tangent stiffness matrix for each element and then assemble the global stiffness matrix. The additional iterations and the matrix inverse operations will slow down the computational speed when the number of elements becomes large. However, in Algorithm 1 for the nonlinear truss element formulation, the stiffness matrix is directly calculated based on the current state transmission line coordinate and strains.

2.2. Transmission Tower Modeling. The transmission tower is a three-dimensional structure with hundreds of elements. In ANSYS, the tower is modeled based on its actual material and geometry properties. However, the implementation of detailed transmission tower model in MATLAB is time-consuming. Li et al. [33] proposed that the linear lumped mass system can be employed to model the transmission towers; therefore, the complex finite element transmission tower model can be reduced to the lumped mass model with mass concentrated at N critical deformation points. The finite element model and the lumped mass model are shown in Figure 2. The stiffness of the tower is extracted from the ANSYS; first, the flexibility matrix F is computed, and then the stiffness matrix is obtained by the inverse flexibility matrix $K_T = F^{-1}$.

In the ANSYS model, the mass of the transmission tower is distributed in each element, while in the lumped mass model, the mass is concentrated at each node. To find the concentrated mass on each node, eigen analysis is conducted. The procedures to find the mass of each node are as follows:

(1) From ANSYS modal analysis, the first 3N frequencies as diagonal element of Ω are extracted.

(2) In the lumped mass model, assuming for each node, the mass is the total mass divided by the number of nodes as $m = m_t/N$. After the mass of each node is calculated, the assumed mass matrix is assembled to M_A.

(3) The eigenvectors of the mass and stiffness matrix (M_A, K) are calculated as V.

(4) The mass matrix is updated as $M_T = \mathrm{KV}\Omega^{-1}V^{-1}$.

Input:
Unstrained element length: $\mathbf{L}_0$; Elastic modulus: E; Linear thermal expansion coefficient: α
Temperature change: ΔT; Distributed loads in each direction x_i: $\mathbf{w_i}$, $i = 1, 2, 3$
Line initial coordinate $\mathbf{coord}_0$; Mass matrix $\mathbf{M_L}$; Damping matrix $\mathbf{C}$; Initial stiffness matrix $(\mathbf{K_{LC}})_0$
Initial displacement, velocity and acceleration matrix $\mathbf{u}_0$, $\dot{\mathbf{u}}_0$, and $\ddot{\mathbf{u}}_0$;
Newmark-Beta convergence criteria: eps; Elastic catenary convergence criteria: ϵ
Output:
displacement $\mathbf{u}_{i+1}$; velocity $\dot{\mathbf{u}}_{i+1}$; acceleration $\ddot{\mathbf{u}}_{i+1}$
Begin:
1.0 Initial parameters calculation
1.1 State determinations: the force $(\mathbf{f_s})_0$ and the initial tangent stiffness matrix $(\mathbf{K_{LC}})_0$
1.2 Solve $\mathbf{M}_L\ddot{\mathbf{u}}_0 = \mathbf{P}_0 - \mathbf{C}\dot{\mathbf{u}}_0 - (\mathbf{K_{LC}})_0\mathbf{u}_0 \longrightarrow \mathbf{u}_0$
1.3 Select Newmark-Beta parameters γ and β, and time interval $\mathrm{d}t$
1.4 Calculate $\mathbf{a}_1 = 1/\beta\,\mathrm{d}t^2\mathbf{M}_L + \gamma/\beta\mathrm{d}t\mathbf{C}n!/r!(n-r)!$; $\mathbf{a}_2 = 1/\beta\mathrm{d}t\mathbf{M}_L + (\gamma/\beta - 1)\mathbf{C}$
2.0 Calculations for each time instant, $i = 0, 1, 2, \ldots$
2.1 Initialize $j = 1$, $\mathbf{u}_{i+1}^{(j)} = \mathbf{u}_i$, $(\mathbf{f_s})_{i+1}^{(j)} = (\mathbf{f_s})_i$ and $(\mathbf{K_{LC}})_{i+1}^{(j)} = (\mathbf{K_{LC}})_i$
2.1 $\widehat{\mathbf{P}}_{i+1} = \mathbf{P}_{i+1} + \mathbf{a}_1\mathbf{u}_i + \mathbf{a}_2\dot{\mathbf{u}}_i + \mathbf{M}_L\ddot{\mathbf{u}}_i$
3.0 For each iteration, $j = 1, 2, 3, \ldots$
3.1 The residual force $\widehat{\mathbf{R}}_{i+1}^{(j)} = \widehat{\mathbf{P}}_{i+1} - (\mathbf{f_s})_{i+1}^{(j)} - \mathbf{a}_1\mathbf{u}_{i+1}^{(j)}$
3.2 Check convergence; if $\widehat{\mathbf{R}}_{i+1}^{(j)} < eps$, skip the following steps and go to step 4.0; otherwise, implement the following steps:
3.3 $(\widehat{\mathbf{K}}_{\mathrm{LT}})_{i+1}^{(j)} = (\mathbf{K_{LC}})_{i+1}^{(j)} + \mathbf{a}_1$
3.4 Solve $(\widehat{\mathbf{K}}_{\mathrm{LC}})_{i+1}^{(j)}\Delta\mathbf{u}_{i+1}^{(j)} = \widehat{\mathbf{R}}_{i+1}^{(j)} \longrightarrow \Delta\mathbf{u}_{i+1}^{(j)}$
3.5 $\mathbf{u}_{i+1}^{(j+1)} = \mathbf{u}_{i+1}^{(j)} + \Delta\mathbf{u}_{i+1}^{(j)}$
3.6 Update the line coordinate $\mathbf{coord}_{i+1}^{j+1} = \mathbf{coord}_{i+1}^{j} + \Delta\mathbf{u}_{i+1}^{(j)}$
3.7 Update $(\mathbf{f_s})_{i+1}^{(j+1)} = (\mathbf{f_s})_{i+1}^{(j)} + (\mathbf{K_{LC}})_{i+1}^{(j)}\Delta\mathbf{u}_{i+1}^{(j)}$
3.8 Update the line tangent stiffness
3.8.1 For element $el = 1 : N$
3.8.2 Extract the two element ends coordinate from $\mathbf{coord}_{i+1}^{j+1}$ as $I(x_1, x_2, x_3)$ and $J(x_1, x_2, x_3)$
3.8.3 From (16), calculate $\mathbf{w}$
3.8.4 From (25c), calculate the internal nodal force vector f_i at $I(f_1, f_2, f_3)$
3.8.5 Compute target length in each direction $L_{0x_i} = J(x_1, x_2, x_3) - I(x_1, x_2, x_3)$
3.8.6 Initialize the convergent parameter dl
3.8.7 While $dl > \epsilon$
3.8.8 Calculate parameter c_1 using (16)
3.8.9 Calculate the force in x_i at J using (24c)
3.8.10 Calculate the end force at node I and J using (10)
3.8.11 Calculate the projection length $\mathbf{L}_{xi}$ of the element at Cartesian coordinates using (15)
3.8.12 Calculate $\mathbf{dl} = \mathbf{L}_{xi} - \mathbf{L}_{0xi}$
3.8.13 Calculate the flexibility matrix F_e using (19)
3.8.14 Update the internal force incremental $\mathbf{df} = \mathbf{F}_e/\mathbf{dl}$
3.8.15 Update the internal force vector at node $I(x_1, x_2, x_3)$ as $\mathbf{f}_i + \mathbf{df}$
3.8.16 Calculate the stiffness matrix $\mathbf{k_e}$ using (21)
3.8.17 Assemble the element stiffness $\mathbf{k_E}$ using (22)
3.8.18 Assemble the global stiffness matrix $\mathbf{K_{LC}}$
3.9 Replace j by $j + 1$ and repeat steps 3.1 to 3.8; after converge, denote final displacement value as $\mathbf{u}_{i+1}$, and the coordinate of the line as $\mathbf{coord}_{i+1}$
4.0 Calculate the velocity and acceleration for time instant $i + 1$
$\dot{\mathbf{u}}_{i+1} = \gamma/\beta\mathrm{d}t(\mathbf{u}_{i+1} - \mathbf{u}_i) + (1 - \gamma/\beta)\dot{\mathbf{u}}_i + \mathrm{d}t(1 - \gamma/\beta)\ddot{\mathbf{u}}_i$,
$\ddot{u}_{i+1} = 1/\beta\mathrm{d}t^2(u_{i+1} - u_i) - \gamma/\beta\mathrm{d}t\dot{u}_i + (1/2\beta - 1)\ddot{u}_i$
5.0 Replace i by $i + 1$ and implement steps 2.0 to 4.0 for time instant $i + 1$
$*$ $\mathbf{K_{LC}}$: the tangent stiffness of the transmission line using nonlinear truss element; L refers to transmission line; C refers to catenary element

Algorithm 2: Nonlinear Newmark-Beta method for elastic catenary element formulation.

Here, K is the stiffness matrix extracted from ANSYS from the abovementioned method; N is the number of nodes; M_A is the assumed tower mass matrix; and M_T is the calculated tower mass matrix. The fidelity of the tower lumped mass model is validated through static analysis and dynamic response under static and dynamic wind loading in Section 4.2.

2.3. Transmission Tower-Line Model Development. The coupling effects between the transmission tower-line system cannot be ignored during the static and dynamic analyses [18]. For this reason, the coupling terms must be taken into consideration during the formulating of the tower-line system global stiffness and mass matrix. In the numerical and ANSYS models, the transmission tower and line is

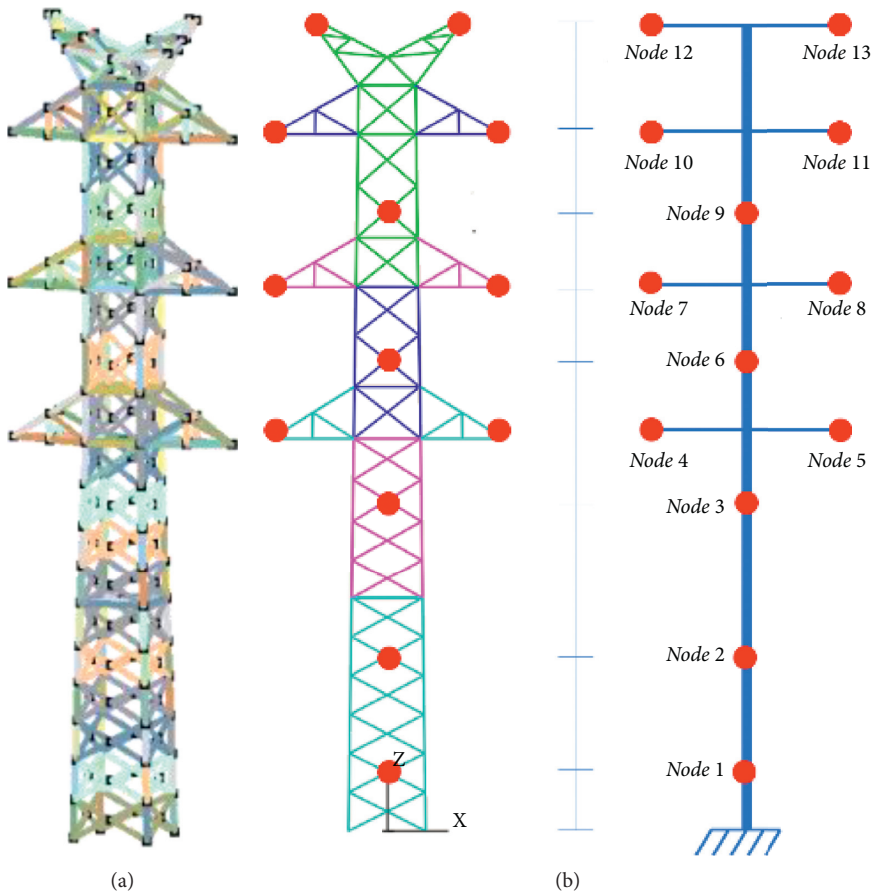

Figure 2: Single transmission tower model. (a) ANSYS/LS-DYNA model. (b) MATLAB lumped mass model.

considered as pinned connection [18]. At the tower and line coupled nodes, the stiffness and mass in each direction is directly added as K^C and M^C. With the transmission tower-line system assembled, the system will deform to balance the transmission line end forces under gravity loading. Hence, the static analysis of the transmission tower-line system under gravity loading should be conducted first to establish the system initial state before the static and dynamic analyses [15]. Figure 3 describes the flowchart of the development of the transmission tower-line numerical model procedure.

In Figure 3, the cable model has two candidates, in which the formulation of the two candidates is derived in Section 2.1. From the 3D nonlinear truss element stiffness formulation derivation, an initial strain should be applied to make the stiffness matrix stable. However, the default commercial software assigned initial strain to the nonlinear truss element model does not reflect the actual strain state of the cable under gravity loading. As a result, an initial strain calibrated nonlinear truss element model is developed by adopting the initial strain and initial shape calculated from elastic catenary finite element model. To validate the accuracy and fast convergence of the calibrated nonlinear truss element model, the ANSYS auto-gravimetric initial strain and shape finding algorithm in ANSYS by Zhang et al. [21] is also implemented.

3. Investigation of Single Transmission Line Model Performance

To first investigate the performance of transmission lines with different element models, both nonlinear truss element model and elastic catenary element model are developed. In the transmission tower-line system, the transmission line contains ground wires and conductors installed in different locations of the tower. Figure 4 illustrates the layout and coordinate system of the transmission lines in the transmission tower-line system. In this figure, two groups of transmission lines are referred, namely, the ground wire and conductor. In each transmission line group, except the location differences, the material and span are identical. Consequently, to find the initial shape of the transmission lines, only one transmission line in each group is implemented. For the ground wire, the line is fixed at the coordinate of $(0, -3, 31.5)$ meter and $(200, -3, 31.5)$ meter is utilized to conduct the static and dynamic analysis, whereas for the conductor, the line placed at coordinate $(0, -4.44, 26.9)$ meter and $(200, -4.44, 26.9)$ meter is used. Table 1 shows the material properties and the geometry of the ground wire and conductor of transmission lines on account of gravity loading. Here, the sag of the ground wire and conductor is different due to the material property

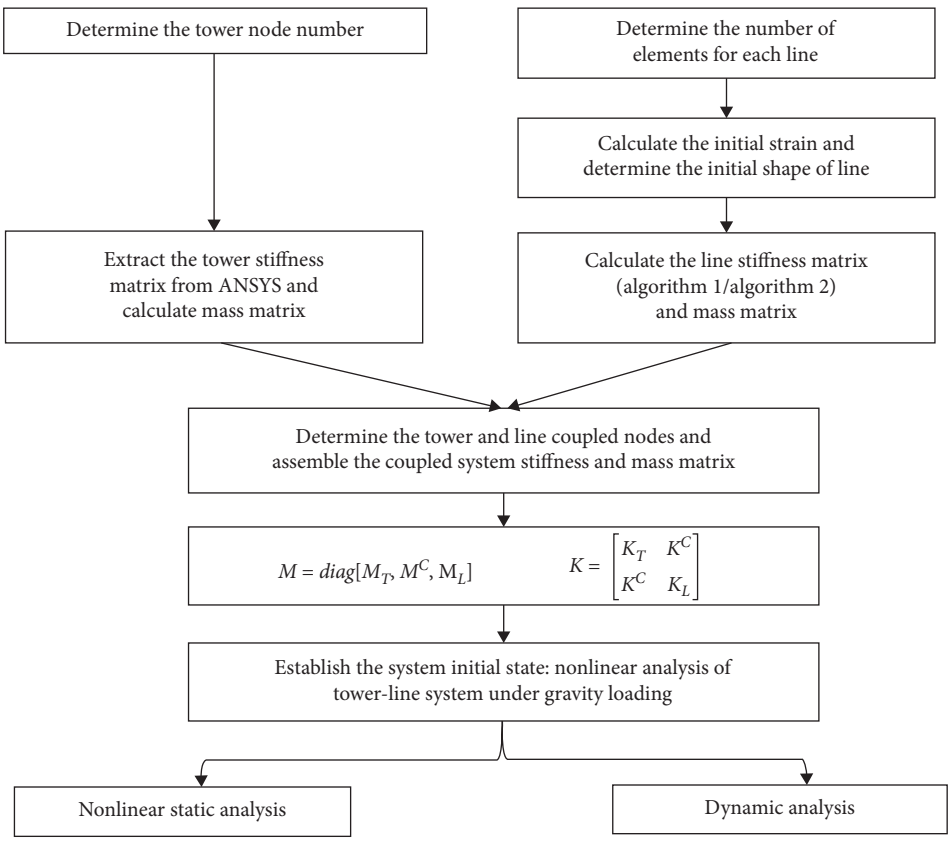

Figure 3: Flowchart of developing coupled transmission tower-line system model.

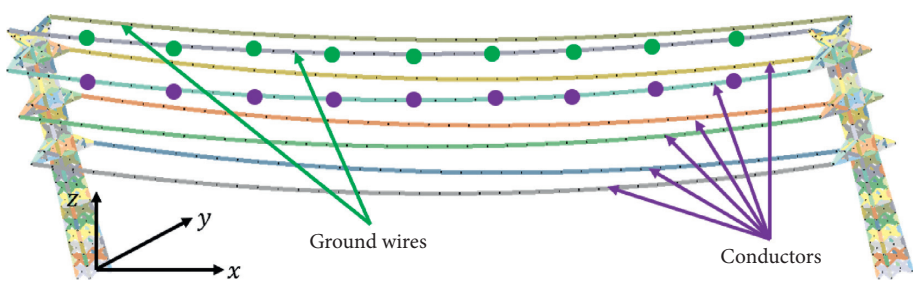

Figure 4: Layout and coordinate system of the transmission lines in the transmission tower-line system.

Table 1: Transmission line properties.

	Elastic modulus (GPa)	Density (kg/m^3)	Cross-sectional area (m^2)	Maximum sag (m)	Unstrained length (m)
Ground wire	78	4602	$3.29E-04$	2.9	199.913
Conductor	67	1780	$6.05E-04$	3.7	200.033

differences. Hence, the initial shape and initial strain of ground wire and conductor need to be found separately.

3.1. Nonlinear Truss Element Model Shape Calibration and Initial Strain Calibration for Transmission Line. At initial state, the transmission line deforms to a shape resulted to its self-weight. From cable structure analysis, the deformed shape of the transmission line under gravity loading is catenary with strains caused by the deformation in the model. As Zhang et al. [21] mentioned that the initial strain and initial shape was critical to establish the transmission line finite element model, it is necessary to accurately find the initial shape and the corresponding initial strain of the transmission line under self-weight accurately. Zhang et al. [21] proposed an initial shape and initial strain finding method using nonlinear truss in ANSYS software. The key concepts of the proposed method are as follows: first, a broad grid range of the transmission line initial strains is assumed and the initial strain in ANSYS transmission line model is

applied to do autogravimetric analysis; then, the search grid is gradually narrowed down so that the calculated value (for example, the sag of the cable) and the target value difference are less than the predefined convergence criteria (for example, the relative error is less than 1%); and finally, the shape and initial strain of the transmission line are determined. From the key concepts, it is clear that lots of iterations are needed to achieve the predefined convergent criteria. In this paper, elastic catenary finite element model is utilized to find the initial shape and strain of the transmission line under gravity loading. Although the catenary equation or parabolic equation will give similar initial shape and initial strain of the transmission line, the elastic catenary finite element model can further be applied to transmission line and transmission tower-line system static and dynamic analysis.

3.2. Initial Shape and Response Assessment. The assessment of single transmission line performance is developed and compared with different models and commercial software packages: (1) elastic catenary cable element in MATLAB; (2) calibrated nonlinear truss element in ANSYS; (3) ANSYS autogravimetric initial shape and strain finding; (4) SAP2000, and (5) ANSYS LS-DYNA model. In this section, the initial shape of the transmission line and their static responses will be discussed first, and later a comparison of transmission dynamic response due to earthquake and wind loading presented.

3.2.1. Shape of Cable Structure under Gravity and Static Wind Loading. The initial shape of the ground wire and conductor under gravity loading is shown in Figures 5 and 6. In Table 2, the sag difference between SAP2000 and elastic catenary finite element model is 0.001%. The small sag difference between the two models is made because SAP2000 makes use of the same elastic catenary finite element for the transmission line modeling. Using calibrated nonlinear truss element in ANSYS, the ground wire and conductor difference with respect to elastic catenary finite element is less than 0.02%. However, ANSYS autogravimetric method calculated sag difference corresponding to elastic catenary finite element is 0.50% and 0.71% for the ground wire and conductor, respectively. Compared with the ANSYS autogravimetric method, the calibrated nonlinear truss element gives more accurate results. Besides, to find the initial shape and initial strain of the transmission lines, the ANSYS autogravimetric method tried and compared several initial strains to find the optimal one. Figure 7 illustrates the ANSYS auto-gravimetric method initial strain calculation and initial shape determination procedure. At first round grid search, the ANSYS auto-gravimetric method implements a broad range of initial strains, which is $1.0E-7$ to $1.0E-3$. The sag of each strain is calculated and then compared with the target sag to determine whether the applied initial strain is small or large. After several strains are tried, a smaller range of initial strains can be determined, which is $1.0E-4$ to $1.0E-3$. Then, the process is repeated to gradually narrow down the initial strain search range until the desired initial strain is obtained. With the optimal initial strain obtained, the initial shape of the transmission line can be found by using the auto-gravimetric analysis in ANSYS.

The input static wind force is computed from the wind speed. Based on ASCE manual 74 [34] and ASCE 7–10 [35], the static wind force in the transverse and longitudinal direction is as follows:

$$F_t = \gamma_w \mathrm{QK}_z K_{zt} v^2 G_t \cos\Psi \mathrm{C}_{\mathrm{ft}} A_{mt}, \tag{33}$$

$$F_l = \gamma_w \mathrm{QK}_z K_{zt} v^2 G_t \sin\Psi C_{fl} A_{ml}, \tag{34}$$

where v is the wind speed at height z; Ψ is the wind incident angle; γ_w is the load factor; Q is the numerical constant; K_z is the velocity pressure exposure coefficient; K_{zt} is the topographic factor; G is the tower gust response factor; A_{mt} and A_{ml} is the projection area in transverse and longitudinal direction; and C_{ft} and C_{fl} is the force coefficient in transverse and longitudinal direction.

The wind speed at height z is governed by the power law as

$$\frac{v}{\overline{v}_s} = \left(\frac{z}{z_s}\right)^{\alpha}, \tag{35}$$

where $\overline{v}_s$ is the basic wind speed at standard height z_s and α is the power law exponent that represents the surface roughness. The basic wind speed defined in ASCE 7-10 [35] is a three-second gust speed at 10 m above the ground in Exposure C. Thus, the standard height z_s is 10 m.

In equations (33) and (34), the basic wind speed and wind angle should be determined. In the extreme wind map from ASCE Manual 74 [34], 54 m/s is the most dominant basic wind speed in Texas region. Accordingly, the basic wind speed for the transmission line static analysis takes 54 m/s and the wind angle is perpendicular to the span of the line, which is the y direction in Figure 4. Since there are 100 elements in the transmission line finite element model with the maximum height difference to be the sag value, which is small comparing with the transmission line length, only several representative nodes are necessary to generate the wind speed and apply the wind force. For the ground wire and conductor, the node at every 20 m in x direction is chosen as the representative node; as a result, there are nine representative nodes in the transmission line, which are shown as the dots in Figure 4 for the ground wire and conductor.

Figures 8 and 9 illustrate the static deformation using different transmission line models and their differences with respect to elastic catenary finite element model. From the results, the SAP2000 model and the nonlinear truss calibrated model differences in all directions are less than 0.1%, whereas the ANSYS auto-gravimetric method maximum difference is more than 4%. While in the initial strain finding, the calculated sag difference between the elastic catenary element and the ANSYS auto-gravimetric method is less than 1%, and the small calculated sag difference enlarges the error in the static analysis using ANSYS autogravimetric method.

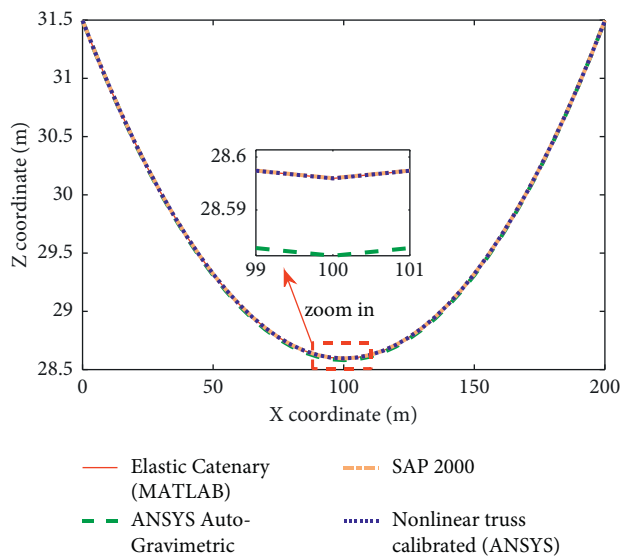

Figure 5: Ground wire initial shape.

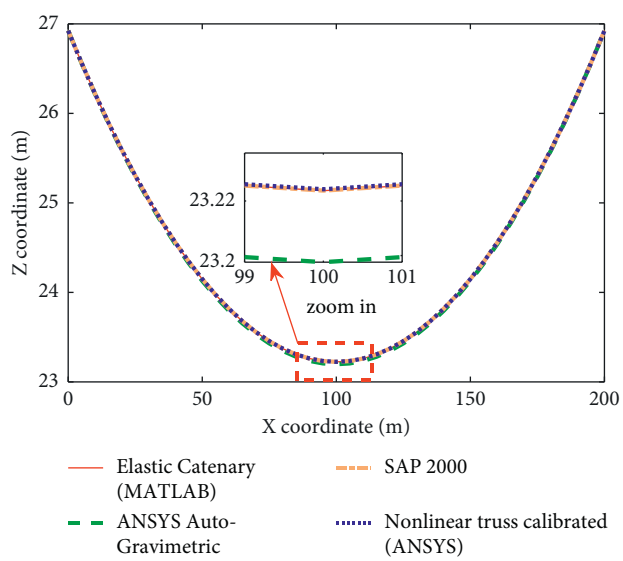

Figure 6: Conductor initial shape.

Table 2: Transmission line initial shape finding method calculated sag difference with respect to elastic catenary finite element model.

	Calculated line sag difference (%)		
	ANSYS auto-gravimetric	SAP 2000	Calibrated nonlinear truss (ANSYS)
Ground wire	0.504	0.001	0.000
Conductor	0.708	0.001	0.014

3.2.2. Dynamic Response of Cable Structure with Earthquake and Dynamic Wind Loading. The displacement time-history analysis of the system under dynamic loading is studied to verify the dynamic properties of the transmission line model. Because the transmission lines cross different terrains, which may be intense wind flow and earthquake zone, it is necessary to compare the different transmission line model displacement responses under seismic and dynamic wind loading. In the static analysis, the ground wire and conductor are compared separately but with the same methodology. For dynamic analysis, only the conductor is taken to investigate the performance of different finite element models. To quantitatively compare the displacement response difference, root-mean-squared-error (RMSE) is used as the error indicator.

$$\mathrm{RMSE} = \sqrt{\frac{\sum_{n=0}^{N-1} (x[n] - y[n])^2}{N}} \times 100\%. \tag{36}$$

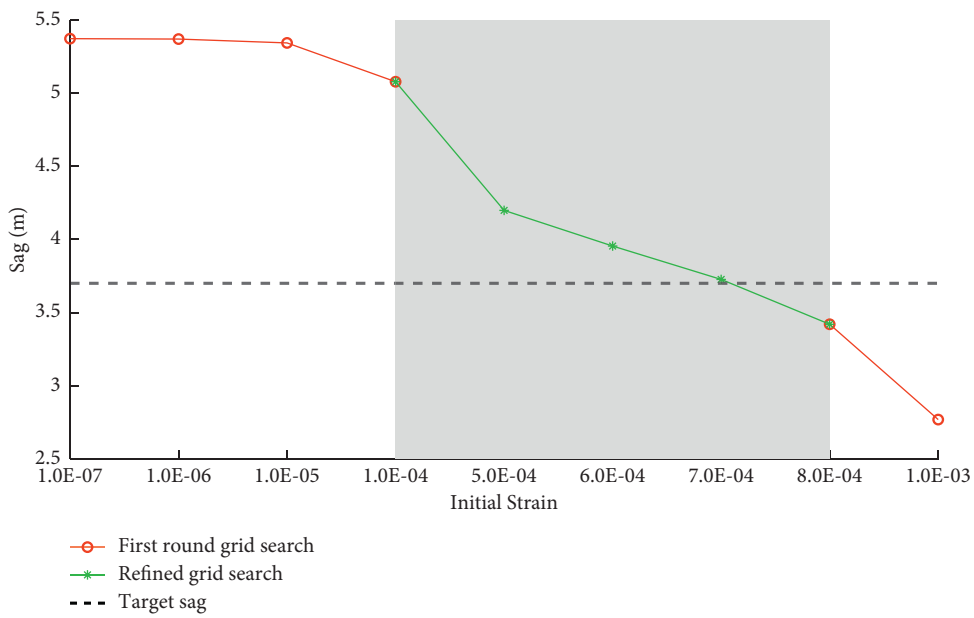

Figure 7: ANSYS auto-gravimetric method initial strain finding iterations for the conductor.

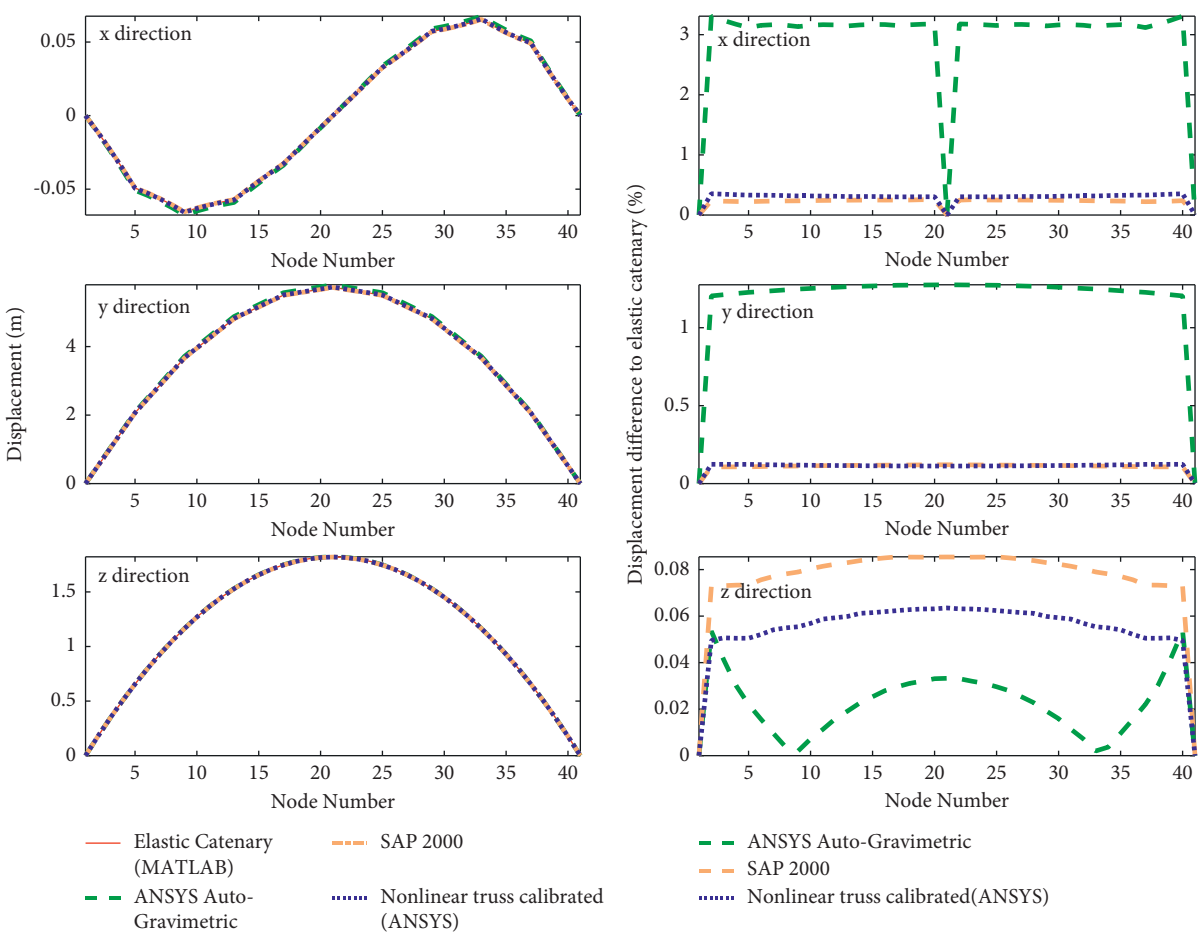

Figure 8: Ground wire static response.

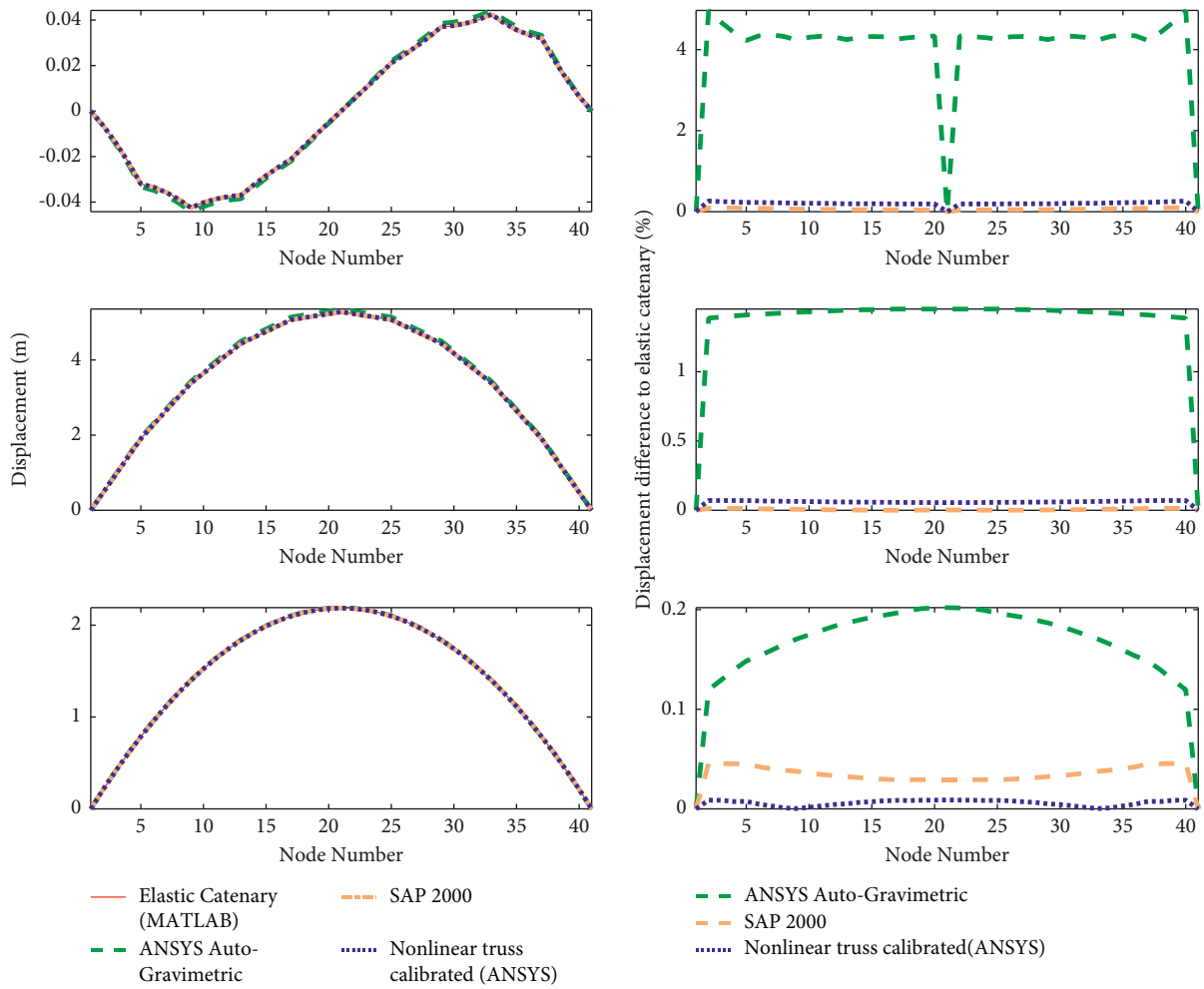

Figure 9: Conductor static response.

(1) Earthquake loading: the El-Centro ground motion acceleration data is used as the benchmark to evaluate the performance of the models. The earthquake loading is applied in the transverse direction of the transmission line as the transmission line has smaller stiffness in that direction.

Figure 10 shows the transmission line middle position displacement time-history in y and z directions. The x direction displacement is not shown because the displacement at that direction is zero due to structural symmetry. In this figure, it is clear that the LS-DYNA model displacement is different from other models. Table 3 quantitatively illustrates that the RMSE between the LS-DYNA model and the elastic catenary element in the y and z is 67.54% and 78.78%, respectively. Those large RMSEs demonstrate that the LS-DYNA model does not obtain the correct transmission line displacement time-history. The reason behind those large RMSEs is that, in the LS-DYNA model, the initial strain of the transmission line is implicitly implemented to the stiffness formulation. From the LS-DYNA displacement time-history, this implicitly applied initial strain is a small value that only aimed at stabilizing the nonlinear truss element stiffness formulation. However, in Table 3, SAP2000 model and the calibrated nonlinear truss model maximum RMSE is less than 4%, demonstrating that those two models are comparable with the elastic catenary finite element model. Additionally, the ANSYS auto-gravimetric method gives acceptable results, but it is clear that the displacement at transverse direction has larger difference, which is 10.89%, compared with SAP2000 and calibrated nonlinear truss model.

(2) Dynamic wind loading: the dynamic wind speed consists of basic and fluctuating wind speed. According to Davenport [36], the basic wind speed profile over height is governed by the power law equation (35). The fluctuating wind speed is computed from the basic wind speed, in which the spatial and temporal correlation is taken into consideration. Based on the Shinozuka theory [37], the fluctuating wind speed $\{v_1(t), v_2(t), \ldots, v_{np}(t)\}$ at time t is

$$v_k(y_k, z_k, t) = \sqrt{2(\Delta\omega)} \sum_{m=1}^{k} \sum_{l=1}^{N} \left|H_{jm}(\omega_{ml})\right| \cos \left(\omega_{ml} t - \theta_{km}(\omega_{ml}) + \Phi_{ml}\right), \quad k = 1, 2 \ldots, np, \tag{37}$$

$$\omega_{ml} = (l-1)\Delta\omega + \frac{m}{N}\Delta\omega, \quad l = 1, 2, \ldots, N, \tag{38}$$

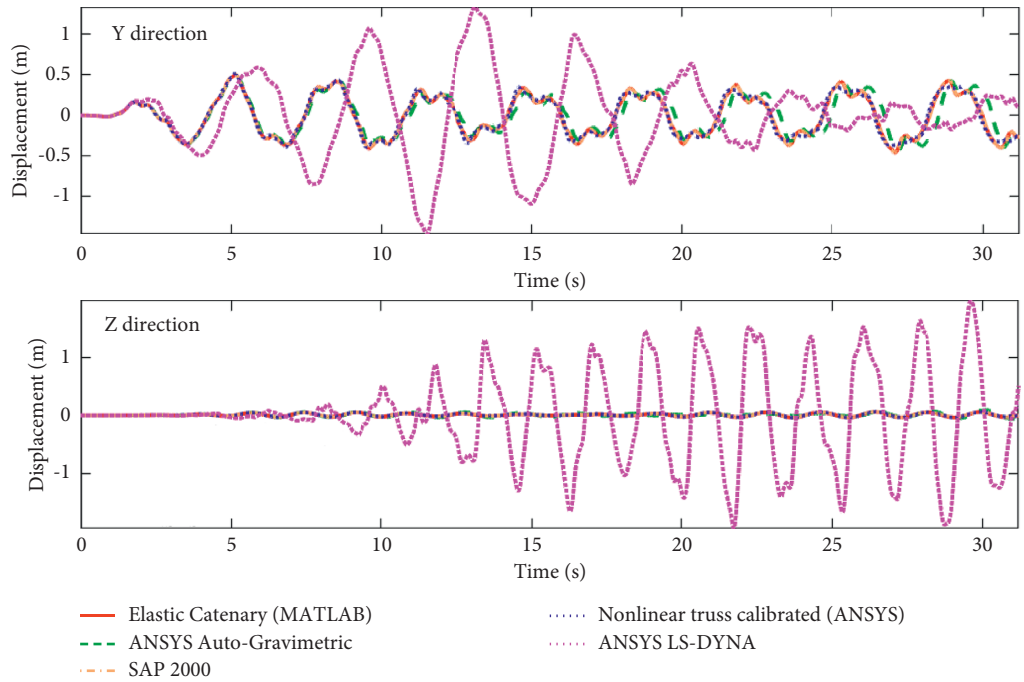

Figure 10: Conductor middle position displacement time-history under El-Centro earthquake.

Table 3: Conductor middle position displacement RMSE between each model and the elastic catenary model under El-Centro earthquake loading.

	Transmission model			
	SAP2000	ANSYS auto-gravimetric	Calibrated nonlinear truss	LS-DYNA
Y direction (%)	0.25	10.89	3.50	67.54
Z direction (%)	0.13	1.64	0.17	78.78

where N is an arbitrarily large positive number; $\Delta\omega = \omega_{\text{up}}/N$, the frequency increment; ω_{up} is the cut-off frequency; that is, when $\omega > \omega_{\text{up}}$, $S(\omega) = 0$; Φ_{ml} is uniformly distributed random phase angle in $[0, 2\pi]$. θ_{km} is the $H(\omega)$ phase angle. In engineering, $S(\omega)$ and $H(\omega)$ are real matrices; thus, $\theta_{km} = 0$. H_{jm} is the $S(\omega)$ Cholesky decomposed matrix as in

$$S(\omega) = H(\omega)H^*(\omega)^T. \tag{39}$$

In equation (39), the fluctuating wind spectral density matrix $S(\omega)$ is calculated from Davenport auto-correlation spectrum and cross-correlation spectrum [36].

Due to the limitations in SAP2000 software, the dynamic wind loading cannot be applied. For this reason, the elastic catenary, ANSYS auto-gravimetric method, nonlinear truss calibrated model, and LS-DYNA model are compared.

In Figure 11, the nonlinear truss calibrated model and the elastic catenary model displacement time-history is overlapped, and the ANSYS auto-gravimetric method displacement time-history deviates after some time instant, whereas the LS-DYNA model displacement time-history far off the rest models. In Table 4, the RMSE at the transverse direction for the nonlinear truss calibrated model, the ANSYS auto-gravimetric model, and the LS-DYNA model is 1.14%, 14.93%, and 133.02%, which quantitatively illustrates the accuracy of the models.

In summary, from the dynamic wind loading cases, transmission line displacement response magnitude and trend in LS-DYNA is far off from the rest models. Therefore, with the default software parameter settings, LS-DYNA is not suitable for the transmission line and transmission tower-line coupling modeling unless the initial strain of the transmission line can be accurately applied to the model. The ANSYS auto-gravimetric transmission line model gives relative accurate static and dynamic response compared to the elastic catenary finite element model, whereas the nonlinear truss calibrated model structural static and dynamic properties are close to elastic catenary finite element model. The differences between the nonlinear truss calibrated model and ANSYS auto-gravimetric model, both being implemented in ANSYS software, come from the initial strain and the initial shape calculation differences under gravity loading. The initial shape of the transmission line determines the coordinates of the nonlinear truss element. In Algorithm 1, the nonlinear truss element stiffness formulation takes the coordinate and the strain of the truss element into consideration. Eventually, the difference in the initial strain and initial shape brings about different nonlinear truss element stiffness.

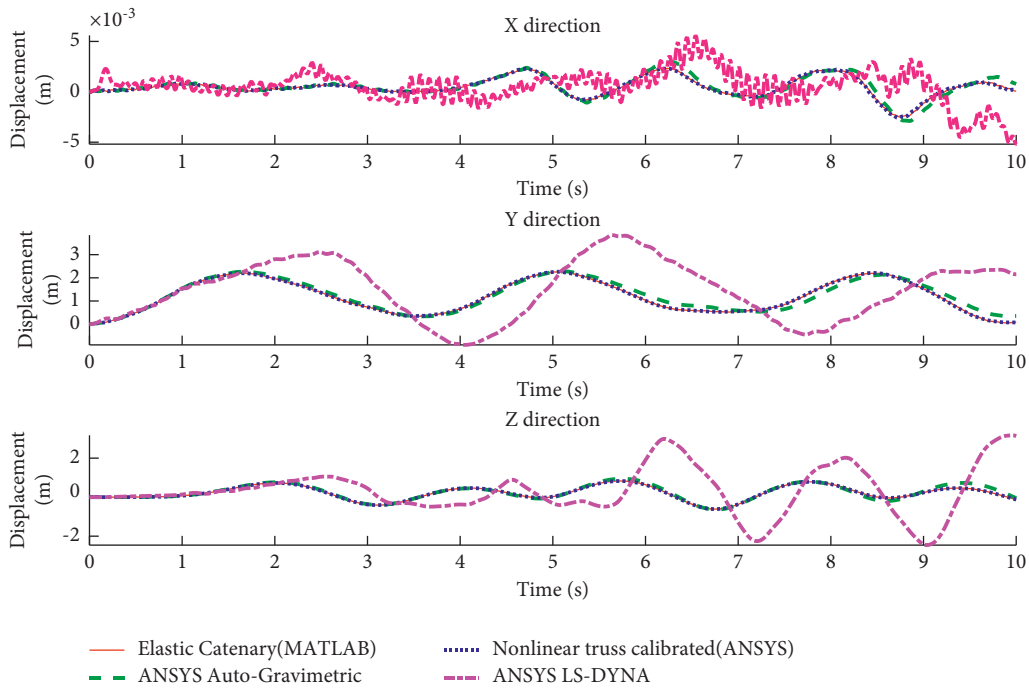

Figure 11: Conductor middle position displacement time-history under wind loading.

Table 4: Conductor middle position displacement RMSE between each model and the elastic catenary model under dynamic wind loading.

	Transmission line model		
	ANSYS auto-gravimetric method	Nonlinear truss calibrated	LS-DYNA
x direction (%)	0.03	0.01	0.19
y direction (%)	14.93	1.14	133.02
z direction (%)	8.51	0.28	121.56

4. Development of Transmission Tower-Line System Model

In Section 3, the single cable lumped mass models have been compared with the detailed line model in ANSYS Transient and LS-DYNA. To develop an accurate transmission tower-line model, the transmission tower dynamic model and the coupling between tower and line requires careful validation. To achieve computational efficiency, the optimal number of elements in both nonlinear truss element cable model and elastic catenary element cable model is studied. To verify the coupling in the developed transmission tower-line system are captured, five models are cross compared: (1) lumped mass transmission tower coupled with elastic catenary cable element line in MATLAB (ECE-MATLAB); (2) lumped mass transmission tower coupled with calibrated nonlinear truss element line in MATLAB (NLTc-MATLAB); (3) transmission tower coupled with calibrated nonlinear truss element line in ANSYS (NLTc-ANSYS); (4) ANSYS auto-gravimetric model (ANSYS Auto-Gravimetric); and (5) ANSYS LS-DYNA model (LS-DYNA). Moreover, as Fei et al. [38] showed that the tower top displacement is a good indicator to reflect the dynamic response of the transmission tower-line system; eventually, the tower top maximum displacement and the displacement time-history root difference indicator are compared with respect to the ANSYS model to verify the accuracy of the lumped mass model. In the transmission tower-line model, the insulators are not considered. Moreover, from the state-of-the-art transmission tower-line models, each transmission line is aggregated to single transmission line instead of split transmission line.

4.1. Single Tower Lumped Mass Tower Model. The transmission tower studied is a steel-made, L-shaped cross-sectional suspension tower with a height of 31.5 m. The transmission tower is a design for the Texas region from Tort et al. [39], which is based on the ASCE Manual 74 [34] using the commercial software PLS-TOWER. The properties of the lines are in Table 1, which is provided by Xue et al. [18]. As shown in Figure 1, the lumped mass tower model has 13 nodes. The tower stiffness and mass matrix are calculated based on the method in Section 2.2.

The static wind loading calculation is based on Section 3.2.1. In the extreme wind map from ASCE Manual 74, 54 m/s basic wind speed is the most dominant wind speed in Texas region. Hence, the basic wind speed for the transmission tower static analysis takes 54 m/s. The wind angle is

chosen as 30° to verify the lumped mass tower model x and y direction stiffness formulation.

The lumped mass transmission tower static displacement under static wind loading displacement difference with respect to that from the ANSYS detailed model is shown in Figure 12. From this figure, it is clear that, in all directions, the maximum displacement difference is less than 0.15%, indicating that the stiffness matrix in the lumped mass model is with high accuracy.

The dynamic wind force generation method is described in Section 2.3. The displacement time-history responses are compared at two selected nodes: one is on the tower main body (Node 3) and the other is at the tower top (Node 12). To quantitatively measure the difference between the transmission tower lumped mass and ANSYS detailed model displacement time-history without the effects of the displacement magnitude, the difference indicator is considered as [40]

$$D_e = \frac{\sqrt{\sum_{n=0}^{N-1} (x[n] - y[n])^2 / N}}{\sqrt{\sum_{n=0}^{N-1} (x[n])^2 / N}}. \quad (40)$$

In Figure 13, the lumped mass model and the ANSYS model node 3 and node 12 displacement time-history in all directions are close to each other. In Table 5, the displacement difference indicator between the lumped mass model and ANSYS model is less than 4%. The small discrepancy implies that the lumped mass model captured the dynamic properties of the ANSYS model. However, in Table 5, the LS-DYNA model displacement time-history minimum difference with respect to the ANSYS model reaches 17.75%, which is relatively large.

To conclude, from the single tower static and dynamic analysis, the lumped mass can be treated as an alternative model to the ANSYS detailed model. The LS-DYNA model has relatively large displacement difference to the ANSYS model.

4.2. Transmission Line Element Size Reduction. The span of the transmission line is 200m; therefore, to accurately simulate the transmission line, large number of finite elements will be used. However, the number of elements of the transmission line has a great impact on the computational time and accuracy of the model. Hence, the frequency domain analysis is performed to find the optimal number of elements. Figure 14 shows the frequency components of the ground wire and the conductor in different transmission line models. The transmission line has been divided into 10, 20, 40, and 100 elements. From the frequency differences plot, using 40 elements for all the transmission line models, the first ten frequencies difference is less than 1%. As a result, 40 element numbers is chosen as the optimal element number for the transmission line.

4.3. Tower-Line Coupling Validation on a One-Span Two-Line System. To validate the accurate representation of transmission tower-line coupling in the proposed model, responses of the one-span two-line transmission tower-line system are compared. The two transmission lines are ground wires, whose material properties are shown in Table 1. The span between two towers is 200 m. Figure 15 illustrates the two different directions of the wind speed. When the wind speed direction is along the longitudinal direction, the wind angle is annotated 0°, and when the wind speed direction is along the transverse direction, the wind angle is annotated 90°. To cross validate the transmission tower-line models, coupling effects are successfully captured and the wind speed 10 m/s and wind angle 30° are chosen. The displacement of the left tower and one ground wire middle position displacement time history is compared because those two points are good indicators to reflect the tower and cable dynamic properties.

Figure 16 shows the structure tower top and ground wire middle position displacement time-history between the different models under wind loading. In this figure, the NLTc-ANSYS and ANSYS auto-gravimetric model displacement time-history are overlapped. Tables 6 and 7 quantitatively measure the displacement time-history difference indicator using equation (40) between the ANSYS auto-gravimetric model and the NLTc-ANSYS model at tower top and line middle position. In Table 6, the tower top displacement difference between the ANSYS auto-gravimetric model and the NLTc-ANSYS model is less than 1%. In Table 7, the ground wire displacement difference between those two models is 4.14% and 8.23% for y and z directions, which are larger than the tower displacement time-history difference. The reason is that the initial strain calculated from the ANSYS auto-gravimetric model is different from the NLTc-ANSYS model, so that the ground wire end force transferred to the tower is different. However, since the stiffness of the tower is much larger than the ground wire, the displacement difference is smaller at the tower top.

In Tables 6 and 7, the ECE-MATLAB and NLTc-MATLAB displacement difference with respect to each other is small. In Table 6, the tower top displacement difference in the x and y directions are smaller than 1%. However, in the z direction, the displacement difference is around 10%. The reason behind the relatively large RMSE is that, in ANSYS, the geometric nonlinearity is also applied to the transmission tower. With the applied gravity loading in the system, the geometric nonlinearity will stiffen the tower, which leads to the smaller displacement comparing with MATLAB lumped mass model.

Additionally, in Figure 16, the LS-DYNA models displacement time-history is different from other models. In Tables 6 and 7, the LS-DYNA maximum displacement time-history difference is 18.16% and 84.44% for the tower top and ground wire position, which manifests that the LS-DYNA model does not simulate the structure dynamic behavior with high accuracy.

In general, the ECE-MATLAB, NLTc-MATLAB, NLTc-ANSYS, and ANSYS auto-gravimetric model are comparable with each other and with high fidelity, while the errors from transmission line modeling in LS-DYNA have further propagated and impacted largely on the transmission tower top response.

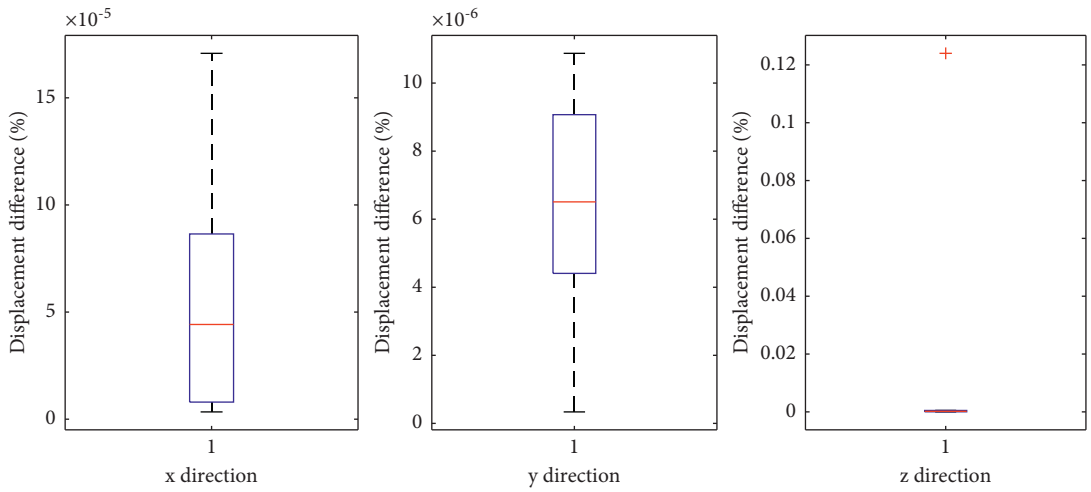

Figure 12: The lumped mass tower model static displacement difference corresponding to ANSYS (%).

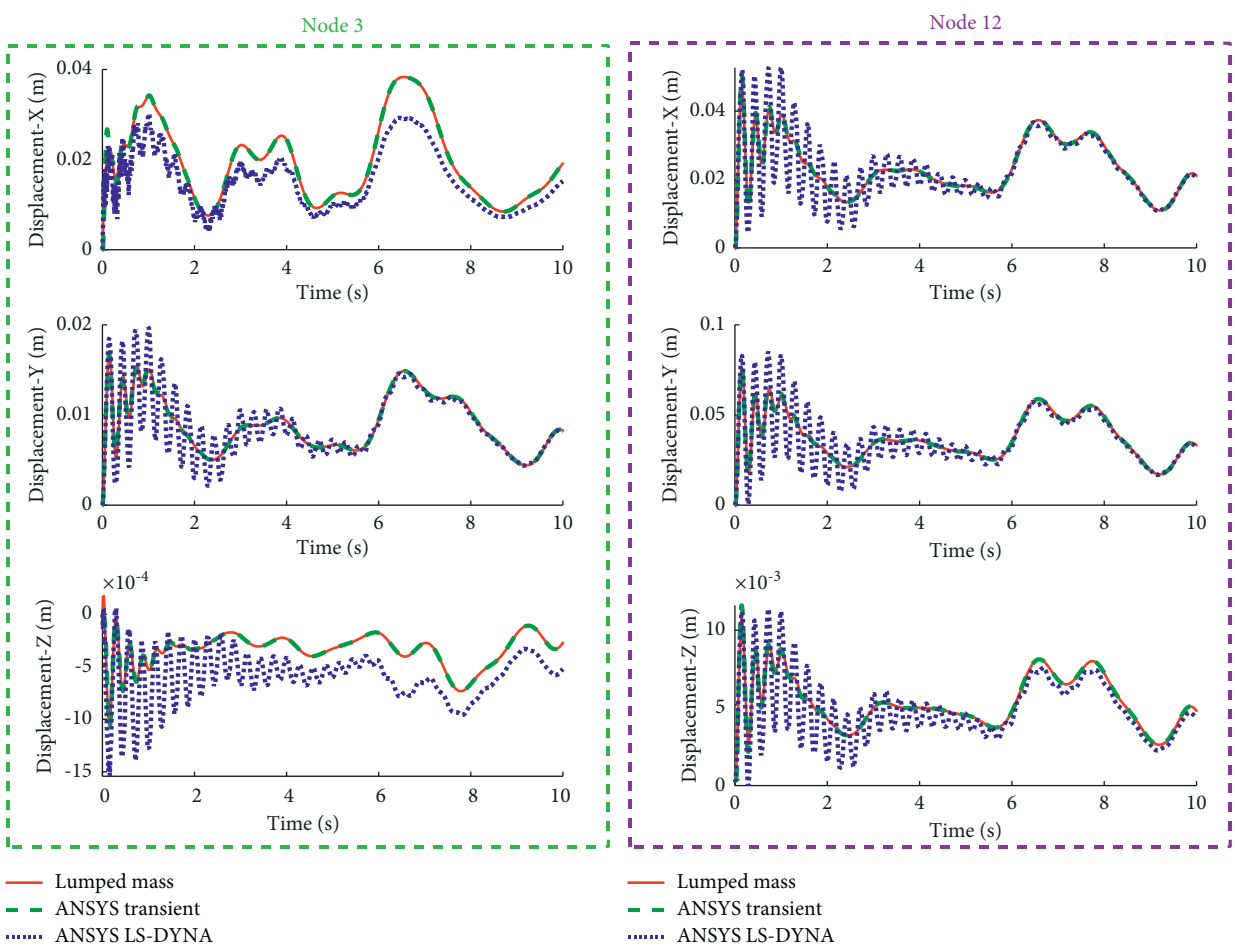

Figure 13: Single tower dynamic displacement at nodes 3 and 12 under wind loading.

5. Performance of Full Transmission Tower-Line System Model during Wind Loadings

Finally, the developed transmission tower-line model is applied to the full setup. The transmission tower is designed with eight transmission lines attached: six conductors and two ground wires. As is illustrated in the one-span two-line model, the LS-DYNA model displacement time-history response deviates from other models. In addition, the performance of transmission tower-line model with calibrated nonlinear truss element line in ANSYS (NLTc-ANSYS) delivers the most accurate result, which is

Table 5: Single tower dynamic displacement time-history D_e indicator between each model and the ANSYS model.

		x direction (%)	y direction (%)	z direction (%)
Node 3	Lumped mass model	2.95	1.96	3.78
	ANSYS LS-DYNA model	29.04	26.27	45.86
Node 12	Lumped mass model	1.61	2.03	3.05
	ANSYS LS-DYNA model	17.75	19.22	22.23

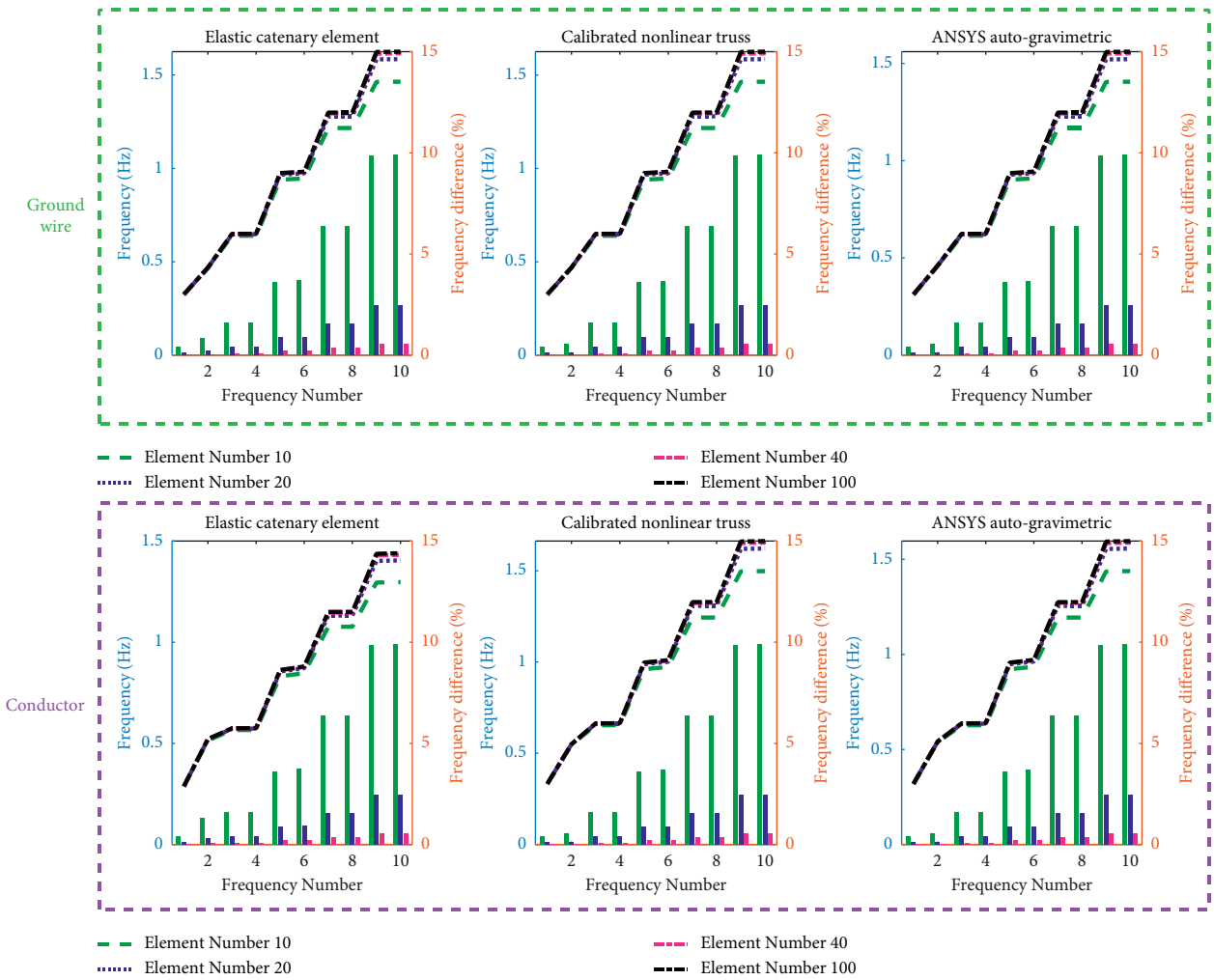

Figure 14: Transmission line size reduction.

considered as the reference model. Hence, in the full model, the rest of the three different models are compared: (1) lumped mass transmission tower coupled with elastic catenary cable element line in MATLAB (ECE-MATLAB); (2) lumped mass transmission tower coupled with calibrated nonlinear truss element line in MATLAB (NLTc-MATLAB); and (3) ANSYS auto-gravimetric model.

The total GPU time in each model has been recorded and compared to illustrate the efficiency of the models under different wind loadings. There are totally six dynamic wind loadings applied to the transmission tower-line models. The wind speeds are 10 m/s and 20 m/s. For each wind speed, three wind angles 0°, 30°, and 90° are used to generate the dynamic wind loading. For the total displacement time-history comparison, only wind speed 20 m/s at angle 30° is chosen to illustrate the difference of the proposed models. At each wind speed and wind angle, two nodes in the tower and the cable middle position at each line are chosen to illustrate the displacement time-history. The selected points are illustrated in Figure 17. For dynamic wind loading simulation of the transmission tower-line model, the time interval in ANSYS model is determined at 0.01 s. ANSYS software also automatically interpolates the input force when the convergence is not meet. The time interval for the lumped mass model is selected as 0.0025 s for optimal computational efficiency and accuracy trade-off.

To quantitatively measure the response of the three models, the tower top maximum displacement and the RMSE

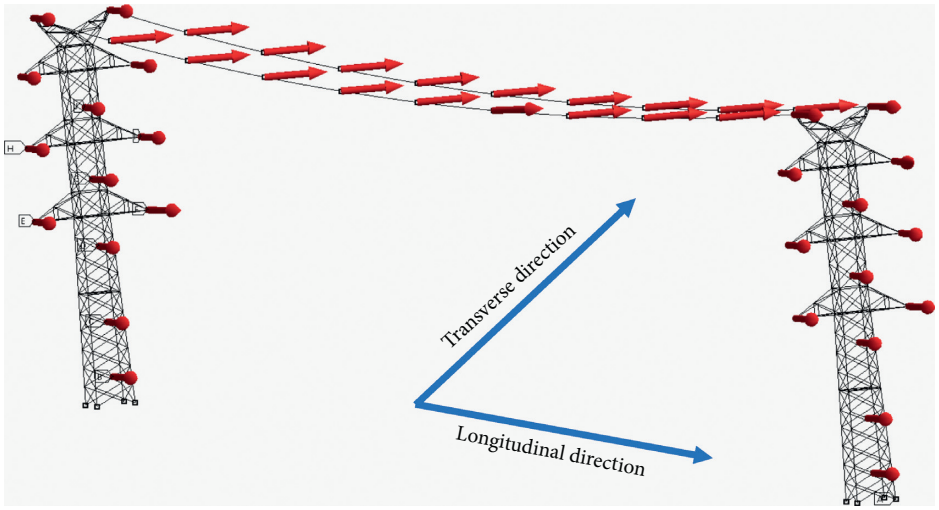

Figure 15: The illustration of the dynamic wind applied force points and the direction.

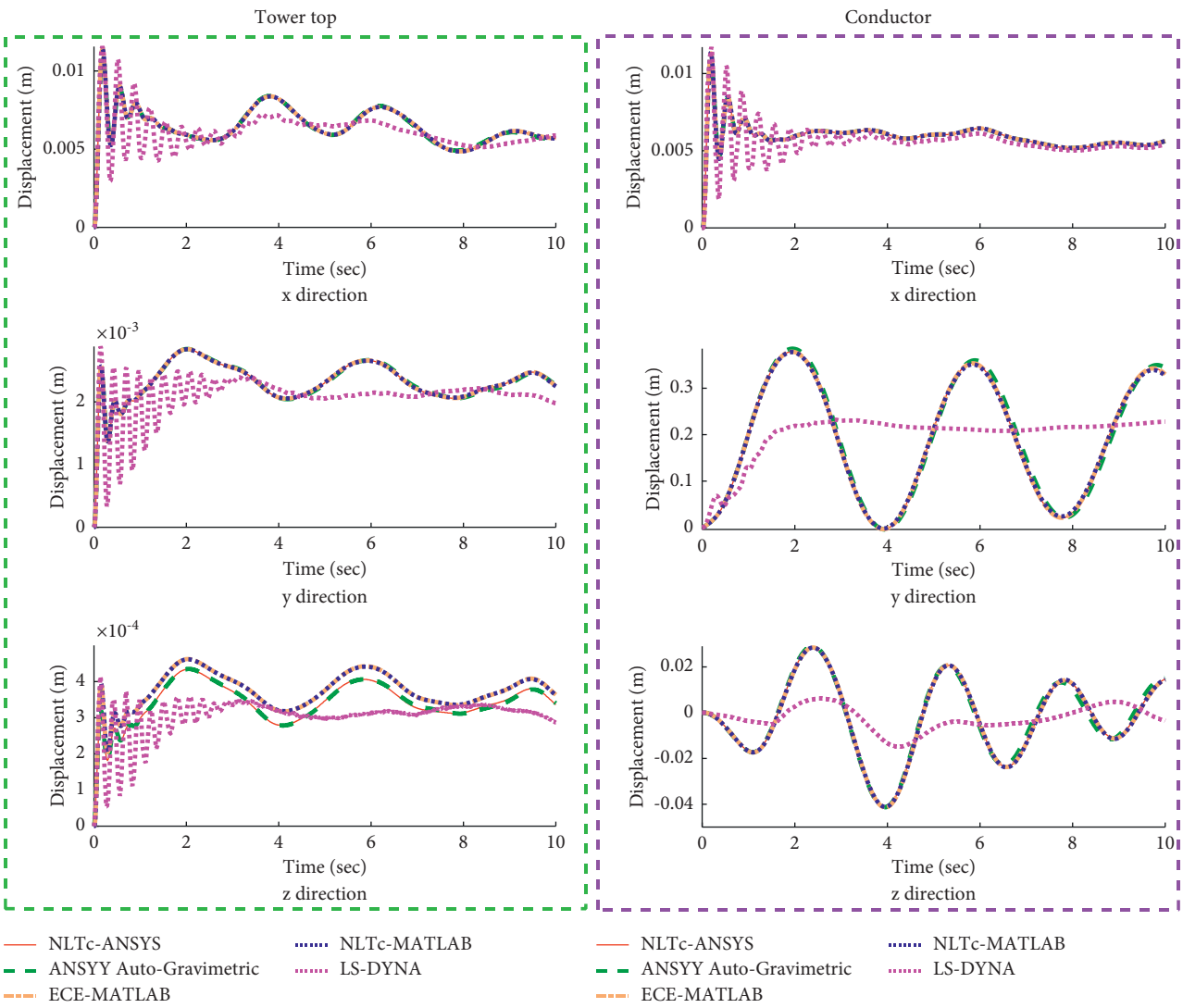

Figure 16: One-span two-line transmission tower-line model displacement at tower top and cable middle position.

Table 6: One-span two-line tower top dynamic displacement time-history D_e difference indicator between each model and the ANSYS model.

	x direction (%)	y direction (%)	z direction (%)
ANSYS auto-gravimetric	0.7307	0.7159	0.9544
ECE-MATLAB	0.8762	0.2880	9.2953
NLTc-MATLAB	0.8722	0.3276	9.2916
LS-DYNA	12.6718	16.1300	18.1636

Table 7: One-span two-line line middle dynamic displacement time-history D_e difference indicator between each model and the ANSYS model.

	x direction (%)	y direction (%)	z direction (%)
ANSYS auto-gravimetric	0.0980	4.1373	8.2330
ECE-MATLAB	0.9475	0.2365	1.6704
NLTc-MATLAB	0.9988	0.8910	1.6977
LS-DYNA	11.7811	54.3502	84.4399

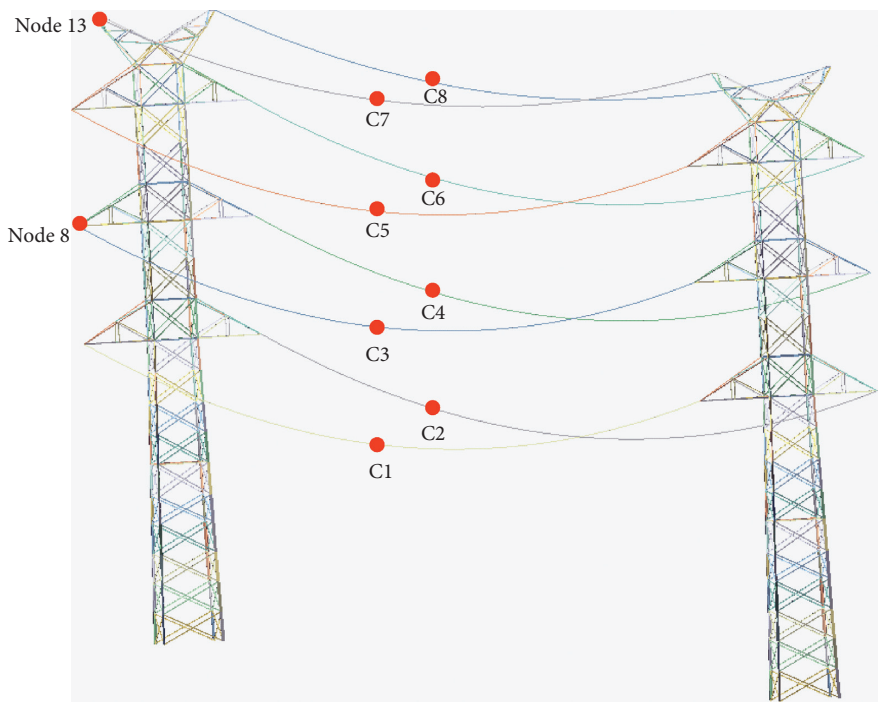

Figure 17: The displacement time-history extracting nodes.

between the three different models and the NLTc-ANSYS model are chosen as difference indicators. Figure 18 shows the displacement time-history of the full transmission system using different models, given the same dynamic wind loading with wind speed 20m/s at angle 30°. It also demonstrates similar results between four models. To quantify the result accuracy of different models, the tower top displacement and the RMSE between the models under different wind speeds and wind angles are listed in Tables 8 and 9.

In Table 8, the ANSYS auto-gravimetric model maximum tower top displacement difference corresponding to the NLTc-ANSYS model at all tested wind speeds and wind angles is less than 0.05%. Additionally, both the NLTc-MATLAB and ECE-MALTAB model maximum tower top displacement differences are less than 0.1%. The maximum tower top displacement is a single value that is used to determine the accuracy of the models. Consequently, to check the differences between the models at all-time instant, the RMSE is employed.

Table 9 summarizes the RMSE between the three different models and the NLTc-ANSYS model at different wind speeds and wind angles. In Table 9, for the ANSYS auto-gravimetric model, at the same wind speed 10 m/s, the largest RMSE is 0.1% at wind angle 90 and at wind speed 20 m/s; as the wind angle increases from 0° to 90°, the RMSE increases from 0.012% to 0.17%. Comparing between different models, the only difference between the ANSYS auto-gravimetric model and the NLTc-ANSYS model is in the transmission line initial strain and initial shape determination. The small initial strain and initial shape difference

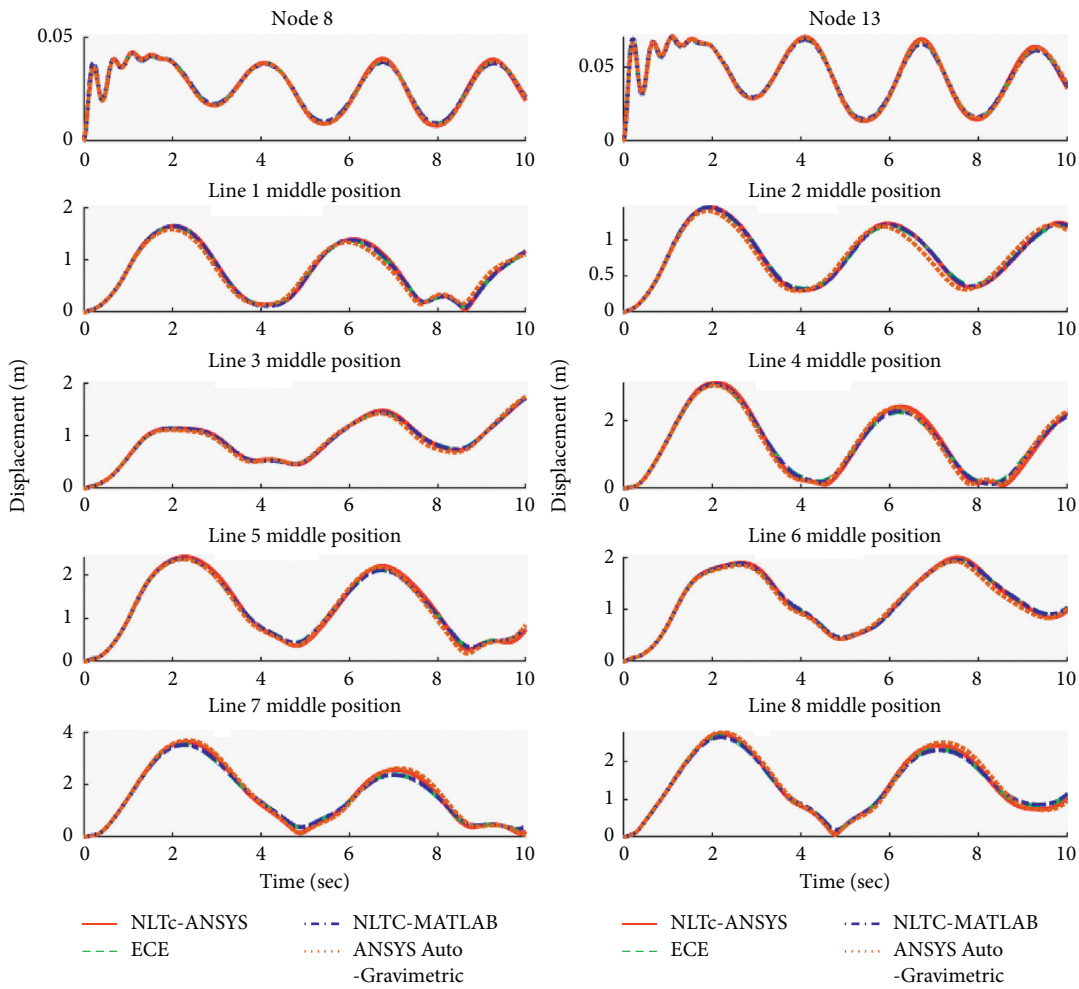

Figure 18: One-span eight-line nodes 8 and 13 total displacement time-history comparison at wind speed 20 m/s and angle 30°.

Table 8: One-span eight-line tower top maximum displacement difference corresponding to NLTc-ANSYS model at different wind speeds and wind angles.

	Maximum displacement (m)			
	Absolute	Difference (%)		
	NLTc-ANSYS	NLTc-MATLAB	ECE-MATLAB	ANSYS auto-gravimetric
S10 m/s A00	0.0132	0.0298	0.0293	0.0023
S10 m/s A30	0.0112	0.0067	0.0053	0.0072
S10 m/s A90	0.0453	0.0931	0.0814	0.0427
S20 m/s A00	0.0455	0.0534	0.0528	0.0024
S20 m/s A30	0.0709	0.0079	0.0090	0.0063
S20 m/s A90	0.1610	0.0813	0.0901	0.0126

S: wind speed; A: wind angle.

Table 9: One-span eight-line tower top displacement time-history RMSE corresponding to NLTc-ANSYS model at different wind speeds and wind angles.

	Tower top displacement RMSE (%)		
	NLTc-MATLAB	ECE-MATLAB	ANSYS auto-gravimetric
S10 m/s A00	0.0076	0.0072	0.0053
S10 m/s A30	0.0130	0.0123	0.0048
S10 m/s A90	0.1790	0.1589	0.1007
S20 m/s A00	0.0391	0.0401	0.0122
S20 m/s A30	0.1357	0.1097	0.0945
S20 m/s A90	0.6872	0.7970	0.1690

S: wind speed; A: wind angle.

Table 10: One-span eight-line tower computational time for difference models at different wind speeds and wind angles.

	Computation GPU time (s)			
	NLTc-ANSYS	NLTc-MATLAB	ANSYS auto-gravimetric	ECE-MATLAB
S10 m/s A00	532	191	514	354
S10 m/s A30	512	188	494	352
S10 m/s A90	470	195	481	357
S20 m/s A00	520	175	518	325
S20 m/s A30	515	175	493	322
S20 m/s A90	502	172	491	323
Averaged	508.5	182.67	498.5	338.83

S: wind speed; A: wind angle.

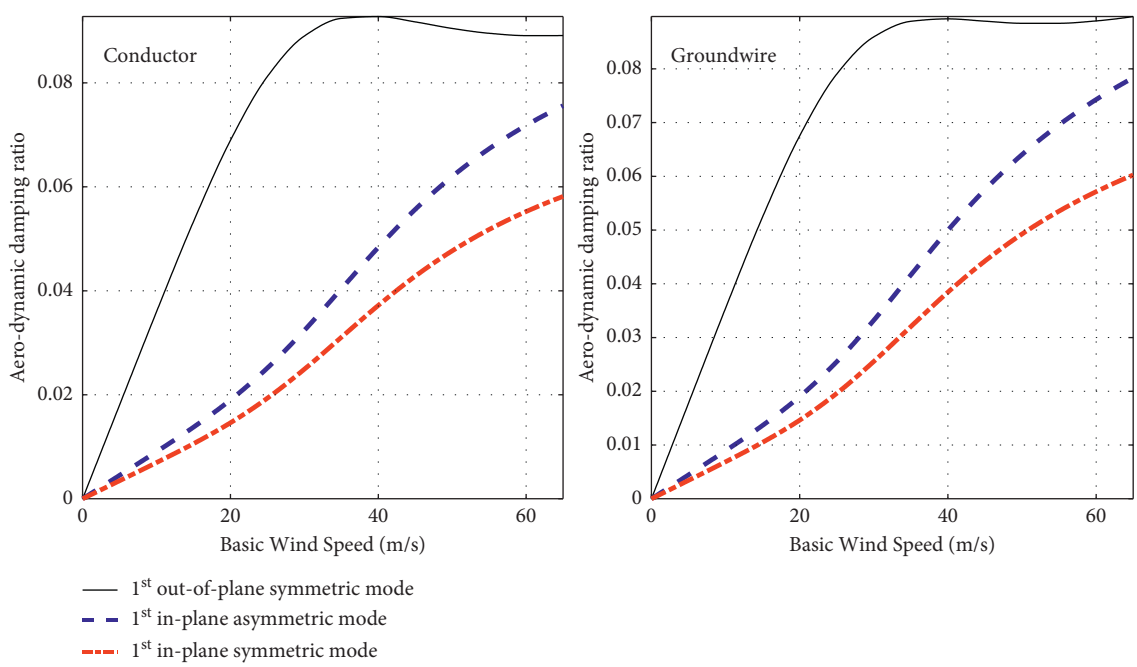

Figure 19: The correlation of aerodynamic damping ratios and wind speeds.

adds to the differences in the dynamic analysis enlarging the RMSE. However, such an impact can be negligible. For the two proposed open-source models, at wind speed 10 m/s, the maximum RMSE errors of NLTc-MATLAB and ECE-MATLAB are 0.18% and 0.16% respectively, which are similar to the performance of the ANSYS auto-gravimetric model. At wind speed 20 m/s, the largest RMSE for the NLTc-MATLAB and ECE-MATLAB model is 0.68% and 0.80%, which are 4 and 4.7 times larger than the ANSYS auto-gravimetric model. The relatively large RMSE at a larger wind speed is due to the plastic deformation of the tower in the ANSYS model. It is suggested that nonlinearity should be considered in the lumped mass model, to encounter the plastic deformation, local buckling, and the failure mechanism of the transmission tower in the future model development.

Another important aspect to evaluate the transmission tower-line model is the computational efficiency. Table 10 summarizes the computational time in each wind speed at each angle and the averaged computational time for different models. In Table 10, ANSYS-based models cost similar computational time around 500 sec, whereas the NLTc-MATLAB and ECE-MATLAB model take 183 and 338 seconds in average to run the simulation, respectively. Therefore, the benefit of using open-source models, especially the ones with nonlinear truss element, is clearly demonstrated. Such a benefit will be further significant when longer simulation time history is needed, or more transmission towers are included. Comparing between the two transmission lines element models, the elastic catenary element based model consumes additional 90% computational time as compared to the nonlinear truss element based model. For calculating the dynamic response of elastic catenary cable element, as stated in Algorithm 2, the determination of the transmission line stiffness matrix in each sub-iteration at each single time step requires the flexibility matrix to be first computed, and then the stiffness matrix is obtained by the inverse calculation of the flexibility matrix. Consequently, the computational burden increased significantly due to the complexity of inverting the flexibility matrix with the increased number of nodes. By contrast, calculating the transmission line dynamic response with the nonlinear truss

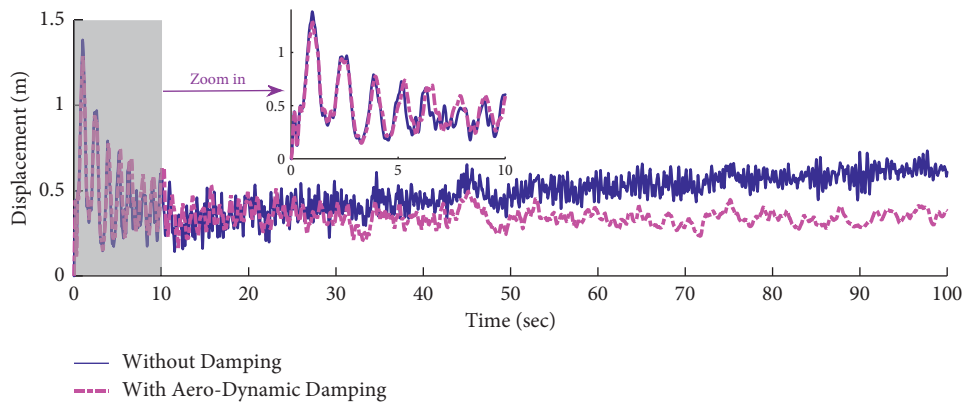

(a)

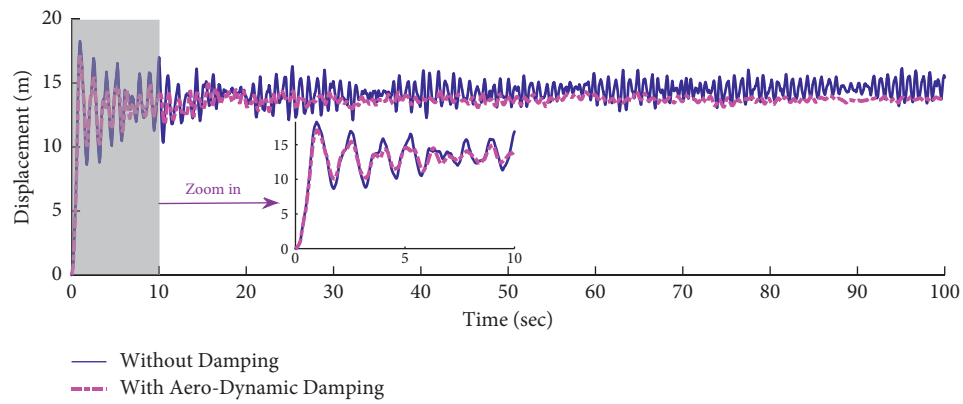

(b)

Figure 20: One-span eight-line model dynamic displacement response comparison with and without aerodynamic damping.

element, as introduced in Algorithm 1, the stiffness matrix is directly obtained by implementing the coordinates and strains of the element to the stiffness matrix.

6. Application of Open-Source Package Full Transmission Tower-Line Model on Extreme Wind Speed Scenario with Aerodynamic Damping Implementation

In Section 5, the comparison between the ANSYS models and the open-source MATLAB models showed that the open-source MATLAB model consumes less computational time with the same level of accuracy. Among the open-source MATLAB models, the transmission line with initial strain calibrated nonlinear truss element (NTLc) is computationally superior to the transmission line model with elastic catenary element formulation (ECE). Therefore, to investigate the effects of the aerodynamic damping on the transmission line system, the open-source NLTc-MATLAB model is implemented. Moreover, as mentioned in Section 4.1, the most dominant extreme wind speed in Texas region is 54 m/s. Hence, the basic wind speed utilizes 50 m/s to generate the dynamic wind speed and wind force for the full transmission tower-line system.

Figure 19 shows the correlation between the aerodynamic damping ratios and the basic wind speed for the conductors and the ground wires. In Figure 19, the aerodynamic damping ratios

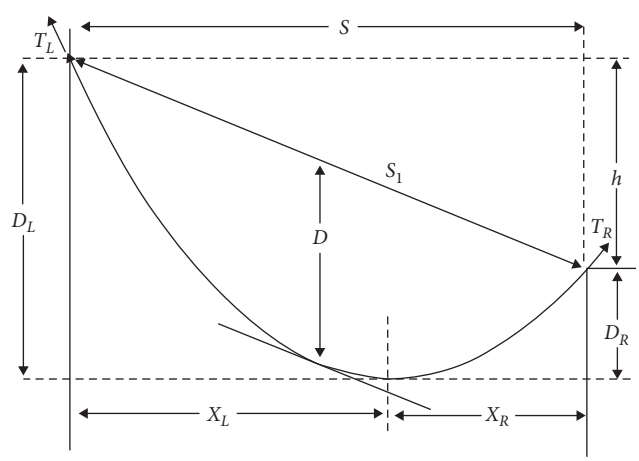

Figure 21: Inclined transmission line configuration.

are positively correlated with the wind speed. For the first out-of-plane symmetric mode, the aerodynamic damping ratios are not monotonically increased with the wind speed due to the influence of the static position of the transmission line [31].

The displacement time-history of the transmission tower-line system with and without aerodynamic damping in Figure 20 illustrates that the aerodynamic damping has suppressed the vibration of the system. However, in Figure 20, the effect of the aerodynamic damping is not

Table 11: 1st 220 kV suspension tower's angle size (New York).

Group label	Angle size	Group type
G1	$6 \times 4 \times 0.5$	Leg
G2	$6 \times 6 \times 0.375$	Leg
G3	$6 \times 4 \times 0.375$	Leg
G4	$5 \times 5 \times 0.375$	Leg
G5	$4 \times 4 \times 0.375$	Leg
G6	$4 \times 4 \times 0.4375$	Leg
G7	$3 \times 2.5 \times 0.1875$	Leg
G8	$1.5 \times 1.5 \times 0.125$	Others
G9	$1.5 \times 1.5 \times 0.125$	Others
G10	$2 \times 2 \times 0.1875$	Crossing diagonal
G11	$2 \times 2 \times 0.1875$	Crossing diagonal
G12	$2 \times 2 \times 0.125$	Crossing diagonal
G13	$1.5 \times 1.5 \times 0.125$	Others
G14	$2 \times 2 \times 0.125$	Crossing diagonal
G15	$1.75 \times 1.75 \times 0.1875$	Crossing diagonal
G16	$1.5 \times 1.5 \times 0.125$	Others
G17	$1.75 \times 1.75 \times 0.1875$	Crossing diagonal
G18	$1.5 \times 1.5 \times 0.125$	Others
G19	$1.75 \times 1.75 \times 0.125$	Crossing diagonal
G20	$1.5 \times 1.5 \times 0.125$	Others
G21	$1.75 \times 1.75 \times 0.125$	Crossing diagonal
G22	$1.5 \times 1.5 \times 0.125$	Others
G23	$1.75 \times 1.75 \times 0.125$	Crossing diagonal
G24	$1.5 \times 1.5 \times 0.125$	Others
G25	$1.5 \times 1.5 \times 0.125$	Crossing diagonal
G26	$1.5 \times 1.5 \times 0.125$	Others
G27	$1.5 \times 1.5 \times 0.125$	Others
G28	$1.5 \times 1.5 \times 0.125$	Others
G29	$1.5 \times 1.5 \times 0.125$	Others
G30	$1.5 \times 1.5 \times 0.125$	Others
G31	$1.5 \times 1.5 \times 0.125$	Others
G32	$1.5 \times 1.5 \times 0.125$	Others
G33	$1.5 \times 1.5 \times 0.125$	Others
G34	$1.5 \times 1.5 \times 0.125$	Others
G35	$1.5 \times 1.5 \times 0.125$	Others
G36	$1.5 \times 1.5 \times 0.125$	Others
G37	$1.5 \times 1.5 \times 0.125$	Others
G38	$1.5 \times 1.5 \times 0.125$	Others
G39	$1.5 \times 1.5 \times 0.125$	Others
G40	$1.5 \times 1.5 \times 0.125$	Others
G41	$1.5 \times 1.5 \times 0.125$	Others
G42	$1.5 \times 1.5 \times 0.125$	Others
G43	$1.5 \times 1.5 \times 0.125$	Others
G44	$1.5 \times 1.5 \times 0.125$	Others
G45	$2 \times 2 \times 0.125$	Crossing diagonal
G46	$2 \times 1.5 \times 0.125$	Crossing diagonal
G47	$1.5 \times 1.5 \times 0.125$	Others
G48	$1.5 \times 1.5 \times 0.125$	Others
G49	$1.5 \times 1.5 \times 0.125$	Others
G50	$1.5 \times 1.5 \times 0.125$	Others
G51	$2 \times 1.5 \times 0.125$	Crossing diagonal
G52	$1.5 \times 1.5 \times 0.125$	Crossing diagonal
G53	$1.5 \times 1.5 \times 0.125$	Crossing diagonal
G54	$1.5 \times 1.5 \times 0.125$	Others
G55	$1.5 \times 1.5 \times 0.125$	Others
G56	$1.5 \times 1.5 \times 0.125$	Crossing diagonal
G57	$1.5 \times 1.5 \times 0.125$	Others
G58	$1.5 \times 1.5 \times 0.125$	Others

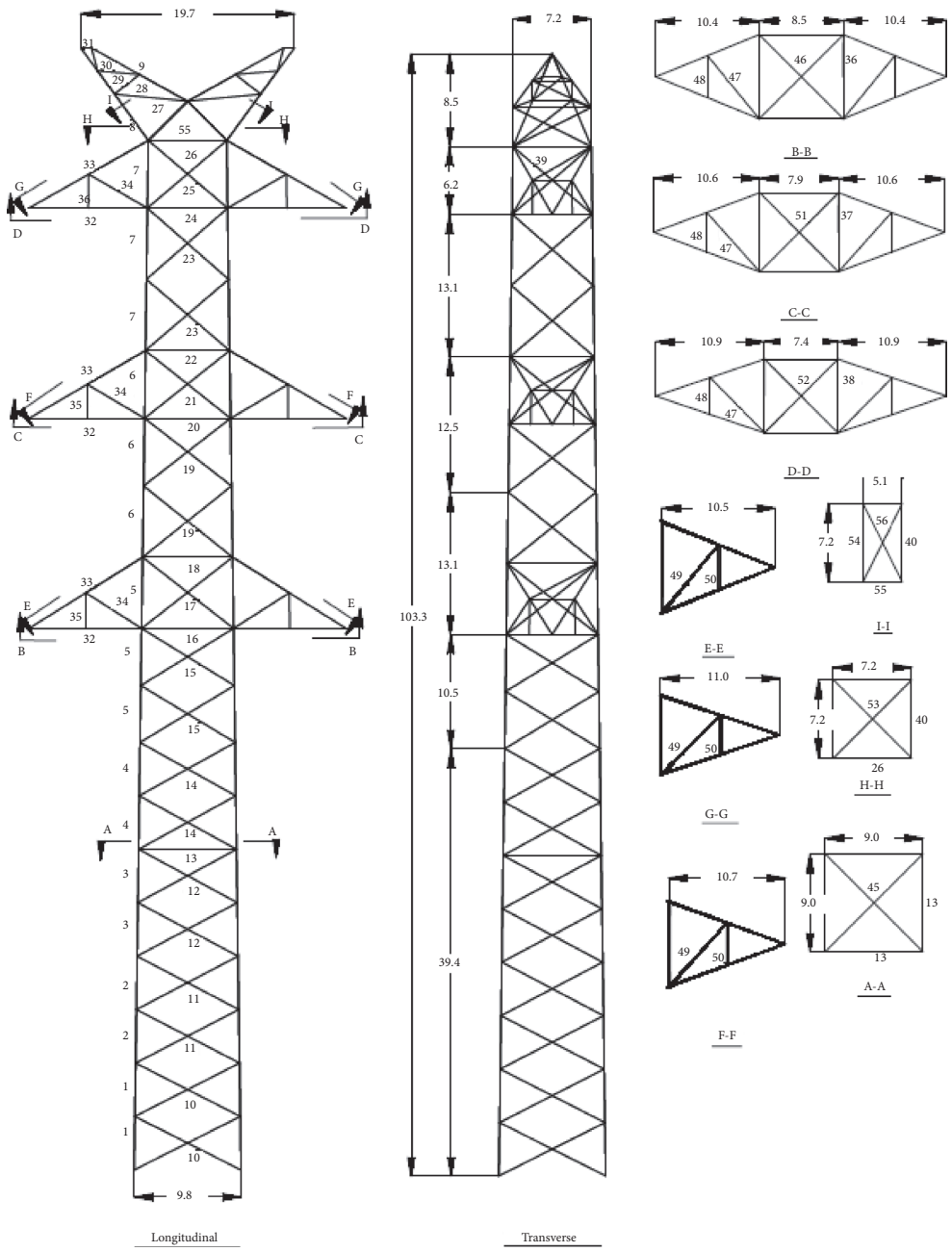

Figure 22: 1st 220 kV suspension tower layout.

significant to the system. The reason is that, as shown in Figure 19, the aerodynamic damping ratios are small because of the taut transmission line configurations (small sag-to-span ratio) in the model.

7. Conclusion

In this paper, two different three-dimensional transmission tower-line models are investigated and developed in open-source MATLAB software package and compared with ANSYS commercial software model. The paper compares the performance of transmission tower-line system model with using nonlinear truss element or elastic catenary element for transmission line modeling. From the results of the study, the following conclusions can be drawn and suggestions made:

(i) The initial strain of the nonlinear truss element has a great impact on the shape finding of the transmission line and consequently the small discrepancy of the initial strain will propagate to the transmission line static and dynamic analysis, which will enlarge the errors in the transmission tower-line models. Calibrating the nonlinear truss model initial strain and initial shape with elastic catenary finite element model will improve the dynamic response accuracy.

(ii) The LS-DYNA default nonlinear truss element model uses uncalibrated initial strain; consequently, the LS-

DYNA computed responses for both the single line and tower-line coupled system simulation deviate largely from other model outputs.

(iii) Two open-source MATLAB transmission tower-line full models are successfully developed and implemented. The developed models demonstrate accurate representation of transmission tower-line coupling phenomenon.

(iv) The computational time for running a two-tower eight-line model is reduced by 66% with using the open-source model as compare to the commercial software.

(v) Both the elastic catenary finite element and calibrated nonlinear truss element model give accurate static and dynamic responses as the transmission line model candidates. The calibrated nonlinear truss transmission line model computational efficiency is better than the elastic catenary transmission line model.

(vi) A linear lumped mass tower model can reproduce the static and dynamic responses of the transmission tower model in ANSYS in low to middle wind speed, where plastic deformation in the transmission tower does not dominate the dynamic response.

(vii) The open-source transmission tower-line package can integrate the aerodynamic damping into consideration. For the specific transmission tower-line model, the effect of the aerodynamic is not significant due to the taut transmission line configurations.

In summary, this paper develops high fidelity three-dimensional transmission tower-line system models in open-source MATLAB package by using lumped tower model with two different transmission line models, namely, the elastic catenary finite element line model and the nonlinear truss calibrated line model. Those models can be implemented to stand-alone transmission line and the coupled transmission tower-line system static and dynamic analysis. However, if the transmission tower elastic-plastic deformation is considered, the lumped mass models in the open-source MATLAB package results will be different from the model in ANSYS because the lumped mass tower model is assumed to be elastic. In the future, transmission tower material nonlinearity should also be considered.

Appendix

A. Calculating the Initial Tension of the Transmission from Sag

In the open-source package, to calculate the configuration of the transmission line, one of the two initial parameters need to be provided: (1) the initial tension and (2) the initial length (unstrained length). Given any one of the two parameters, another parameter can be calculated from the equations in Section 2.1.2. If the sag of the transmission line is given, the following equations needed to be implemented to calculate the initial tension [41].

When the transmission line is level span, then the tension of the conductor is obtained by solving the following equation:

$$D = \frac{H}{w}\left(\cos h\left(\frac{ws}{2H}\right) - 1\right), \tag{A.1}$$

where D is the observed sag; H is the conductor horizontal tension; and w is the weight of the conductor.

When the transmission line is inclined as shown in Figure 21, the tension of the conductor is obtained by solving the following equation:

$$y(x) = \frac{H}{w}\left(\cos h\left(\frac{wx}{H}\right) - 1\right), \tag{A.2}$$

where $y(x)$ is the conductor height relative to the lowest point.

For the left and right end point,

$$\begin{aligned} y_L &= D\left(1 - \frac{h}{4D}\right)^2, \\ y_R &= D\left(1 + \frac{h}{4D}\right)^2. \end{aligned} \tag{A.3}$$

Therefore, by plugging equations (A.3) into (A.2), the left and right horizontal tension can be calculated.

In equation (A.3), h is the height difference between two points; D is the sag; H is the conductor horizontal tension; and w is the weight of the conductor.

B. Transmission Tower Layout and Member Size

1st 220 kV suspension tower's angle size (New York) is shown in Table 11. 1st 220 kV suspension tower layout is shown in Figure 22.

Data Availability

The transmission tower-line model data used to support the findings of this study are included in the article.

Disclosure

Any opinions, findings, and conclusions or recommendations expressed in this study are those of the authors and do not necessarily reflect the views of the National Science Foundation.

Conflicts of Interest

The authors declare that they have no conflicts of interest.

Acknowledgments

This study was based on the work supported by the University of Utah and the National Science Foundation under award numbers 2004658 and 2112758.

References

[1] Michael National Oceanic and Atmospheric Administration, "National weather service national hurricane center tropical cyclone report hurricane michael," 2019.

[2] A. Y. Shehata, A. A. El Damatty, and E. Savory, "Finite element modeling of transmission line under downburst wind loading," *Finite Elements in Analysis and Design*, vol. 42, no. 1, pp. 71–89, 2005.

[3] A. R. Kemp and R. H. Behncke, "Behavior of cross-bracing in latticed towers," *Journal of Structural Engineering*, vol. 124, no. 4, pp. 360–367, 1998.

[4] M. J. Alam and A. R. Santhakumar, "Reliability analysis and full-scale testing of transmission tower," *Journal of Structural Engineering*, vol. 122, no. 3, pp. 338–344, 1996.

[5] Q. Xie and L. Sun, "Experimental study on the mechanical behavior and failure mechanism of a latticed steel transmission tower," *Journal of Structural Engineering*, vol. 139, no. 6, pp. 1009–1018, 2013.

[6] L. Tian, L. Guo, R. Ma, X. Gai, and W. Wang, "Full-scale tests and numerical simulations of failure mechanism of power transmission towers," *International Journal of Structural Stability and Dynamics*, vol. 18, no. 9, 2018.

[7] R. C. Battista, R. S. Rodrigues, and M. S. Pfeil, "Dynamic behavior and stability of transmission line towers under wind forces," *Journal of Wind Engineering and Industrial Aerodynamics*, vol. 91, no. 8, pp. 1051–1067, 2003.

[8] Y. Momomura, H. Marukawa, T. Okamura, E. Hongo, and T. Ohkuma, "Full-scale measurements of wind-induced vibration of a transmission line system in a mountainous area," *Journal of Wind Engineering and Industrial Aerodynamics*, vol. 72, pp. 241–252, 1997.

[9] H. Z. Deng, R. J. Si, X. Y. Hu, and C. Y. Duan, "Wind tunnel study on wind-induced vibration responses of a UHV transmission tower-line system," *Advances in Structural Engineering*, vol. 16, no. 7, pp. 1175–1185, 2013.

[10] H. Z. Deng, H. J. Xu, C. Y. Duan, X. H. Jin, and Z. H. Wang, "Experimental and numerical study on the responses of a transmission tower to skew incident winds," *Journal of Wind Engineering and Industrial Aerodynamics*, vol. 157, pp. 171–188, 2016.

[11] Q. Xie, Y. Cai, and S. Xue, "Wind-induced vibration of UHV transmission tower line system: wind tunnel test on aeroelastic model," *Journal of Wind Engineering and Industrial Aerodynamics*, vol. 171, pp. 219–229, 2017.

[12] X. Fu and H. N. Li, "Dynamic analysis of transmission tower-line system subjected to wind and rain loads," *Journal of Wind Engineering and Industrial Aerodynamics*, vol. 157, pp. 95–103, 2016.

[13] X. Fu, H. N. Li, and G. Li, "Fragility analysis and estimation of collapse status for transmission tower subjected to wind and rain loads," *Structural Safety*, vol. 58, pp. 1–10, 2016.

[14] X. Fu, H.-N. Li, L. Tian, J. Wang, and H. Cheng, "Fragility analysis of transmission line subjected to wind loading," *Journal of Performance of Constructed Facilities*, vol. 33, no. 4, Article ID 04019044, 2019.

[15] J. X. Li, H. N. Li, and X. Fu, "Stability and dynamic analyses of transmission tower-line systems subjected to conductor breaking," *International Journal of Structural Stability and Dynamics*, vol. 17, no. 6, Article ID 1771013, 2017.

[16] L. Tian, X. Zhang, and X. Fu, "Fragility analysis of a long-span transmission tower-line system under wind loads," *Advances in Structural Engineering*, vol. 23, no. 10, pp. 2110–2120, 2020.

[17] L. Tian, R. Ma, H. Pan, C. Qiu, and W. Li, "Progressive collapse analysis of long-span transmission tower-line system under multi-component seismic excitations," *Advances in Structural Engineering*, vol. 20, no. 12, pp. 1920–1932, 2017.

[18] J. Xue, F. Mohammadi, X. Li, M. A. Sahraei, G. Ou, and Z. Pu, "Impact of transmission tower-line interaction to the bulk power system during hurricane," *Reliability Engineering & System Safety*, vol. 203, Article ID 107079, 2020.

[19] H. Keyhan, G. McClure, and W. G. Habashi, "Dynamic analysis of an overhead transmission line subject to gusty wind loading predicted by wind-conductor interaction," *Computers & Structures*, vol. 122, pp. 135–144, 2013.

[20] G. McClure and M. Lapointe, "Modeling the structural dynamic response of overhead transmission lines," *Computers & Structures*, vol. 81, no. 8, pp. 825–834, 2003.

[21] Q. Zhang, X. Fu, L. Ren, and Z. Jia, "Modal parameters of a transmission tower considering the coupling effects between the tower and lines," *Engineering Structures*, vol. 220, Article ID 110947, 2020.

[22] H. T. Thai and S. E. Kim, "Nonlinear static and dynamic analysis of cable structures," *Finite Elements in Analysis and Design*, vol. 47, no. 3, pp. 237–246, 2011.

[23] G. Tibert, "Numerical Analyses of cable Roof Structures," Thesis, KTH, Stockholm, Sweden, 1999.

[24] H. B. Jayaraman and W. C. Knudson, "A curved element for the analysis of cable structures," *Computers & Structures*, vol. 14, no. 3, pp. 325–333, 1981.

[25] M. A. A. Salehi, A. Shooshtari, V. Esmaeili, and A. Naghavi Riabi, "Nonlinear analysis of cable structures under general loadings," *Finite Elements in Analysis and Design*, vol. 73, pp. 11–19, 2013.

[26] H. M. Irvine, *Cable Structures*, Dover Publications, NY, USA, 1992.

[27] M. G. Crusells, F. C. Filippou, and R. L. Taylor, "A mixed formulation for nonlinear analysis of cable structures," *Computers & Structures*, vol. 186, pp. 50–61, 2017.

[28] https://github.com/xiaozhuanran/TL-package.

[29] B. J. Jürgen and K.-J. Bathe, *Finite Element Procedures*, Prentice Hall. xiv, Englewood Cliffs, N.J., USA, 1996.

[30] D. Stengel, K. Thiele, M. Clobes, and M. Mehdianpour, "Aerodynamic damping of nonlinear movement of conductor cables in wind tunnel tests, numerical simulations and full scale measurements," *Journal of Wind Engineering and Industrial Aerodynamics*, vol. 169, pp. 47–53, 2017.

[31] D. Wang, X. Chen, and J. Li, "Prediction of wind-induced buffeting response of overhead conductor: comparison of linear and nonlinear analysis approaches," *Journal of Wind Engineering and Industrial Aerodynamics*, vol. 167, pp. 23–40, 2017.

[32] A. Chopra and B. Murali, *Dynamics-of-structures*, Pearson Education, London, UK, 2019.

[33] H. N. Li, W. L. Shi, G. X. Wang, and L. G. Jia, "Simplified models and experimental verification for coupled transmission tower-line system to seismic excitations," *Journal of Sound and Vibration*, vol. 286, no. 3, pp. 569–585, 2005.

[34] ASCE, *Guidelines for Electrical Transmission Line Structural Loading*, 3rd ed. Guidelines for Electrical Transmission Line Structural Loading. American Society of Civil Engineers, Reston, VA, USA, 2009.

[35] American Society of Civil Engineers, *Minimum Design Loads for Buildings and Other Structures*, ASCE/SEI 7-22, American Society of Civil Engineers, Reston, VA, USA, 2022.

[36] A. G. Davenport, "The spectrum of horizontal gustiness near the ground in high winds," *Quarterly Journal of the Royal Meteorological Society*, vol. 87, no. 372, pp. 194–211, 1961.
[37] M. Shinozuka and G. Deodatis, "Simulation of stochastic processes by spectral representation," *Applied Mechanics Reviews*, vol. 44, no. 4, pp. 191–204, 1991.
[38] Q. Fei, H. Zhou, X Han, and J. Wang, "Structural health monitoring oriented stability and dynamic analysis of a long-span transmission tower-line system," *Engineering Failure Analysis*, vol. 20, no. 3, pp. 80–87, 2012.
[39] C. Tort, S. Şahin, and O. Hasançebi, "Optimum design of steel lattice transmission line towers using simulated annealing and PLS-TOWER," *Computers & Structures*, vol. 179, pp. 75–94, 2017.
[40] G. Ou, A. I. Ozdagli, S. J. Dyke, and B. Wu, "Robust integrated actuator control: experimental verification and real-time hybrid-simulation implementation," *Earthquake Engineering & Structural Dynamics*, vol. 44, no. 3, pp. 441–460, 2015.
[41] L. L. Grigsby, *The Electric Power Engineering Handbook-Five Volume Set*, CRC Press, Boca Raton, FL, USA, 2012.

Hindawi
Shock and Vibration
Volume 2021, Article ID 7403365, 11 pages
https://doi.org/10.1155/2021/7403365

Research Article

Numerical Study on the Mechanical Properties of Transmission Tower K-Joints under Cyclic Loading

Jia-xiang Li, Chao Zhang, Shu-hong Wang, and Sheng-qiang Yin

Department of Civil Engineering, Northeastern University, Shenyang, Liaoning Province, China

Correspondence should be addressed to Chao Zhang; zhangchao_neu@126.com

Received 20 September 2021; Accepted 21 October 2021; Published 8 November 2021

Academic Editor: Bing Qu

During the vibration of a transmission tower, the joints will be subjected to a reciprocating load. To obtain the accurate state of the transmission tower under the load, the mechanical properties of the joints under the vibration load must be considered. In this paper, the mechanical properties of typical K-joints in transmission tower structures are studied by numerical simulation. The failure mode of the K-joint under cyclic loading is also analyzed. The mechanical properties of the K-joint are discussed from the aspects of hysteretic characteristics, stiffness degradation, energy dissipation capacity, and ductility evaluation, and the influencing factors are discussed. The results show that the failure mode of the K-joint is related to the bolt grade and steel strength. When analyzing K-joints, the moment-rotation hysteresis curve should be combined with the realistic parameters of joints to consider the hysteretic behavior of the K-joint. The results provide a theoretical reference for the accurate modeling of transmission towers.

1. Introduction

Joints are the connecting parts between structural components. The mechanical characteristics of joints have a significant impact on the entire structure. In traditional analysis methods, joints are often assumed to be hinged or rigid. In fact, the mechanical characteristics of joints are between ideal hinged joints and complete rigid joints. They have a certain rotational stiffness and can bear part of the bending moment when a certain rotation occurs. To obtain the true mechanical response of structures, semirigid joints must be considered [1–3]. At present, research on semirigid joints mostly focuses on the beam-column connections of frame structures. Zhu et al. [4] obtained the moment-rotation curve of the bolted end plate in the range of elasticity, plasticity, ultimate, and fracture by experiment, gave the failure mechanism of the structural components, and compared it with AISC design guide and European standard. The results showed that both methods underestimate the ultimate moment of joints. Based on the two-parameter exponential model, Zhou et al. [5] proposed a practical analysis model of the moment-rotation relation, which can predict the ultimate flexural capacity of steel beams to concrete-filled steel tube column connections with bidirectional bolts with different size parameters and material properties. Faridmehr et al. [6] carried out cyclic loading tests on rigid and semirigid steel beam-column connections. The results show that the rigid connection has a greater energy dissipation capacity and equivalent hysteretic damping ratio under a larger interstory drift angle. However, lattice structures such as towers and grids are composed of structural steel, steel pipes, or composite section bars, and semirigid joints are completely different from beam-column joints. According to the connection mode, joints can be roughly divided into bolt and welded joints. During installation, the steel pipe is often welded, and some areas are connected with bolts. Shao et al. [7] and Dodaran et al. [8] studied the structural performance of tubular K-joints at high temperature, and the results showed that the ultimate strength of the joints would decrease with increasing temperature. Feng et al. [9, 10] studied the effect of different parameters on the failure mode and bearing capacity of stainless steel tubular K-joints through experimental and numerical methods and proposed a formula to accurately predict the ultimate stress of tubular K-joints.

Due to frequent maritime accidents, the offshore platform will accidentally collide. Therefore, Lu et al. [11] studied the mechanical characteristics of tubular K-joints of offshore platforms under impact loading by experiments and simulations. The results show that in numerical simulation, it is essential to accurately define the dynamic characteristics of materials for predicting the impact response of the K-joint. In addition to the grid structure, tubular steel towers are also basically composed of welded structures and have the characteristics of lightweight and good mechanical characteristics. Li et al. [12, 13] studied the bearing capacity of tubular K-joints with 1/2 or 1/4 annular plates by full-scale experiments. The results indicated that annular plates can improve the bearing capacity of the joints. The angle steel is mostly connected by bolts. For convenient installation, there is a structural clearance of approximately 1.5 mm–4.0 mm between the bolt shank and hole, which causes relative sliding between structural members, also known as bolt slippage. The sliding distance depends on the relative position of the bolt shank in the bolt hole and clearance size. Jiang et al. [14, 15] studied joint slip by experiments and numerical simulations. The results show that bolt slip not only affects the displacement of the transmission tower but also affects the ultimate bearing capacity and failure mode of the transmission tower. Yang et al. [16] and An et al. [17] studied the influence of different parameters on the load-deformation curve of bolted joints through tensile tests and finite element simulations of transmission tower bolt joints. The results showed that when analyzing the transmission tower structure, if the joint slip effect was ignored, the axial stiffness of the joints would be significantly overestimated. To accurately predict the tower deflection, Gan et al. [18] proposed a joint-slippage model based on the component method to predict the tower deflection. For K-joints, Zhao et al. [19] used the component method to derive the calculation model of the initial rotational stiffness of the angle steel tower K-joints and corrected it by combining five full-scale tests. It was verified that the number of bolts and bolt spacing were important factors affecting the initial stiffness of such joints. Yang et al. [20] improved the traditional unit load method by studying the K-joint of the crank arms of UHV cat-head transmission towers.

However, the above studies are all for the static calculation of transmission towers, which are not suitable for dynamic calculation. As a high-rise structure, the transmission tower will be subjected to severe wind, ice shedding, earthquakes, and other loads during service, which will cause the vibration of the transmission tower, threaten the normal operation of the transmission tower, and even lead to the collapse of the transmission tower [21]. During the vibration of the transmission tower, joints will be subjected to cyclic loading. Previous studies have shown that the failure mode, ultimate bearing capacity, and ultimate deformation capacity of steel structure joints are different under both monotonic and cyclic loading [22]. In the vibration process of a transmission tower, the loading state (size and direction) of joints will change, and the model obtained by the monotonic loading test cannot well reflect the mechanical characteristics of the joint in the dynamic process. Therefore, it is necessary to study the cyclic loading of typical transmission tower joints to determine the mechanical characteristics in the vibration process. Li et al. [23] analyzed the hysteretic performance of transmission tower typical bolt joints under cyclic loading and studied the effects of bolt slip on the hysteresis performance joints. The results showed that the hysteretic effect of bolt slip should be considered when calculating the dynamic response of the transmission tower. Ma et al. [24] proposed a hysteretic model of single-bolted angle joints considering cyclic bolt slip, which can more effectively study the joint behavior of towers.

A review of the abovementioned works indicates that the mechanical characteristics of K-bolt joints under cyclic loading should be studied. In this paper, the K-joint of a 500 kV transmission tower is employed as the research object, and the hysteresis characteristics of the K-joint under cyclic loading are studied by numerical simulation. In Section 2, the numerical model of the K-joint in an actual transmission tower is established. In Section 3, the moment-rotation hysteretic curves of the K-joint are analyzed. In Section 4, the stiffness degradation of the K-joint is discussed. Then, the energy dissipation capacity of the K-joint is analyzed in Section 5. In Section 6, the failure mode of the K-joint is discussed, and finally, Section 7 concludes the study.

2. Models and Scenarios

2.1. Finite Element Model. In this paper, a K-joint of a 500 kV tower was selected as the research object, and the large-scale finite element analysis software ANSYS was used for modeling. The model is composed of a main angle steel, a gusset plate, two kinds of branch angle steel, and 10 bolts, as shown in Figure 1. Considering the calculation accuracy and efficiency, all components of the K-joint are simulated by 3D 8-node structural solid element SOLID185, the grids are divided into hexahedrons, and the grids are subdivided in the contact area of components. There are a total of 32 contact pairs in the finite element model, which can be divided into four categories, namely, the contact between the main angle steel and the gusset plate, the contact between the branch angle steel and the gusset plate, the contact between the nut and the component, the contact between the bolt head and the component, and the contact between the bolt shank and the bolt hole. Except for the bond contact mode between the bolt head and the component, the standard contact mode is adopted, and friction is considered. Since the solid element selects 8-node SOLID185, the surface-to-surface contact element adopts 3D 4-node CONTA173, which corresponds to the 3D target element TARGE170. To facilitate loading, the MPC184 element is used to establish rigid beams at the end of branch angle steel, and a rigid area is created to couple the end of branch angle steel with the end of rigid beams.

2.2. Bolt Pretension. The selected K-joints are connected by bolts, and the preload element PRETS 179 is used in ANSYS to apply the pretension force. The element can define a pretension section within any 2D or 3D structure and

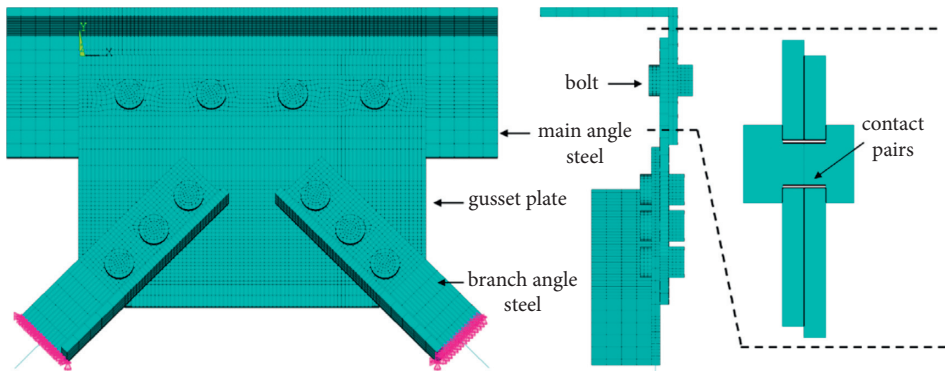

Figure 1: K-joint finite element model.

generate a preloaded area. The relationship between the bolt pretension force and initial torque is shown in the following equation:

$$P_c = \frac{T_c}{k \cdot d}, \tag{1}$$

where P_c = bolt pretension force; T_c = initial torque of bolts; $k = 0.05$, average torque coefficient of bolt connection sets, which can be determined from the relevant provisions of JGJ82-2011 Technical specification for high-strength bolt connections of steel structures [25]; and d = bolt diameter.

After the pretension force is applied, if the component around the bolt is slightly warped, it indicates that the pretension force is correctly applied.

2.3. Material Parameter. Q345 is adopted for the steel of connectors, and 6.8 grade M20 bolts are used. The friction coefficient between the connectors and between the nut and the connector is 0.3, and the eccentric distance is 50 mm. The elastic modulus of the steel is 206 GPa, the elastic modulus of the bolt is 195 GPa, and the Poisson ratio of both is 0.3. The tensile strength and yield strength of the bolts were determined according to GB/T3098.1-2010 Mechanical properties of fastener bolts, screws, and studs [26].

The constitutive relation of the components and bolts adopts the elastic-plastic model with a strengthened section, considering the Bauschinger effect, as shown in Figure 2 [27]. In Figure 2, ε_y = yield strain; $\varepsilon_{cu} = 0.02$, ultimate strain; σy = yield stress; and σ_{cu} = ultimate stress.

2.4. Simulated Conditions. In this paper, 13 groups of scenarios were simulated. The component thickness was 10 mm, and M20 bolts were used. The effects of initial torque, friction coefficient, eccentric distance, bolt hole diameter, strength of connectors, bolt spacing, and bolt grade on the hysteretic characteristics of the K-joint were studied, and the specific parameters are shown in Table 1.

The loading method is controlled by load, which is loaded synchronously along the inclined direction at the end of the rigid beam and subjected to cyclic loading of tension and compression. First, according to 25%, 50%, and 75% of the yield load, each cycle, after reaching yield, according to 10% of the ultimate load gradually increased, three times for each cycle.

The calculation method of the rotation angle and moment is illustrated in Figure 3, which are calculated by equations (2)–(5).

$$u_{\text{sum}} = \sqrt{u_x^2 + u_y^2}, \tag{2}$$

$$\sin\frac{\theta}{2} = \frac{1/2u_{\text{sum}}}{\sqrt{e^2 + w_h{}^2}}, \tag{3}$$

$$\theta = \arccos\left(1 - 2\sin^2\frac{\theta}{2}\right), \tag{4}$$

$$M = F \cdot e, \tag{5}$$

where θ = rotation angle of joint; u_x and u_y = displacement of measuring point; e = eccentric distance; and w_h = half width of gusset plate.

3. Moment-Rotation Hysteretic Curve

Since the resultant force borne by the K-joint does not pass through the centroid of the main angle steel bolt group, the moment will be generated at the centroid of the bolt group, and the gusset plate will rotate by eccentric force. In this section, the rotation angle of the gusset plate is taken as the horizontal axis and the moment is taken as the vertical axis, and the moment-rotation hysteretic curve is drawn, as shown in Figure 4.

It can be found from the figure that

(1) In the process of repeated loading, due to the existence of clearance, the bolt will slip a certain distance, which causes the hysteresis curve to be a pinched, anti-S shape.

(2) The fullness of the hysteresis curve is related to the bolt initial torque, friction coefficient, eccentricity, clearance, component strength, bolt spacing, and bolt grade. Compared with Cases 1, 2, and 3, the curve shape will be more plump when the bolt initial torque is increased, as shown in Figures 4(a)–4(c). Compared with Cases 1, 4, and 5, the curve still

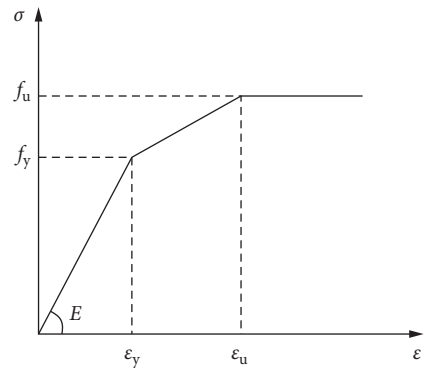

Figure 2: Constitutive relation.

Table 1: Numerical scheme.

Case no.	Initial torque (N·m)	Friction coefficient of component	Friction coefficient of nut	Eccentric distance (mm)	Bolt hole diameter (mm)	Component material	Bolt spacing (mm)	Bolt grade
Case 1	100	0.3	0.3	50	22	Q345	100	6.8
Case 2	125	0.3	0.3	50	22	Q345	100	6.8
Case 3	150	0.3	0.3	50	22	Q345	100	6.8
Case 4	100	0.2	0.3	50	22	Q345	100	6.8
Case 5	100	0.4	0.3	50	22	Q345	100	6.8
Case 6	100	0.3	0.3	50	22	Q420	100	4.8
Case 7	100	0.3	0.3	50	22	Q420	100	6.8
Case 8	100	0.3	0.3	50	22	Q420	100	8.8
Case 9	100	0.3	0.3	50	22	Q420	100	10.9
Case 10	100	0.3	0.3	50	22	Q345	80	6.8
Case 11	100	0.3	0.3	100	22	Q345	100	6.8
Case 12	100	0.3	0.3	50	20	Q345	100	6.8
Case 13	100	0.3	0.2	50	22	Q345	100	6.8

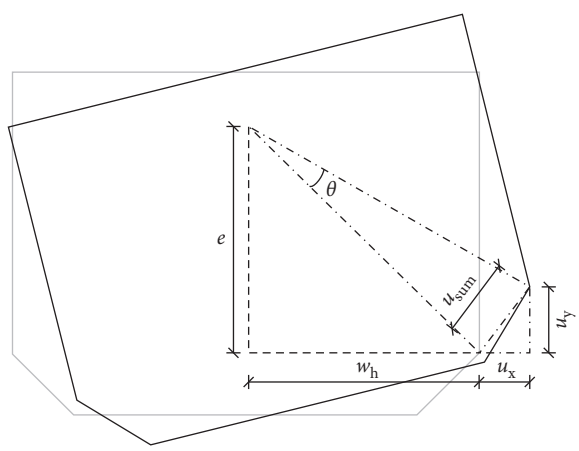

Figure 3: Diagram of rotation angle.

becomes full when the friction between members is increased, as shown in Figures 4(d) and 4(e). This is because increasing the bolt initial torque can make the members connected by bolts fit more closely and, in a sense, achieve the effect of increasing friction. Therefore, more energy is dissipated in the cycle process. As shown in Figures 4(a) and 4(g), when the member steel changes from Q345 to Q420, the ultimate bending moment increases from 21.21 kN·m to 24.75 kN·m, an increase of 16.7%. Compared with Cases 6, 7, 8, and 9, when the bolt grade is changed from 4.8 to 6.8, the ultimate bending moment increases from 16.92 kN·m to 24.75 kN·m, which increases by approximately 46.3%, and the curve is also

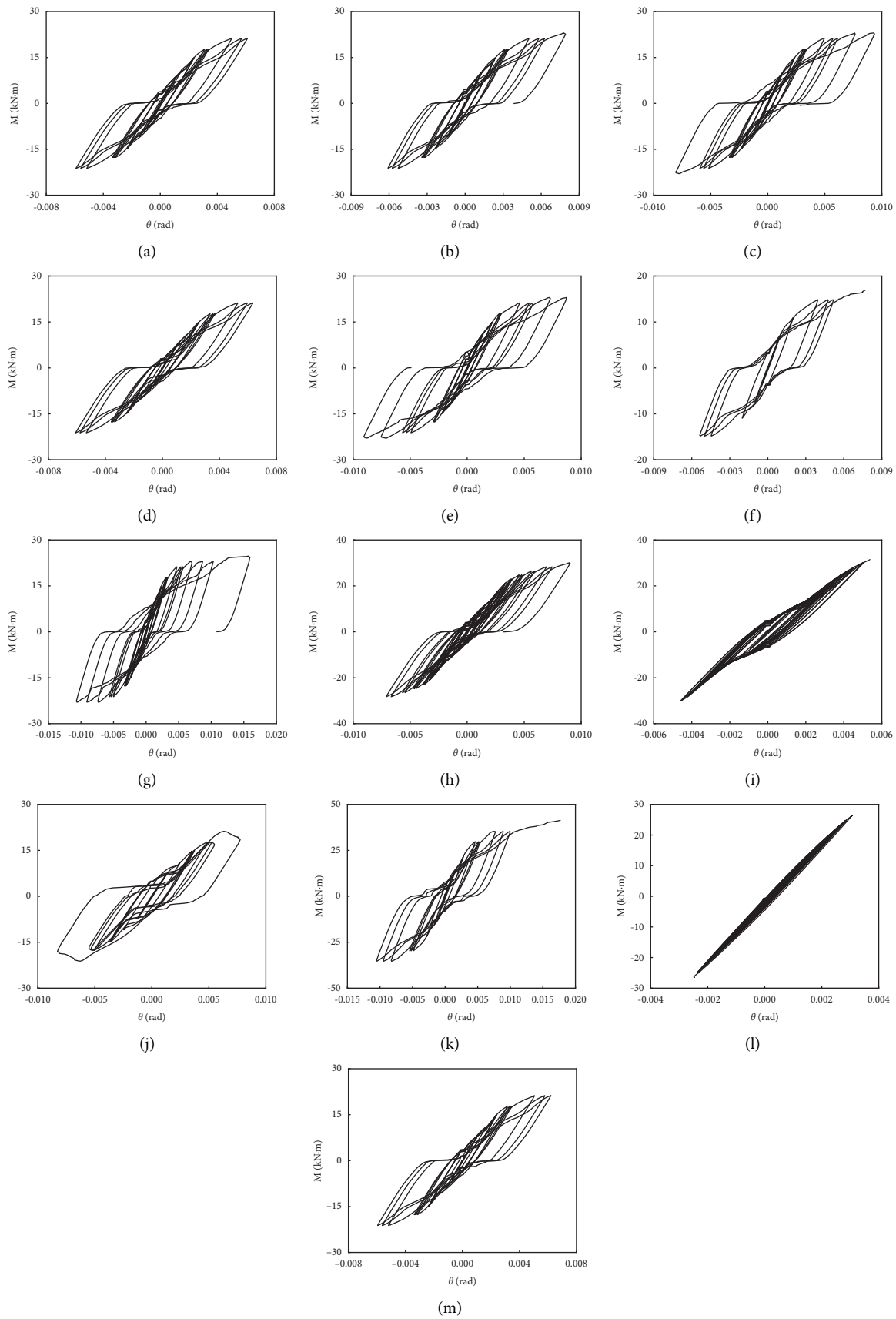

Figure 4: Moment-rotation hysteretic curve. (a) Case 1. (b) Case 2. (c) Case 3. (d) Case 4. (e) Case 5. (f) Case 6. (g) Case 7. (h) Case 8. (i) Case 9. (j) Case 10. (k) Case 11. (l) Case 12. (m) Case 13.

plumper, as shown in Figures 4(f) and 4(g). As the bolt grade increases from 8.8 to 10.9, the ultimate bending moment increases from 30.05 kN·m to 31.47 kN·m, which is an increase of only approximately 4.7%, but the curve is more pinched, as shown in Figures 4(h) and 4(i). The reason for these two opposite trends in the hysteresis curves is that they have different failure modes. The failures in Cases 6 and 7 are caused by bolt failure, while the failures in Cases 8 and 9 are caused by branch angle steel buckling, which will be described in detail in Section 6.

For K-joints, the rotation of the gusset plate is unfavorable to the hysteretic performance. When the spacing of the main angle steel bolt is reduced, the constraints at both ends of the gusset plate are also reduced, and the gusset plate will have a larger rotation angle under the same force, as shown in Figure 4(j). Compared with Cases 1 and 11, when the bending moment is the same, Case 11 has a larger rotation angle. According to equations (3) and (4), when the eccentric distance e increases, the rotation angle θ will also increase. As shown in Figure 4(l), when the clearance is reduced, the bolt and the bolt hole are equivalent to welding. Since the main angle steel bolt cannot slip, the rotation amplitude of the gusset plate is reduced relative to the case with slip when the bending moment is the same. Comparing Cases 1 and 13, it can be seen that the hysteresis curve has almost no change because the area of the nut is too small, and the friction coefficient cannot have decisive effects on the results.

(3) In each loading process, the slope of the curve decreases with increasing load, indicating that the connection stiffness of the joint gradually degenerates, and the residual deformation continues to accumulate and increase, which is mainly related to the yield of members and bolts and the slip of bolts.

In conclusion, the shapes of the hysteretic curves with different parameters are very different, among which the clearance, bolt grade, and member strength have the greatest influence. In addition, it is not enough to evaluate the hysteretic performance of the K-joints only by moment-rotation curve, and it needs to be judged by actual parameters.

4. Stiffness Degradation

One of the nonlinear properties of the structure beyond elasticity is the change in structural stiffness. Stiffness degradation means that under cyclic loading, when the same peak load is maintained, the displacement of the peak point increases with increasing cycle times; that is, the stiffness of the structure or component decreases with increasing repeated loading times. According to the regulations in the JGJ/T101-2015 Specification for seismic testing of buildings [28], the secant stiffness $K_{\theta i}$ under each cycle is calculated by equation (6) in this section.

$$K_{\theta i} = \frac{|+F_i| + |-F_i|}{|+X_i| + |-X_i|}, \tag{6}$$

where $+F_i$ and $-F_i$ = the load value of the ith forward and reverse peak points and $+X_i$ and $-X_i$ = the displacement value of the ith forward and reverse peak points.

Figure 5 shows the secant stiffness $K_{\theta i}$ of the moment-rotation curve for each cycle of the joint. As shown in the figure, compared with Cases 6, 7, 8, and 9, the overall stiffness of Cases 6 and 7 shows a downward trend, while the stiffness of Cases 8 and 9 decreases first, and the decline range is smaller than that of Cases 6 and 7. This is because Cases 6 and 7 use ordinary bolts, and joint failure is due to the failure of the bolts. However, high-strength bolts are used in Cases 8 and 9, and joint failure is caused by the buckling of the branch angle steel. When the branch angle steel reaches the yield strength, it becomes the main stress part. At this time, the gusset plate is less affected by the load, so the stiffness tends to be flattened.

It can also be seen from the figure that Case 12 eliminates the bolt clearance, and the entire stiffness is high. In addition, the stiffness of the K-joint with a small bolt spacing is generally low, while the stiffness degradation of other cases is generally gentle.

In addition, Table 2 shows the initial stiffness $K_{\theta o}$ of the joint under various cases, namely, the ratio of the sum of the absolute values of the load at the forward and reverse peak points under the first loading to the sum of the corresponding displacement. It can be seen from the comparison that in the elastic range, the initial stiffness of each case is similar, but reducing the clearance can significantly improve the initial stiffness of the joint.

5. Energy Dissipation Capacity

When the structure enters the plastic state, there is residual deformation and energy loss after unloading. Under cyclic loading, the area enclosed by the moment-rotation hysteresis loop represents the energy consumption. The energy dissipation coefficient C_e and equivalent viscous damping coefficient ξ_{eq} are usually used to evaluate the energy dissipation capacity of components [28]. The formulas are as follows:

$$C_e = \frac{S_{(ABC+CDA)}}{S_{(OBE+ODF)}},$$
$$\xi_{eq} = \frac{1}{2\pi} \cdot \frac{S_{(ABC+CDA)}}{S_{(OBE+ODF)}}, \tag{7}$$

where $S(ABC + CDA)$ = the area enclosed by the hysteresis curve in Figure 6 and $S(OBE + ODF)$ = the sum of the area of triangles OBE and ODF.

The total energy consumption W_t, equivalent viscous damping coefficient ξ_{eq}, and energy dissipation coefficient C_e of the joint in the limit state are calculated, as shown in Table 3.

It can be seen from Table 3 that increasing the member strength and bolt grade and increasing the friction between components will lead to an increase in the total energy

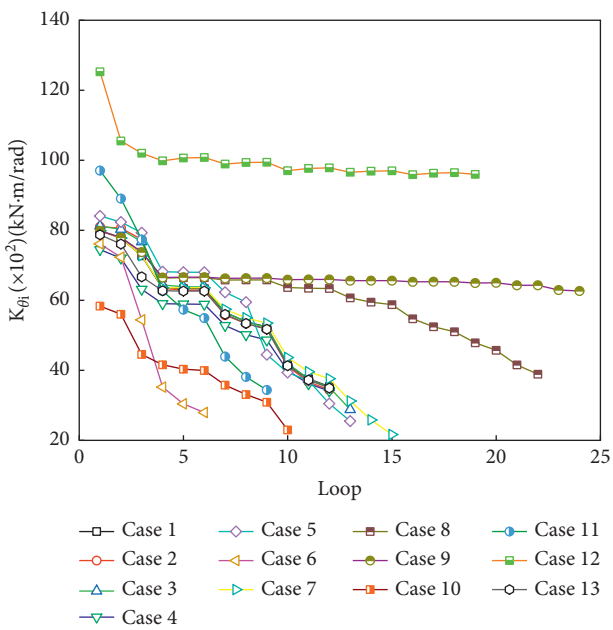

Figure 5: The stiffness degradation of moment-rotation curve.

Table 2: Initial stiffness.

Case	Initial stiffness (kN·m/rad)
1	7983.26
2	8099.91
3	8119.99
4	7447.76
5	8408.83
6	7609.41
7	7983.27
8	7984.07
9	7984.06
10	5833.96
11	9705.45
12	12524.77
13	7872.30

consumption, which indicates that these measures can improve the energy consumption of the joint. In addition, it can be seen from Table 3 that increasing the eccentricity and reducing the spacing of the main angle steel bolts will improve the energy dissipation capacity of the K-joint. However, from the hysteresis curve, increasing the eccentricity and reducing the spacing of the main angle steel bolts will cause a greater bending moment and rotation angle, which will lead to early failure of the K-joint. It cannot be simply considered that this will improve its energy dissipation capacity.

6. Failure Morphology

When the transmission tower is subjected to wind, earthquakes, and other loads, the components of the transmission tower are often subjected to repeated loads. The most unfavorable loading state for K-joints is that one side of the branch angle steel bears tension and one side of the branch angle steel bears compression. At this time, since the resultant force acting point of branch angle steel under the load does not pass through the centroid of the bolt group on the main angle steel, a moment will be generated at the centroid of the bolt group, resulting in the rotation of the gusset plate under the eccentric load, as shown in Figure 7.

6.1. Effect of Bolt Grade. To study the influence of bolt grade on the failure mode of the joint, bolts of grade 4.8, grade 6.8, grade 8.8, and grade 10.9 were used in Cases 6, 7, 8, and 9, respectively. According to the simulation results, the failure mode of Case 6 is consistent with that of Case 7, and the failure mode of Case 8 is consistent with that of Case 9. Here, Case 6 and Case 9 are selected for comparison.

Figure 8 shows the failure form of the K-joint in Case 6, that is, the bolt is damaged, and its deformation is far more than that of the other components. Figure 8(a) shows that rotation of the gusset plate occurs, and the deformation of the other components is not obvious, which is particularly clear in Figures 8(b)–8(d). From Figure 8(e), it can be seen that the main angle steel bolts have an obvious torsional trend, and the plastic strain of the main angle steel bolt is 0.08, which is much larger than 0.042 of the branch angle steel bolt, which shows that the failure of the main angle steel bolt is more serious than that of the branch angle steel bolt. The diagonal bolt shows only a shear state, and the plastic strain of the bolt shank is continuous, as shown in Figure 8(f).

Figure 9 shows the failure mode of the K-joint in Case 9; that is, the branch angle steel has obvious buckling, while the bolt deformation is not obvious. Figure 9(a) shows that the failure mode of Case 9 is obviously different from that of Case (6), and its branch angle steel shows obvious buckling. It can be seen from Figures 9(b)–9(d) that the deformation of components is greater than that of Case 6, and the deformation of branch angle steel is the most significant.

Compared with Cases 6 and 9, the plastic strain of the branch angle steel in Case 6 reached 0.0021, and that of the main angle steel bolt was 0.08, while the strain of branch angle steel in Case 9 was 0.036, and that of the bolt was 0.009, and the results were exactly the opposite. This is because in Case 6, 4.8 grade ordinary bolts were used, whose shear strength is lower than that of the component, so the bolt was cut off, resulting in joint failure. Grade 10.9 high-strength bolts were used in Case 9, whose shear strength was higher than that of the component. Under cyclic loading, joint failure was caused by buckling due to the weak strength of the inclined material.

The failure mode of the K-joint is related to the bolt grade. When the strength of the component is certain, improving the bolt grade can avoid the joint failure caused by bolt shear fracture. However, if the bolt grade is too high, the branch angle steel will buckle before the bolts are snipped, resulting in the failure of the K-joint.

6.2. Effect of Component Strength. Cases 1 and 7 are selected for analysis. Grade 6.8 ordinary bolts were used, and the components were Q345 and Q420 steel. By analyzing

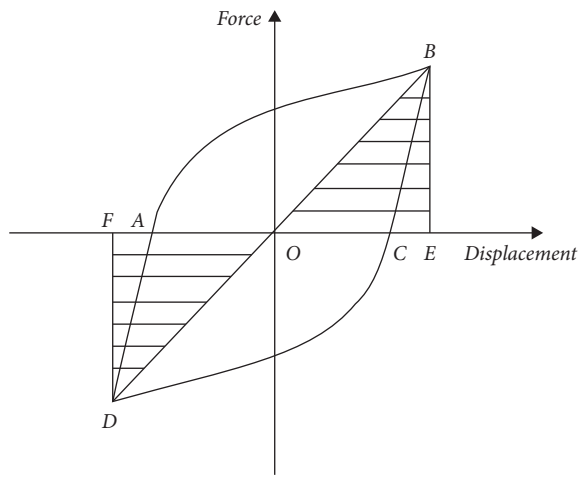

Figure 6: Calculation of the energy dissipation coefficient.

Table 3: Energy consumption index of the K-joint.

Case	Total energy consumption W_t (kN·m·rad)	Equivalent viscous damping coefficient ξ_{eq}	Energy dissipation coefficient C_e
1	376.109	0.108	0.676
2	488.015	0.117	0.732
3	654.693	0.152	0.953
4	370.817	0.107	0.673
5	705.373	0.151	0.948
6	225.899	0.154	0.969
7	1192.207	0.193	1.212
8	840.243	0.091	0.574
9	662.233	0.072	0.451
10	498.925	0.209	1.315
11	1197.311	0.150	0.942
12	92.665	0.027	0.168
13	376.088	0.107	0.672

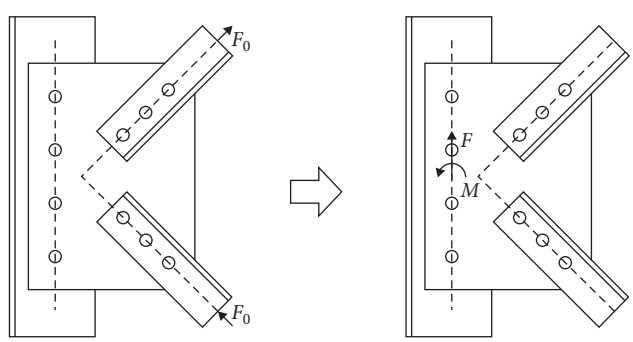

Figure 7: Mechanism of the K-joint under the most unfavorable load.

Figure 10(a), it can be seen that the joint component of Case 1 did not have large deformation, and compared with Figures 10(b) and 10(c), the bolt strain reached 0.038, and the branch angle steel strain was 0.012, indicating that the joint failure of Case 1 was the same as that of Cases 6 and 7, which was caused by bolt failure. It is obvious from Figures 10(c) and 10(f) that the deformation of branch angle steel in Case 7 is much less than that in Case 1.

Therefore, when the load is certain, improving the steel strength of the component can reduce the deformation of the component and improve the bearing performance of the joint.

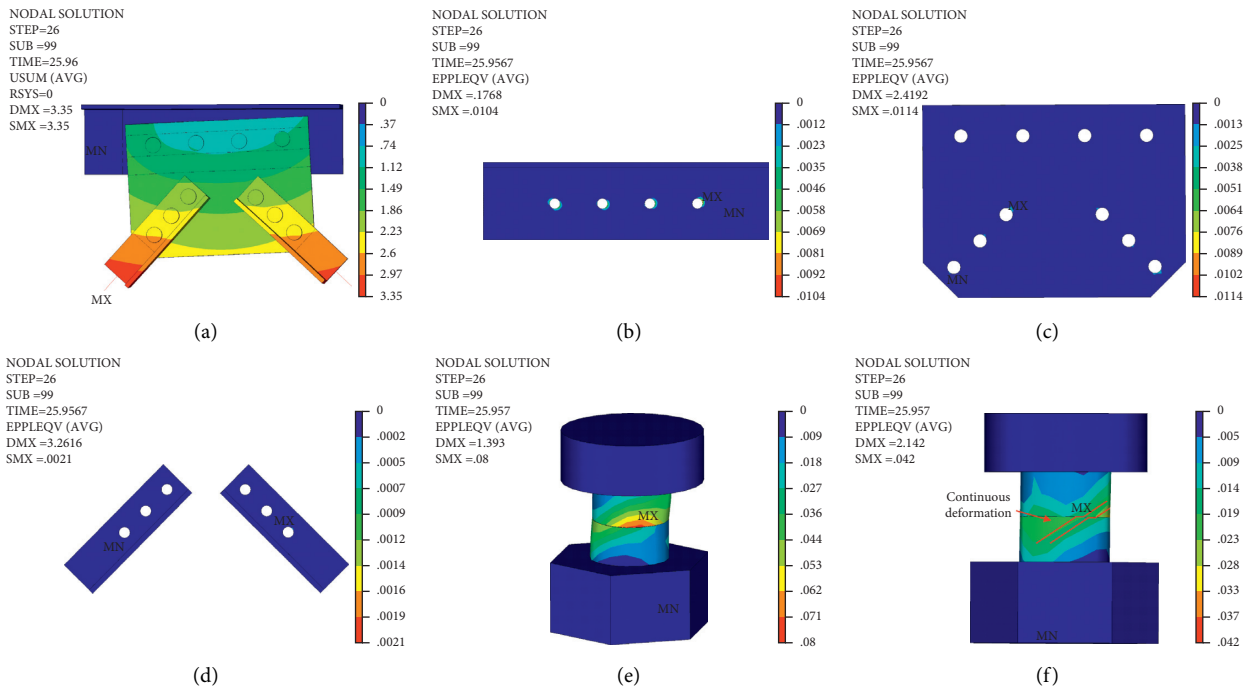

Figure 8: Simulation results for Case 6. (a) Displacement of joint. (b) Plastic strain of main angle steel. (c) Plastic strain of gusset plate. (d) Plastic strain of branch angle steel. (e) Plastic strain of bolts on main angle steel. (f) Plastic strain of bolts on branch angle steel.

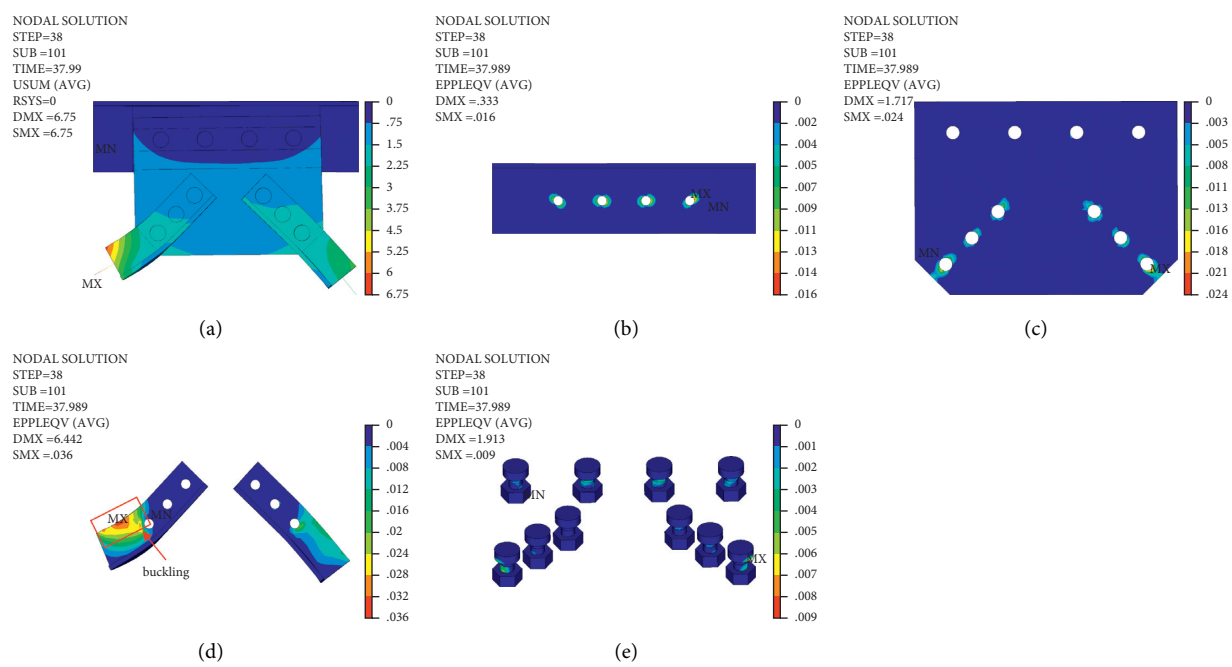

Figure 9: Simulation results for Case 9. (a) Displacement of joint. (b) Plastic strain of main angle steel. (c) Plastic strain of gusset plate. (d) Plastic strain of branch angle steel. (e) Plastic strain of bolts.

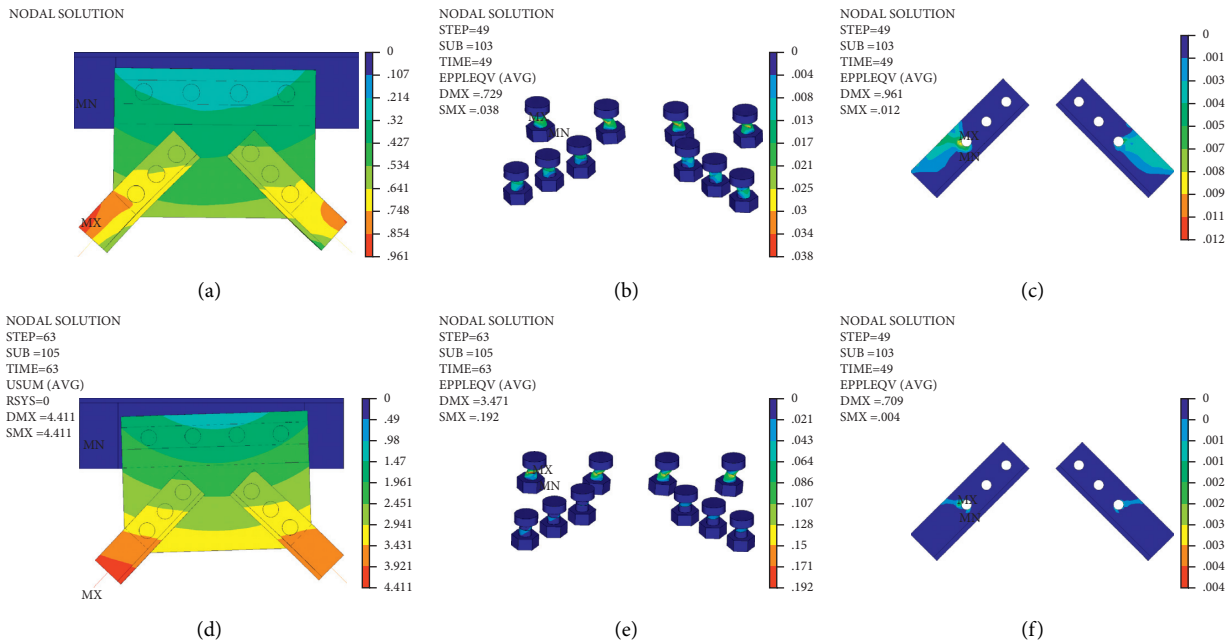

Figure 10: Simulation results for Cases 1 and 7. (a) Displacement of joint in Case 1. (b) Plastic strain of bolts in Case 1. (c) Plastic strain of branch angle steel in Case 1. (d) Displacement of joint in Case 7. (e) Plastic strain of bolts in Case 7. (f) Plastic strain of branch angle steel in Case 7.

7. Conclusion

In this paper, numerical simulations were performed to study the mechanical characteristics of K-joints under cyclic loading. The failure mode of the K-joints was analyzed. The mechanical properties of the K-joint were discussed from the aspects of the hysteresis curve, stiffness degradation, and energy dissipation capacity. The following conclusions were drawn:

(1) The hysteretic behavior of the K-joint is affected by the bolt initial torque, friction coefficient, eccentricity, clearance, component strength, bolt spacing, and bolt grade. Increasing the bolt initial torque, increasing the friction between components, improving the strength of components, selecting high-strength bolts, or reducing the clearance can improve the hysteretic characteristics of this type of joint.

(2) The failure mode of the *K*-joint is related to the bolt grade and component strength. When the strength of the component is certain, increasing the bolt grade can avoid the joint failure caused by bolt shear fracture. However, if the bolt grade is too high, the branch angle steel will first undergo buckle failure, resulting in K-joint failure. Therefore, special attention should be given to the selection of bolt grade and steel type.

(3) If *K*-joints have eccentricity, the main bolt group will not only bear shear force but also receive a bending moment, showing a torsional shear state. The bolt of branch angle steel only bears the shear force, so the main bolt will be damaged before the bolt of branch angle steel. In practice, the eccentricity should be reduced as much as possible. If it cannot be reduced, the grade of the main bolt should be strengthened.

(4) In the loading process, if the bolt is damaged, the secant stiffness will decrease rapidly. If the branch angle steel yields, the secant stiffness decreases gently.

(5) Increasing the eccentricity and reducing the spacing of the main angle steel bolt can improve the energy dissipation capacity of the K-joint, but it will accelerate the destruction of the K-joint.

Data Availability

No data were used to support this study.

Conflicts of Interest

The authors declare that they have no conflicts of interest.

Acknowledgments

This study was financially supported by the National Natural Science Foundation of China (grant no. 51808100) and Liaoning Provincial Natural Science Foundation of China (grant no. 2019-ZD_0004).

References

[1] C. Díaz, P. Martí, M. Victoria, and O. M. Querin, "Review on the modelling of joint behaviour in steel frames," *Journal of Constructional Steel Research*, vol. 67, no. 5, pp. 741–758, 2011.

[2] I. Faridmehr and M. Hajmohammadian Baghban, "An overview of progressive collapse behavior of steel beam-to-

column connections," *Applied Sciences*, vol. 10, no. 17, p. 6003, 2020.

[3] R. Al-fisalawi, A. Khalid, and M. Al-kamal, "Performance of semi-rigid steel connections under monotonic and cyclic loadings: a review," in *Proceedings of the Iop Conference Series: materials Science and Engineering*, no. 1, p. 1067, Prague Czech Republic, September 2021.

[4] C. Zhu, K. J. R. Rasmussen, S. Yan, and H. Zhang, "Experimental full-range behavior assessment of bolted moment end-plate connections," *Journal of Structural Engineering*, vol. 145, no. 8, pp. 1–12, 2019.

[5] G. Zhou, Y. An, D. Li, and J. Ou, "Analytical model of moment-rotation relation for steel beam to CFST column connections with bidirectional bolts," *Engineering Structures*, vol. 196, no. 2, Article ID 109374, 2019.

[6] I. Faridmehr, M. M. Tahir, M. H. Osman, and M. Azimi, "Cyclic behaviour of fully-rigid and semi-rigid steel beam-to-column connections," *International Journal of Steel Structures*, vol. 20, no. 2, pp. 365–385, 2020.

[7] Y. Shao, S. He, and D. Yang, "Prediction on static strength for CHS tubular K-joints at elevated temperature," *Ksce Journal of Civil Engineering*, vol. 21, no. 3, pp. 900–911, 2017.

[8] N. Azari Dodaran, H. Ahmadi, and M. A. Lotfollahi-yaghin, "Parametric study on structural behavior of tubular K-joints under axial loading at fire-induced elevated temperatures," *Thin-Walled Structures*, vol. 130, pp. 467–486, 2018.

[9] R. Feng, C. Tang, Z. Chen, K. Roy, B. Chen, and J. B. M. Lim, "A numerical study and proposed design rules for stress concentration factors of stainless steel hybrid tubular k-joints," *Engineering Structures*, vol. 233, no. 52, Article ID 111916, 2021.

[10] R. Feng, J. Lin, and X. Mou, "Experiments on hybrid tubular K-joints with circular braces and square chord in stainless steel," *Engineering Structures*, vol. 190, pp. 52–65, 2019.

[11] Y. Lu, K. Liu, Z. Wange, and W. Tang, "Dynamic behavior of scaled tubular k-joints subjected to impact loads," *Marine Structures*, vol. 69, Article ID 102685, 2020.

[12] F. Li, H.-z. Deng, and X.-y. Hu, "Resistance of gusset-tube DK-joints stiffened by 1/2 annular plates in transmission towers," *Journal of Constructional Steel Research*, vol. 159, pp. 560–573, 2019.

[13] F. Li, H. Deng, and X. Hu, "Design resistance of longitudinal gusset-tube k-joints with 1/4 annular plates in transmission towers," *Thin-Walled Structures*, vol. 144, Article ID 106271, 2019.

[14] W. Q. Jiang, Z. Q. Wang, G. Mcclure, G. L. Wang, and J. D. Geng, "Accurate modeling of joint effects in lattice transmission towers," *Engineering Structures*, vol. 33, no. 5, pp. 1817–1827, 2011.

[15] W. Jiang, Y. Liu, S. Chan, and Z. Q. Wang, "Direct analysis of an ultrahigh-voltage lattice transmission tower considering joint effects," *Journal of Structural Engineering*, vol. 143, no. 5, Article ID 4017009, 2017.

[16] F. Yang, B. Zhu, and H. Xing, "THE slip characteristics and parametric study of bolted connections for transmission towers," *Engineering Mechanics*, vol. 34, no. 10, pp. 116–127, 2017, in Chinese.

[17] L. An, J. Wu, and W. Jiang, "Experimental and numerical study of the axial stiffness of bolted joints in steel lattice transmission tower legs," *Engineering Structures*, vol. 187, pp. 490–503, 2019.

[18] Y.-d. Gan, H.-z. Deng, and C. Li, "Simplified joint-slippage model of bolted joint in lattice transmission tower," *Structure*, vol. 32, pp. 1192–1206, 2021.

[19] N. Zhao, Z. Li, and H. Liu, "Calculation model of initial stiffness of angle steel tower k-joints," *Engineering Mechanics*, vol. 31, no. 4, pp. 93–101, 2014, in Chinese.

[20] F. Yang, B. Zhu and Z. Li, Numerical analysis and full-scale experiment on k-joint deformations in the crank arms of lattice transmission towers," *The Structural Design of Tall and Special Buildings*, vol. 27, no. 5, p. 1448, 2018.

[21] J. Li, G. Mcclure, and S. Wang, "Ensuring the structural safety of overhead transmission lines by design," *Journal of Aerospace Engineering*, vol. 34, no. 3, Article ID 4021010, 2021.

[22] M. Saleem and M. Saleem, "Cyclic shear-lag model of steel bolt for concrete subjected to impact loading," *Journal of Materials in Civil Engineering*, vol. 30, no. 3, Article ID 04018023, 2018.

[23] J. Li, B. Wang, J. Sun, and S. H. Wang, "Numerical simulation study on hysteresis characteristics of transmission tower bolt joints," *Journal of Northeastern University*, vol. 41, no. 11, pp. 1633–1639, 2020, in Chinese.

[24] L. Ma and P. Bocchini, "Hysteretic model of single-bolted angle connections for lattice steel towers," *Journal of Engineering Mechanics*, vol. 145, no. 8, Article ID 04019052, 2019.

[25] Jgj82-2011, *Technical Specification for High Strength Bolt Connections of Steel structures*, China Architecture & Building Press, Beijing, China, 2011, in Chinese.

[26] Gb/T3098 1-2010, *Mechanical Properties of Fasteners-Bolts, Screws and Studs*, Standards Press of China, Beijing, China, 2010, in Chinese.

[27] J. Li, H. Li, and X. Fu, "Stability and dynamic analyses of transmission tower-line systems subjected to conductor breaking," *International Journal of Structural Stability and Dynamics*, vol. 17, no. 6, Article ID 1771013, 2017.

[28] Jgj/T101-2015, *Specification for Seismic Test of Buildings*, China Architecture & Building Press, Beijing, China, 2015, in Chinese.

Hindawi
Shock and Vibration
Volume 2021, Article ID 2323758, 16 pages
https://doi.org/10.1155/2021/2323758

Research Article

Effect of the Bracing System on the Probability of Collapse of Steel Structures under Maximum Credible Earthquake

Alireza Kianmehr

Civil and Environmental Engineering, Tarbiat Modares University, Tehran, Iran

Correspondence should be addressed to Alireza Kianmehr; alireza.kianmehr@modares.ac.ir

Received 7 August 2021; Revised 30 August 2021; Accepted 17 September 2021; Published 18 October 2021

Academic Editor: Li Tian

Simple bracing frames can be divided into two types in terms of concentric or eccentric. Concentric bracing frames are frames that intersect with other structural members at one point in the structure along the bracing members. Otherwise, the braced frame will be eccentric. It is said empirically that due to this type of shaping, eccentric bracing frames exhibit more ductile behavior and concentric bracing frames exhibit more stiff behavior. This behavioral difference caused this study to be numerically computing for five frames, including unique concentric and eccentric bracing frames of 5 and 10 stories and an ordinary 5-story concentric bracing frame. Their tensions and drift ratios should be acceptable for the use of residential buildings. Using the primary two steps of the new PEER probabilistic framework, namely, probabilistic seismic hazard analysis and structural analysis, which leads to the drawing of fragility curves, the probability of collapse is obtained to compare the safety capability of these frames according to their different characteristics against earthquakes. The results show that increasing the ductility or increasing the number of floors or the height of these systems can reduce collapse. Also, according to the results of the probability of collapse obtained in frames with 5-story concentric bracing frames, it can be said that some of the current regulations, which work based on previous approaches of analysis, can lead to unsafe structures with a high probability of collapse.

1. Introduction

In the bracing frame, more stability stiffness and uncertainty can be created by connecting the braces to the beams and columns. Moreover, considering the simple connections throughout the frame, the whole structure can be designed more economically. The ductility of such frames is classified into two types, ordinary and special, in Iranian Standard 2800. Ordinary frames cannot be used for structures with a height of more than 15 meters or for sites with very high seismicity and structures with high importance such as hospitals. The types of such frames are shown in Figure 1. In this figure, frame a, diagonal bracing, frames b and c, respectively, inverted V and V bracing, and frame d, x-braced, are cross braces, which have the highest stiffness among all frames, and also frame e shows k-shaped bracing, which from the perspective of the tenth topic of National Building Regulations of Iran is not allowed [1].

In eccentric bracing frames, the extension of the bracing members, unlike the concentric bracing frames, does not meet at one point in the structure and are centered along the column, the middle of the beam, or the end of the other braces in an opening. At the deliberate deviation of the created center, the link beams are placed, depending on their length, shear yield, flexural, or shear-flexural behavior expected with the yield created in this section due to abnormal lateral loads such as. The earthquake does not spread to other structural members and acts as a seismic fuse [3]. Several models of structural arrangement types in eccentric bracing frames are shown in Figure 2. Another difference between the concentric and eccentric bracing systems, as seen in Figure 2, is the presence of transverse stiffeners in the link

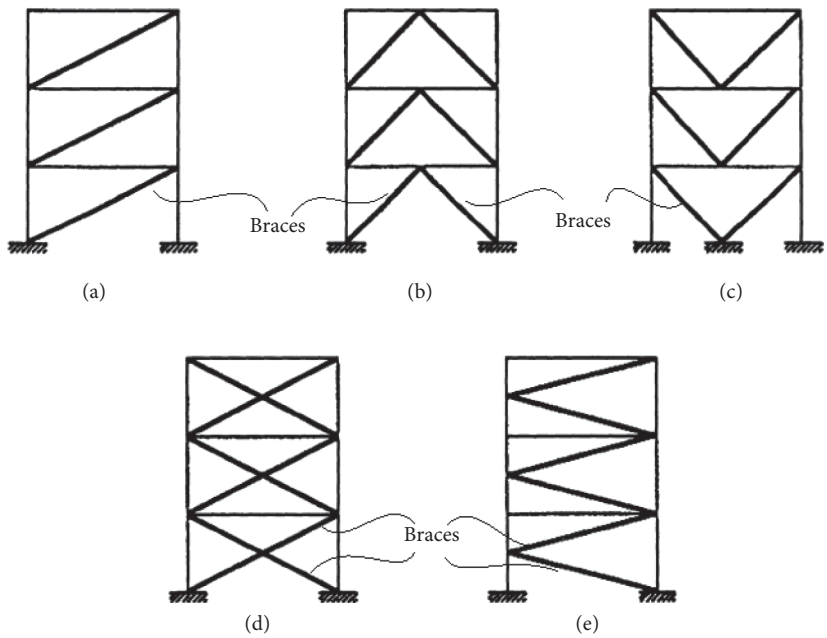

Figure 1: Configuration types of concentric bracing frames [2].

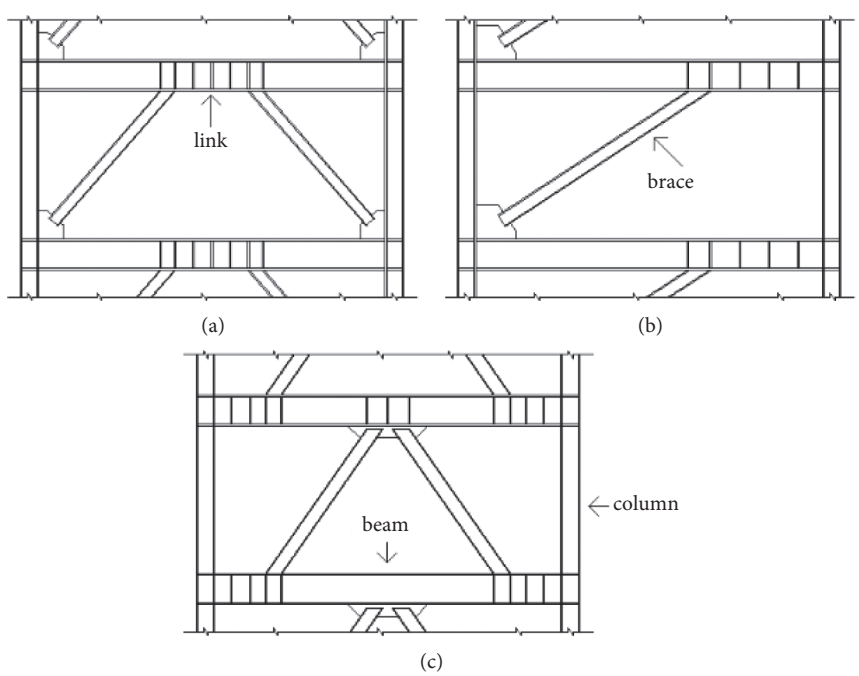

Figure 2: Several schematic models of various structural member arrangement models in frames with eccentric bracing systems [4].

beam due to the shear force and the flexural moment within it due to earthquake forces.

Eccentric bracing frames can exhibit good cyclic behavior and hysteresis if controlled by structural members with high ductility. Iranian Standard 2800 only allows remarkable ductility for such frames and the National Building Regulations No. 10 stated, "The larger the length of the link beam, the less the rotation and deformation." Figure 3 shows the stress expansion in one of the designed connection beams. Significant progress has been made in seismic hazard estimation in recent years. In the framework of the PEER method, the probability of damage to structures due to earthquakes is estimated. In this regard, the Pacific Earthquake Engineering Research Institute is a building risk assessment that is the basis for the next generation of seismic design codes. In this method, the probability of structural failure is determined by the possible combination of hazard and vulnerability functions of structures. The result can be expressed as the probability of various economic losses. In summary, the design approach includes specifying the performance goal (e.g., the

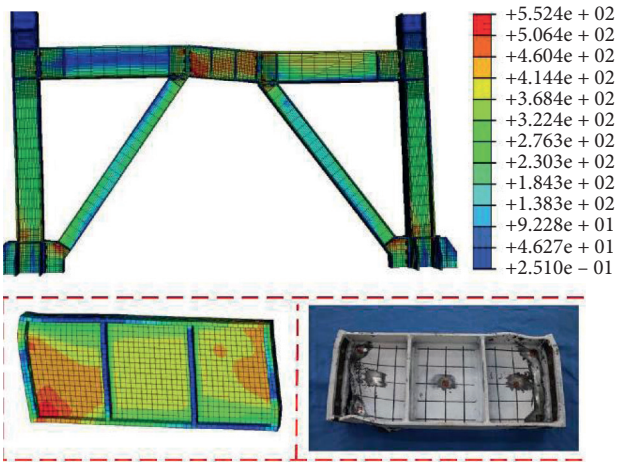

Figure 3: Simulated stress propagation in an eccentric bracing frame and its laboratory sample [6].

acceptable probability of collapse and acceptable financial losses) and associated seismic risk, obtaining engineering parameters to select the system, and finally comparing the performance goal with existing criteria [5].

Figure 4 shows the proposed PBEE framework for design based on probabilistic performance and minimizing the probability of collapse. The framework includes risk analysis, structural analysis, damage analysis, and loss analysis. But if just probability of a collapse needed, the first 2 steps can be the answer. To analyze seismic hazards, the final output is the "IM" parameter or intensity measure, which is taken from hazard curves. Various parameters can be used as intensity measures, such as the maximum ground acceleration in the record (PGA) or spectral acceleration in the first mode (SA (T1)). In the past, when talking about the capacity of the structure, the strength of the structure and related components was associated with the mind, but now the seismic design is based on the emphasis on deformation capacity and energy dissipation. In this regard, the structural response is the engineering demand criterion or EDP, which is generally expressed for a certain level of intensity criterion, and the maximum drift is between classes of its types. In other words, when we talk about the probability of collapse due to maximum ground excitations, we are talking about the probability of reaching the level of various engineering demands (such as drift), which is based on the intensity criteria corresponding to the collapse threshold in the structure. The main relation for the probabilistic expression of the components of PBEE methodology can be expressed by the probability theory of Equation (1), where λ is equal to the rate of occurrence; $G[x \mid y] = P[X > x \mid Y = y]$ means complementary to the cumulative distribution of X under the condition of Y. Data between each stage are distilled into four variables: ground motion Intensity Measure (IM), Engineering Demand Parameter (EDP), Damage Measure (DM), and one or more Decision Variables (DV):

$$\lambda(\mathrm{DV}) = \iiint G < \mathrm{DV} \mid \mathrm{DM} > \mathrm{d}G < \mathrm{DM} \mid \mathrm{EDP} > \mathrm{d}G < \mathrm{EDP} \mid \mathrm{IM} > \mathrm{d}\lambda(\mathrm{IM}). \quad (1)$$

However, if only the first two steps of the PBEE framework in equation (1) are considered, it will take the form of equation (2):

$$\lambda(\mathrm{Collapse}) = \int_{\mathrm{IM}}^{\infty} P\langle \mathrm{Collapse} \mid \mathrm{IM} = \mathrm{im}_i \rangle \mid \mathrm{d}\lambda(\mathrm{IM}). \quad (2)$$

In a study, Yaser Mozaffari and Abbas Akbarpour investigated the estimation of the behavior of structures with eccentric bracing exposed to near-field earthquakes. This study has exposed the same structures to 10 earthquakes, and the focal length of the selected earthquakes is less than 10 km. Based on the performed analyses, they have examined and compared the response of the structures, which is based on the interstory drift and have concluded that in all structures, with each increase in the length of the link beam, these drifts increase. Also, the type of link beam (vertical or horizontal) was considered adequate on the shear base of the studied models [8]. In a study of fragility curves, Bakhshi and Soltanieh developed simple concentric bracing frames for residential use. They reported that a significant number of collapses occur when the braces on the first floor fail and collapse due to the limited possibility of redistribution of forces after that, which was repeated with increasing intensity [9]. Yang et al. investigated the different arrangements of braces (x, v, I, ...). They observed that to satisfy the requirements of CSA S16 in the design of bracing frames and to have an allowable probability of collapse if concentric bracing with X arrangement is used (so that the intersection point of the braces on the bracing beam is one in between), the minimum required steel can be used. This study also concluded that although this arrangement will be the most economical type of bracing arrangement in the structure, it will have a shorter service life [10].

In 2010, Vamvatsikos and Fragiadakis used incremental dynamic analysis to estimate the sensitivity and uncertainty of seismic performance of structures; they found that ductility, negative strength, and negative resistance have high sensitivity in estimating the performance of structures [11]. Lin et al. worked on the effectiveness of braced frames by studying 6 structures with BRB and EBF systems in 6- and 20-story class systems using 20 far and near field records. In this study, they concluded that the effectiveness of the added brace depends on the height and type of ground movements. The bracing frame added in normal ground movements can reduce drift and the possibility of collapse, which is especially true in short-rise buildings. However, in near-field earthquakes, the concentration of failure in the weak floors of the structure increases, and it becomes more difficult to

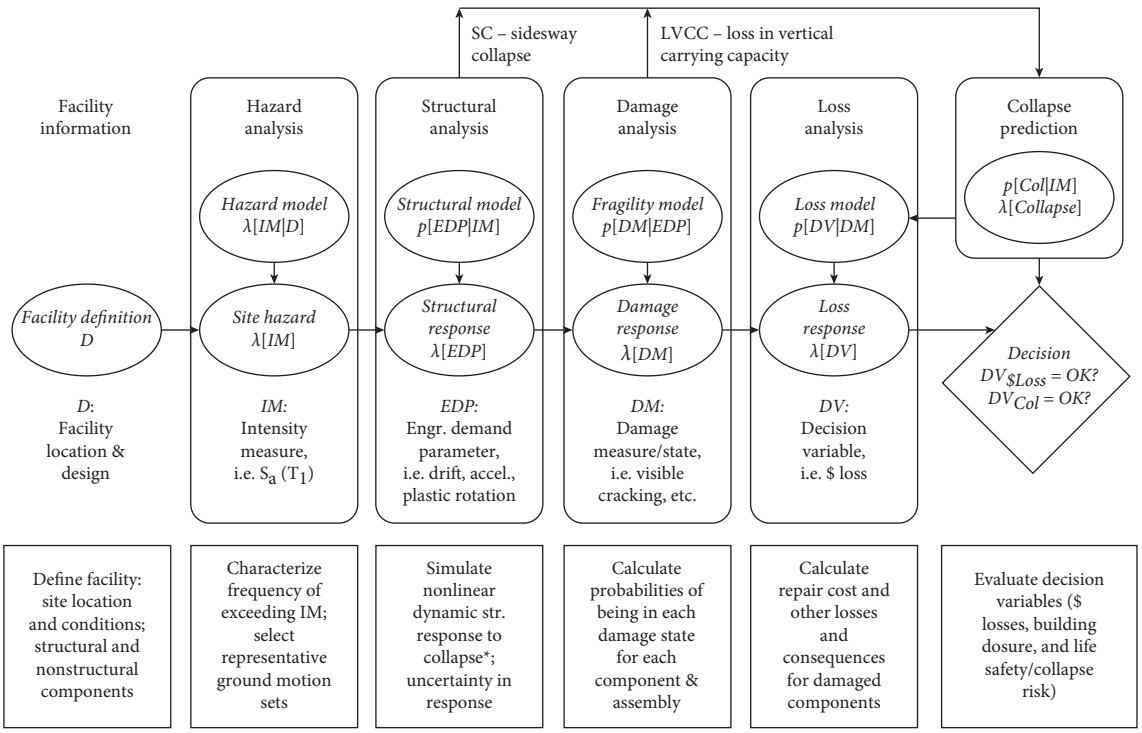

Figure 4: Provided PBEE framework for design based on probabilistic performance and minimizing the probability of collapse [7].

control the failure in the link beam or BRB braces. Therefore, only a limited amount of braced frames added can help resist ground motion near the source [12]. In the present study, to understand the effect of stiffness and ductility, a simple eccentric steel bracing system has been selected as a more ductile system and a simple concentric bracing system as a system with higher stiffness. Performance-based structures tied to the fundamentals of probability science can answer the following questions and discuss the results:

(1) Can simple structural frames that can be designed from the point of view of regulations have an acceptable probability of collapse against maximum ground excitations?

(2) Given the presence of concentric or eccentric bracing systems in simple steel frames, what will be the safety of each of these systems compared with the other?

Using these analytical methods to analyze structures against a phenomenon with completely indeterminate features can inform structural designers about the reliability of the methods of analysis of previous design regulations against earthquakes. Recently, the use of probabilistic analysis methods for the design and analysis of structures has been allowed. The methods used in this research will apply to real projects under design [13].

2. Seismic Parameters and Hazard Analysis

2.1. Engineering Demand Parameter (EDP). In this study, the maximum interstory drift ratio (MIDR) has been selected because the functional level studied was the prevention of the total collapse of the structure. The mentioned criterion has been used in most of the previous researches, and its limits have been mentioned in the newest regulations.

2.2. Seismic Intensity Measure. In selecting the IM seismic intensity measure, three criteria of practicality, efficiency (dispersion), and completeness (adequacy) are essential. One of the desirable properties of a selected IM is less dispersion. The relationship between structural response and seismic intensity measure can be written as equation (3) or (4), where SD is equal to the average response of the structure (DM) under seismic intensity (IM):

$$\mathrm{SD} = a.\mathrm{IM}^{b}, \tag{3}$$

or

$$\ln(\mathrm{SD}) = b.\ \ln(\mathrm{IM}) + \ln(a). \tag{4}$$

The efficiency criterion is measured with the scattering rate in the middle estimation of the results obtained from nonlinear dynamic analysis. An efficient intensity measure reduces the amount of change in the estimated need for an applied intensity measure. Applying an efficient intensity measure reduces the dispersions in the median estimate of the results of nonlinear dynamic analysis. In general, the smaller the scatter of IDA curves with changing seismic acceleration records, the more efficient the IM index used is than the PGA index because Sa(T1) is more efficient. For example, the dispersion of the results is less. Therefore, the

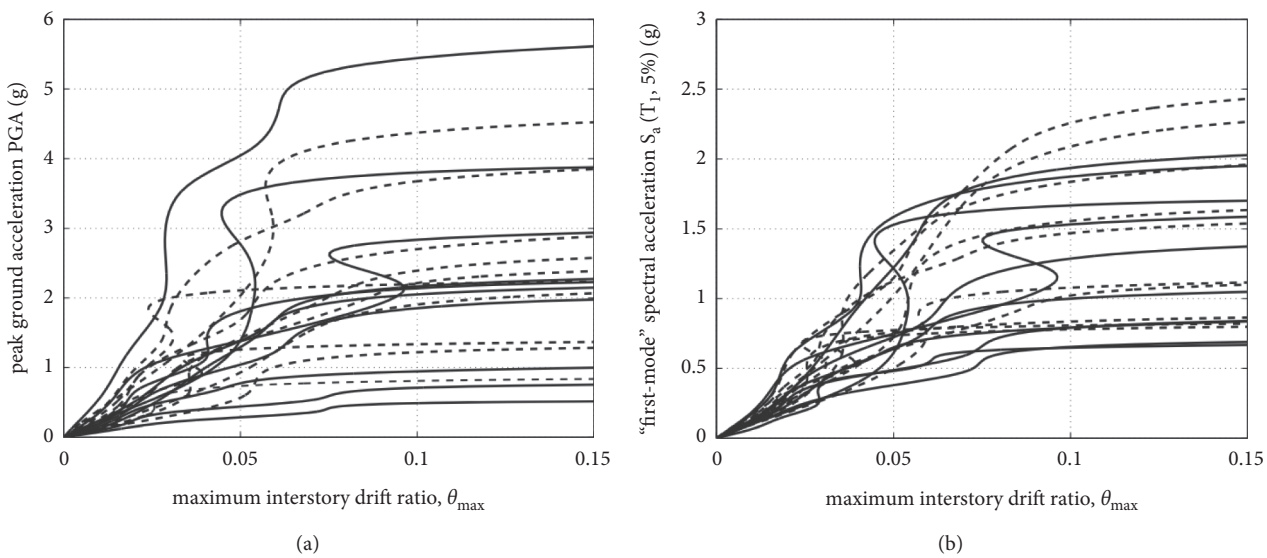

Figure 5: IDA curves for, T1 = 2.2 sec, a 9-story steel moment-resisting frame with fracturing connections plotted against (a) PGA and (b) Sa (T1, 5%) [15].

purpose of efficiency is to reduce changes in IDA curves due to record change.

Figure 5 shows the IDA cure handle of a 9-story steel structure. IDA can be used to determine IM for collapse capacity. In this case, Sa (T1) is better than PGA for this structure because the scatter of IM values with a straight line is less than the previous case (in this figure, the same vertical scales are not considered to see the graphs better, but if the scales are the same, the difference in scattering can be seen better now). Therefore, the seismic intensity parameter according to Shome [14] is spectral acceleration corresponding to the period of the first mode period for damping of 5%, so Sa (T1, 5%) is considered in this study.

2.3. Site Selection, Uniform Hazard Spectrum, and Records. The results of the Iran Seismic Hazard Analysis project, which was carried out by a research team at the University of Tehran, have been placed in the database of the Vice President for Strategic Planning and Supervision as a valid study. In the written report of the project, 3 sites with different soil information and in different parts of Tehran have been selected in terms of seismicity and their uniform hazard spectrum has been obtained [16]; if we want to assume in this study that the models under study are built on type 3 soil, the information obtained according to what was selected for site 2 in the project and with the specifications of Table 1 can be used for the next steps of probabilistic analysis. Uniform hazard spectra of 2475 and 475 years are obtained from the mentioned hazard curves (Figure 6), and the uniform hazard spectrum of 2475 years is used for the following stages of research.

2.4. Selection Ground Motion Records. Because we intend to obtain the structural response using incremental dynamic analysis, the first step in the process of evaluating the performance of drawing IDA curves is to prepare a set of seismic accelerometers so that this set indicates the seismicity of the area. Therefore, in the first step, ground motion records should be selected by almost similar conditions of the region in terms of fault mechanism, distance to the desired site, and the magnitude of the earthquake [17]. The FEMA-P695 guideline for seismic design of structures introduces two categories of near-field and far-field records, which are suitable for seismic design of structures against

Table 1: Coordinates and soil type of the selected site.

Site	Coordinates	Soil type (2800)	Soil type (NEHRP)
2	(51.42E, 35.64N)	III	D

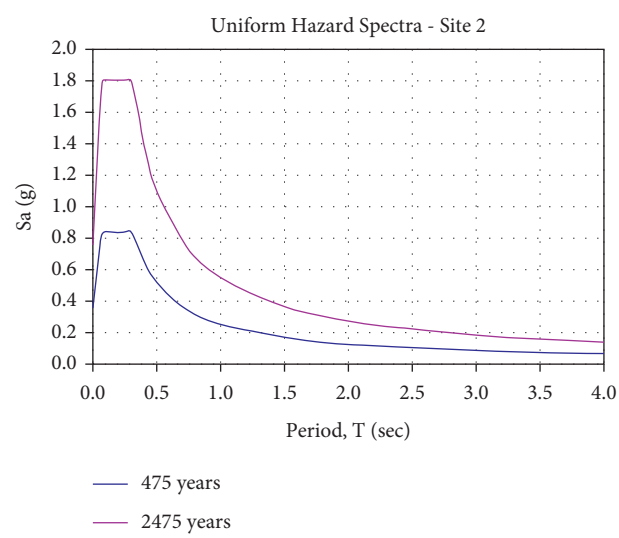

Figure 6: Uniform hazard spectrum of 475 and 2475 years of site no. 2 [16].

MCE earthquakes regardless of the scale factor. To meet the site requirements of the structures in question in the records [18], only records have been selected that had geotechnical conditions of the seismic station with site conditions such as average shear wave velocity up to 30 m depth (V_{S30}) by soil classification of Type 3 from the point view of Standard 2800. It should be noted that this standard specifies the desired speed range of 175 to 375 meters per second. According to the consideration of these conditions, a total of 16 records of far-field and 4 records of near-field without impact have been selected for nonlinear analysis (Table 2) according to the recommendation of Shome [14]. Also, to compare the difference in spectral accelerations associated with each record in each of the frames under study (due to the difference between the main period in each frame compared with the other frame), the spectral acceleration of each frame for its main period is obtained according to the equivalent seismic acceleration spectrum of each record (Table 3).

3. Modeling Frames

3.1. Generalities of Modeling Discussion. The mentioned models have a height of 3 meters on all floors, and also, according to Figure 7 the plan of structures has 6 bays in the X direction and 5 bays in the Y direction. Also, the footing of the columns is articulated, and the interaction of soil and structure has been avoided. It is assumed that each of the studied frames is a two-dimensional frame on the right side of the frames in the Y direction among the frames in the three-dimensional model of the mentioned structure (the frame in the direction of righter north-south axis in the plan of Figure 7). After designing the structural members of the 3D model according to what you will see below, the 2D frame designed while preserving the effects of the 3D structure has been used for incremental dynamic analysis. Also, the loading of structures according to the sixth article of National Regulations of Iran for dead and live load is considered to be 500 and 200 kg/m^2, respectively, which are connected linearly on the beams in proportion to their load-bearing surface; that is, 3.6 meters from the length of the load-bearing floor is distributed. In these frames, there are no irregularities in the 3D model, including irregularities in the distribution of stiffness.

According to the subject of the present study, the composite slab is one of the most widely used types of roofs in steel structures choose, which transfers its load one-way due to the placement of secondary beams. The secondary beams are of IPE160 type and are located at a distance of 50 cm from each other. Also, the thickness of the slab is considered to be 12 cm according to Article 9 of the National Building Regulations of Iran. Also, for reinforcement of slabs in both directions, rebar number 12 (diameter = 12 mm) with $Fy = 400$ MPa is distributed every 15 cm.

For easier reference to each of the systems, the XXX-X naming format is used, the first 3 letters stand for the type of structural system and the last letter indicates the number of floors. Table 4 lists the modeled frames and the abbreviation for each. Modeling of frames in OpenSees uses the concentrated plasticity approach with zero-length rotational springs at the end of each member. The middle elastic member "modelasticbem2d" with "bill material" modifies the stiffness matrix. Uniformity is achieved by changing the maximum resistance and the load resistance to the curve with dynamic cyclic loading such as an earthquake. The damping of the frames is calculated by assuming its uniform distribution in the whole frame by the Rayleigh method and assuming the damping ratio of 5% [19]. Because in this method the damping of the frame is a ratio of the stiffness and mass of the structure, it should be known that the mass of the structure is placed directly on the end nodes. The effect of P-Δ on modeling through supported columns has been considered according to the research of Krawinkler et al. [20]. The specifications of steel materials related to beams, columns, and braces also reinforced concrete used materials related to slabs are also mentioned in Table 5.

3.2. Concentric Bracing Frames. According to the tenth article of the Iran National Building Regulations in this type of lateral bearing system, the models are designed in two categories of ordinary and extraordinary ductility. In ordinary ductility, the bracing members are designed for tensile force only and with a slimming coefficient λ_{md}. So even if the braces cannot experience nonlinear behavior before buckling due to lateral load, their design is acceptable. However, in the remarkable ductility, none of the mentioned facilitators is used. The braces' compression ratio is more diminutive than λ_{hd}. Standard 2800 introduces 15 meters of the maximum allowable height due to these differences in the design of a structure frame with an ordinary concentric bracing frame. Accordingly, the ordinary concentric bracing model is made only for a 5-story frame. It is noteworthy that the structure for the study of this research will be a 2-dimensional frame taken from one of the 3D structure frames. The braces of this group of models are cross-shaped, and their arrangement in the selected plan and frame is presented in Figures 8 and 9. The sections obtained in the design by the criteria of Article 10 of the National Building Regulations of Iran and Standard 2800 for different members of concentric frames are listed in Table 6, and an example of each type of sections used is shown schematically in Figure 10.

For modeling in OpenSees software and performance analysis of frames, the buckling of compression members is proposed. In this regard, the local buckling of the members will not be a control due to the selection of all structural sections of the seismically compacted rolled type, and the global buckling of these members can be controversial. To accentuate the hysterical behavior of the frame, the rotational springs capture hysteretic flexural behavior, including deterioration through the modified Ibarra-Medina-Krawinkler (IMK) model. This modeling approach for columns can capture story mechanisms [21, 22].

In terms of the buckling behavior of braces, according to the recommendation of Urim and Mahin [23], each brace is divided into ten smaller "nonlinear fiber elements." It is made of braces and with corotational geometric

Table 2: Selected records for incremental dynamic analysis.

No.	Earthquake			Station data			
	Name	Station	Magnitude	VS_30 (m/s)	PGA (g)	Site-source distance	Field distance
1	Northridge	Beverly Hills	6.7	356	0.52	17.2	Far field
2	Northridge	Canyon country-WLC	6.7	309	0.48	12.4	Far field
3	Duzce	Turkey Bolu	7.1	326	0.82	12	Far field
4	Imperial Valley	Bonds	6.5	223	0.76	2.7	Near field
5	Imperial Valley	Delta	6.5	275	0.35	22	Far field
6	Imperial Valley	El Centro	6.5	196	0.38	12.5	Far field
7	Imperial Valley	Chihuahua	6.5	275	0.28	7.3	Near field
8	Kobe	Shin-Osaka	6.9	256	0.24	19.2	Far field
9	Kocaeli	Duzce	7.5	276	0.36	15.4	Far field
10	Northridge	Saticoy	6.7	281	0.42	12.1	Near field
11	Landers	Yermo Fire	7.3	354	0.24	23.6	Far field
12	Landers	Coolwater SCE	7.3	271	0.42	19.7	Far field
13	Loma Prieta	Capitola	6.9	289	0.53	15.2	Far field
14	Loma Prieta	Gilroy	6.9	350	0.56	12.8	Far field
15	Kocaeli, Turkey	Yarimca	7.5	297	0.31	4.8	Near field
16	Superstition Hills	El Centro	6.5	192	0.36	18.2	Far field
17	Superstition Hills	Poe Road	6.5	208	0.45	11.2	Far field
18	Cape Mendocino	Rio	7	312	0.55	14.3	Far field
19	Chi-Chi	CHY101	7.6	259	0.44	10	Far field
20	San Fernando	Hollywood Stor	6.6	316	0.21	22.8	Far field

Table 3: Spectral acceleration per response spectrum equivalent to each seismic record.

	Time periods (s)				
	OBF-5	SBF-5	SBF-10	EBF-5	EBF-10
Record no.	0.65	0.58	0.85	0.8	1.18
	Spectral accelerations per record (~g)				
	OBF-5	SBF-5	SBF-10	EBF-5	EBF-10
1	1.179	1.024	0.900	0.934	0.580
2	1.214	1.287	1.079	1.015	0.263
3	1.300	1.193	0.773	0.935	0.627
4	1.120	0.997	0.725	0.846	0.506
5	1.446	1.380	1.082	1.262	0.357
6	1.043	1.020	0.718	0.675	0.559
7	0.767	0.771	0.826	0.924	0.321
8	0.943	1.443	0.774	0.870	0.408
9	0.449	0.429	0.296	0.345	0.228
10	0.527	0.573	0.277	0.410	0.301
11	0.737	1.003	0.355	0.396	0.345
12	0.663	0.903	0.319	0.356	0.311
13	1.693	1.731	1.001	1.070	0.917
14	1.863	1.740	0.785	0.974	0.379
15	0.696	0.906	0.507	0.439	0.775
16	0.626	0.815	0.456	0.395	0.698
17	0.693	0.820	0.525	0.647	0.453
18	1.863	1.740	0.785	0.974	0.379
19	0.573	0.762	0.868	0.744	0.633
20	1.043	1.020	0.718	0.675	0.559

transformation system. At the end of each member, the zero-length rotating springs are placed following the assumptions mentioned in the other members of Sections 1–3 to consider the effects of the presence of the gusset plate in the connection zones. Figure 11 provides a similar view of the modeling method in the present study for the execution details at the connection zone of the beam and the brace to the column.

Figure 12 also schematically shows the mathematical model of the arrangement of the springs for a braced bay of the frames.

In horizontal beams with hinges, according to Hsiao [25], in addition to end rotating springs, due to the simple system type in the bracing frames of the main beam element, the "Beam with hinge" element should be used and create a "pin" at both ends of the beams. Therefore, the buckling

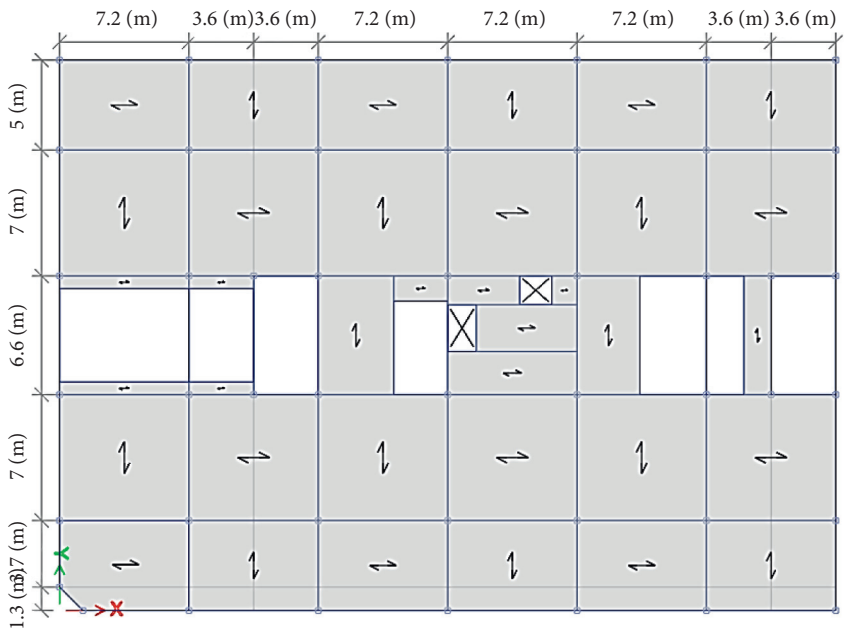

Figure 7: Plan of structures and load-bearing direction of floors.

Table 4: Naming the frames under study.

No	System	Number of floors	Symbol
1	Ordinary concentrically braced frame	5	OBF-5
2	Special concentrically braced frame	5	SBF-5
3	Special concentrically braced frame	10	SBF-10
4	Special eccentrically braced frame	5	EBF-5
5	Special eccentrically braced frame	10	EBF-10

Table 5: Specifications of steel and concrete materials used.

Steel material type ST-37	
Elasticity module, E	$2.1 * 10^7$ ton/m^3
Yield stress, F_y	24000 ton/m^2
Ult. strength, F_u	37000 ton/m^2
Weight per volume	7.85 ton/m^3
Concrete material type C-25	
Elasticity module, E	$2.5 * 10^6$ ton/m^3
Rebars yield stress, F_y	40000 ton/m^2
Transverse rebar yield stress, fys	37000 ton/m^2
Weight per volume	2.5 ton/m^3
Compressive strength	2800 ton/m^2

behavior of the braces can occur in or out of the plane. Concentric restraints are crosswise and with a connecting plate at the point of collision of the two restraints and the point of impact with the beams, the vertical and axial forces are not absorbed in the gusset plate. In this regard, the research of Astaneh-Asl et al. from the University of Michigan (1981 to 1986) showed that the cyclic behavior of brace sheets strongly depends on the buckling direction of the brace member. This means that when the bracing member buckles in-plane, three plastic hinges can form in the member, one in the middle of each member's length and one at each end of each member just outside the gusset plate. Therefore, the braces rotate at the hinge place. However, just after the gusset plate, we will have a detailed behavior due to the simplicity of the structural frame system. The brace behaves almost elastically in this type of buckling [26]. The mathematical model of the bracing frame can include the hinges at the end of the members. However, in reality, due to the connection of the gusset plate, we will not see the hinge behavior exactly at the connection. We see this exactly after the gusset plate.

3.3. Eccentric Bracing Frames

3.3.1. Frame Modeling with Eccentric Bracing. The conditions of the abutment and the arrangement of the restraints are modeled as structures with concentric restraints. The Standard 2800 for such frames only confirms remarkable ductility. Therefore, only 2 structural models have been made in such frames. The length of the beam is decided by the criteria of Article 10 of the National Building Regulations of Iran and Code 360 of the Iran Program and Budget Organization. Also, in this case, the Standard 2800 factor of performance related to the calculation of earthquake coefficient in these frames is considered one unit higher than other link beams, so in this study, to optimize sections due to seismic force reduction, the length of link beams is less than that. It is noteworthy that both the shear and flexural behavior of the beams are considered in modeling and analysis to pay attention to the responses. Figure 13 shows an overview of a 10-story frame model and a 3D model. Also, the sections obtained in the design by the criteria of Article 10 of the National Building Regulations of Iran and Standard 2800 for different members of Eccentric frames are listed in

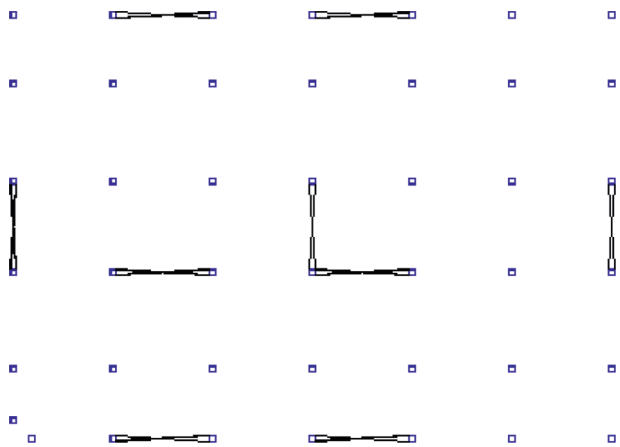

Figure 8: Arrangement of braces in the plan.

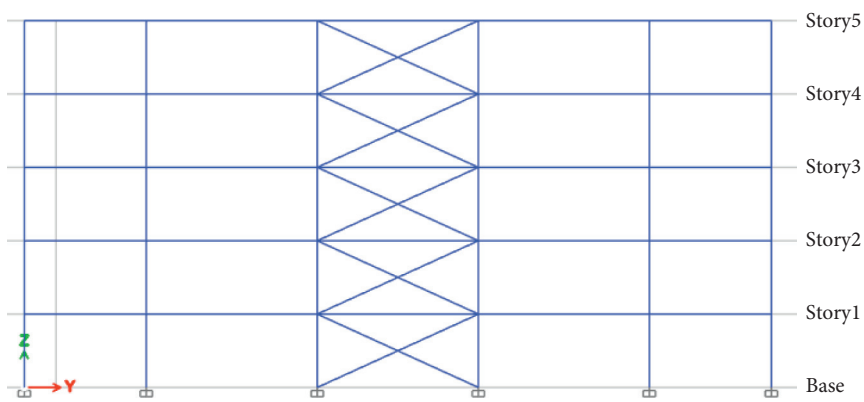

Figure 9: View of the selected two-dimensional frame.

Table 6: Sections obtained for different structural members in frames with concentric bracing.

Floor	Column	Beam	Brace
OBF-5			
1 to 5	BOX 450 ∗ 450 ∗ 20	IPE 330	TUBO 200 ∗ 200 ∗ 20
SBF-5			
1 to 5	BOX 450 ∗ 450 ∗ 30	IPE 330	TUBO 180 ∗ 180 ∗ 20
SBF-10			
1 to 5	BOX 450 ∗ 450 ∗ 25	IPE 450	TUBO 180 ∗ 180 ∗ 20
6 to 10	BOX 400 ∗ 400 ∗ 25	IPE 360	TUBO 180 ∗ 180 ∗ 20

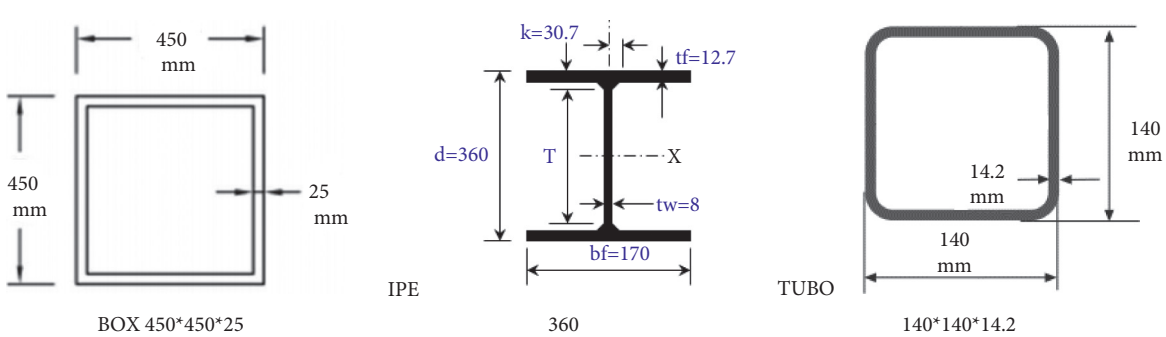

Figure 10: An example of each section type that used in concentric bracing frames.

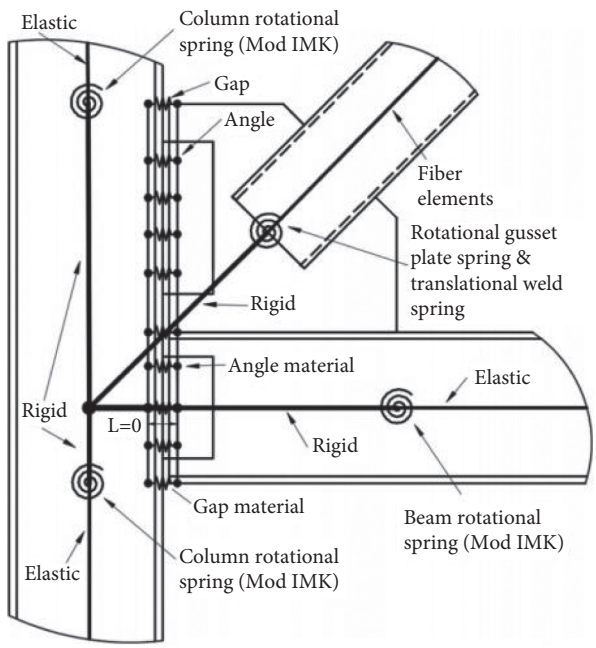

Figure 11: Numerical model schematic for connection zone of a braced frame beam-column [24].

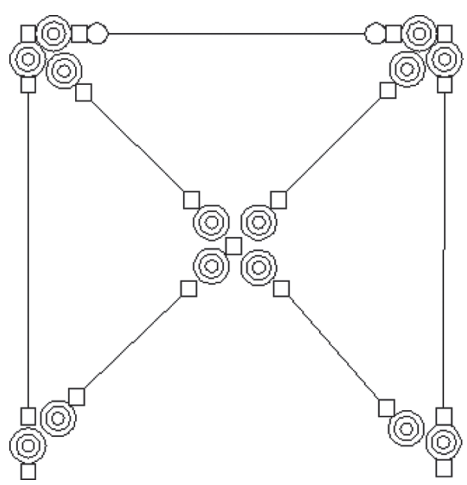

Figure 12: Mathematical model of a single bay concentric bracing frame.

Table 7, and for an example, the execution detail used for one of the link beams is shown schematically in Figure 14.

Main beams in these frames can have simple connections to the columns in cases where the link beam is located in the middle of the beam and away from the columns and connection zones [2]. Considering the mentioned effects, as mentioned by Hu et al., it is possible not to assume an interaction between shear and flexural behavior in the beam [27] because according to the classification in AISC360-16 and Code 360 of Iran, the behavior of link beams in modeled frames according to their length of 50 cm is in the category of shear behavior. It should be noted that according to Popov's research, $e = 1.6 * Mp/Vp$ is the boundary between shear and flexural behavior in these frames [3, 28]. According to Figure 15 with two rotating springs and two transfer zero-length springs at the end of the member, the mathematical model of the link beam simultaneously observes its shear behavior and flexural behavior.

According to Figure 16, modeling of other members according to their modeling in the frames of other structural systems of this research has been done with a concentrated plasticity approach.

3.3.2. Validation of Modeling Method. Shi et al. performed an experimental study on an eccentric bracing frame [29]. In this experiment, which is on a frame with geometric characteristics according to Figure 17, by pushing the frame, they drew a push curve according to Figure 18, which is used for modeling validation. In this experiment, they have for steel material $E = 210\,\mathrm{kN/mm^2}$ and $Fy = 306\,\mathrm{N/mm^2}$.

According to the experimental conditions, this frame was modeled in OpenSees and ETabs software. The push curve was drawn, which can be seen in Figure 19. In order to compare the results of the experiment by Shi et al. and the modeling performed according to the frames of this experiment, the ultimate force and displacement endured are collected (Table 8). The results show that the difference between the experimental results and the modeling in both software is less than 10%.

4. Analysis of Models

4.1. Incremental Dynamic Analysis of Frames. By selecting the first earthquake record and its first scale (one-tenth "g" (acceleration of gravity) higher in each step), the incremental dynamic analysis of the introduced frame begins to record the displacements of the frame at each story by the excitation pattern of its base and the maximum amount of interstory drift and its acceleration. The title of the representative point of this scale is recorded from each record and the frame response in other scales until the maximum class displacement reaches the mentioned limit in the drift criteria. The algorithm is repeated for each record, and IDA diagrams of each record can be drawn. The response of a structure under ground motion can be estimated with appropriate accuracy by performing a dynamic analysis of time history. One of the most important drawbacks of applying nonlinear dynamic analysis is the sensitivity of the response to selected accelerometers. The presentation of incremental dynamic analysis and estimation of responses based on the application of probabilistic relations have to a large extent be compensated for this weakness in practice. The results of IDA analysis obtained from this method along with 16,50,84% percentiles (the smaller percentiles in the chart are higher than the larger percentiles) and the probability density function (PDF) of the data are plotted in Figures 20–22, in addition to the points selected due to the reduction of stiffness to 20% of the elastic stiffness of each curve. Further examination is indicated in these curves.

4.2. Collapse Prevention Performance Level. Collapse prevention performance level refers to the performance level

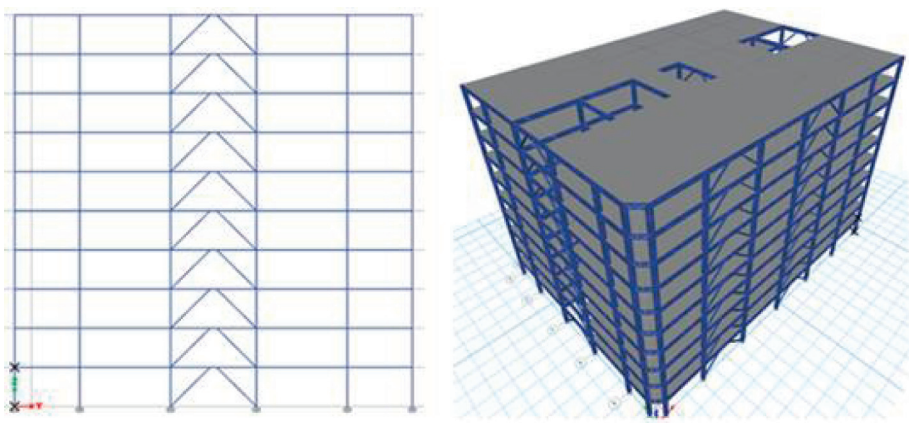

Figure 13: Overview of a simple structural frame model with an eccentric bracing system.

Table 7: Sections obtained for different structural members in frames with an eccentric bracing system.

Floor	Column	Beam	Brace	Link beam stiffner
EBF-5				
1 to 5	BOX 450 ∗ 450 ∗ 25	IPE 360	TUBO 140 ∗ 140 ∗ 14.2	7 ∗ 2PL 34 ∗ 9 ∗ 1
EBF-10				
1 to 5	BOX 450 ∗ 450 ∗ 25	IPE 500	TUBO 180 ∗ 180 ∗ 20	7 ∗ 2PL 47 ∗ 10 ∗ 1
6 to 10	BOX 400 ∗ 400 ∗ 25	IPE 450	TUBO 180 ∗ 180 ∗ 20	7 ∗ 2PL 42 ∗ 9 ∗ 1

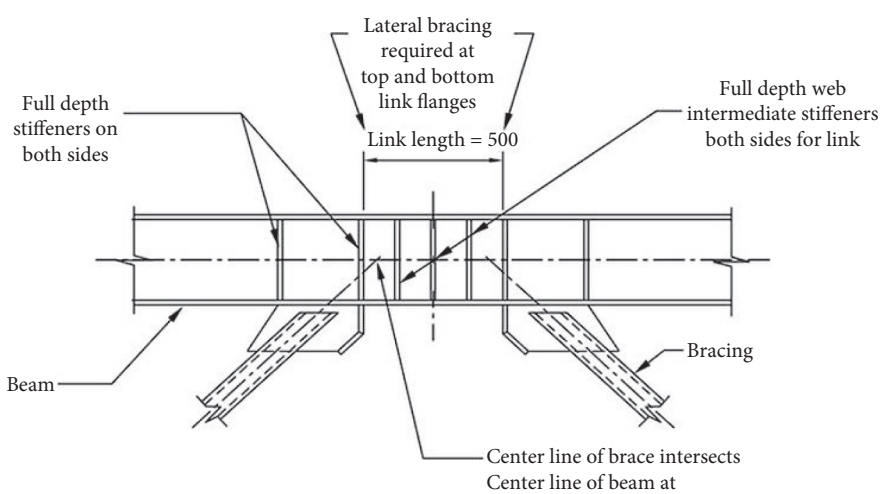

Figure 14: A schematic example of the execution detail used for one of the link beams.

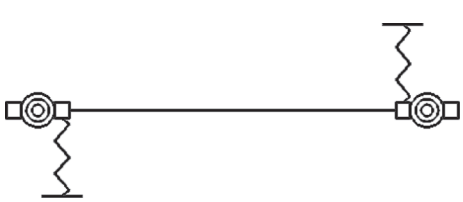

Figure 15: Schematic model of link beams in eccentric frames.

predicted to cause extensive damage to the structure due to an earthquake. However, the structure collapses and lateral losses are minimized. In this case, there is a significant reduction in stiffness and strength of the lateral force system.

In this study, FEMA-356 indicates a drift limit of 5% for frames up to 8 floors and FEMA-273 for higher frames such as 10-story bracing frames. This drift ratio is acceptable up to 4% [30]. The model is performed to the extent that if static instability occurs in the structure with decreasing degrees of uncertainty, the collapse will be probable. In other cases, the hysteresis curve of the braces in tension and pressure according to their behavior due to the possibility of buckling in modeling according to what was mentioned in the relevant section will be the criterion for calculating the displacements [25]. In conclusion, in Table 9, the limits that have been used for the drift criterion in collapse for each system in fragility analysis and the functional level of

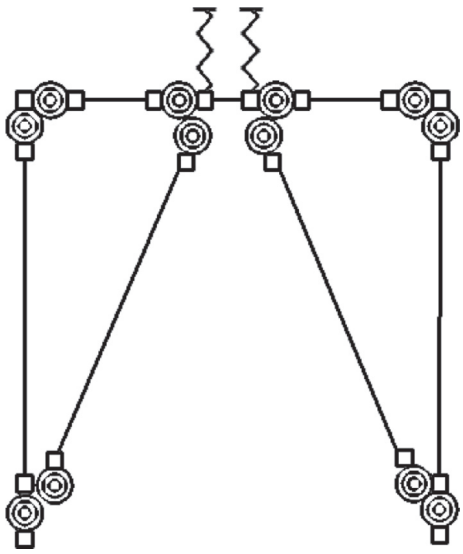

Figure 16: Analytical model of an eccentric bracing single bay frame.

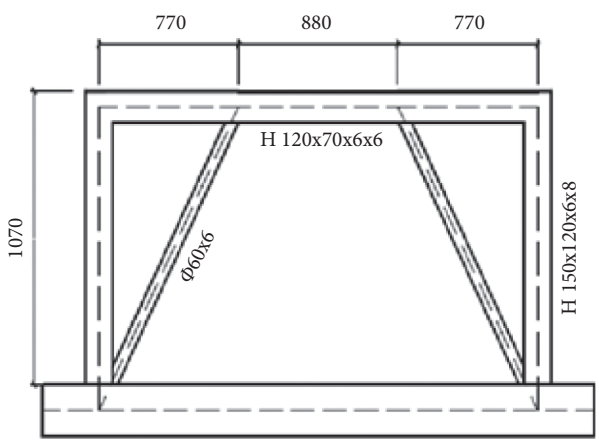

Figure 17: Geometric characteristics and sections used in the experiment by Shi et al. [29].

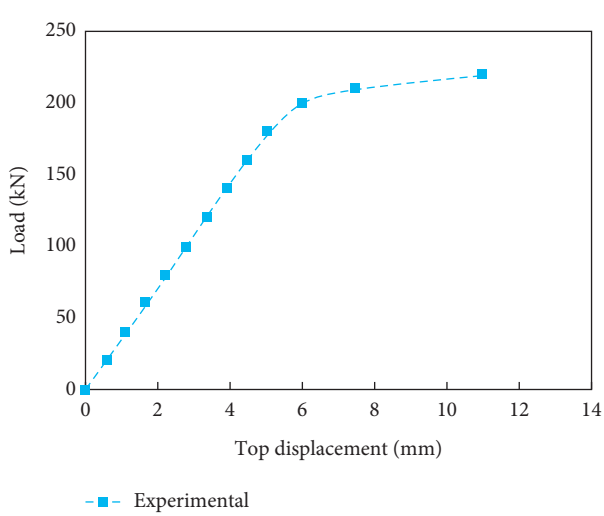

Figure 18: Frame push curve resulting from experiment [29].

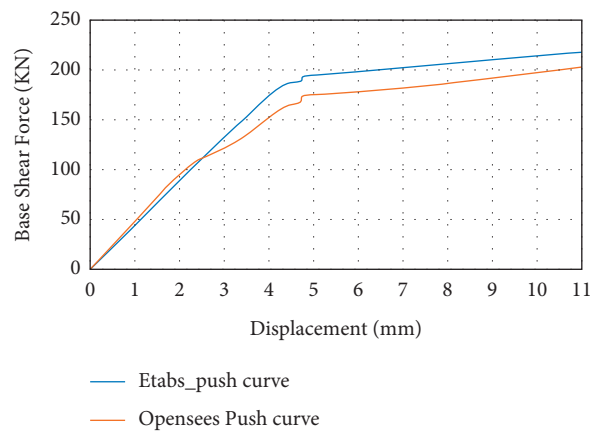

Figure 19: Results obtained from eccentric frame modeling in OpenSees and ETabs software.

collapse as the level considered for systems review in this research can be seen.

4.3. Uncertainties. To draw fragility curves and estimate the probability of collapse, we are faced with two main categories of uncertainty. Some of these uncertainties are inherent, and some are cognitive. For inherent uncertainties or record-to-record FEMA-P695, use the variance of the original data used to plot the fragility curves resulting from incremental dynamic analysis (spectral accelerations corresponding to the level of collapse threshold performance in each branch of the IDA curves in each frame) to consider this parameter. Cognitive uncertainties arise from differences in the definition of assumptions, ambiguous or unknown factors. FEMA-P695 identifies 3 parameters related to cognitive uncertainties (design, modeling, and test data) by qualitatively ranking their values. The designer must know in which category the assumptions are assumed to be excellent, good, average, or poor. In this research, the amount of 0.35 (average certainty) is assumed for these 3 parameters. Also, the final values of the uncertainty parameters, which is the 2nd root of the sum of the squares of all 4 uncertainties, are obtained for the studied models according to Table 10.

4.4. Achieving Fragility Curves. The fragility curve requires a change in the original variance of the data to be obtained from the combination of uncertainty parameters with "x" "μ" is an inversion of the natural logarithm of the middle of the data, "σ" is a variance of the data, and finally "Φ" is the Laplace integral. Using equation (5), new fragility curves can be obtained according to Figures 23–25 that gives the percent of probability of collapse against Sa (T1, 5%).

$$F(x) = \Phi\left(\frac{\ln x - \mu}{\sigma}\right). \tag{5}$$

4.5. Collapse Probability Analysis. In Sections 2 and 3, a uniform hazard spectrum was drawn for earthquakes with a

Table 8: Results of software modeling and validation by the experiment of Shi et al.

	Ultimate force (kN)	Ultimate displacement (mm)
Experiment (Shi et al.)	220	11
ETabs	219	11.32
OpenSees	207	11.92

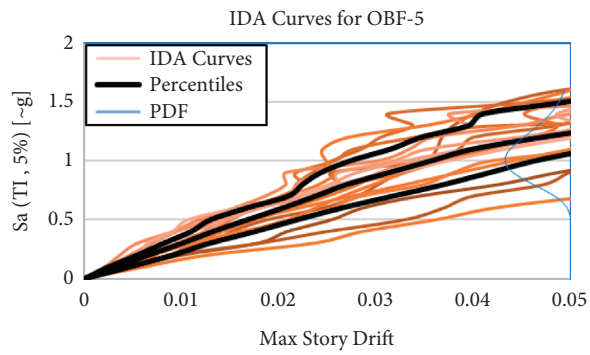

Figure 20: IDA curves obtained for OBF-5.

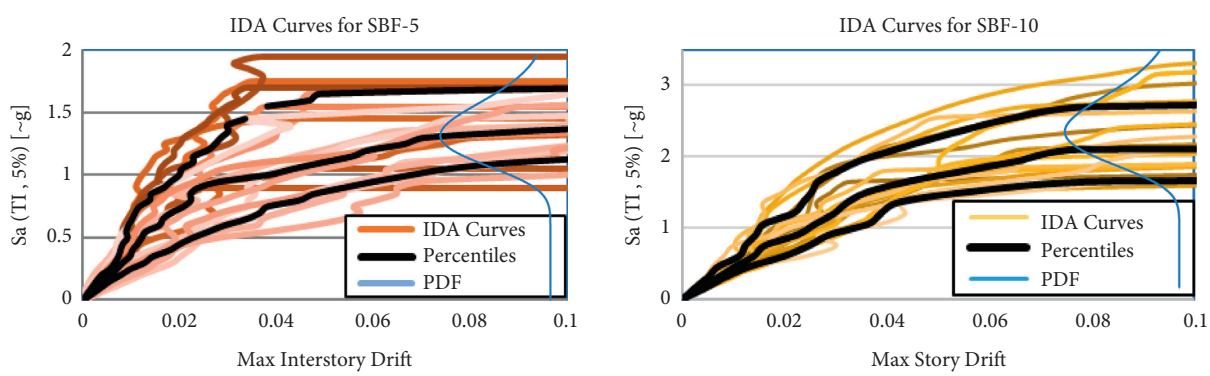

Figure 21: IDA curves obtained from right to left for SBF-10 and SBF-5, respectively.

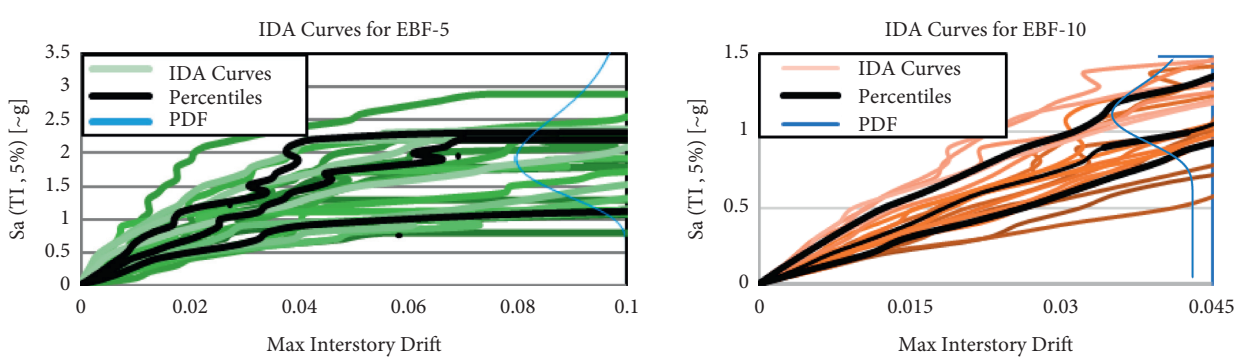

Figure 22: IDA curves obtained from right to left for EBF-5 and EBF-10.

return period of 2475 years. Based on this spectrum and the periodicity obtained for dynamic models of frames in OpenSees software, the amount of spectral acceleration can be taken from the mentioned hazard spectrum. This spectral acceleration uses fragility curves drawn for each model. The probability of their collapse can be deduced. In Table 11, the probabilities of the collapse of the studied models are obtained for the maximum ground motions.

In Table 11, once with only fragility curves in terms of record-to-record uncertainty and once with all uncertainties, the probability of collapse is obtained; in this study, the probabilities of collapse are obtained in the case of more

Table 9: Drift limit of collapse prevention for various structural systems.

No.	Frame	Limit	Ref.
1	OBF-5	0.05	FEMA-356
2	SCBF-5	0.05	FEMA-356
3	EBF-5	0.05	FEMA-356
4	SCBF-10	0.04	FEMA-273
5	EBF-10	0.04	FEMA-273

Table 10: Uncertainty parameters and their combination results.

Frame	Mean	Record to record	Design	Modeling	Test data	Total
OBF-5	0.53	0.21	0.35	0.35	0.35	0.64
SCBF-5	0.33	0.19	0.35	0.35	0.35	0.64
EBF-5	0.58	0.32	0.35	0.35	0.35	0.69
SCBF-10	0.85	0.22	0.35	0.35	0.35	0.64
EBF-10	0.56	0.17	0.35	0.35	0.35	0.63

uncertainty. We have, in all cases, been more in terms of uncertainty due to changes in fragility curves in the acceleration of the spectra. In addition, the acceptable limit for this type of analysis is the probability of total collapse of structures of similar importance to residential buildings is 10% (Table 11); the results show a deviation from this acceptable limit in the SBF-5 and OBF-5, which can be a warning for the design regulations of steel structures in the field of such structures. This is because in the design of structural models of this study, all the necessary controls in National Building Regulations of Iran and Standard 2800 have been observed.

5-story models with concentric bracing, whether extraordinary or ordinary ductility, as previously mentioned, could not be within the acceptable range in terms of the probability of collapse in both systems; in addition, for the fragility curves of EBF systems, the surface under the chart is higher, the periodicities of concentric bracing frames are generally shorter, and due to the uniform hazard spectrum, they have highest spectral acceleration, which makes it a higher probability of collapse for concentric bracing frames. So we can sometimes see that such designed structures with conventional codes are not within acceptable limits. It is also observed between different structural systems that if a more ductile type is used (for example, a particular concentric bracing frame instead of an ordinary concentric bracing frame), the probability of collapse will decrease.

Comparing the designed 10-story models, the results show that for 10-story frames, special concentric bracing and eccentric bracing have acceptable seismic safety. Even the acceptable range shows that one of the essential points in choosing a structural system is to pay attention to their performance due to changes in mass and stiffness due to changes in height and number of floors. It can also be said that special concentric bracing frames and unique eccentric bracing frames in the 10-story elevation system are safe against collapse. Table 12 shows the probability of collapse for significant buildings such as hospitals and national museums.

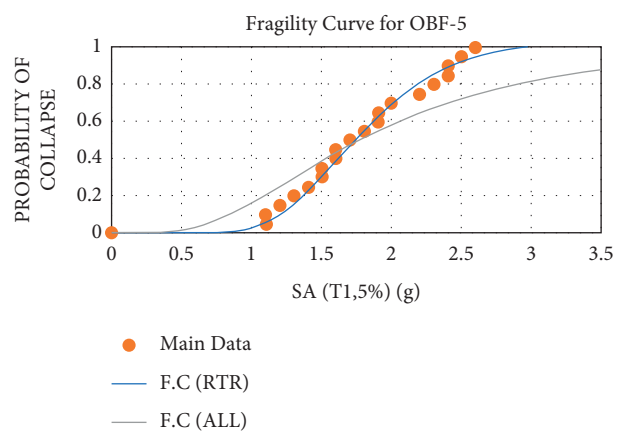

Figure 23: Fragility curves of OBF-5 frame with all uncertainties.

5. Summary and Conclusion

In this research, 5 steel is used for structural frames in different structural systems heights such as simple construction frames. These frames were then evaluated for probabilities at the performance level of collapse prevention. The results obtained, although not used in general to all structures, but in the field of this research include the following:

(i) Considering that the frames studied in this research are designed based on the codes of National Building Regulations and Standard 2800, which are the common structure design regulations in Iran, and considering that 2 frames with bracing including SBF-5 and OBF-5, the probability of collapse was higher than acceptable. That means these codes need revision.

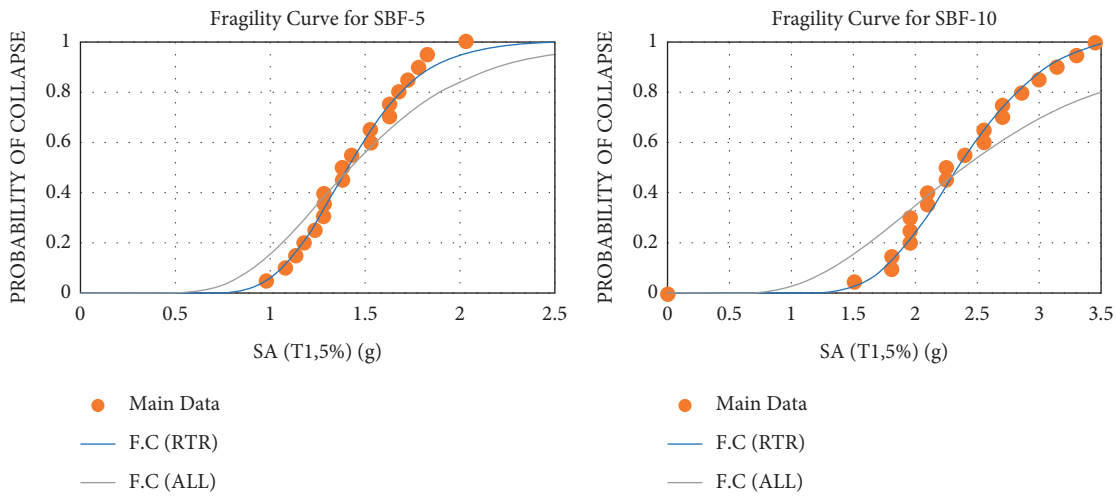

Figure 24: Fragility curves of SBF-5 and SBF-10 frames with all uncertainties.

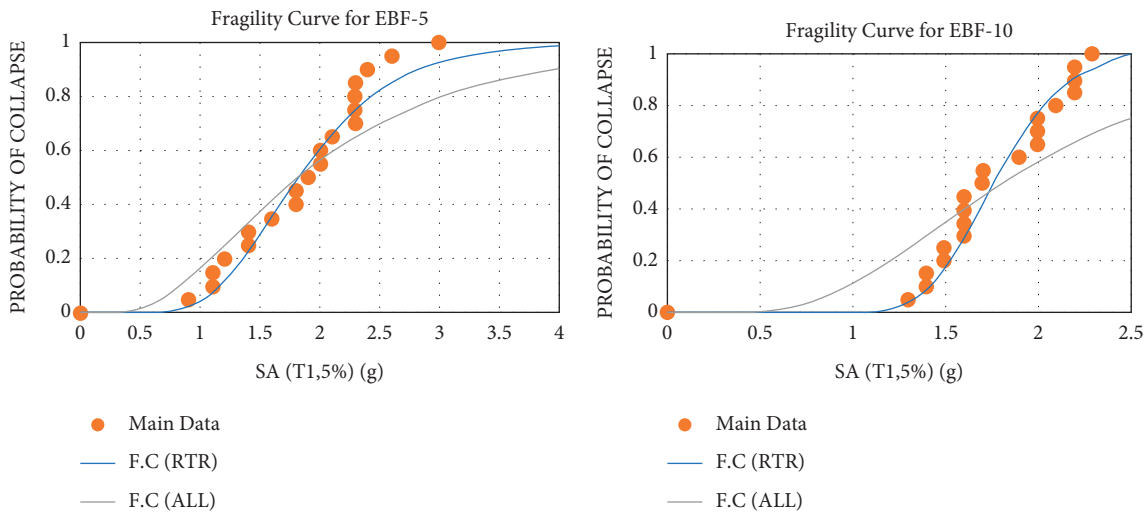

Figure 25: Fragility curves of EBF-5 and EBF-10 frames with all uncertainties.

Table 11: Probability of collapse of structural frames.

Frame	Spectrum		Collapse probability	
	Period (s)	Acceleration	RTR	ALL
SBF-5	0.587	1.07	0.04	0.14
SBF-10	0.848	0.74	0.0001	0.01
OBF-5	0.65	0.97	0.02	0.15
EBF-5	0.842	0.75	0.005	0.07
EBF-10	1.179	0.53	0.003	0.015

Table 12: Probability of collapse for important members in structural stability and noncritical members [13].

Target reliability (conditional probability of failure) by the MCE_r shaking hazard (%)		
Risk category	For structural stability	For noncritical members
I, II	10	25
III	5	15
IV	2.5	9

(ii) Increasing ductility in systems (such as using unique frames instead of ordinary frames) could reduce the probability of collapse.

(iii) One of the essential points in choosing a structural system is to pay attention to their performance due to changes in mass and stiffness due to changes in height or number of floors. For example, among 5-story frames, only the EBF-5 frame is within the acceptable

probability of collapse. However, in 10-story frames, both the SBF system and the EBF system were able to have an acceptable probability of collapse. For 10-story frames, the probability of collapse in both systems can be used instead of residential use for more important use, such as hospitals.

Data Availability

The data used to support the findings of this study are included within the article.

Conflicts of Interest

The authors declare no conflicts of interest.

References

[1] I. Mhud, *National Building Code, Part 10, Steel Structure Design*, Ministry of Housing and Urban Development, Tehran, Iran, 2009.

[2] F. Naeim, *The Seismic Design Handbook*, Springer Science & Business Media, Springer, Berlin, 1989.

[3] E. P. Popov and M. D. Engelhardt, "Seismic eccentrically braced frames," *Journal of Constructional Steel Research*, vol. 10, pp. 321–354, 1988.

[4] S. D. Hague, "Eccentrically braced steel frames as a seismic force resisting system," Master's thesis, Kansas State University, Manhattan, KN, USA, 2013.

[5] N. Ghorbani and A. Korzeniowski, "Adaptive risk hedging for call options under cox-ingersoll-ross interest rates," *Journal of Mathematical Finance*, vol. 10, no. 4, pp. 697–704, 2020.

[6] Q. Shi, S. Yan, X. Wang, H. Sun, and Y. Zhao, "Seismic behavior of the removable links in eccentrically braced frames with semirigid connections," *Advances in Civil Engineering*, vol. 2020, Article ID 9405107, 26 pages, 2020.

[7] G. G. Deierlein and C. B. Haselton, "Developing consensus provisions to evaluate collapse of reinforced concrete buildings," in *Proceedings of the US-Japan DaiDaiToku/NEES Workshop on Seismic Response of Reinforced Concrete Structures*, pp. 7-8, Tokyo, Japan, 2005.

[8] J. Yaser Mozaffari and N. Abbas Akbarpour, "Assessing behavior of structural due to near-field earthquake," *International Journal of Civil Engineering and Building Materials*, vol. 2, no. 2, 2012.

[9] A. Bakhshi and H. Soltanieh, "Development of fragility curves for existing residential steel buildings with concentrically braced frames," *Scientia Iranica*, vol. 26, no. 4, pp. 2212–2228, 2019.

[10] T. Y. Yang, H. Sheikh, and L. Tobber, "Influence of the brace configurations on the seismic performance of steel concentrically braced frames," *Frontiers in Built Environment*, vol. 5, p. 27, 2019.

[11] D. Vamvatsikos and M. Fragiadakis, "Incremental dynamic analysis for estimating seismic performance sensitivity and uncertainty," *Earthquake Engineering & Structural Dynamics*, vol. 39, no. 2, pp. 141–163, 2010.

[12] K.-C. Lin, C.-C. J. Lin, J.-Y. Chen, and H.-Y. Chang, "Seismic reliability of steel framed buildings," *Structural Safety*, vol. 32, no. 3, pp. 174–182, 2010, þ.

[13] Asce 7-10, *Minimum Design Loads for Buildings and Other Structures*, American Society of Civil Engineering (ASCE), Reston, VA, USA, 2010.

[14] N. Shome, *Probabilistic seismic demand analysis of nonlinear structures*, Stanford University, Phd thesis, 1999.

[15] D. Vamvatsikos and C. Allin Cornell, *Seismic performance, capacity and reliability of structures as seen through incremental dynamic analysis*, Stanford University, Phd thesis, 2002.

[16] Y. Bozorgnia, M. Rahnama, and M. Berberian, "Probabilistic seismic hazard analysis, phase I–greater Tehran regions," Final report, Faculty of Engineering, University of Tehran, Tehran, Iran, 2008.

[17] A. Azarbakht and M. Dolšek, "Progressive incremental dynamic analysis for first-mode dominated structures," *Journal of Structural Engineering*, vol. 137, no. 3, pp. 445–455, 2011.

[18] X. Zhao, W. D. Zhu, and Y. H. Li, "Analytical solutions of nonlocal coupled thermoelastic forced vibrations of micro-/nano-beams by means of green's functions," *Journal of Sound and Vibration*, vol. 481, Article ID 115407, 2020.

[19] Federal Emergency Management Agency, "Engineering guideline for incremental seismic rehabilitation," Report No. FEMA-P420, Federal Emergency Management Agency, Washington, DC, USA, 2009.

[20] H. Krawinkler, F. Zareian, D. G. Lignos, and L. F. Ibarra, "Prediction of collapse of structures under earthquake excitations," in *Proceedings of the 2nd International Conference on Computational Methods in Structural Dynamics and Earthquake Engineering*, pp. 22–24, Rhodes, Greece, June 2009.

[21] H. Huang, M. Huang, W. Zhang, and S. Yang, "Experimental study of predamaged columns strengthened by HPFL and BSP under combined load cases," *Structure and infrastructure engineering*, vol. 17, no. 9, pp. 1210–1227, 2020.

[22] D. G. Lignos and H. Krawinkler, "Sidesway collapse of deteriorating structural systems under seismic excitations," Rep. No. TB 172, John A. Blume Earthquake Engineering Center, Stanford, CA, USA, 2009.

[23] P. Uriz and S. Mahin, "Toward earthquake resistant design of concentrically braced steel frame structures," PEER Report 2008/08, University of California, Oakland, CA, USA, 2008.

[24] J. Sizemore, *Inelastic behavior and seismic collapse prevention performance of low-ductility steel braced frames*, Ph.D. dissertation, Dept. of Civil and Environmental Engineering, Univ. of Illinois at Urbana-Champaign, Urbana-Champaign, IL, USA, 2017.

[25] P.-C. Hsiao, *Seismic performance evaluation of concentrically braced frames*, University of Washington, Seattle, WA, USA, PhD diss, 2012.

[26] A. Astaneh-Asl, S. C. Goel, and R. D. Hanson, "Cyclic out-of-plane buckling of double-angle bracing," *Journal of Structural Engineering*, vol. 111, pp. 1135–1153, 1985, þ.

[27] S. Hu, Z. Wang, and Z. Wang, "Practical advanced analysis for eccentrically braced frames," *Advanced Steel Construction*, vol. 11, no. 1, pp. 95–110, 2015.

[28] Z. Alam, L. Sun, C. Zhang, Z. Su, and B. Samali, "Experimental and numerical investigation on the complex behaviour of the localised seismic response in a multi-storey plan-asymmetric structure," *Structure and infrastructure engineering*, vol. 17, no. 1, pp. 86–102, 2020.

[29] Y. J. Shi, J. Xiong, Y. Q. Wang, and G. Liu, "Experimental studies on seismic performance of multi-storey steel frame with eccentric brace," *Journal of Building Structures*, vol. 31, no. 2, pp. 29–34, 2010.

[30] Federal Emergency Management Agency, "NEHRP guidelines for the seismic rehabilitation of buildings," Report No. FEMA-273,, Federal Emergency Management Agency, Washington, DC, USA, 1997.

Hindawi
Shock and Vibration
Volume 2021, Article ID 6971178, 10 pages
https://doi.org/10.1155/2021/6971178

Research Article

A New Radial Spoiler for Suppressing Vortex-Induced Vibration of a Tubular Tower and Its Practical Design Method

Xing Fu,[1,2] Yao Jiang,[1] Wen-Long Du,[1] and Bo-Wen Yan[2,3]

[1]*State Key Laboratory of Coastal and Offshore Engineering, Dalian University of Technology, Dalian 116023, China*
[2]*Key Laboratory of New Technology for Construction of Cities in Mountain Area, Ministry of Education, Chongqing University, Chongqing 400045, China*
[3]*Chongqing Key Laboratory of Wind Engineering and Wind Energy Utilization, School of Civil Engineering, Chongqing University, Chongqing 400045, China*

Correspondence should be addressed to Bo-Wen Yan; bowenyancq@cqu.edu.cn

Received 28 July 2021; Accepted 31 August 2021; Published 27 September 2021

Academic Editor: Bing Qu

Circular section tubular members with smaller wind load shape coefficient and higher stability are widely used in ultra-high-voltage (UHV) transmission towers. However, the tubular members, especially those with a large slenderness ratio, are prone to vortex-induced vibration (VIV) within a specific wind speed range. The sustained vibration of members can easily cause fatigue failure of joints and threaten the operational safety of transmission lines. Consequently, a novel countermeasure for the VIV of tubular towers using a new type of radial spoiler is proposed, whose mechanism is to change the vortex shedding frequency by destroying the large-scale vortexes into small-scale vortexes. Then, the parametric analysis of different variables is carried out based on the orthogonal experiment and numerical simulation, including the height H and length B of the spoiler and the distance S between adjacent spoilers. The results show that the above three parameters all have significant influences on vortex shedding frequency. Additionally, a practical design method of the new radial spoiler is proposed, and the recommended values of H, B, and S are $1D$~$2D$, $1.5H$~$3H$, and $5D$~$12.5D$, respectively, where D is the diameter of the tubular member. Finally, a numerical verification of the suppression effects is carried out, demonstrating that the proposed quick design method is simple and reliable, which can be widely used in the VIV design of tubular towers.

1. Introduction

The ultra-high-voltage (UHV) transmission project has the advantages of long transmission distance, large transmission capacity, and low power loss [1, 2], which dramatically drives technological innovation. Tubular members can increase the bearing capacity and reduce the weight of tower. Therefore, tubular towers are widely used in UHV transmission lines [3, 4].

Nevertheless, the wind will produce shedding vortexes on the leeward side of tubular members alternately within a specific wind speed range [5]. When the shedding frequency of the vortexes is close to the natural frequency of tubular members, the vortex-induced vibration (VIV) occurs, usually accompanied by larger amplitude vibrations. Long-term repetitive vibration may cause the looseness of bolts and the fatigue failure of welds [6], which will affect the operational safety of transmission lines. Consequently, for tubular towers, the prevention and control of the VIV are essential.

The control methods of the VIV are mainly divided into two categories: active control and passive control. The former applies the external forces on the structure automatically through a real-time monitoring system, while the latter adjusts the vortex shedding frequency [7] by altering the aerodynamic shape of the structure. The purpose of both is to interfere with the flow field. Passive control is widely used in practice due to its simple principle and treatment compared with active control. Zdravkovich [8] divided the passive controls into three categories: (1) surface protrusions (helical strakes, fins, etc.); (2) shrouds (perforated shells,

axial rods, etc.); (3) near-wake stabilizers (guiding plates, vanes, etc.), which open the minds for future research. Stansby et al. [9] introduced a spoiler design suitable for the marine environment, whose effectiveness was verified through a model test. Chen et al. [10] found that, for a flexible riser, a positive VIV suppression effect can be achieved by installing the helical strakes with a reasonable geometrical configuration. Larsen et al. [11] found that the VIV of bridges can be significantly suppressed by the guide plate, and guide vane arrangements are proved to be equally efficient for other shallow box girders with the correct installation method.

Currently, VIV countermeasures are mainly concentrated on ocean and bridge engineering, ignoring electric power engineering, especially the tubular transmission towers. For tubular towers, stiffening cables are usually used to suppress the VIV via reducing the deformation and the slenderness ratio of tubular members; two ends are fixed on the main members and the tubular members, respectively. However, this method has not yet been employed widely due to the need for connection plates reserved on the main members. Consequently, Jingbo et al. [12] proposed a parameter design method of the antivibration hammer to suppress the VIV of tubular members, which has a positive effect. However, its application is restricted due to the lack of a mature algorithm for the damping of steel strand current.

Based on previous studies, a new type of radial spoiler is proposed to suppress the VIV of tubular towers. Then, the parameters of the spoiler are analyzed, and a design method is given based on numerical simulation and orthogonal experiment. Finally, two cases are taken to verify the applicability of the design method.

2. A New Radial Spoiler for the VIV Control

2.1. Detailed Description. In this section, a new type of radial spoiler (after this referred to as "spoiler" for convenience) based on the passive control method is proposed. A spoiler comprises two half steel pipes (the steel type is Q345, with the elastic modulus of 206 GPa and the yield strength of 345 MPa) connected by high-strength bolts. Three same steel plates, with a width of H, a length of B, and a thickness of 3 mm, are welded on each half steel pipe at equal intervals. The distance between the adjacent spoilers is S. Rubber gaskets are arranged between the tubular members and spoilers to increase the contact area and avoid loosening. The specific design is shown in Figure 1.

2.2. Case Verification and Suppression Mechanism. To reveal the suppression mechanism of the proposed method, the VIV of a tubular member is simulated. A member with a large slenderness ratio is selected, with an outer diameter D of 159 mm, an inner diameter d of 151 mm, a length L of 8320 mm, and a mass $\overline{m}$ of 15.26 kg/m, which is more prone to the VIV. The connection style of the joint is shown in Figure 2, and the x-axis and y-axis are the strong transverse direction and weak transverse direction, respectively.

Some related research illustrates that the response of strong transverse direction can be ignored when the VIV occurs in the members whose joints are connected by the style shown in Figure 2 [13]. Accordingly, only the response of weak transverse direction is considered. The vibration in the weak transverse direction can be simplified as a continuous beam hinged at both ends; hence, the natural circle frequency $\omega_n = \pi^2/L^2\sqrt{EI/\overline{m}}$; i.e., the natural frequency $f_n = \omega_n/2\pi$. The wind speed U corresponding to the VIV can be obtained from

$$U = \frac{f_s D}{St}, \tag{1}$$

where f_s is vortex shedding frequency and St is the Strouhal number, equaling 0.21 in the subcritical region [14]. When the VIV occurs, $f_s = f_n$, $U = 6.3 \times 0.159/0.2 \approx 5$ m/s.

To accurately simulate the vortex-induced force of wind field acting on the tubular member, the calculation domain and the mesh are set up accurately, as shown in Figure 3. The calculation domain is set as $28\ D \times 16\ D \times L$; the distance between the tubular member and inlet, outlet, upper, and lower is $8D$, $20D$, $8D$, and $8D$, respectively, while the influence of blocking rate can be ignored [15]. The boundary conditions are velocity inlet and pressure outlet; the upper, lower, left, and right boundary conditions are symmetrical. The surface boundary condition of the tubular member is slip wall.

Previous researches had shown that the spanwise grid height needs to be less than $0.0065D$ to capture more accurate simulation results for the flow around a three-dimensional cylinder [16]. Thus, the spanwise grid height is set as $0.006D$ in this paper. The selected turbulence model is large-eddy simulation (LES) technique, which is more precise than the Reynolds-average Navier-Stokes (RANS) technique in three-dimensional simulation [17]. PISO algorithm is used to solve the coupling problem of pressure and velocity, and the least-squares cell-based method is applied for gradient interpolation. The second-order implicit scheme is employed for transient scheme, and the second-order scheme is used for pressure difference and momentum difference. The height of the first mesh layer is set as 3.79×10^{-5} m to satisfy the condition that the nondimensional wall distance y^+ is less than 1 [18], and the iteration time step is 2×10^{-4} s.

Figure 4 displays the time history of the lift coefficient C_l, where C_l is defined as $C_l = F_l/0.5\rho_a U^2 D$, F_l is lift force, and ρ_a is air density. It can be noticed that the lift coefficient oscillates periodically and the amplitude has obvious three-dimensional pulsation characteristics, which is due to the influence of spanwise spatial characteristics of flow field. The vortex shedding frequency f_s can be obtained from the power spectral density (PSD) curve of the lift coefficient, as shown in Figure 5. At that point, $f_s = f_n = 6.3$ Hz, which is close to the member's natural frequency, and the structural resonance occurs under the action of VIV.

Table 1 compares the simulation results and the results obtained from Norberg's wind tunnel test [19].

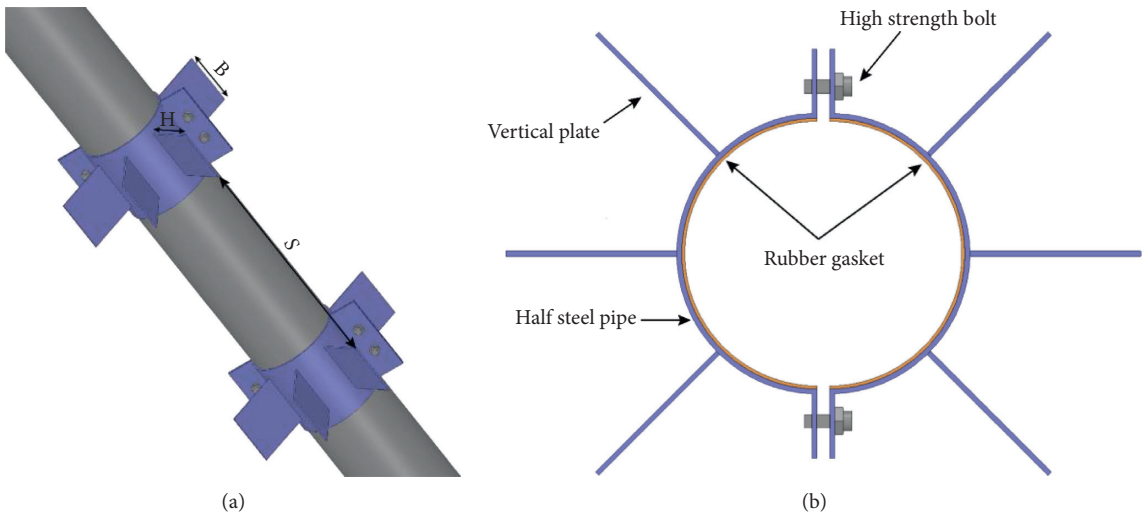

Figure 1: The design scheme of the new spoiler. (a) Basic parameters. (b) Geometric details of the spoilers.

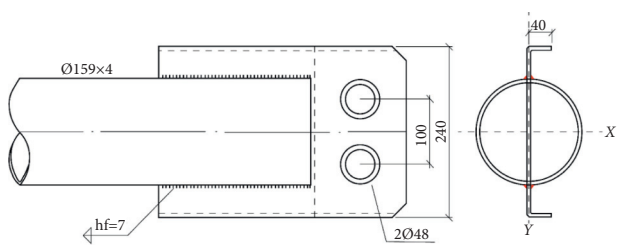

Figure 2: The connection style of the joint.

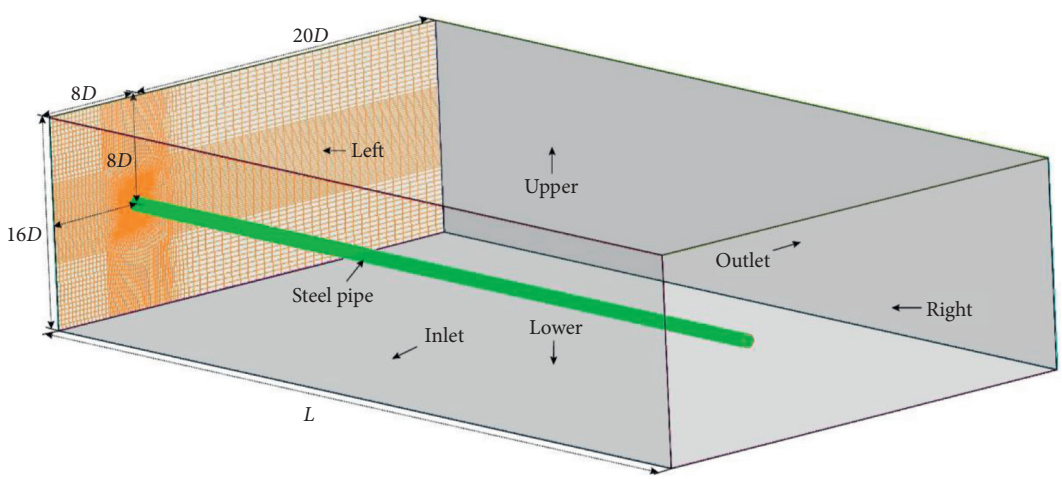

Figure 3: The computational domain and mesh generation.

The Reynolds number of this experiment was about 25000. Compared with the data of Norberg's wind tunnel under this Reynolds number, it is found that the average drag coefficient $\overline{C}_d$, Strouhal number St, and the root mean square of the lift coefficient RMS_{Cl} are very close, which indicates the reliability of numerical simulation results. Consequently, grid independence verification will not be carried out in the following research.

To reveal the suppression mechanism of the spoiler, two spoilers are installed on the member for numerical simulation. The parameters are as follows: $H = 100$ mm, $B = 300$ mm, and $S = 800$ mm. The calculation model is shown in Figure 6. The corresponding time history and PSD of the lift coefficient are shown in Figures 7 and 8, respectively. It can be seen that the lift coefficient amplitude decreases obviously with the spoilers installed, and f_s

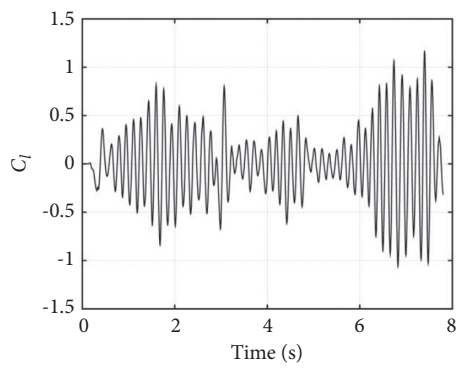

Figure 4: Time history of lift coefficient.

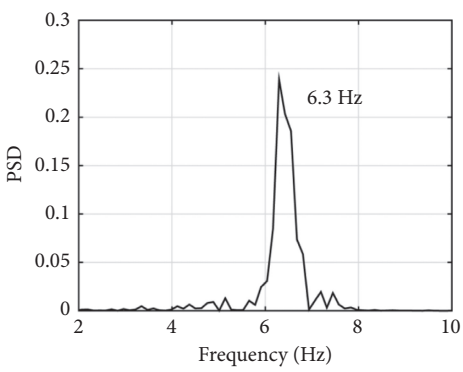

Figure 5: PSD of lift coefficient.

Table 1: Comparison of experimental and numerical results.

Method	$\overline{C}_d$	St	RMS_{Cl}
Numerical simulation	1.17	0.19	0.47
Norberg's test	1.19	0.19	0.49
Relative error	1.7%	0.0%	4.1%

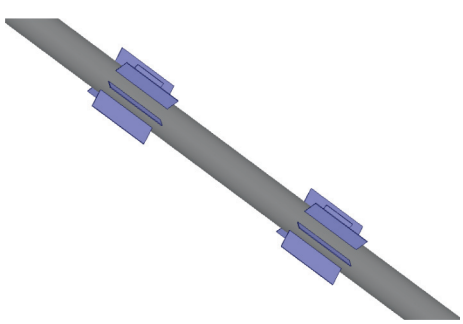

Figure 6: The calculation model with two spoilers.

decreases from 6.3 Hz to 1.15 Hz, which avoids resonance by making the vortex shedding frequency away from the member's natural frequency. The VIV is suppressed, indicating the availability of the spoilers.

Figure 9 reveals the contour of vortex cores with the spoilers. The spoilers destroy the large-scale vortexes into small-scale vortexes, which weaken the intensity of vortexes and reduce the fluid forces, and this is the primary suppression mechanism of the spoiler toward the VIV.

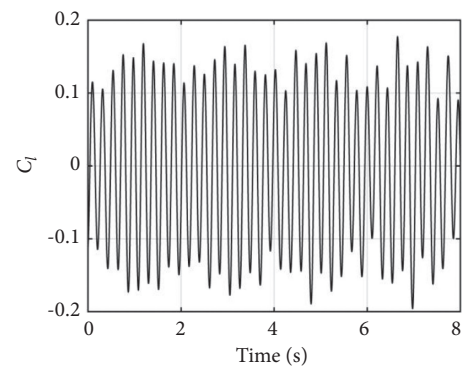

Figure 7: Time history of lift coefficient (with spoilers).

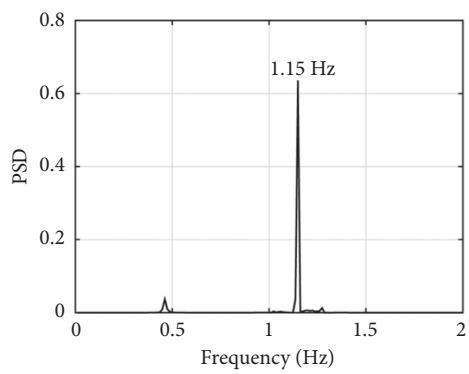

Figure 8: PSD of lift coefficient (with spoilers).

3. Parametric Analysis

In Technical Regulations of the Design of Steel Tubular Towers of Overhead Transmission Lines (DL/T5254-2010) [20], the VIV can be limited by reducing the slenderness ratio to increase the first-order vibration critical wind speed of tubular members, but this method will increase the weight of the tower prominently. Therefore, some members are still selected with a large slenderness ratio in the practical design. Thus, VIV still occurs under certain conditions. Based on a wind tunnel test, Jing-Bo et al. [21] pointed out that the VIV can be restrained by installing some axially distributed short ribs on the surface of steel tubes, or replacing circular cross section steel tubes with multi-ribbed steel tubes. However, only conceptual design cannot meet practical engineering needs.

The spoiler for VIV suppression proposed in this paper has a good effect with the advantages of easy installation, simple processing, and convenient transportation. The parametric analysis of H, B, and S of the spoiler is carried out next to provide a design method for the prevention of the VIV of tubular towers.

3.1. Orthogonal Experiment. Orthogonal experimental design is a method to study multiple factors and multiple levels by selecting some representative points from the

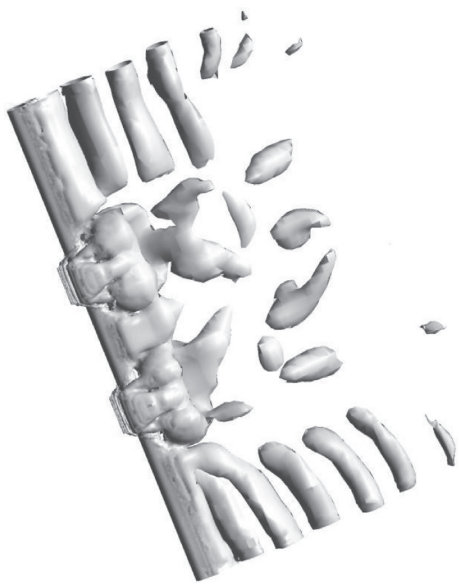

Figure 9: Vortex cores (with spoilers).

comprehensive test according to the orthogonality. Orthogonal experimental design can significantly reduce the number of tests; that is because the selected representative points have the characteristics of uniform dispersion. Therefore, this method has been widely used in a multitude of fields.

To explore the influence of H, B, and S on the vortex shedding frequency, five different levels (No. 1–5) are set for each factor. 125 (5^3) groups of numerical experiments need to be carried out if the conventional method of control variates is adopted, which will consume an abundance of computing resources and time on account of the complexity and high consumption of resources of the 3D simulation wind field. Therefore, the orthogonal experimental design and some representative experiments are employed to optimize the simulation scheme.

Set $H = a\ D$, $B = bH$, and $S = c\ D$ with the intention of facilitating the research and expression. Consequently, Table 2 displays the factors a, b, and c with five levels. We optimize the experiment scheme via applying a $L_{25}(5^2)$ orthogonal experiment table, and the simulation number is reduced from 125 to 25, of which the simulation scheme is shown in Table 3.

H, B, and S are rounded upward for the convenience of processing in practical engineering. The evaluation index of the suppression effect is measured by the vortex shedding frequency f_s, and FLUENT is employed to perform 25 numerical tests with the same calculation method in Section 1. Case No.12 is designated as an example to demonstrate the simulation process. The levels of the factors a, b, and c are 2, 2, and 3, respectively, and $a = 0.65$, $b = 1.5$, $c = 10$, i.e., $H = a\ D = 100$ mm, $B = bH = 150$ mm, and $S = c\ D = 1600$ mm. In order to reduce the amount of calculation, the height of the calculation domain is set as 6 m, as shown in Figure 10, and two spoilers are installed for parametric analysis.

The lift coefficient C_l is obtained from the simulation results, and the vortex frequency f_s can be obtained from the PSD of C_l. The results of the 25 cases are set out in Figure 11. The value above the blue bar is the vortex frequency f_s of each case, and the red horizontal line indicates the vortex frequency without spoilers; i.e., $f_s = f_n = 6.3$ Hz. It can be seen that there are apparent suppression effects in every case, verifying the effectiveness of the spoilers again. Theoretically, the greater the difference between f_s and f_n, the better the suppression effect. For the convenience of designers, the vortex frequency f_s is linearly converted to the corresponding score SC; i.e., $SC = 100 - 100 f_s / f_n$. The limit f_s is 0 Hz, and $SC = 100$. Figure 11 is converted to Figure 12 with this rule.

Table 2: Factors and levels.

Level	Factors		
	a	b	c
1	0.2	1	5
2	0.65	1.5	7.5
3	1.1	2	10
4	1.55	2.5	12.5
5	2	3	15

3.2. Result Analysis. In order to further analyze the contribution of various factors and levels to the suppression of vortex shedding, the extremum difference analysis method with the advantages of simple calculation and intuitive image is applied to analyze the results of the orthogonal experiments, including calculation and judgment. The calculation includes the extremum difference and experiment indexes. The extremum difference can be calculated by

$$R_j = \max\left(K_{j1}, K_{j2}, K_{jm}\right) - \min\left(K_{j1}, K_{j2}, K_{jm}\right) \quad j = a, b, c\ m = 1, 2, 3, 4, 5, \tag{2}$$

where K_{jm} is the sum of the experiment indexes corresponding to the m level of the factor j, i.e., the sum of SC, and R_j is the extremum difference of the factor j.

The optimal level of the factor j and the optimal level combination of each factor can be judged by the size of K_{jm}. R_j reflects the change range of the experiment index when factor j level changes. The larger the R_j is, the greater the influence of this factor on the index is, and the more paramount it is. Consequently, the primary and secondary factors can be judged according to the size of R_j. The calculation and judgment of the extremum difference analysis are directly carried out in Table 4.

For the sake of more intuitively reflecting the influence law and trend of each factor and level on f_s, the trend chart of level and K_{jm} is drawn with level as abscissa and K_{jm} as ordinate, as shown in Figure 13.

4. Design Method and Numerical Verification

4.1. Practical Design Method. According to the magnitude of extreme difference, the primary and secondary sequence of the three factors is $a > b > c$, i.e., $H > B > S$. The optimal level

Table 3: Simulation scheme.

Case number	Factors		
	a	b	c
1	1	1	1
2	2	5	1
3	3	4	1
4	4	3	1
5	5	2	1
6	1	2	2
7	2	1	2
8	3	5	2
9	4	4	2
10	5	3	2
11	1	3	3
12	2	2	3
13	3	1	3
14	4	5	3
15	5	4	3
16	1	4	4
17	2	3	4
18	3	2	4
19	4	1	4
20	5	5	4
21	1	5	5
22	2	4	5
23	3	3	5
24	4	2	5
25	5	1	5

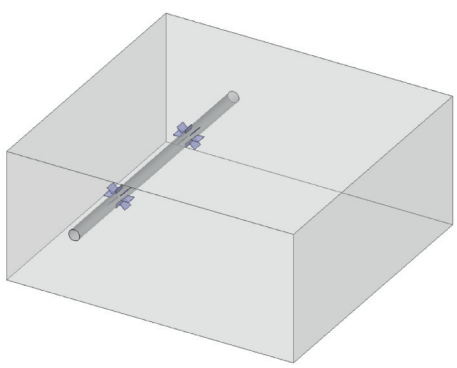

Figure 10: The calculation domain (with spoilers, case No. 12).

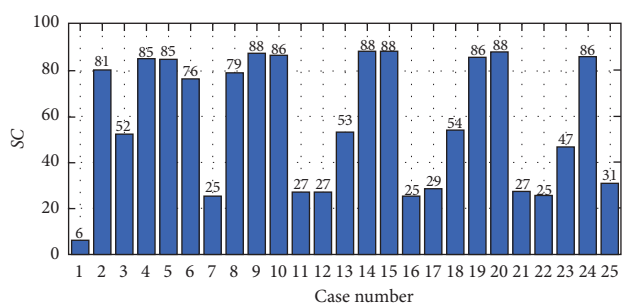

Figure 12: The values of SC with different case number.

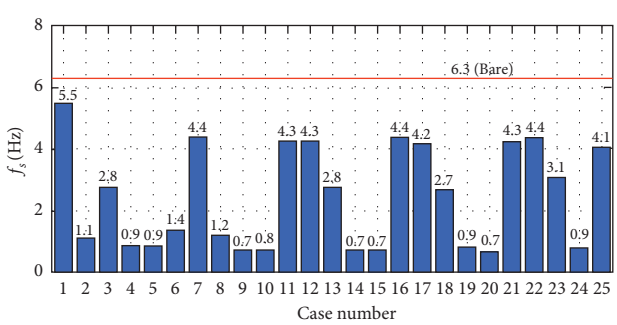

Figure 11: The values of f_s with different case number.

Table 4: Result analysis.

Index	Factors		
	a	b	c
K_{j1}	161	201	309
K_{j2}	187	328	354
K_{j3}	285	274	283
K_{j4}	433	278	280
K_{j5}	378	363	216
R_j	272	162	138
Primary and secondary order	1	2	3
Best level combination	4	5	2

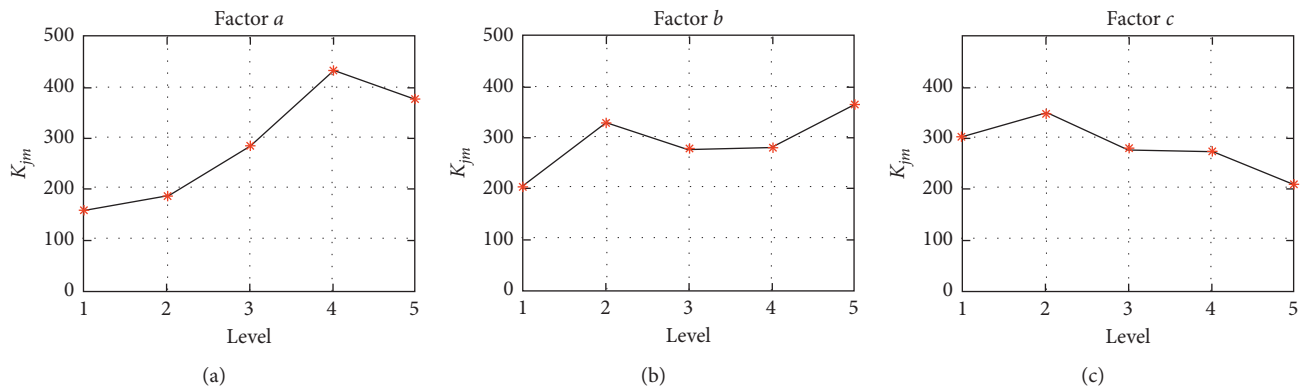

Figure 13: The level and K_{jm} trend diagrams of each factor. (a) Factor a. (b) Factor b. (c) Factor c.

combination is the fourth level of factor a, the fifth level of factor b, and the second level of factor c; i.e., $H = 1.55\ D$, $B = 3H$, $S = 7.5\ D$. Vortex shedding does not need to be completely suppressed for practical engineering design, only to keep the vortex shedding frequency away from the member's natural frequency. Generally, the 50% suppression effect meets the engineering requirements, and the corresponding score SC is greater than or equal to 250 points. Therefore, the design method of the spoiler is as follows according to the trend diagram:

$$H = 1\ D \sim 2\ D, \tag{3}$$

$$B = 1.5H \sim 3H, \tag{4}$$

$$S = 5\ D \sim 12.5\ D. \tag{5}$$

Based on the previous research, the design process of the spoiler is sorted out, as proved in Figure 14. Firstly, the outer diameter D of the tubular member is determined; then the height H and width B of the spoiler are determined according to equations (3) and (4); then the distance S between the adjacent spoilers is determined according to equation (5). Additionally, the number m of the spoilers is determined combined with the length L of the member.

The parameter m should satisfy the following formula: $mB + (m-1)S < L$, i.e., $m < (L+S)/(B+S)$, and it is rounded down to avoid the spoilers being too close to the gusset plate. When m is even, one spoiler is set on both sides at the distance $S/2$ from the center, and then every S is evenly set on both sides. When m is odd, one spoiler is set in the center of the member, and then every S is evenly set on both sides.

4.2. Numerical Verification

4.2.1. Example 1. To validate the applicability of the design method, the tubular members used in Deng's wind tunnel test are selected [22]. The basic parameters are as follows: $D = 70$ mm, $L = 4598$ mm, the slenderness ratio $\lambda = 200$, and the joint style is the same as Figure 2. According to the design method proposed in the previous section, the size of

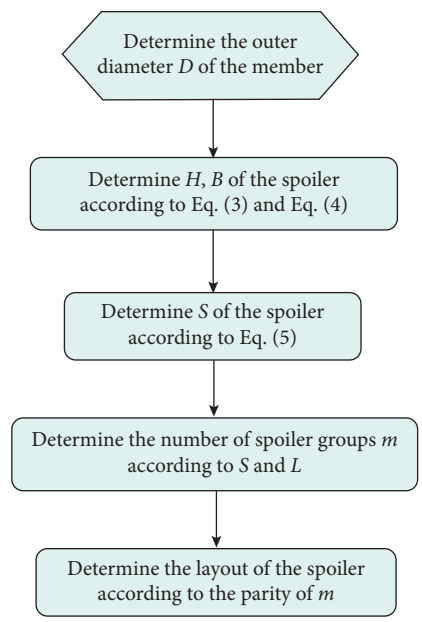

Figure 14: Design process of the proposed spoiler.

the spoilers is selected as $H = 1.5\ D = 105$ mm, rounded up to 110 mm, $B = 2\ H = 220$ mm, $S = 12.5D = 875$ mm, rounded up to 900 mm; the layout scheme is demonstrated in Figure 15.

In Deng's wind tunnel test, the wind speed is 3.5 m/s when the VIV occurs, and the amplitude in the weak transverse direction is the largest. The natural frequency in the weak transverse direction is 10.2 Hz. On employing the method in Section 1, the height of the first mesh layer is 4.82×10^{-5} m, and iteration time step is 2×10^{-4} s. Figure 16 displays the comparison of the lift coefficient and its PSD before and after the installation of spoilers. The vortex shedding frequency is 10.28 Hz without the spoilers, which is close to the member's natural frequency. After the spoilers are installed, the vortex shedding frequency is reduced to 2.27 Hz, which is away from the member's natural frequency.

4.2.2. Example 2. In addition, the auxiliary member with a small slenderness ratio is selected to verify the effectiveness of the method. The basic parameters are as follows:

Figure 15: The layout of Example 1.

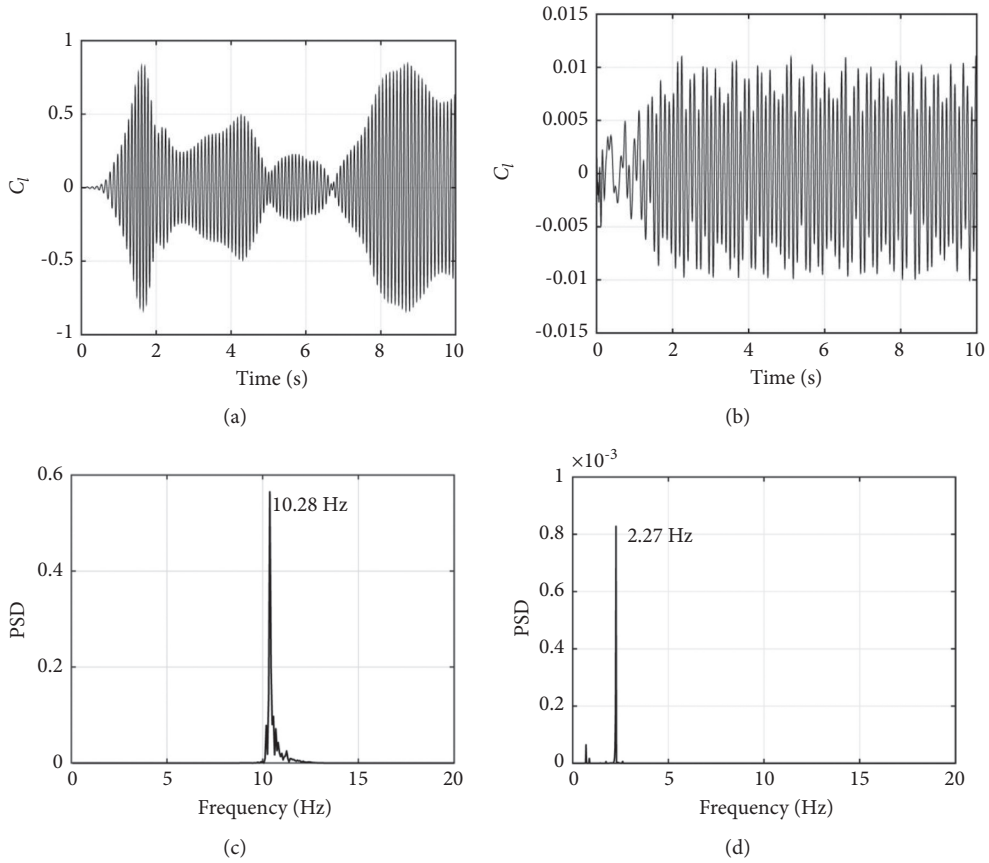

Figure 16: Comparison of lift coefficient and PSD with and without spoilers for Example 1. (a) Time history of lift coefficient (bare). (b) Time history of lift coefficient (with spoilers). (c) PSD of the lift coefficient (bare). (d) PSD of the lift coefficient (with spoilers).

Figure 17: The layout of Example 2.

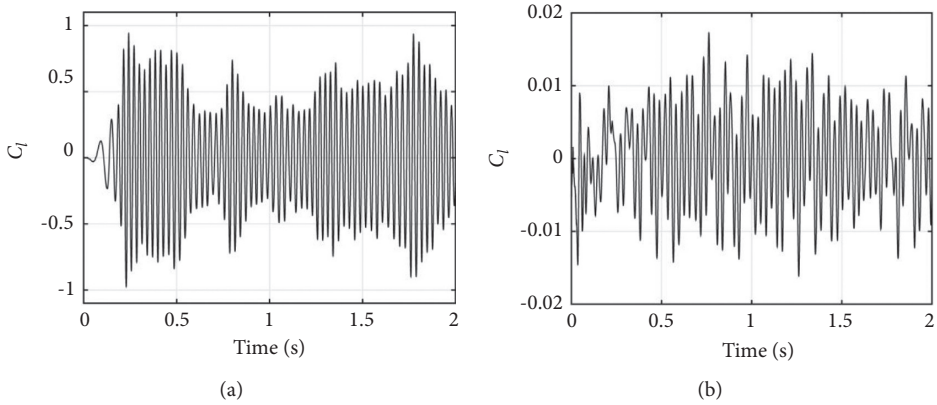

Figure 18: Continued.

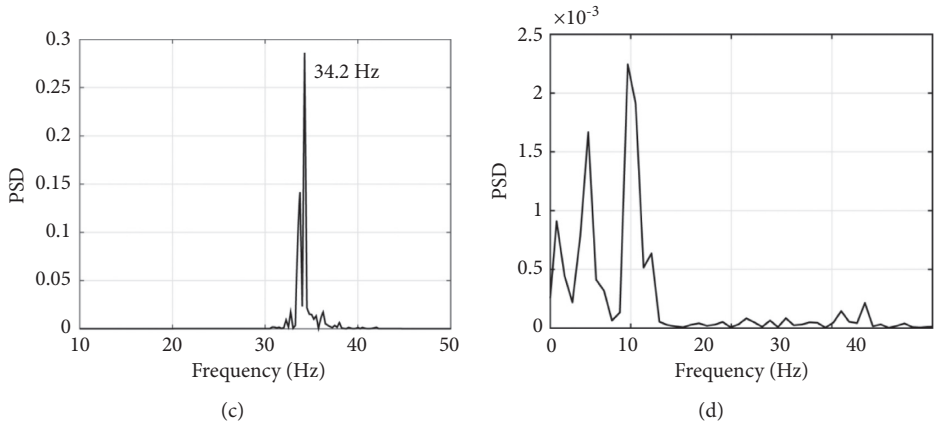

Figure 18: Comparison of lift coefficient and PSD with and without spoilers for Example 2. (a) Time history of lift coefficient (bare). (b) Time history of lift coefficient (with spoilers). (c) PSD of the lift coefficient (bare). (d) PSD of the lift coefficient (with spoilers).

$D = 70$ mm, $L = 2354$ mm, the slenderness ratio $\lambda = 100$, and the joint style is the same as Figure 2. The natural frequency in the weak transverse direction is 34.19 Hz. The spoiler scheme is the same as case 1 due to the same diameter, as shown in Figure 17.

Figure 18 compares the lift coefficient and its PSD with and without the spoilers. The vortex shedding frequency is 34.2 Hz without the spoilers, which is close to the natural frequency of the member, and the VIV occurs, while the dominant frequency of vortex shedding frequency is reduced to 10 Hz installing the spoilers, and the VIV is suppressed.

In the above two cases, the suppression effects of VIV are all obvious, proving the effectiveness of the quick design method, which can be widely used in practical engineering.

5. Concluding Remarks

This study proposed a new type of radial spoiler to suppress the VIV of tubular towers. The suppression mechanism of the spoilers is revealed. Meanwhile, the effectiveness is verified with the aid of numerical simulation method. Then, the practical design method is given based on the parametric analyses of the height H, length B, and distance S conducted by the orthogonal experiment. Finally, the applicability of the design method is verified by two examples. The main conclusions can be summarized as follows:

(1) The new type of spoilers can effectively suppress the VIV of tubular members, and the suppression mechanism is that the spoilers can destroy the vortex structures and reduce the vortex shedding frequency.

(2) The recommended values of H, B, and S are $1D$~$2D$, $1.5H$~$3H$, and $5D$~$12.5D$, respectively. The design scheme of the spoiler can be obtained through the outer diameter D of the member quickly.

(3) The applicability of the design method is verified through two examples, and the results show that the design method is simple and reliable, which provides a new idea for the prevention and control of VIV in tubular towers.

Data Availability

The data of member dimensions and numerical simulations used to support the findings of this study are included within the article.

Conflicts of Interest

The authors declare that they have no conflicts of interest.

Acknowledgments

This research was supported by the Opening Fund of Key Laboratory of New Technology for Construction of Cities in Mountain Area, Ministry of Education (grant no. LNTCCMA-20210112) and the National Natural Science Foundation of China (grant no. 52078104).

References

[1] X. Fu, H.-N. Li, G. Li, Z.-Q. Dong, and M. Zhao, "Failure analysis of a transmission line considering the joint probability distribution of wind speed and rain intensity," *Engineering Structures*, vol. 233, Article ID 111913, 2021.

[2] S. Liang, L. Zou, D. Wang, and H. Cao, "Investigation on wind tunnel tests of a full aeroelastic model of electrical transmission tower-line system," *Engineering Structures*, vol. 85, pp. 63–72, 2015.

[3] L. Tian, J. Liu, C. Chen, L. Guo, M. Wang, and Z. Wang, "Experimental and numerical analysis of a novel tubular joint for transmission tower," *Journal of Constructional Steel Research*, vol. 164, Article ID 105780, 2020.

[4] M. Zhang, G. Zhao, and J. Li, "Nonlinear dynamic analysis of high-voltage Overhead transmission lines," *Shock and Vibration*, vol. 2018, pp. 1–35, 2018.

[5] F. Wang, K. Du, J. Sun, F. Huang, and Z. Xiong, "Shaking table Array tests of an ultra-high-voltage cup-type transmission tower-line system," *Shock and Vibration*, vol. 2019, pp. 1–20, 2019.

[6] X. Fu, H.-N. Li, G. Li, and Z.-Q. Dong, "Fragility analysis of a transmission tower under combined wind and rain loads," *Journal of Wind Engineering and Industrial Aerodynamics*, vol. 199, Article ID 104098, 2020.

[7] G. S. Baarholm, C. Martin Larsen, and H. Lie, "Reduction of VIV using suppression devices—an empirical approach," *Marine Structures*, vol. 18, no. 7, pp. 489–510, 2005.

[8] M. M. Zdravkovich, "Review and classification of various aerodynamic and hydrodynamic means for suppressing vortex shedding," *Journal of Wind Engineering and Industrial Aerodynamics*, vol. 7, no. 2, pp. 145–189, 1981.

[9] P. K. Stansby, J. N. Pinchbeck, and T. Henderson, "Spoilers for the suppression of vortex-induced oscillations (Technical note)," *Applied Ocean Research*, vol. 8, no. 3, pp. 169–173, 1986.

[10] D.-Y. Chen, L. K. Abbas, G.-P. Wang, X.-T. Rui, and W.-J. Lu, "Suppression of vortex-induced vibrations of a flexible riser by adding helical strakes," *Journal of Hydrodynamics*, vol. 31, no. 3, pp. 622–631, 2019.

[11] A. Larsen, S. Esdahl, J. E. Andersen, and T. Vejrum, "Storebælt suspension bridge–vortex shedding excitation and mitigation by guide vanes," *Journal of Wind Engineering and Industrial Aerodynamics*, vol. 88, no. 2, pp. 283–296, 2000.

[12] Y. Jingbo, L. Xilai, D. Songtao et al., "Study on suppression method with dampers against vortex-shedding induced wind vibration of transmission steel tubular tower members," *Building Structure*, vol. 46, no. 14, pp. 30–35, 2016.

[13] H. Deng and Z. Zhao, "Numerical simulation of vortex-induced vibration of steel tubular members in transmission tower," *Journal of Tongji University*, vol. 45, no. 1, pp. 9–15, 2017.

[14] C. H. K. Williamson and R. Govardhan, "A brief review of recent results in vortex-induced vibrations," *Journal of Wind Engineering and Industrial Aerodynamics*, vol. 96, no. 6-7, pp. 713–735, 2008.

[15] X. Fu, H.-N. Li, and T.-H. Yi, "Research on motion of wind-driven rain and rain load acting on transmission tower," *Journal of Wind Engineering and Industrial Aerodynamics*, vol. 139, pp. 27–36, 2015.

[16] P. Parnaudeau, J. Carlier, D. Heitz, and E. Lamballais, "Experimental and numerical studies of the flow over a circular cylinder at Reynolds number 3900," *Physics of Fluids*, vol. 20, no. 8, pp. 212–287, 2008.

[17] J. Franke and W. Frank, "Large eddy simulation of the flow past a circular cylinder at ReD=3900," *Journal of Wind Engineering and Industrial Aerodynamics*, vol. 90, no. 10, pp. 1191–1206, 2002.

[18] X. Fu, W.-L. Du, H.-N. Li, G. Li, Z.-Q. Dong, and L.-D. Yang, "Stress state and failure path of a tension tower in a transmission line under multiple loading conditions," *Thin-Walled Structures*, vol. 157, Article ID 107012, 2020.

[19] C. Norberg, "Flow around a circular cylinder: aspects of fluctuating lift," *Journal of Fluids and Structures*, vol. 15, no. 3, pp. 459–469, 2001.

[20] *Technical Regulations of the Design of Steel Tubular Towers of Overhead Transmission lines National Energy Administration*, Beijing, China, 2011.

[21] Y. Jing-Bo, L. Zheng, and W. Jing-Chao, "Prevention of steel tube UHV transmission tower aeolian vibration," *Electric Power Construction*, vol. 29, no. 9, pp. 10–13, 2008.

[22] H. Z. Deng, Q. Jiang, F. Li, and Y. Wu, "Vortex-induced vibration tests of circular cylinders connected with typical joints in transmission towers," *Journal of Wind Engineering and Industrial Aerodynamics*, vol. 99, no. 10, pp. 1069–1078, 2011.